Structural Performance of Horizontal Axis Wind Turbine Blade

Othman AL-KHUDAIRI

This thesis is submitted in partial fulfilment of the requirements of the University for the Award of PhD

Supervised by:

Associate Professor Homayoun Hadavinia

School of Mechanical & Automotive Engineering

Faculty of Science, Engineering and Computing

Kingston University London

February 2014

Dedicated to

I dedicate this PhD to my grandfather Fakhri Al-Khudairi (died in 2007) who stood there in front of family when I was eight years old, said I would achieve greatness in life and I would be a person to look out for in the future. I also like to dedicate this work to my parents Alaa Al-Khudairi and Suhad Al-Khudairi who funded my PhD and gave me the opportunity to better myself.

Declaration

I Othman Al-Khudairi hereby certify that I had personally carried out the work presented in this thesis entitled Structural Performance of Horizontal Axis Wind Turbine Blade except where otherwise indicated and acknowledged. The work presented is original and has been carried out under supervision of my Director of Study Associate Professor Homayoun Hadavinia.

Signature .....

Othman Al-Khudairi

Student ID K0424132

Date .2. May..2014

Structural Performance of Horizontal Axis Wind Turbine Blade

Othman Al-Khudairi

Submitted for the degree of Doctor of Philosophy

February 2014

Abstract

The power output from a wind turbine is proportional to rotor swept area and as a result in the past 30 years continuous effort has been made to design larger blades. In this period, the blade length has been increased about 10 times since 1980s to present time. With the longest blade currently measuring more than 100m in length, wind turbine blade designers and manufacturers face enormous challenges to encounter the effect of increased weight and other loads on fatigue durability of the blade. Wind turbine blades are mainly made from glass fibre reinforced plastic (GFRP) composite materials. As a result, in the design of various parts of wind turbine blades such as the shear web, spar cap and the aerofoil the fatigue behaviour of FRP materials is required. The performance of these parts as well as the adhesively bonded joint under fatigue loading is crucial for structural integrity of a long lasting blade.

During operation, delamination can initiate and propagate shortening blade life; hence, characterisation of failure envelope of GFRP laminates under different loading mode is necessary. In this regard in this project, quasi-static tests were carried out to find mode I, mode II and mixed mode I/II delamination fracture toughness using DCB, ENF and MMB tests and the fracture envelope was established for various mode mixity.

In the next stage, the stress-lifetime (S-N) diagrams of the GFRP was studied. Fatigue-life experiments on three different types of loading, i.e. tension-tension at R=0.1, 0.5, tension-compression at R=-1 and compression-compression at R=2 and R=10 were performed. From the results of S-N diagrams, the constant life diagrams (CLD) for 90° and 0° fibre directions were constructed. CLD diagrams are useful for prediction of fatigue lifetime for loading condition that no experimental data available.

The analysis of delamination crack propagation under cyclic loading was next area of the research. The onset life and propagation delamination crack growth of 0//0 interface of GRFP laminate in mode I loading using DCB specimens was investigated and the G_{Ith} from the onset life test was determined. From the fitted curve to mode I experimental propagation data the Paris' law coefficient for the laminated GFRP in mode I was determined.

The mode II fatigue crack growth in laminated 0//0 GFRP material was also investigated using ENF specimens. The fatigue behaviour in this mode is analysed based on application of Paris' law as a function of energy release rate for mode II loading. From the fitted curve to experimental data, the Paris' law coefficient for the laminated GFRP in mode II was determined. The effect of fatigue delamination growth on fracture surface was studied by fractography analysis of SEM images of fracture surfaces.

Studying the behaviour of GFRP under cyclic loading and delamination under static and dynamic load led to full-scale testing of wind turbine blade to establish damage tolerance of the blade under cyclic loading. The sensitivity of wind turbine blade to damage has considerable interest for turbine operators and manufacturers. For full-scale fatigue testing, calibration test and modal analysis of a 45.7m blade has been done and moment-strain diagram and natural frequencies of the blade were obtained. Next, the blade sensitivity to damage under fatigue loading was investigated. The blade has been damaged intentionally by initially inserting a crack of 0.2m between the shear web and spar cap and later it was extended to 1m. The effect of these damages on the modal shape, natural frequencies and strains at various locations of the blade were investigated. The damaged blade fatigue tested, the structural integrity and growth of damage were monitored, and the results were discussed.

Finally for the improvement of delamination resistance for joints between spar beam and aero-shell stitching method was used. T-beam and box beam joint were chosen as the platform for testing the stitching effect on the delamination. Various pattern of stitching was applied and the optimum pattern was determined.

List of Publications

Al-Khudairi O., Hadavinia H., Ghasemnejad H., Lewis E., (2014), Characterisation of fatigue behaviour of GFRP composite laminate of wind turbine blade. International Conference on Composite Materials and Renewable Energy Application, (ICCMREA), Tunisia.

Mitchell S., Al-Khudairi O., Volkov K., Hadavinia H., (2014), Aerodynamic characteristics of a single aerofoil for vertical axis wind turbine blades, Journal of Renewable Energy, submitted.

Al-Khudairi O., Hadavinia H., Lewis E., Osborne B. and Bryars L. S., (2013) Chapter 12: Building Delamination Fracture Envelope under Mode I/Mode II Loading for FRP Composite Materials. In Advanced Composite Materials for Automotive Applications: Structural Integrity and Crashworthiness, pp. 293–310. Editor Ahmed Elmarakbi. Publisher: Wiley; 1 edition, ISBN: 978-1-118-42386-8.

Al-Khudairi O., Hadavinia H., Lewis E., Osborne B. and Bryars L. S., (2012), Determining Fracture Envelope of Laminated FRP Composite for Application in Horizontal Axis Wind Turbine Blade. The XVII International Conference on Mechanics of Composite Materials (MCM2012), Latvia, 2012.

Acknowledgments

This dissertation is the result of four years of hard work. During those years, my life has completely changed. For that first and most of all I would like to thank my Director of Study Associate Professor Homayoun Hadavinia who recommended and supervised this project. He continuously guided me through my PhD, the queries that I came across and always being available when I needed help. I would also like to thank my supervisory team Dr Konstantin Volkov for his guidance with CFD simulation, Dr Hessam Ghasemnejad for his help in Chapter 7 and I would like to convey my sincere gratitude to Mr Eoin Lewis for his assistance at various levels in the course of my study.

I would like to thank Alex Vine for helping me in various mechanical testing, Cliff Searle for assisting me in wind tunnel tests, Richard Gidden for SEM analysis, technical staff John MacBean, Dean Wells, Martin Theobald and David Haskell in the machine shop and Barry Wade in the auto lab at School of Mechanical & Automotive Engineering in Kingston University.

Special thanks to all who were involved at the National Renewable Energy Centre (NaREC) in UK for full scale testing of wind turbine blade in my project. That made my mind open to industrial aspect of full scale testing of the blade and this thesis would not have been the same without the work carried out at NaREC.

I would also like to thank the library staff at Kingston University for helping me to find the information I needed and how to reference my work accordingly.

Finally I enjoyed working and having good time with my friends Joko Sedyono, Fatih Dogan, Alex Kustalan, Ahmad Maleki and Vanessa Izzard.

Othman Al-Khudairi (MSc, BEng)

Kingston University London

4 February 2014

Table of Contents

List of Figures

List of Tables

1

Introduction

Until the early 1970s, wind power was mainly used to provide mechanical power to pump water or to grind grain. At the beginning of modern industrialization, the use of the unsteady wind energy resource was substituted by fossil fuel fired engines which provided a more consistent and stable power source distributed by the electrical grid [1].

The two oil embargoes of 1973 and 1979 and the awakening green movement in the Western societies gave a real boost to the Danish wind turbine industry and set the stage for the present era of wind power. The search for new sources of energy such as wind power to provide electrical energy has increased and the latter half of the 20th century saw spectacular changes in the technology. Blades that had once been made of sail or sheet metal progressed through wood to advanced fibre reinforced polymer (FRP) composites.

The first wind turbines for electricity generation had already been developed at the beginning of the 20th Century. During 1974-1985 the NASA wind turbines were developed under a program to create a utility-scale wind turbine industry in the U.S. The details of various designs are shown in Figure 1.1. In total 13 experimental wind turbines were made in four

major different wind turbine designs. This research and development program pioneered many of the multi-megawatt turbine technologies, including: steel tube towers, variable-speed generators, FRP composite blades, partial-span pitch control, as well as aerodynamic, structural, and acoustic engineering design capabilities. The large wind turbines developed under this effort set several world records for diameter and power output. For the first time sectioning of the blade was used in the design of two-blade rotor MOD-5B that enabled easy transport of the blades. The cluster of three 2.5 MW MOD-2 wind turbines produced 7.5 MW of power in 1981. The 4 MW WTS-4 held the world record for power output for over 20 years. In 1987, the MOD-5B at rated power 3.2 MW was the largest wind turbine operating in the world with a rotor diameter of nearly 100m. Although the later units were sold commercially, none of the two-bladed machines were ever put into mass production. From 1980 through the early 1990s the oil price declined by a third and many turbine manufacturers left the business. The commercial sales of the NASA/Boeing Mod-5B, for example, came to an end in 1987 when Boeing Engineering and Construction announced they were "planning to leave the market because low oil prices are keeping windmills for electricity generation uneconomical."[2]

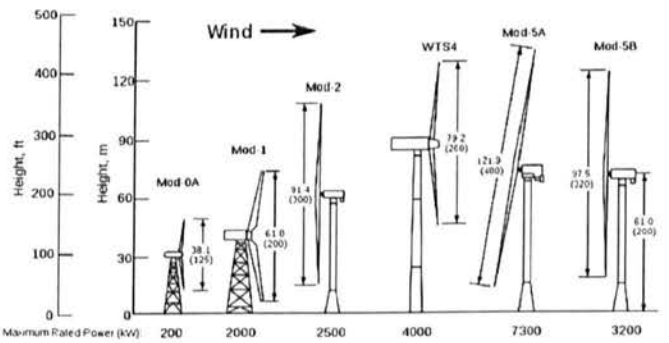

Fig. 1.1. Comparison of NASA wind turbines [2].

As the 21st century began, fossil fuel was still relatively cheap, but rising concerns over energy security, global warming, and eventual fossil fuel depletion led to an expansion of interest in all available forms of renewable energy. The fledgling commercial wind power industry began expanding at a robust growth rate of about 30% per year, driven by readily available of wind resources, and falling costs due to improved technology. The steady run-up in oil prices after 2003 led to increasing fears that peak oil was imminent, further increasing interest in commercial wind power.

Wind energy technology itself has moved very fast towards new dimensions. At the end of 1989, 300 kW horizontal axis wind turbine (HAWT) with a 30m rotor diameter was the state-of-the-art. Only 10 years later, 1500 kW turbines with a rotor diameter of about 70m were available from many manufacturers. Several projects using 2 MW wind turbines with a rotor diameter of 74m was installed at the end of the last century. In 2006, Kensche *et al.* developed 5 MW class wind turbine blade in Germany [3]. The latest wind turbines Enercon E126 with a capacity of 7.5 MW output have been developed in Germany with a 127m rotor diameter [4]. However so far the world's longest turbine blade at almost 85m is Samsung's 7MW installed in Scotland. At the end of the first half of 2013, worldwide wind capacity has reached 296 GW, 318 GW expected for full year [5]. Note that HAWT has a maximum achievable efficiency of 59.3% (Betz limit). This maximum theoretical efficiency has yet to be achieved.

Figure 1.2 shows the average wind speed across Europe at 50m above sea level, indicating that north of Great Britain and south of France produces wind at speeds greater than 7.5 m/s and the lowest wind speeds are around northern Italy and east of France at less than 4.5 m/s.

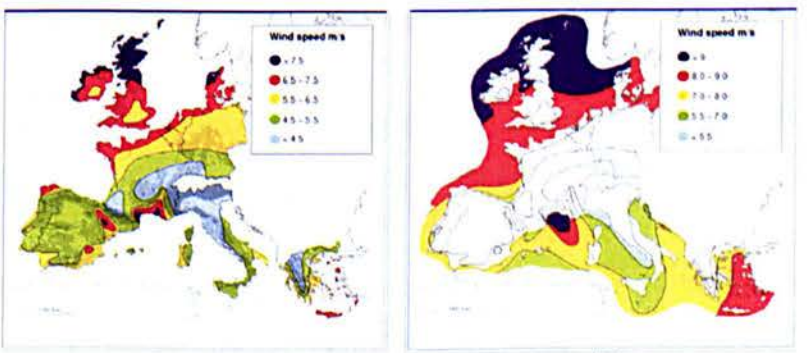

(a) (b)

Fig. 1.2. Wind condition at 50m height (a) Onshore (b) Offshore [6]

Figure 1.3 shows the offshore wind potential in Europe by 2020. This shows that as a whole wind energy has great potential in the EU. The United Kingdom and Germany are estimated to produce more energy from wind than any other country across Europe.

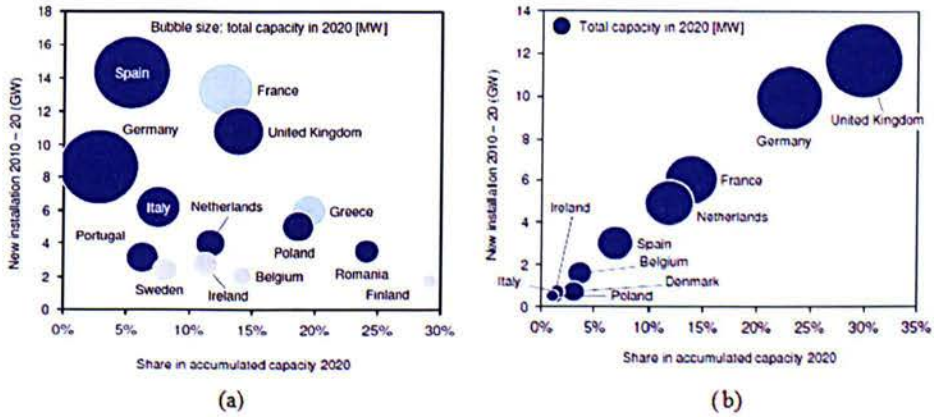

Fig. 1.3. Wind potential in Europe by 2020: (a) Onshore (b) Offshore [7]

The EU passed the 100 GW milestone in 2012, adding a record 11.9 GW of wind capacity in 2012 for a total exceeding 10.6 GW. By the end of 2012 Germany remained Europe's largest market, rebounding strongly with its highest installations in a decade (2.4 GW), for a total of 31.3 GW. The U.K. ranked second for new installations in Europe for the second year running, adding 1.9 GW (45% offshore) for more than 8.4 GW by year's end; it now ranks third regionally for total capacity, behind Germany and Spain, and sixth globally. The U.K. plans to almost triple the amount of wind capacity by 2020 to meet the target of getting 15 percent of power demand from renewable energy sources. [8]

Global demand for renewable energy continued to rise throughout 2011 and 2012, supplying an estimated 19% of global final energy consumption in 2011 (the latest year for which data are available), with a little less than half from traditional biomass. Useful heat energy from modern renewable sources accounted for an estimated 4.1% of total final energy use; hydropower made up about 3.7%; and an estimated 1.9% was provided by power from wind, solar, geothermal, and biomass, and by biofuels. [8]

Total renewable power capacity worldwide exceeded 1,470 GW in 2012, up about 8.5% from 2011. Globally, wind power accounted for about 39% of the renewable power capacity added in 2012, followed by hydropower and solar PV, each accounting for approximately 26%.

Figure 1.4 shows the world total installed wind turbine energy capacity at the end of first half of 2013. It is estimated that wind energy will provide up to 8% of the world's electricity consumption by 2020.

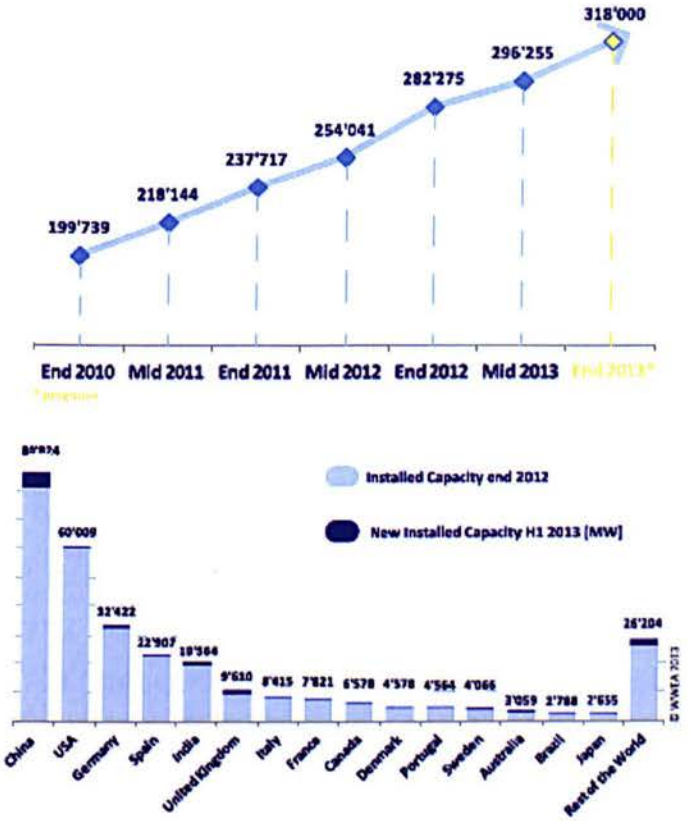

Fig. 1.4. Total installed global wind power capacity 2010-2013 (MW) [5]

1.1 Background to blade structure

Turbine designs continue to evolve in order to reduce costs and/or optimise performance, with trends towards longer blades, new materials such as glass and carbon fibre for blades whilst working at places with lower wind speeds. As a result, in the design of wind turbine blades the selection of materials and aerodynamic shape are fundamental. The requirements for blade's material are to be stiff, strong and light. The blade shape should be aerodynamics to provide maximum lift and minimum drag.

Imagine there is a flexible wheat stalk in a field bending under the influence of the wind as depicted in Figure 1.5. By cutting the wheat stalk, inside will be seen a cylindrical thin-walled, hollow structure common in many plants. The stalk evolved to become as it is, because in this way it could withstand the wind by large displacements. The turbine blade can be compared with a wheat stalk as shown in Figure 1.5. They have certain structural similarities: Both structures experience large displacements caused by wind forces, where the wheat stalk and the blade bend due to both drag and lift forces. Therefore wind turbine blades

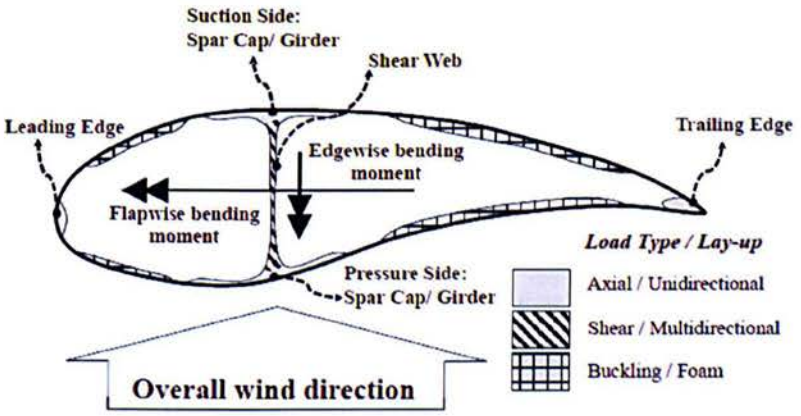

Fig. 1.6. Typical cross section of a wind turbine blade [10].

To get a building permit for the wind turbine, a certificate for its design is required. This certificate is delivered when the design requirements with respect to standards and guidelines used in wind energy are fulfilled. IEC 61400-1 and Germanischer Lloyd (GL) 2010 are two of such guidelines which are widely accepted and referred to in designing a wind turbine or any of its components for onshore applications. Most of the load calculations and design criteria are assessed using IEC-61400-1 [11].

The design of a wind turbine components start with loads analysis in the structure so as to have a check on its engineering integrity. The purpose of load analysis is to ensure no physical damage occurring in a wind turbine and its components during the entire lifetime. To be able to do a load analysis, a wind turbine site and its conditions need to be defined based on the selected location of the wind turbine. The collected wind history data are applied in the simulation of the wind turbine to check the integrity of the turbine during its planned lifetime.

Aerodynamics, structures, materials and production methods are four major pillars in wind turbine design. In the context of structure and aerodynamics, a wind turbine blade can be considered a crucial component in a wind turbine package, governing its cost and energy production. Primarily, its design is driven by the aerodynamic requirements (due to its direct impact on efficiency and power production), but economics (and mass) mean that the blade shape is a compromise to keep the structure robust, materials cheaper and lighter, and cost of construction (production) reasonable. In a nutshell, the choice of materials and manufacturing process will also have an influence on how thin (hence aerodynamically ideal) and complex the blade can be built. For example, carbon fibre material is stiffer and stronger than infused

have to be light and flexible and thus they are slender, thin-walled, and hollow. The structural difference of the blade compared to the stalk, is that the shape is not cylindrical but rather a rectangular hollow beam encased with an aerofoil shape shell. In both cases, this similarity in evolution conveys the importance of good structural design [9].

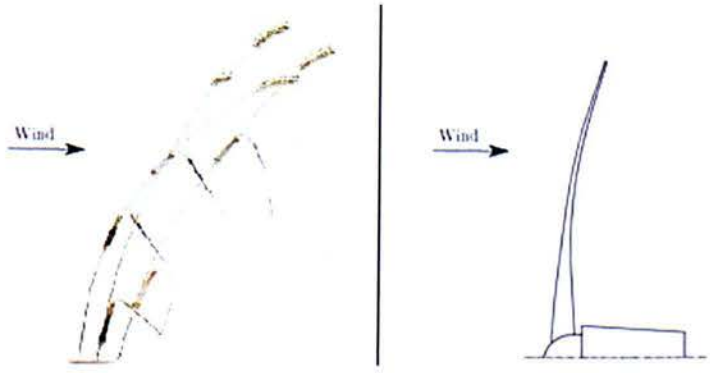

Fig. 1.5. Analogy between a wheat stalk and a wind turbine blade [9].

A wind turbine blade is predominantly loaded in flapwise and edgewise direction and its cross section can be divided into load carrying parts, and parts that are geometrically optimized for aerodynamic performance. However, in the design of wind turbine blade, there is a compromise between structural integrity and aerodynamic performance. The flapwise loads are mainly carried by the spar whilst edgewise loads are taken partially by spar and partially, if present, by reinforcement in the leading and trailing edges. Usually shear webs that connect the two spar caps are made from sandwich structures. They are made of skins from bi-directional FRP laminate with a core in the middle, and provide shear strength to the blade. The remainder of the blade is constructed from multi-directional FRP material and sandwich structure with FRP skin layers and a core material from foam or balsa wood in between, ensuring aerodynamic geometry, low mass, resistance to torsion and high buckling resistance. As can be seen from Figure 1.6 in the area where the spar caps support the shell, no foam exists in the sandwich structures. This is beneficial as it allows the spar caps to be better separated to carry the bending loads and hence is beneficial from both cost and strength perspective. Figure 1.6 indicates the load bearing cross section of a typical wind turbine blade [10].

glass fibre along the fibre direction but manufacturing and cost constraints might prevent it from being used in an actual application. Hence it is important to consider an integrated approach while designing wind turbine blades.

1.2 Research objectives

The long-term onshore wind farm practice has shown that blade failures account for about 10% of all wind turbine failures reported [12,13] and result in over 15% of total downtime of the turbines [14,15], which means a significant revenue loss to operators.

The main factors in design of large wind turbine blades are blade stiffness, light weight, long lifespan, and the cost/kW power production. Over the years since the start of regeneration of wind turbine back in 1970, many contributions from industry and academics have helped to address some of these issues, such as the most important factors to be dealt with when up-scaling blades. Work on material characterization and load mitigation and health monitoring techniques have also contributed to finding ways of extending or monitor blade life.

The objectives of this thesis are focused on structural performance and damage tolerance of wind turbine blades and to characterise delamination behaviour in GFRP material under monotonic and fatigue loading.

1. The quasi-static delamination in Mode I, Mode II and mixed Mode I/II are investigated by testing double cantilever beam (DCB), end notched flexural (ENF) and mixed mode bending (MMB) specimens under monotonic loading. So far the majority of research work on delamination has been done under monotonic loading and there are few published works on delamination under fatigue loading.
2. The delamination under dynamic cyclic loading in Mode I, Mode II are investigated by fatigue testing double cantilever beam (DCB) and end notched flexural (ENF) specimens. Initiation threshold toughness and propagation are characterised in this part of the work.
3. GFRP materials are the preferred materials in large wind turbine blades structures and as the blades are expected to endure 10^8-10^9 cycles in their service life, the fatigue characterisation of GFRP for load ratios of tension-tension; tension-compression and compression-compression investigated and the S-N diagram are obtained. The constant life diagram (CLD) of the GFRP is extracted from S-N diagrams.

4. The damage tolerance of large scale wind turbine blades is examined by carrying out tests on a full scale wind turbine blade at a length of 45.7m. For the full scale blade, modal analysis testing, calibration pull test and fatigue testing are investigated. By inserting a crack in the blade the frequency response and strain gauge readings are used to monitor the deterioration of the health of the blade. Acoustic emission and crack visualisation are also used to monitor the behaviour of the crack propagation on the blade throughout the experiments.

5. Strengthening the blade's structure using stitching technique is explored. The through-thickness strength of joints in the blade is examined by various stitching pattern and an optimum pattern is found.

1.3 Research layout

This thesis is organised in 9 chapters as described below:

Chapter 1: covers a short summary of the role of HAWTs in energy supply and an outlook on the future growth of wind power and set objectives of the project and the outline of the thesis.

Chapter 2: presents a literature review on the history of wind technology, operation of wind turbines, aerodynamic sources of fatigue loading, different loads applied on wind turbine blades, material requirements on wind turbine blades, historical damage and failures of wind turbine blades, full scale wind turbine blade testing, design load-envelope testing, blade testing methods, literature review of fatigue testing on HAWT blades, fatigue test control methodology and fatigue analysis of wind turbine blade.

Chapter 3: addresses characterisation of laminated FRP composite under modes I, mode II and mixed mode loading. In this work, three different types of experiment are used to measure the delamination fracture toughness i.e. for mode I- Double Cantilever Beam (DCB) test, for mode II- End Notch Flexure (ENF) test and for mixed mode I/II- Mixed Mode Bending (MMB) test. The failure envelope for selected laminated GFRP was found under various loading modes.

Chapter 4: deals with fatigue performance of GFRP in three different types of loading, i.e. tension-tension at R=0.1, 0.5, tension-compression at R= -1 and compression-compression at R= 2 and R=10. The Constant Life Diagram (CLD) for 0° and 90° fibre directions are obtained. During cyclic loading of the blade there is always the possibility of delamination growth. In this chapter delamination fatigue crack growth in Mode I using DCB specimen and in Mode II using ENF specimen, has been studied. Threshold delamination fracture toughness was measured according to ASTM fatigue onset life test and constant amplitude cyclic displacement fatigue test was conducted to establish the delamination growth rate as a function of maximum cyclic energy release rate. The material constants for total life delamination growth rate were obtained from the tests.

Chapter 5: discusses calibration and modal testing of large scale wind turbine blade for uncracked and cracked blades. In each case the blades natural frequencies were obtained for the fatigue testing of a full blade.

Chapter 6: presents fatigue testing of a full scale wind turbine blade by placing a resonant exciter on the blade. Resonance occurs when the blade's natural frequency (due to its structural and inertial properties) matches the frequency of external excitation. Sensitivity of the blade to damage under fatigue loading has been examined and the results presented.

Chapter 7: covers failure behaviour of composite materials in the skin-stiffener of wind turbine blade structures. Laminated composite beams were stitched using synthetic fibres and the mechanical performances of the joints were investigated. Four different joints of bonded T-beam; stitched T-beam; bonded box-beam and stitched box-beam were studied. These specimens were tested under quasi-static loading condition to compare the failure resistance of adhesive and stitched bonding methods.

Chapter 8: provides the overall conclusion of research performed and some recommendations for future work have been suggested.

1.4 References

[1] Ackermann, T. and Soder, L., (2000) Wind energy technology and current status, Renewable and Sustainable Energy Reviews, Vol.4, pp315-374.

[2] NASA wind turbines, http://en.wikipedia.org/wiki/NASA_wind_turbines.

[3] Kensche W.C., (2006) Fatigue of composite for wind turbines, International Journal of Fatigue 28 1363-1374.

[4] Enercon, Magazine for wind energy, Issue 04, 2007.

[5] 2013 Half-year Report, The World Wind Energy Association (WWEA).

[6] European wind atlas, Riso.

[7] Fact Book Renewable Energy, RWE, 2013.

[8] REN21. 2013. Renewables 2013 Global Status Report

[9] Rosemeier M., (2013) Non-linear ultimate limit state analysis of a wind turbine blade, Master's thesis, Denmark Technical University (DTU).

[10] Nijssen R., (2006) Fatigue life prediction and strength degradation of wind turbine rotor blade composites, Ph.D. dissertation, TU Delft.

[11] WindTurbines- Part 1: Design Requirements, IEC, Geneva, Switzerland Std. IEC 61 400- 1, Rev. Edition 3.

[12] Tavner. P. J, Xiang. J, and Spinato. F, (2007) Reliability analysis for wind turbines, Journal of Wind Energy, Vol. 10(1), pages 1–18, 2007.

[13] Ribrant J., and Bertling L., (2007) Survey of failures in wind power systems with focus on Swedish wind power plants during 1997-2005, IEEE Transactions on Energy Conversion, EC22 (1), pp. 167-173.

[14] Winstats Newsletter, vol. 17, no. 2, Forlaget Vistoft, Spring 2004.

[15] Tavner P. J., (2012) Offshore wind turbines: Reliability, availability & maintenance, ISBN: 978-1-84919-229-3, IET Press.

2

Literature Review

2.1 Introduction

Wind turbine blades have been increased in size since 1985, reported at 15m in diameter and currently over 180m in diameter. During this period our knowledge has also increased about various wind turbines problems.

The power train components of a wind turbine are subjected to a highly irregular loading condition. Turbine blades are prone to fatigue since they are long and slender with very a high aspect ratio and as they are cantilevered at the root end, create high bending moments at their root. The actual loads that contribute to fatigue of a wind turbine originate from a variety of sources. These include steady loads from high winds; periodic loads from wind shear, yaw error, yaw motion, gravity; stochastic loads from turbulent flow; transient loads from such events as gusts, starts and stops, and resonance-induced loads from vibration of the structure. As a result the number of fatigue cycles experienced by the blades is of orders of magnitude greater than other rotating machineries. The design lifetime of a modern wind

turbine is 20 to 30 years and the wind turbine is almost always unattended. In comparison a motor vehicle is frequently maintained and has a typical operational life of about 160,000 km, equivalent to 4 months of continuous operation. Thus wind technology has a unique technical identity and unique R&D demands in the level of severity of the fatigue loading. The severity of load in wind turbines is compared with several other structures in Figure 2.1. It is clear the wind turbine has the highest load variability and the least predictability of load and response whilst the number of cycles experienced is the highest [1]. This issue is a challenge in fatigue design of wind turbines.

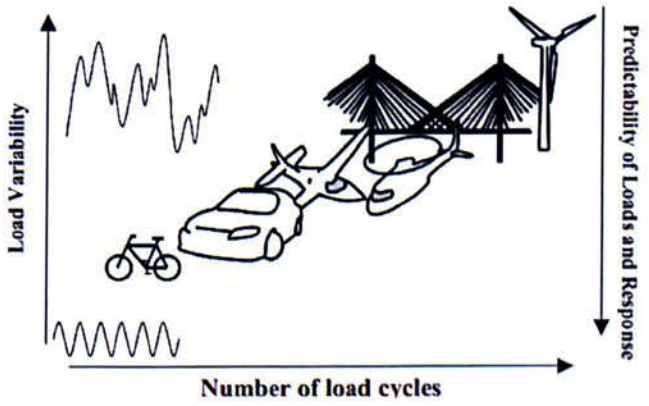

Fig. 2.1. Comparison of load variability and prediction reliability in different structures [1]

During operation, the wind turbine blade is experiences large edgewise and flapwise bending moments plus the self-weight of blade. These loads introduce cyclic stresses in the spar beam, in aero-shell, and in adhesive joints. Inevitably over a long period, delamination between composite plies, debonding along adhesive joints, and splitting cracks along fibres will initiate. As fatigue plays a crucial contribution in blade loading, the designer must reinforce the blade so that it is able to withstand more than 20 years of service. Another design requirement that should be taken into account is that the blade should have sufficient strength to withstand extreme loading conditions. Also the blade bending stiffness must be properly designed to allow minimal clearance between the turbine tower and the blade tip during the operation. Wind turbine blade design requirements are specified by the IEC 61400-1 international specifications [2].

Inspection of wind turbines should be minimised, especially when they are installed offshore, therefore fatigue design of blades is extremely important and should be carried out with great care. Wind turbines are usually designed for a life of 20 to 30 years, during this lifetime the

turbine usually undergoes more than 10^8 load cycles [3]. In Figure 2.2 the lifetime of wind turbines is compared with several other structures. It is impractical to take the blade through so many cycles in laboratory testing because that would take several years to complete. Hence, in laboratory testing an increased load is usually adopted to achieve an equivalent amount of damage accumulated after about 1 million cycles, allowing the testing to be completed in just a few weeks.

Many blades natural frequency is typically below 1 Hz, especially for larger blades it is at or below 0.3 Hz. Even with a frequency of 1 Hz, 10^8-10^9 cycles would take about 3 to 32 years of testing! Therefore accelerated testing methodology is used to transform the estimated fatigue life of 10^8-10^9 cycles of variable amplitude loading on a turbine blade over its lifetime to a damage equivalent 1 to 3 million constant amplitude cycles that can be applied in the lab. The tests are carried out at a raised load level, so that 1 to 3 million cycles would suffice to reach the equivalent fatigue damage.

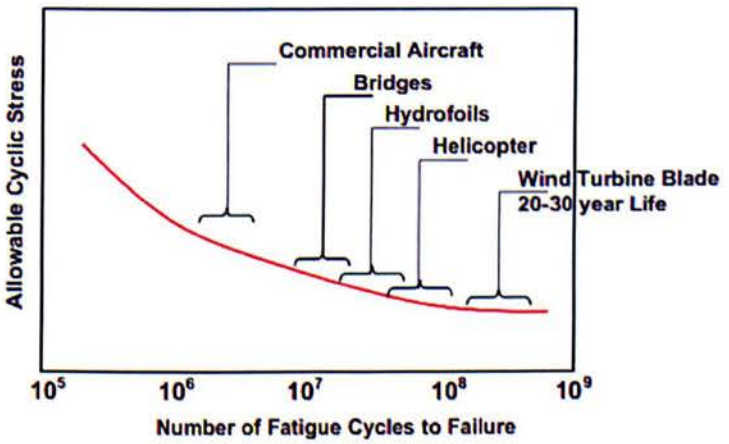

Fig. 2.2 Comparison of fatigue lives of wind turbines with other structures [1].

As well as fatigue, turbine blades are also exposed to many other hostile factors such as high temperatures, rain, hail, snow, icing, sunlight, lightning etc.

2.2 History of wind technology

History shows that the earliest known use of wind power was on sail boats. Later the technology developed from sail boats to sail type windmills. Windmills were designed and developed to pump water and grind grain. The Persians designed windmills with vertical sails

made of wood or bundles of reeds that were attached to the central vertical shaft by horizontal struts.

In China 200 years after the Persian windmill, the vertical axis windmill was used. The earliest documentation of the Chinese windmill dated back to 1219 A.D when Yehlu Chhu-Tshai presented the documentation for water pumping and grain grinding [4]. One of the most successful applications of wind power, still in use to this day, is the water pumping machines on the island of Crete.

In Cleveland, Ohio, Charles F. Brush designed a windmill that generated electricity in 1888. The design uses multiple blades, with a rotor diameter of 17 meters and a large tail to turn the rotor out of the wind direction. This design was the first to include a step-up gearbox between the rotor and the generator. In 1891, Dane Poul La Cour developed the first electrical wind turbine that was designed using aerodynamic principals which included four bladed rotors with primitive aerofoil shapes and low-solidity. This design was implemented in the best European tower mills. The La Cour wind turbine was practical and from 1918 spread throughout Denmark. They each generated up to 25kW of electrical output. In 1920; fan and sail types windmills were dominant rotor designs; they had been tried and found, that they could generate considerable amounts of electricity. In the United States developments in wind turbine systems were inspired by airplane propellers and the monoplane wings. Parris-Dunn and Jacobs Winds-electric in the mid-1920's produced the first small electrical-output wind turbines, these were made using modified propellers to drive direct current generators. In 1931 Russia developed the first bulk power generator using wind, this was the 100kW Balaclava wind generator. Between 1935-1970 experimental wind farms in Europe and America were constructed proving that wind turbines would work. In 1941 in Vermont, the largest horizontal axis wind turbine of its time produced 1.25 MW with a 53.3m diameter rotor called the Smith-Putnam wind turbine. From 1973 to 1986 the commercial wind turbine market evolved from domestic & rural applications producing from 1 to 25 kW energy, to an intermediate scale producing 50-600 kW.

Over the last 20 years wind turbines have been developed dramatically, using different blade designs; one bladed, two bladed and three bladed HAWT; the three bladed HAWT is the most commercially successful design but it is also faces major fatigue problems.

2.3 Horizontal axis wind turbine (HAWT)

The distinguishing feature of the horizontal axis wind turbine is that the low speed main shaft is placed horizontally with respect to the structural tower. A wind turbine generates electricity using the flow of the wind over the blades to spin the main shaft and gearbox, which in turn spins the generator shaft, this results in the electrical output. An overview of a HAWT is shown in Figure 2.3. The generated power from a wind turbine with a rotor swept area A, at a wind speed V can be found from

$$P = \frac{1}{2} C_p \rho A V^3 \tag{2.1}$$

where ρ is air density and C_p is power coefficient of wind turbine. The maximum theoretical $C_p = \frac{16}{27}$ is called Betz's limit. As the density of air is low, this leads directly to the large size of a wind turbine. The rotor diameter has been steadily increasing since 1985, in theory the higher swept area and higher velocity means more power can be produced. Figure 2.4 shows the evolution of blade diameter size since 1985. However, the sizes of wind turbines do have constraints, for example although in HAWT the rated power scales as the square of blade length but strength scales as the square of blade length, mass scales as the cube of blade length, inertia scales as fifth power of the blade length. Therefore materials limit the turbine's ultimate structural feasibility. Figure 2.5 shows the trend of increasing blade mass with increase in rotor diameter for a 3-bladed HAWT.

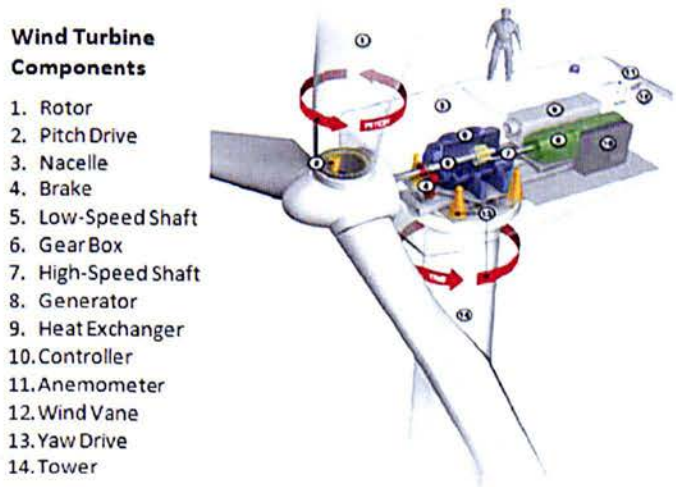

Fig. 2.3. Detailed drawing of components on HAWT [5].

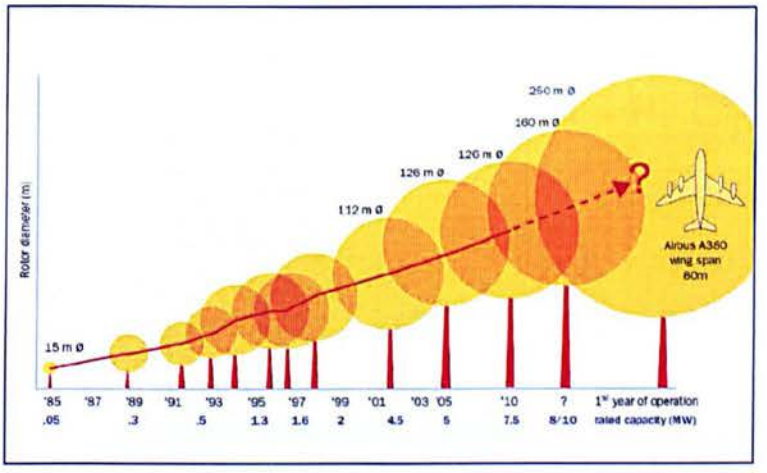

Fig. 2.4. Evolution of rotor diameters since 1985 [6].

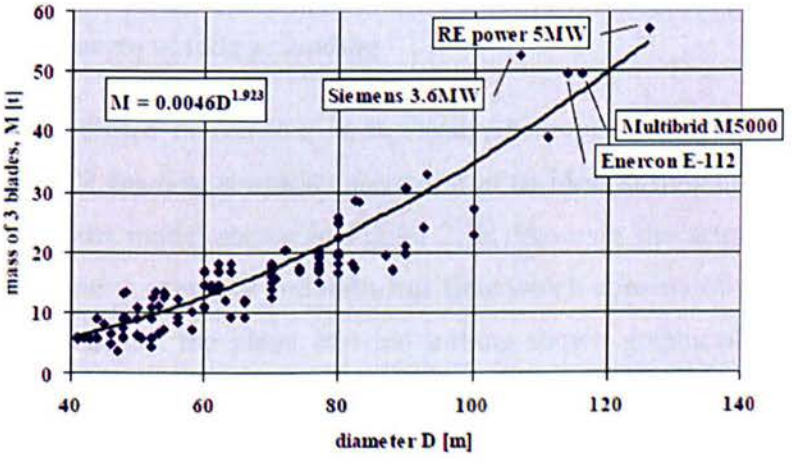

Fig. 2.5. Blade mass scaling [7].

Figure 2.6 shows variation of 3-bladed HAWT specific cost ($/kW) with respect to blade diameter. In onshore wind turbines, the minimum cost of energy is achieved between 3MW and 3.5MW. In offshore wind turbines, the minimum cost of energy is achieved between 9MW and 10MW. As the demand for energy is on the rise and since the wind turbine power output is proportional to cube of wind velocity and swept area, manufactures are tending to produce bigger and bigger wind turbines, since the air velocity increases at the higher altitude.

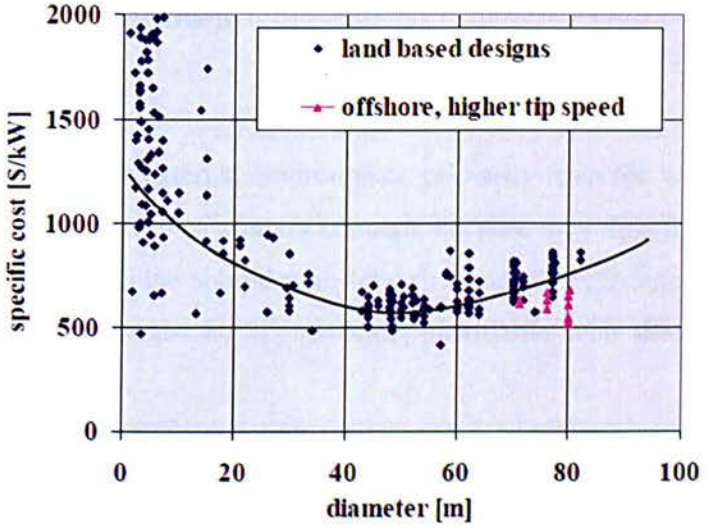

Fig. 2.6. Scaling of wind turbine price/kW [7].

2.4 Aerodynamic sources of fatigue loading

The easiest way to regard the airflow is as steady, homogenous, uniform, and fixed in direction (see Figure 2.7a). The simplest description of an ideal airflow on a wind turbine is the uniform wind shear model shown in Figure 2.7b. However the actual airflow passing through a wind turbine is unsteady and turbulent flow which consists of rapid velocity and pressure fluctuations across the plane of wind turbine shown graphically in Figure 2.7c. Downwind turbine rotors experience added turbulence from the wake of the air passing around the tower and nacelle.

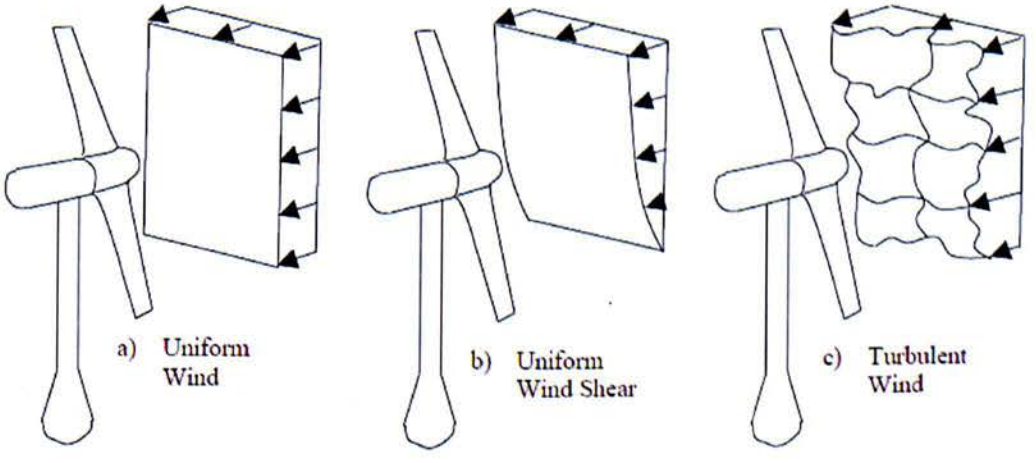

Fig. 2.7. Natural wind characteristics [8].

2.5 Design Aspect of Turbine Blade

2.5.1 Blade loads

The result of forces from the external environment, primarily from the wind, creates stresses in the blades. These stresses are of primary concern, because they directly affect the lifetime of the wind turbine. The turbine should withstand the loads it experiences, and the costs to make it structurally sound must be economically justifiable with the value of energy it produces.

The categories of loads a HAWT must withstand include:

- Static loads
- Steady loads associated with rotation, such as centrifugal force
- Cyclic loads due to wind shear, blade weight and yaw motion
- Short duration impulsive loads such as when blades passing through tower shadow
- Stochastic loads due to turbulence
- Transient loads due to starting and stopping
- Resonance induced-loads due to excitations near the natural frequency of the structure

Figure 2.8 illustrates various loading HAWT are subjected during its operation.

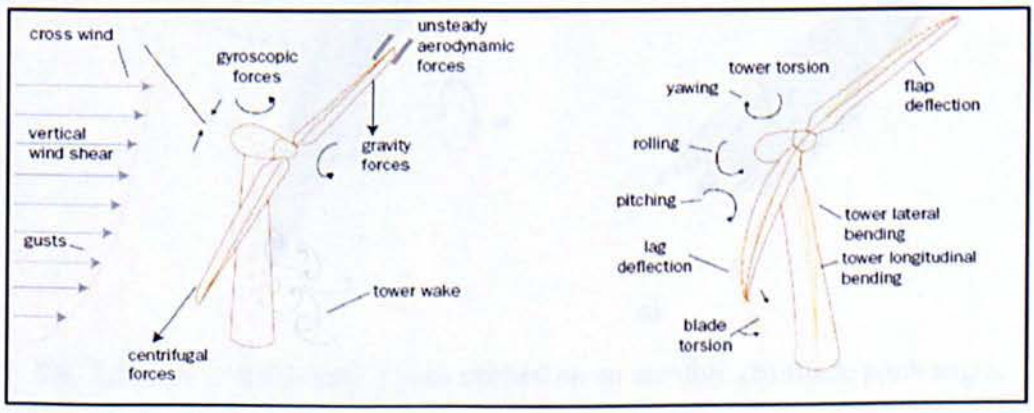

Fig. 2.8. Loads on HAWT blade [7].

Pressure distribution around an aerofoil typically used on wind turbine blade at its typical angle of attack is illustrated in Figure 2.9. The forces applied on an object by a fluid as it flows over the object are due to pressure and viscous stresses. The surface of an aerofoil falls into two sections, pressure side and suction side. The pressure on the suction side is less than the flow stream pressure, which effectively suck the airfoil upward. The pressure side applies

pressure on the lower surface of the airfoil, which is greater than the incoming flow stream pressure and pushes the airfoil upward.

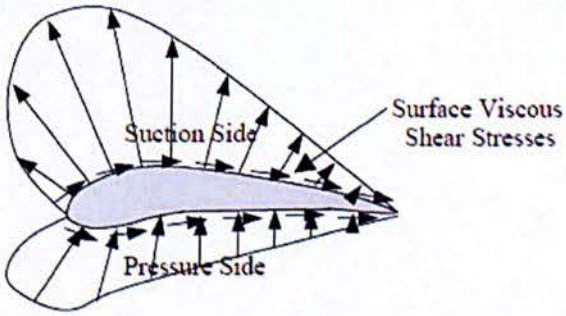

Fig. 2.9. Pressure and viscous shear stresses exerted on an airfoil [8].

The aerodynamic forces acting on an aerofoil are the lift and drag forces. The component of force normal to chord line is the lift force and the component of force acting parallel to the chord line is the drag force. A representation of the forces acting on aerofoil causing lift and drag is shown in Figure 2.10 together with blade pitch angle along the blade.

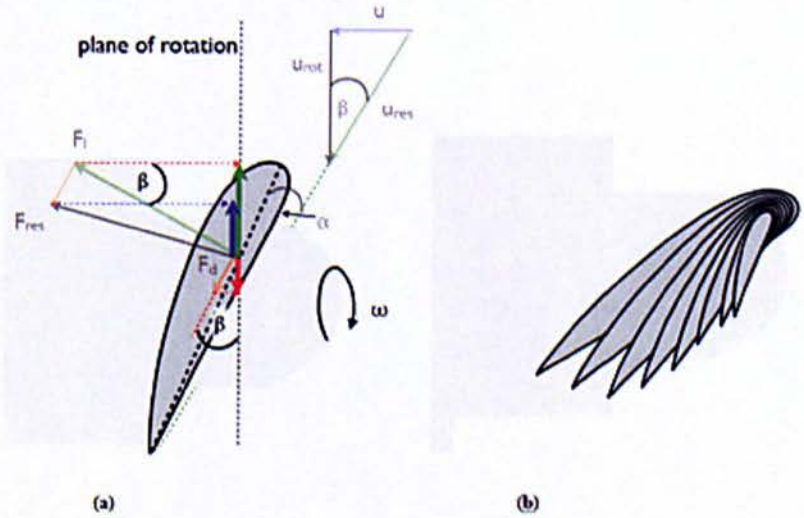

Fig. 2.10. (a) Aerodynamic forces exerted on an aerofoil, (b) Blade pitch angle.

Dimensionless coefficients of lift and drag provide a convenient way to compare the aerodynamic characteristics of different aerofoils, regardless of their size, and are given by

$$C_L = \frac{F_L}{\frac{1}{2}\rho U^2 A} \tag{2.2}$$

$$C_D = \frac{F_D}{\frac{1}{2}\rho U^2 A} \tag{2.3}$$

where F_L and F_D are lift and drag forces, U is the apparent flow velocity as seen by the aerofoil and ρ is the air density. The apparent flow velocity is a result of the aerofoil having motion relative to the flow. An aerofoil varies by way of length in the span-wise direction (span, S) and length in the flow-wise direction (chord length, C). The reference area of the aerofoil is then given by $A=CS$.

The torque coefficient and the power coefficient are

$$C_T = \frac{T}{\frac{1}{2}\rho U^2 AR} \tag{2.4}$$

$$C_P = \frac{P}{\frac{1}{2}\rho U^3 A} \tag{2.5}$$

where U is the incoming velocity of a wind, P is the mechanical power produced by the wind turbine, T is the mechanical torque on the axis of a wind turbine, and A is the projected area of a wind turbine.

The moment applied to blades can be divided into two components, which are shown in Figure 2.11. Flapwise bending moment is applied by wind which is perpendicular to the rotor plane, whilst edgewise bending moment is caused by the weight of blade and the torque driving the blades.

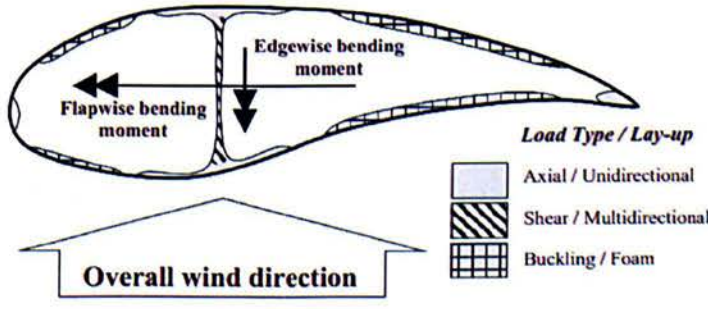

Fig. 2.11. Loads applied on blade [1].

2.5.2 Review of past research work on fatigue of blade

In the following, a literature review on the main research works carried out on the fatigue behaviour of wind turbine blades will be discussed. This review will highlight various aspects of fatigue testing on a wind turbine blade.

Veers and Winterstein [9] discussed procedures for analyzing and processing the measured loads in order to use them in fatigue design and reliability analysis. They proposed to use the moment of distributed loads on wind blades in fatigue analysis.

Noda and Flay [10] modelled the fatigue damage in the blade root. They simulated a single blade motion and examined the effect of different parameters such as: turbulence intensity, mean wind speed, wind shear, vertical wind component, dynamic stall, stall hysteresis, and blade stiffness. They compared the life in a low wind speed, low turbulence intensity site with a high wind speed, high turbulence intensity site.

Freebury and Musial [11] tried to convert wind turbine blade design loads to equivalent damage constant amplitude loads and load ratios. In their method loads are not converted to stresses, instead moment versus cycles (M-N) is produced. They used an iterative optimization program that converges to a constant amplitude load and a load ratio that minimizes sensitivity to the M-N curves range.

Li *et al.* [12] used strip theory to obtain distribution of aerodynamic loads on wind turbine blades. They studied the stiffening effect of rotating blades using multi-body dynamic method. They obtained dynamic stress response caused by dynamic loads such as aerodynamic, gravitational and centrifugal loads, using a finite element method. Palmgren-Miner's linear fatigue damage accumulation rule was used to estimate the life of GRP blades.

Kong *et al.* [13] estimated the fatigue life of a medium scale wind turbine they had manufactured by using the S–N damage model, the load spectrum and Spera's empirical formulae. They proposed a specific fatigue design procedure using sample load spectrum data extracted from short time operation. They rearranged these data as: layer numbers, wind speeds, cycles per layer, normalized maximum, minimum, cyclic and average loads and stress ratios in time order. They used Spera's empirical formulae to calculate fatigue loads such as flapwise and chordwise bending moments. The allowable fatigue strength was defined from results obtained by Mandel [27] for glass/epoxy materials. They verified that their designed blades satisfy the fatigue life of 20 years. Hammerum [14] used a spectrally based technique to estimate fatigue life of wind turbine blades. This method gives fatigue damage as a function of spectral moments of load history.

Epaarachchi and Clausen [15] presented a method to create a fatigue loading procedure using detailed short-term aeroelastic and wind measurements along with averaged long-term wind data from the Australian Bureau of Meteorology. Their measurements showed that blade does not respond instantaneously to changes in wind speed.

For the variable amplitude testing required for fatigue design of wind turbine blades, some standardized load histories like WISPER (WInd SPEctrum Reference) and WISPERX have been proposed. In 1992 Tenhave [16] presented relevant information used to develop these load histories. WISPER is a standardized load sequence for HAWT blades which simulates the load conditions in the flap direction at a point close to the blade root. The spectrum was developed in an IEA working group in 1987 and it is based on measurements from nine different wind turbines in Europe. The sequence represents approximately two months' service of a generic HAWT at a rotation speed of 45 rpm. WISPER consists of a row of 265423 loading reversal end levels. The maximum load corresponds to level 64 and the rest of the load levels are scaled accordingly, with zero load at level 25. The WISPER load sequence is intended for comparative purposes only, i.e., to evaluate materials and structural details, dimensions, design alternatives, and fatigue lifetime prediction procedures. Simulating an operational period of ten years, WISPER has to be run for more than fifty times.

Later WISPERX a new spectrum which contains only one tenth of the cycles present in the WISPER spectrum was developed. The difference between WISPER and WISPERX is that low load cycles (low in range) have been excluded.

LIFE2 code [17] was developed in Sandia National Laboratories for the fatigue analysis of wind turbine components. In this code Miner's damage rule along with rainflow-counting algorithm is used. When instead of simple constant amplitude cyclic load, there is a complex waveform with no obvious mean stress; rainflow-counting algorithm is used to convert this waveform to equivalent stress ranges, i.e. number of stress ranges that will produce same amount of fatigue damage as original waveform.

2.5.3 Material requirements on wind turbine blade

Horizontal axis wind turbines face a wide range of weather conditions whether it is onshore or offshore. Light weight, long fatigue life, high stiffness, corrosion resistant and resistant to lightning are desirable characteristics. The blade material should have a high stiffness to be able to maintain its optimal aerodynamic shape. The complexity of manufacturing today's rotor blades is a challenging task, and selecting appropriate materials to optimize blade life and produce maximum performance is of great importance.

A combination of material selection is used in the rotor blade as the rotor blade increases in length. Figure 2.12 shows the development of the rotor blade, where the mass of the blade increased as the length of the blade increased, the higher end of the curve represents long blades with lengths of up to 100m and the lower end of the curve represents moderately short blades with lengths around 40m, which was common in the 1980's for wind turbine design. By adopting advanced materials and technology, the weight of modern 100m blades has been reduced to around 40 tonnes each while with conventional materials and design it would have been 120 tonnes.

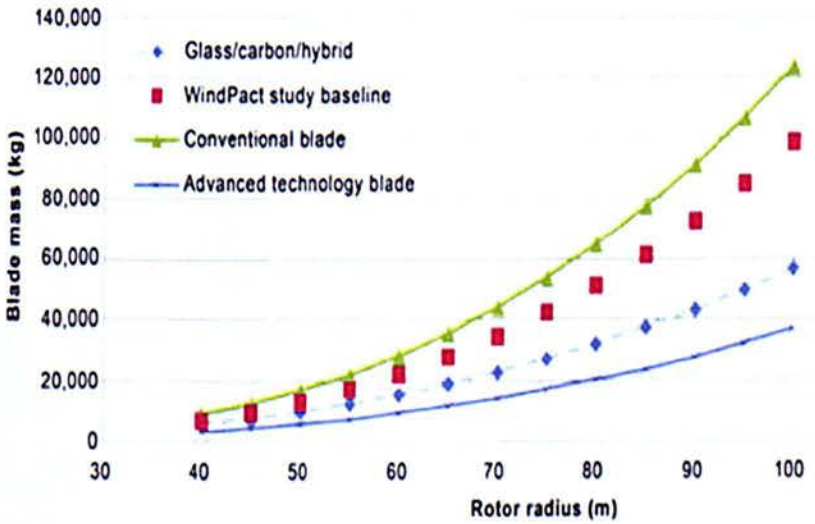

Fig. 2.12. Development of the rotor blade weight vs. length (the symbols specify different manufacturers and processing technologies) [18].

Since wind turbine blades act as a very long cantilever beam, it is important to have a light structural material to reduce bending moment at the root of the blade. Hence FRP composite materials are a very good candidate. The current composite materials employed in wind turbine blades have influenced the design of blades significantly [19]. Layup of polyester or epoxy resin matrix material, with glass fibres has been used. However other type of materials from four material groups; epoxy resin/carbon glass fibres; polyester resin/glass fibre; epoxy resin/glass fibre and epoxy resin/wood are now in common use. It is crucial to select an ideal weight/strength ratio to determine the optimum material and the lay-up combination.

2.6 Review of damage and failure of the blades

In a blade several types of flaw can be present, such as matrix cracking, porosity, debonding, delamination, improper fibre/matrix distribution, fibre misalignment, incompletely cured matrix, improper fibre/resin ratio, bonding defects and foreign inclusions. Figure 2.13 shows examples of blade failures caused by different types of flaws.

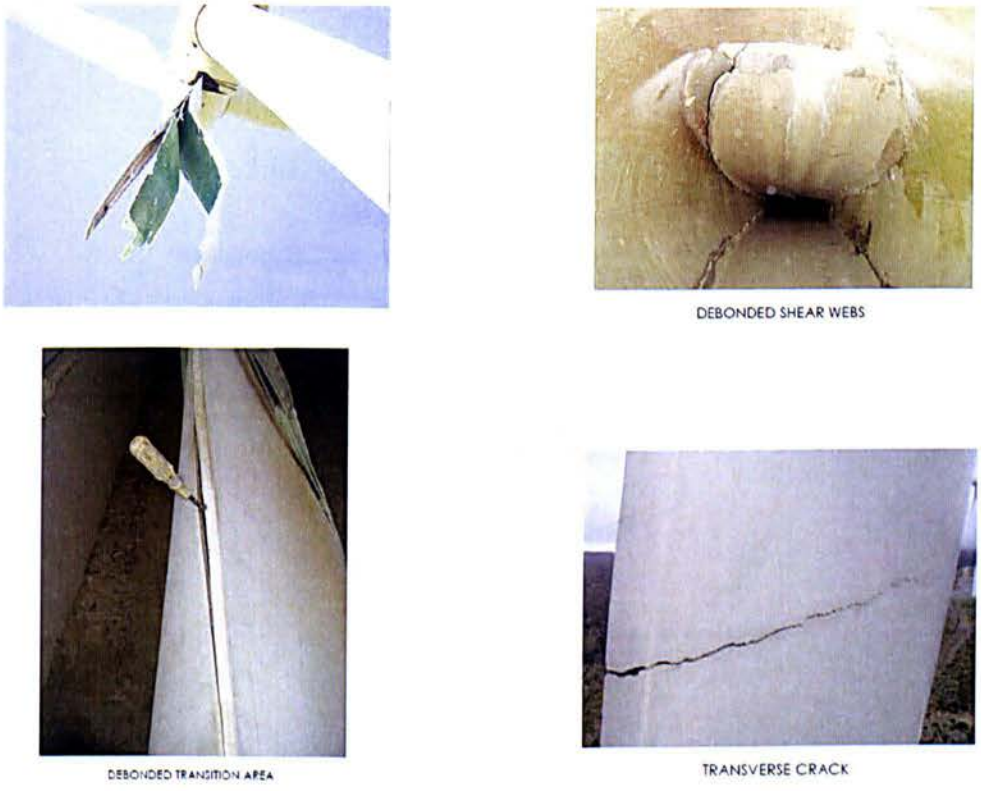

Fig. 2.13. Different types of failure in HAWT blades [20].

Main components of HAWT blade are shown in Figures 2.14. The materials of the blade are usually fibre reinforced plastic (FRP) composite with the bulk of the blade made of glass fibre/epoxy, carbon fibre/epoxy composites, or glass fibre/polyester. The benefit of using FRP materials on HAWT blades is that very long blades can be manufactured without failing due to its own weight. Figure 2.15 shows common damages that experienced on a blade in the past.

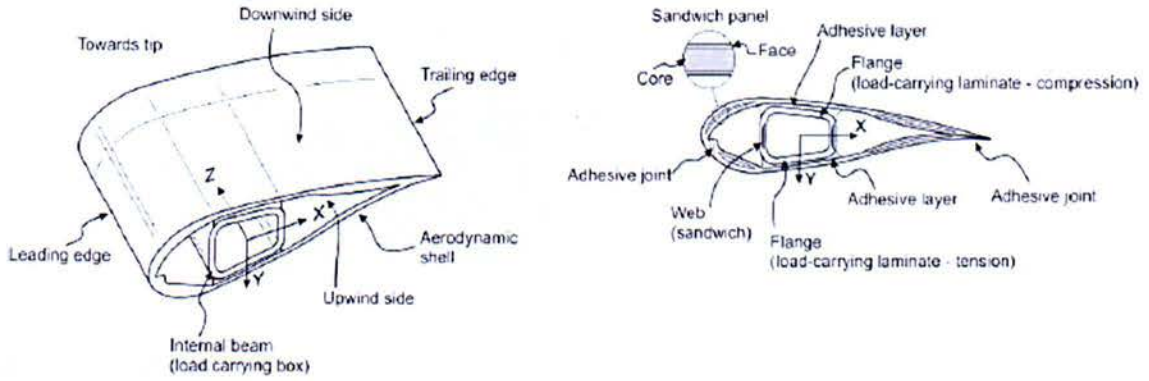

Fig. 2.14. Main components of HAWT blade [21].

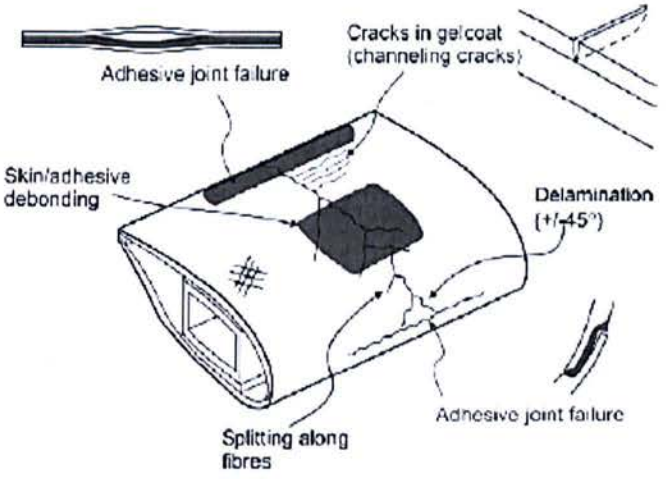

Fig. 2.15. A sketch of common damage types on a blade [21].

Analyses of the fracture surfaces of wind turbines have shown the following failure modes: Skin/adhesive delamination; Adhesive joint failure of leading or trailing edges; Sandwich face/core delamination; Delamination of laminates; Failure in individual laminas (tension, compression, shear/splitting); Skin layer/adhesive delamination due to buckling of the skin; Gelcoat damage (cracking and gelcoat/skin delamination) [22].

While design flaws can be engineered to reduce likelihood of failure, manufacturing flaws may occur at random with respect to type, size and location. Several types of flaws such as porosity, debonding, delaminations, improper fibre/matrix distribution, fibre misalignment, improper fibre/resin ratio, bonding defects, foreign inclusions, incompletely cured matrix, and matrix cracking. Examples of delamination and waviness are shown in Figure 2.16.

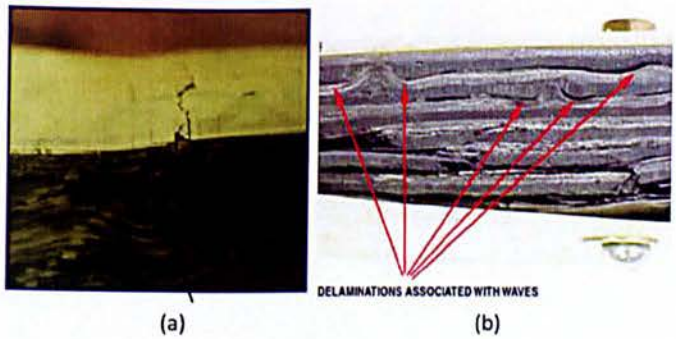

Fig. 2.16. (a) In-plane and (b) out-of-plane waves and delaminations in composite materials and resulting failures [23].

Figure 2.17(a) shows past examples of delamination on the width of the beam, and sandwich debonding and split cracks on the outer box of the beam along the length. Figure 2.17(b) shows a cross-sectional view of the beam and also annotates delamination between the inner and outer shell of the beam, also indicating compression failure and split cracks inside the hollow beam. Figure 2.17(c) shows a cross-sectional view of the beam indicating compression failure, multiple delamination, buckling driven delamination, splitting and split cracks on the surface.

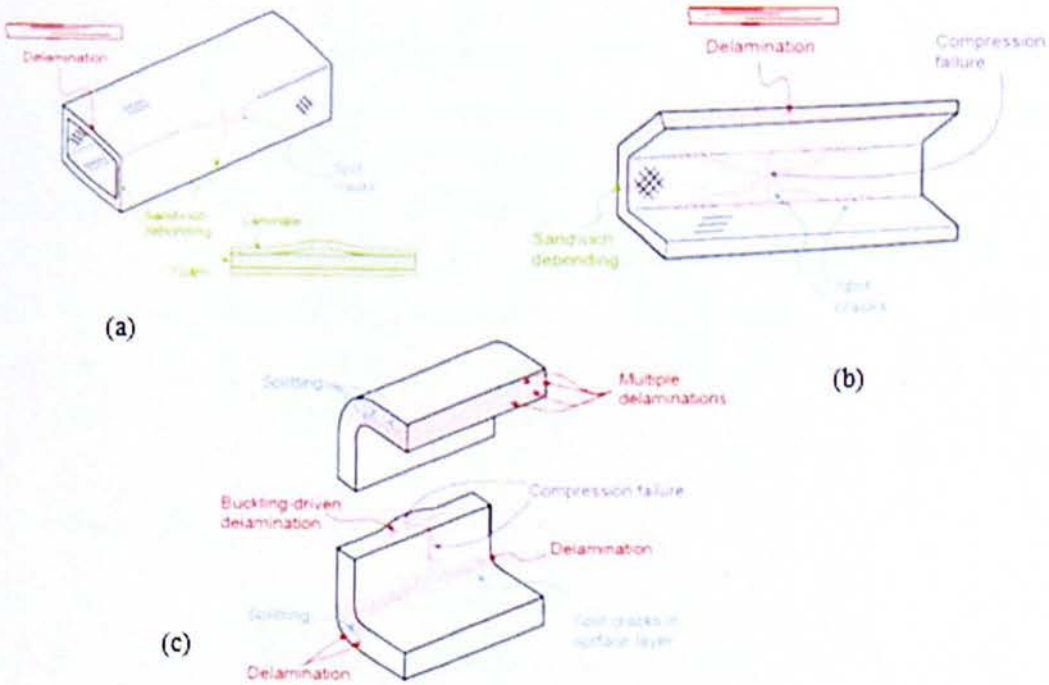

Fig. 2.17. Examples of possible failure and damages forms in wind turbine blades: (a) Box beam under load, (b) Cross-sectional view of spar beam under load, (c) Segments of a blade beam under load [24].

2.7 Full scale wind turbine blade testing procedure

The IEC 61400-23 standard set the technical guideline for a full-scale blade structural testing procedure and how to evaluate the test results as part of design verification of the blade integrity. The standard provides a technical specification for fatigue testing, static strength testing and other tests that may be applied to determine the blade properties. The calculation of design loads with respect to the actual loads is not included within this standard, nor does the technical specification provide a detailed specification of the testing equipment or detailed instructions of the strength testing which can be used to establish basic fatigue or static design data for the blade components.

The essential purpose of wind turbine testing is to validate that the blade has been manufactured to a set of specifications. The data from manufacturing and design of the blade is used to verify that the specified limit state has not been reached when tested; consequently the blade must possess the service life and strength provided in the design. The testing must be able to demonstrate that the blade is able to withstand the fatigue and ultimate load predicted during the design service life.

Wind turbine blade testing is subjected to many constraints from a technical and economical perspective. For example only very few blades (or even one blade) can be tested; the difficulty of detecting certain failures and simulating the distribution of loads on the blade. The testing is a compromise due to the constraints that have to be dealt with in order for the test result to be used to evaluate the limit state. The limit state is used to evaluate and establish the testing load, information about the design must be known to understand where the limit state lies, where the maximum load the structure can sustain within its design requirements.

2.8 Full scale structural testing of blade

Structural testing of the blade provides a direct confirmation of the blade strength, an assessment of design calculations and where the design might be improved. The testing proves the accuracy of the expected strength, and identifying the lowest area of strength.

There are three types of test for the structural performance of a blade; static, dynamic and static failure tests. In the static test the response of the blade is sought under the application of target loading. The target loading is the estimated worst case load scenario in a turbine's lifetime. This is a routine test of the blade and normally the blade remains undamaged in its working conditions. But the objective of a static failure test is to learn how a wind turbine blade fails when it is exposed to a large flapwise/edgewise loads and how failures propagate. As this test is destructive the cost of the test is very high. In dynamic fatigue blade testing cyclic loads are applied to blades at resonant frequency for flapwise (typically 0.5 Hz to 2.0 Hz) or edgewise (typically 2.0 Hz to 5.0 Hz). The cyclic loading is applied to the blade by using blade-based exciter saddles or ground-based exciters. Usually the attached mass to each of the two resonate exciter saddles is adjustable in increments up to 1000 kg. Full scale wind turbine blade fatigue testing follows IEC 61400-23 standard [2].

2.8.1 Static and failure testing

In static testing, loads are applied to the blade statically in one direction to establish its stiffness and strength. This type of test can either be intentionally destructive or non-destructive (see Figure 2.18). This type of testing is done with the purpose of predicting a blade's ability to withstand extreme loads such as those caused by hurricane wind forces or unusual transient conditions.

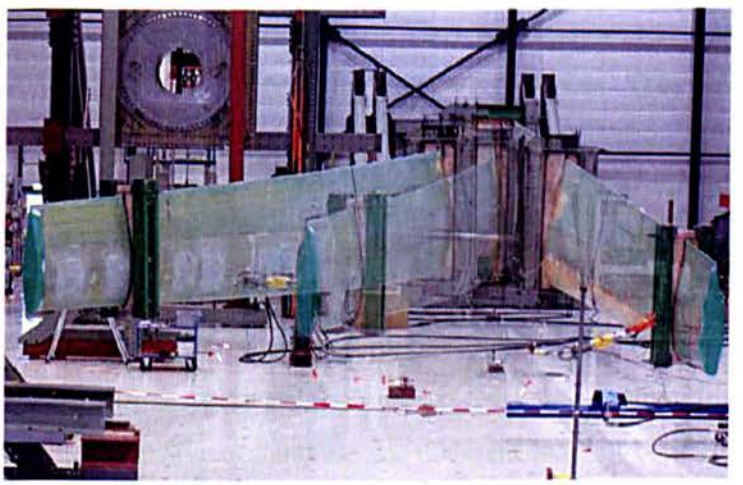

Fig. 2.18. Showing three stages of static blade test [25].

There are many different methods used to perform static testing. A common method is the use of an electric winch system, a simple method to control the blade deformation. Hydraulic

actuators are another option but are an expensive method to use as due to increasing blade lengths the displacement of the blade becomes larger. Another method is to hang ballast weights at specific locations along the blade. In cases where the blade is very long, the blade is attached to a stand at an angle to prevent the tip of the blade touching the ground.

2.8.2 Fatigue testing

Fatigue testing is performed to establish the blade durability with respect to the loading profile. The loading spectrum for fatigue testing should contain between 1 to 5 million cycles. Wind turbine blades are fatigue tested in flapwise and edgewise directions. The loading conditions for static testing are higher than fatigue testing. Fatigue testing on wind turbine blades, can be tested sequentially in single axis machine or simultaneously in dual-axis machine, e.g. edgewise testing followed by flapwise testing. Fatigue testing is used to identify structural defects inherent in either the manufacturing process or the design.

In full scale blade fatigue testing because it would take approximately 30 to 60 years to apply 10^8 load cycles to a blade with the cycle speeds used in blade testing, therefore the test loads are typically amplified to reduce the number of cycles required to complete the tests in just a few months.

On experimental fatigue work, in 1992 Mandell *et al.* [26] studied fatigue behaviour of common materials used in wind turbine blades. They did constant amplitude tensile fatigue tests to more than 10^7 cycles on coupons for different materials. They investigated triaxial and uniaxial composites and studied effects of different parameters like differing matrix materials, manufacturing methods, reinforcement structure, and ply terminations. In 1997 Mandell *et al.* [27] presented the analysis of results from their study on fatigue of composite wind turbine blades during seven years at Montana State University. Their tests were done on fabric E-glass reinforcement. They presented a novel approach to high frequency (100 Hz) testing for high cycle fatigue using mini-coupons. By using a high frequency test they succeeded in obtaining a significant database for different loading conditions to 10^8 cycles. They analyzed the large database of test results for trends and transitions in static and fatigue behaviour with different material parameters. The parameters they considered were: reinforcement, fabric architecture, fibre content, content of fibres oriented in the load direction, matrix material, and loading parameters (tension, compression, and reversed

loading). They identified transition from good fatigue to poor fatigue in different cases. They presented their results in the form of a Goodman diagram appropriate for design purposes. In 2002 Mandell *et al.* [28] reported the various data that they had added to the DOE/MSU database. They investigated the increase of fatigue life due to increase of fibre density and studied some structural aspects that are prone to delamination such as ply terminations, skin-stiffener intersections, and sandwich panel terminations. They used finite element method to predict initiation and growth of delamination in structural details and presented some design recommendation.

Delft *et al.* [29] carried out fatigue testing on glass-fibre reinforced polyester which are used in wind turbine blades, using WISPER and WISPERX variable amplitude loading sequences. They compared the results with constant amplitude tests. They discussed the difference between the lives of specimens tested with WISPER and WISPERX with theoretical estimations. They compared the shape of S-N diagrams resulting from these tests and common design rules.

Sutherland *et al.* [30] tried to predict the fatigue of wind turbine blades using the data base provided by Mandell for fatigue of materials used in blades in USA. They extracted a Goodman diagram from these data for wind turbine blades and used this diagram along with the LIFE2 fatigue code to predict the life of wind turbine blades. In 2005 Sutherland [31] reviewed data that have been provided for fatigue tests of wind turbine materials through several years. This work reviewed data for metals (primarily aluminium), wood and especially fibreglass. Sutherland and Veers [32] tried to estimate the confidence limit for fatigue data obtained for wind turbine blades. They used data from the MSU/DOE and the FACT fatigue databases. Sutherland and Mandell [33] obtained the optimum number of S-N diagrams to build a Goodman diagram. They constructed a Goodman diagram using 13 R values. They used these data to predict the failure of wind turbine blades and coupons employing linear and nonlinear damage models. They compared this prediction with the ones obtained with less detailed Goodman diagrams and concluded that the optimum number of R-values for Goodman diagrams is 5.

Wahl *et al.* [34] investigated the effect of spectral loading on lifetime and residual strength of fibreglass laminates used in wind turbine blades. They carried out many tests (over 1100 tests) for various loading conditions: Repeated block loading at two or more stress levels,

tensile-tensile test, compressive-compressive test, reversing and random standard spectrum. They obtained residual strength at different stages of lifetime and used several lifetime prediction models. Their experiment showed shorter lifetime than that predicted by Miner's rule. They observed that experimental lifetime was one-tenth to one-fifth of the lifetime predicted by theory. They came to following conclusions:

- Linear and nonlinear strength models gave better results.
- The measured strength during lifetime was consistent with these model's predictions
- Load sequencing effects were found to be insignificant.
- The predictions were very sensitive to damage law used when the deviation from constant amplitude loading is bigger.
- Among different models that were used, nonlinear residual strength based prediction with a power law S-N curve extrapolation gave better results.

Chambers *et al.* [35] experimentally investigated the effect of voids on initiation and propagation of static and fatigue flexural failures in unidirectional carbon reinforced composites used in wind turbines.

Nijssen [1] tried to describe the fatigue behaviour of turbine blades under variable amplitude loading using constant amplitude loading tests. He did different tests on fibre glass coupons with different geometries and performed constant and variable amplitude loading and block loading tests. He measured residual strength and investigated strength degradation in unprecedented detail. He concluded that load sequence in block tests is important. He divided the life prediction methodology to four parts:

1- Counting method,
2- S-N curve definition,
3- Constant life diagram formulation
4- Damage accumulation rule

Marin *et al.* [36] studied the parameters that can serve as origin of fatigue failure in composite blades such as superficial cracks, geometrical concentrators, abrupt change of thickness etc. They verified their work using procedures presented in the "Germanischer Lloyd" (GL) standard [37].

2.8.3 Fatigue loading types and methods

The constant amplitude testing load is characterized by a single load cycle that is repeated numerous times where the maximum and minimum loads are fixed and where constant amplitude blade data are easily compared with material coupon data because the same method is used to analyse the data.

Variable amplitude loading is characterized by using load cycles with different mean and magnitude readings. Each load series is repeated over a number of times, where the load ranges through a spectrum of magnitudes and amplitude ratios. Data is more difficult to compare through coupon testing at constant amplitudes, this is due to limit load magnification. However using variable amplitude produces high accuracy in results when matching a design load spectrum because fatigue computation is insensitive to uncertainties in fatigue formulation.

Block loading is a combination of constant amplitude loading test; the load is modified few times after an arranged duration of continuous amplitude cycles. One advantage is to generate fatigue failure by applying blocks of load cycles gradually by increasing the amplitude. As the blade withstands the block of cycles, the load is increased and a new block cycle is carried out. Therefore the process is then repeated until determining one of the following; failure life, failure mode and design margins.

In single-axial loading, the loading is applied by using a load source which does not permit the load direction to change. The load may be applied separately or simultaneously from the leading edge and trailing edge or flap and lead-lag. Applying loads to component separately require two tests to be performed. Therefore performing two separate tests do not result in fatigue damage that is equal to the case of applying combined loads simultaneously, as with multi-axial loading.

In multi-axial loading, loading components are applied independently by the use of appropriate loading equipment. The phase association between the load components should be known and controlled throughout the test. By this method, the blade simultaneously is tested in the spanwise and edgewise directions. This will provide a more realistic representation of the actual stresses that experienced by the blade in real situation.

A single spanwise loading point is often used for fatigue testing. A single point is used to test a large percentage of the blades span, but does not test the entire length of the blade. By increasing the length of the blade section being tested or accuracy of moment distribution, several points are used across the blade to introduce the load. However, by increasing the number of loading points, the test complexity increases and therefore it is better to combine all critical regions of the blade for a single load combination.

The blade is excited to the resonance frequency very close to its first natural frequency. The spanwise load distribution follows the mode shape of the blade; the desired load is reached by adding a load in the required areas. A large section of the blade can be tested in one test. Resonance loading is used for constant amplitude in single axial loading and certain limitations may be overcome by changing the excitation frequency in variable amplitude loading.

2.8.4 Full scale fatigue testing equipments

There are two main types of fatigue testing, single-axis testing and dual-axis testing. In single-axis testing loading is applied either in flapwise or edgewise directions. By contrast, in dual-axis testing loads are applied simultaneously to both flapwise and edgewise directions. In theory dual-axis testing simulates loads experienced in operation better and can result in shorter testing times.

The blade cyclic loading is applied either by a rod connected to the blade (see Figure 2.19) or by a resonance system sitting on the blade. The method behind resonance testing is to excite the blade within a frequency range just below the natural frequency of the test blade, with additional mass being added to achieve the required mean load. This allows the displacement amplitude to be adjusted by varying the exciter frequency. The blade resonance is achieved by connecting exciters to the blade or by moving the base at the blade's fundamental frequency. Hydraulic cylinders or a rotating eccentric mass can be used as exciter and they are usually powered by an electric motor.

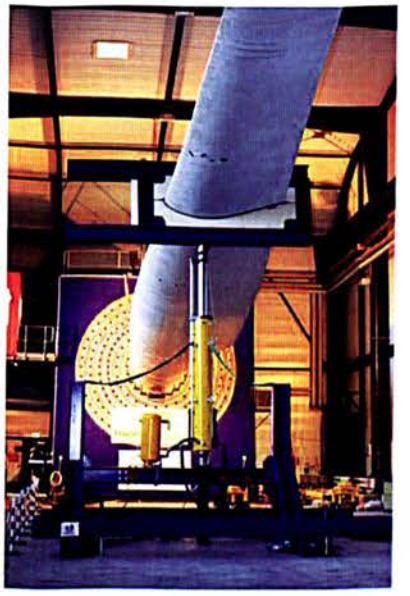

Fig. 2.19. Rotor blade testing at the Fraunhofer Institute for Wind Energy and Energy System Technology IWES.

Single axis resonance tests are either based on analysis or based on bending moment measured through calibrated strain gauges. Dual axis near resonance test is either carried out by variable amplitude block loading or multi point loading [38]. Figure 2.20 shows an example of single axis resonant fatigue testing, which uses a moving mass mounted on the blade to excite at the blade resonant frequency.

Fig. 2.20. Riso single axis resonant fatigue test.

In dual axis tests interactions between two mutually perpendicular directions of flapwise and edgewise occurs simultaneously. The National Renewable Energy Laboratory (NREL) has developed a dual axis forced displacement Blade Resonance Excitation (B-REX) system as shown in Figure 2.21. At the National Renewable Energy Centre (NaREC) also a new dual axis test method for resonant fatigue testing has been developed as shown in Figure 2.22. The NaREC results show that if the bending moment distribution along the length of the blade is accurate, then dual-axis resonant testing results will be much more thoroughly than sequential tests in the flapwise and edgewise directions [40].

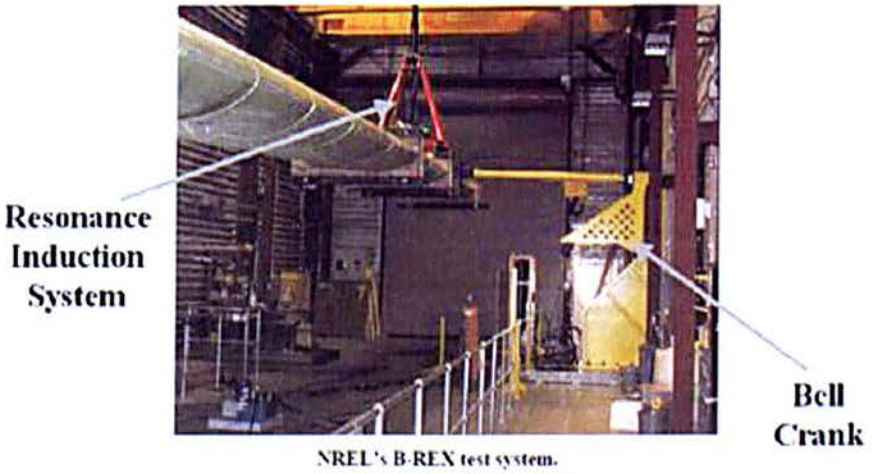

Fig. 2.21. Dual axis forced displacement Blade Resonance Excitation (B-REX) test system [39].

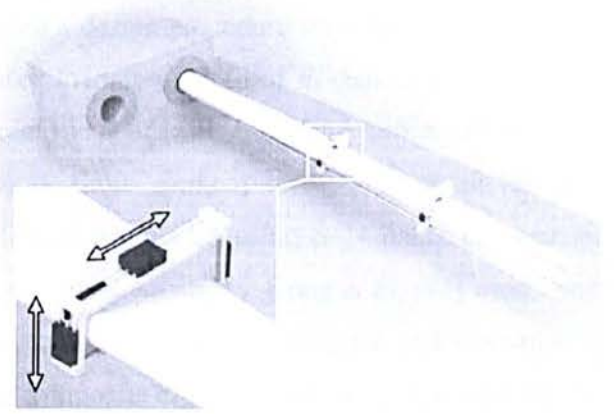

Fig. 2.22. NaREC Dual-axis resonant fatigue testing. [40].

An example of NREL's dual-axis universal resonance excitation (UREX) test method which replaced the bell crack mechanism is shown in Figure 2.23. This exciter applies dual-axis

fatigue loads at multiple resonant frequencies. It was developed and commercialized jointly with MTS. It is modular, scalable and up to 2000 kg of oscillating mass at 0.15 meters of stroke can be added.

Fig. 2.23. UREX dual axis resonance tests system, NWTC, NREL [41].

2.9 Theoretical fatigue models

Sutherland [42] reviewed the different methods used for fatigue design of wind turbines and described the best practice for their analysis. Sutherland and Mandell [43] considered the effect of mean stress on the accumulated damage due to fatigue. They used the updated Goodman diagram to predict the failure stress for coupons and examined three models: linear Miner's rule, nonlinear variation of Miner's rule and generalized nonlinear residual strength model. Nonlinear models used with updated Goodman diagram showed satisfactory results.

Kong *et al.* [44] presented a design procedure for a medium size wind turbine blade made of E-glass/epoxy. They used load cases defined in standards and proposed a composite which could endure the different kinds of loads that wind turbine blades are exposed to. They did a parametric study using a finite element method to obtain an acceptable design. They estimated the fatigue life of the blades using S–N linear damage theory, the service load spectrum, and Spera's empirical equations. Kong *et al.* [45] used Spera's empirical equation to calculate the fatigue loads. Also used S.N diagram and Goodman's diagram to determine the fatigue stresses on a composite blade. The blade design used has 20 year life, the material used on the blade is an E-glass/epoxy.

Shokrieh and Rafiee [46] studied fatigue of wind turbine blades using accumulated fatigue damage modelling. They carried out a static analysis to define the location of fatigue

initiation. Because of the random nature of wind loading they used a stochastic approach. They defined different load cases and used a Weibull distribution.

Rajadurai *et al.* [47] did fatigue life estimation for composite wind turbine blades. They performed finite element analysis and compared the results with experimental data.

Epaarachchi and Clausen [48], experimentally and numerically fatigue tested a 2.5m GFRP wind turbine blade to predict the design life. The test rig used a crank eccentric mechanism to flex the blade by a constant displacement in the flapwise direction, for each of the load cycles. Epaarachchi [49] also studied the effect of mean stress on damage predictions for spectral loading of fibreglass composite coupons. Three models of analysis are used to predict failure: non-linear variation of the Miners rule, the linear Miners rule and the generalized non-linear residual strength model. In continuation of their work, Epaarachchi and Clausen [50] investigated different methods to estimate the lifetime of GFRP composite components for wind turbine blades and aircraft components. The models used for the GFRP where the Palmgren-Miner and linear damage accumulation rule, these being used to calculate the lifetime estimation.

Grujicic *et al.* [51] designed a 1 MW laminated composite blade was designed and stress analysis simulation using ANSYS was carried out to predict the fatigue life of the blade. They discussed structural response analysis, fatigue-life prediction and material selection for 1 MW HAWT blades.

Ronold and Christensen [52] considered fatigue in flapwise bending of wind turbine blades. They calibrated a design code for wind turbine blade fatigue. They used numeric optimization technique with probabilistic and deterministic models to do this calibration. With this code it was possible to prescribe target reliability and get a design with minimum deviation from this target. In Code calibration, partial safety factors were determined such that the minimum deviation was achieved. They considered some representative design cases, each consisting of a particular combination of wind turbines, locations and blade materials.

Veldkamp [53] proposed to make the fatigue design of wind turbine blades conservative enough i.e. to exactly attain target failure probability. The goals of his works were mainly to determine the uncertainty in design and relative importance of stochastic parameters affecting

fatigue life and strengths and to do a comparative review of calculation methods. He determined five groups of stochastic parameters: parameters related to the wind climate, the sea climate, the aerodynamics, the structural model and the material fatigue properties. For each of these groups, distributions were estimated and current calculation models were reviewed. He investigated the fatigue of blades, hub, nacelle and tower and estimated yearly failure probabilities due to fatigue. This work includes good data on wind load distribution.

2.10 Testing standards for wind turbine blade

As part of turbine certification the blade is required to meet international design standards, such as IEC and DNV. This will benefit blade manufacturers in mitigating the technical and financial risk of deploying mass-produced wind turbines. The testing laboratory should strictly follow testing regulations according to the standard ISO 17025, which provides general requirements for the competence of calibration and testing laboratories.

Static and fatigue testing is an essential element of wind turbine certification. In order to conduct valid static and fatigue testing, right loads, right test specimen, and right documentation should be used. The right loads will be based on correct evaluation of extreme load and fatigue load, the selection of the proper safety factors, and the correct set-up and execution of test program. It is desirable to obtain the correct bending moment distribution over as much of the length of the blade as possible. The right blade specimen should be a representative blade. Finally the testing program must be thoroughly documented, capturing the key information required to provide confidence in the test results, the design, and ultimately to achieve certification. The requirements for the structural safety and design loads of wind turbine blade have been specified in the Part 1 of IEC 61400 standard [2]. Also the detailed requirements for full scale blade testing are specified in the standard IEC 61400 Part 23. In addition the detailed qualification of blade materials, design, and manufacturing procedures are required. A new standard DNV-DS-J102: *Design and manufacture of wind turbine blades, offshore and onshore wind turbines* [54] has been issued in October 2010, replacing its previous version DNV-OS-J101 issued in 2004. The new issue provides a more comprehensive and detailed guideline for the development of wind turbine blades. The contents of this standard widely cover the blade material qualification, design analysis, blade manufacturing, blade testing, and documentation requirements. At present, standard serves as detailed guidance to achieve IEC WT-01 certification for wind turbine blades.

2.11 Summary

In this chapter the experimental and design aspects of a HAWT blade has been reviewed from past work presented in the literature. The amount of literature on wind turbine blade is huge [9-17]. This shows the importance of wind energy and specifically the design of wind turbine blades. The focus of this review was on blade fatigue testing methods, materials used for the blade and theoretical fatigue works on the blade.

In early research the loads on wind turbine blades were initially constant amplitude loads, but the effect of variable amplitude loads were investigated more recently, as were the effects of load sequences. There have been some experimental works to report these parameters. These experimental results have been reviewed by others and blade design diagrams, the trends in blade design, and the confidence limit for them are summarised.

There have also been some work that addresses how to convert variable loads experienced by blades to equivalent constant amplitude loads. Some works have tried to offer appropriate load history for fatigue tests of wind turbine blades. More recent works have calculated the aerodynamic loads on wind blades using computational fluid dynamics (CFD) and dynamic stresses in blades using vibration analysis. As mentioned the wind turbines design life span is around 20 to 30 years, and much of the research was directed to estimate the load history in this time period.

There are many works on development of theoretical models and verification of these models in fatigue life prediction of wind turbine blades such as Miner's rule. Because of the stochastic nature of fatigue in wind turbine blades some works have been done on reliability analysis [42-53]. The main focus is to minimize the design deviation from target reliability.

This review established the research areas needs to be focused on by this project, that is, the static and dynamic characterisation of delamination of laminated GFRP composite materials under different loading scenarios, on fatigue behaviour of GFRP materials, full scale blade fatigue testing and damage tolerance of blade. All these issues have been studied and will be discussed in the remaining chapters of this thesis.

2.12 References

[1] Nijssen RPL. Fatigue life prediction and strength degradation of wind turbine rotor blade composites. ISBN-10: 90-9021221-3, Publisher: Knowledge Centre Wind turbine Materials and Constructions (KC-WMC), 2006.

[2] Technical Specification. IEC TS 61400-23 Wind turbine generator systems – Part 23: Full-scale structural testing of rotor blades.

[3] SUPERGEN Wind, Session 5 Wind Turbine Scaling and Control, W. E. Leithead, 25th March 2011

[4] Shepherd, D. Historical Development of the Windmill. National Aeronautics and Space Administration, DOE/NASA/5366-1, Lewis Research Center, Ohio, 1990.

[5] www.desmoinesregister.com

[6] EWEA. Upwind: Design limits and solutions for very large wind turbines. Tech. rep., EWEA, March 2011

[7] Hogg. P. (2010) Wind turbine blade materials, Supergen wind presentation, wind energy technology.

[8] Jonkman J.M., Modeling of the UAE Wind turbine for Refinement of FAST_AD, NREL Technical Report, 2003.

[9] Veers PS, Winterstein SR. Application of measured loads to wind turbine fatigue and reliability analysis. Transactions-American Society of Mechanical Engineers, Journal of Solar Energy Engineering. 1998;120:233-9.

[10] Noda M, Flay R. A simulation model for wind turbine blade fatigue loads. Journal of Wind Engineering and Industrial Aerodynamics. 1999;83:527-40.

[11] Freebury G, Musial WD. Determining equivalent damage loading for full-scale wind turbine blade fatigue tests: National Renewable Energy Laboratory; 2000.

[12] Li D-Y, Ye Z-Q, Chen Y, Bao N-S. Load spectrum and fatigue life analysis of the blade of horizontal axis wind turbine, J. Engineering Mechanics. 2004;6.

[13] Kong C, Kim T, Han D, Sugiyama Y. Investigation of fatigue life for a medium scale composite wind turbine blade. International journal of fatigue. 2006;28:1382-8.

[14] Hammerum K. A Fatigue Approach to Wind Turbine Control: Informatics and Mathematical Modelling, Technical University of Denmark, {DTU}; 2006.

[15] Epaarachchi JA, Clausen PD. The development of a fatigue loading spectrum for small wind turbine blades. Journal of wind engineering and industrial aerodynamics. 2006;94:207-23.

[16] Tenhave A. WISPER and WISPERX: Final definition of two standardised fatigue loading sequences for wind turbine blades. NASA STI/Recon Technical Report N. 1992;94:30872.

[17] Schluter L. L., Programmer's Guide for LIFE2's Rainflow Counting Algorithm, SANDIA Report SAND90–2260, 1991.

[18] Arno van Wingerde, Blades & Rotors Wind Energy R&D support from the European Commission 1 EWEC 2004, London 23rd November 2004.

[19] Scherer. R (1999). Blade design aspects, Renewable energy 16 (1999) 1272-1277

[20] COMPBLADES W/T Blade Repair & Maintenance, Factory: 62 Thrakomakedonon St. 13671 Acharnai, Greece

[21] Brøndsted, Povl; Holmes, John W.; Sørensen, Bent F. Wind rotor blade materials technology. European Sustainable Energy Review, No. 2, 2008, p. 36-41.

[22] Sørensen, Bent F. (2009). Materials and structures for wind turbine rotor blades - an overview. Materials Research Division, Risø National Laboratory for Sustainable Energy, The Technical University of Denmark.

[23] Cairns, D. Improved Wind Turbine Blade Reliability. Sandia Wind Turbine Blade Workshop, 2009.

[24] Sørensen, B. F., Jørgensen, E., Debel, C. P., Jensen, F. M., Jensen, H. M., Jacobsen, T. K., and Halling, K., 2004, "Improved design of large wind turbine blade of fibre composites based on studies of scale effects (Phase 1). Summary report". Riso-R-1390(EN), 36 p.

[25] http://www.wmc.eu/blade.php

[26] Mandell JF, Reed RM, Samborsky DD. Fatigue of fiberglass wind turbine blade materials: Sandia National Laboratories; 1992.

[27] Mandell JF, Samborsky DD. DOE/MSU composite material fatigue database: test methods, materials, and analysis. Sandia National Labs., Albuquerque, NM, United States; 1997.

[28] Mandell JF, Samborsky DD, Cairns, D. Fatigue of composite materials and substructures for wind turbine blades. Sandia National Labs., Albuquerque, NM (US); Sandia National Labs., Livermore, CA (US); 2002.

[29] Van Delft D, De Winkel G, Joosse P. Fatigue behaviour of fibreglass wind turbine blade material under variable amplitude loading. 1997 ASME Wind Energy Symposium1997. p. 180-8.

[30] Sutherland HJ, Mandell JF. Application of the US high cycle fatigue data base to wind turbine blade lifetime predictions. Wind Energy. 1996:78-84.

[31] Sutherland HJ. A summary of the fatigue properties of wind turbine materials. Wind energy. 2000;3:1-34.

[32] Sutherland HJ, Veers PS. The development of confidence limits for fatigue strength data. A collection of 2000 ASME Wind Energy Symposium Technical Papers, AIAA-2000-0063, January 2000.

[33] Sutherland HJ, Mandell JF. Optimized Goodman diagram for the analysis of fiberglass composites used in wind turbine blades. ASME J Solar Energy Engineering. 2005;127:563-9.

[34] Wahl NK, Mandell JF, Samborsky DD. Spectrum fatigue lifetime and residual strength for fiberglass laminates: Montana State University, Bozeman; 2001.

[35] Chambers A, Earl J, Squires C, Suhot M. The effect of voids on the flexural fatigue performance of unidirectional carbon fibre composites developed for wind turbine applications. International Journal of Fatigue. 2006;28:1389-98.

[36] Marín JC, Barroso A, París F, Canas J. Study of fatigue damage in wind turbine blades. Engineering failure analysis. 2009;16:656-68.

[37] Woebbeking. M, (2010). Guideline for the certification of wind turbines. Germanischer Lloyd Industrial Services GmbH, Renewable Certification (GL), Brooktorkai 18, 20457 Hamburg, Germany.

[38] Heijdra, John, Blade testing methods, Overview of new methods for full scale fatigue testing of wind turbine blades, Dutch Wind Workshops, October 2010

[39] White, D., Evaluation of the new B-Rex Fatigue Testing System for Multi-Megawatt Wind Turbine Blades, NREL/CP-500-37075, 2004.

[40] Greaves P.R., Dominy R.G., Ingram G.L., Long H. and Court R., Evaluation of dual-axis fatigue testing of large wind turbine blades, Proc IMechE Part C: J Mechanical Engineering Science 226(7) 1693–1704, 2012.

[41] Blade Testing at NREL's National Wind Technology Center, 2010 Sandia National Laboratory Blade Workshop, Scott Hughes, July 20, 2010.

[42] Sutherland HJ. On the fatigue analysis of wind turbines. SAND99-0089, June 1999.

[43] Sutherland HJ, Mandell JF. The effect of mean stress on damage predictions for spectral loading of fibreglass composite coupons. Wind Energy. 2005;8:93-108.

[44] Kong C, Bang J, Sugiyama Y. Structural investigation of composite wind turbine blade considering various load cases and fatigue life. Energy. 2005;30:2101-14.

[45] Kong. C, Taekhyun. K, Dongju. H, Yoshihiko. S. Investigation of fatigue life for a medium scale composite wind turbine blade. International journal of fatigue 28 (2006) 1382-1388.

[46] Shokrieh MM, Rafiee R. Simulation of fatigue failure in a full composite wind turbine blade. Composite Structures. 2006;74:332-42.

[47] Rajadurai JS, Christopher T, Thanigaiyarasu G, Rao BN. Finite element analysis with an improved failure criterion for composite wind turbine blades. Forschung im Ingenieurwesen. 2008;72:193-207.

[48] Epaarachchi. J. A, and Clausen. P. D (2004). Accelerated Full Scale Fatigue Testing of a Small Composite Wind Turbine Blade Using a Mechanically Operated Test Rig, Structural Integrity and Fracture International Conference (SIF'04). Brisbane, Australia, 26-29 September 2004.

[49] Epaarachchi. J. A (2006). A study on estimation of damage accumulation of glass fibre reinforce plastic (GFRP) composites under a block loading situation, Composite Structures, 75 (1-4), pp. 88-92.

[50] Epaarachchi. J. A, and Clausen. P. D (2006). The development of a fatigue loading spectrum for small wind turbine blades, Journal of Wind Engineering and Industrial Aerodynamics, 94 (4), pp. 207-223.

[51] Grujicic. M, Arakere. E, Subramanian. V, Sellappan. V, Vallejo. A, Ozen. M (2009). Structural-Response Analysis, Fatigue-Life Prediction, and Material Selection for 1 MW Horizontal-Axis Wind-Turbine Blades. Journal of Materials Engineering and Performance. V19(6) August 2010, 790-801.

[52] Ronold KO, Christensen CJ. Optimization of a design code for wind-turbine rotor blades in fatigue. Engineering Structures. 2001;23:993-1004.

[53] Veldkamp D. Chances in wind energy: a probalistic approach to wind turbine fatigue design: Delft University; 2006.

[54] DNV-DS-J102 Standard: design and manufacture of wind turbine blades, offshore and onshore wind turbines, 2010.

3

Building Mode I-Mode II Delamination Fracture Envelope

3.1 Introduction

In wind turbine blade, one of the main sources of damage is delamination, separation of the plies in the low resistance thin resin-rich interface between adjacent layers particularly in sections under compressive loading, or free-edge stresses. This is more of a problem when there is lack of any reinforcement in the thickness direction. Laminated composite materials are prone to damage during trimming, finishing and machining activities which can lead to edge delamination. When subjected to transverse loading, contact stresses, and impact loading they are also susceptible to delamination, fibre pull-out, fibre fracture and local matrix cracking. Other causes of delamination are the existence of contaminated fibres during the manufacturing process, insufficient wetting of fibres, curing shrinkage of the resin, and out-of-plane impact. The existence of high stress gradients near geometric discontinuities in composite structures such as holes, cut-outs, flanges, ply drop-offs, stiffener terminations, bonded and bolted joints promote delamination initiation.

Delamination will cause failures in a typically weak matrix of FRP materials, which can lead to local buckling of the laminate and degradation of the load carrying capacity of the structures. The initiation and rapid propagation of a crack will cause an abrupt change in both sectional properties and load paths within the affected damaged area. Impact often causes internal cracking and delamination in the resin rich zone between the plies for lower energy levels while high impact energies cause penetration and excessive local shear damage. When a low velocity impact happens, the matrix material becomes overstressed resulting in micro cracking which leads to redistribution of the load and the concentration of energy and stress at the inter-ply regions where large differences in material stiffness exist. Compressive loads are sources of continuous growth of the damaged area, with a corresponding decrease of residual strength and the subsequent risk of structural failure under service loads. The presence and growth of delamination in laminates also significantly reduces the overall buckling strength of a structure while delamination grows rapidly in the post-buckling region. In addition, delamination is an important energy absorption mechanism while it reduces the load-carrying capacity in bending and the fatigue life of the structures.

The objective of this chapter is to present test methodologies for fracture mechanics based interlaminar characterisation of delamination fracture envelope of the fibre reinforced plastic (FRP) composite materials. The Double Cantilever Beam (DCB), 3-point End Notched Flexure (3ENF) and Mixed-Mode Bending (MMB) tests will be examined to establish the full delamination failure envelope under various mode mixity ratios G_{II}/G_T. Experimental results will show the detailed procedure for finding the failure envelope for any FRP materials.

3.2 Experimental Studies

There are a number of publications on delamination fracture toughness testing using DCB test in the literature. Among them [1-6] showed that a Double Cantilever Beam (DCB) test is an accurate method to obtain GIC delamination toughness (where GIC is the opening mode I interlaminar fracture toughness). This test is standardised in ASTM D 5528-01 (2007) [7]. For analysis of the experimental data, Modified Beam Theory (MBT), Simple Beam Theory (SBT), Compliance Calibration Method (CCM), Modified Compliance Calibration (MCC) and Experimental Compliance Method (ECM) are used. The experiments were carried out

according to ASTM (2007) standard test method for Mode I interlaminar fracture toughness of unidirectional fibre-reinforced polymer matrix composites [7].

The loading tests on all experiments were carried out using a Zwick/Roell Z050 loading rig which is manufactured by Zwick GmbH. This load cell has a loading capacity of 50kN. The data capture and export from the loading rig was carried out using the Zwick/Roell TestXpert software which comes as part of the apparatus installation. For the fracture toughness testing in the DCB, 3ENF, and MMB tests, it is necessary to observe the fracture front propagation and to capture the data at key stages. To observe this, a travelling microscope was positioned alongside the test specimen and manually migrated along the fracture front as the crack grew.

The film material depends on the material curing temperature. It is a common practice and the most reproducible and simple method to make the initial delamination crack by inserting a starter film during lay-up. It is formed using a very thin non-stick PTFE film with thickness of 20 μm which is added during lay up of the composite laminates. The film will avoid the need for the difficult notching and offers the advantage of knowing the initial conditions. Turmel *et al.* [8] found the effect of different pre-cracking techniques and insert films on the initiation values of the interlaminar fracture resistance.

All specimens used in testing were produced using a unidirectional GFRP prepreg which was stored at a low temperature to increase its working shelf-life. The oven was initially heated to 90 °C for ramping up the aluminium plates and the FRP material to the necessary curing temperature. After 60 minutes, the temperature was increased to 120 °C and it was held for 4 hours at this temperature. All DCB test specimens were produced from $[0_9//0_9]$ lay-up with the initial crack length (a_0) of 50mm, total length (L) of 150mm, thickness (h) of 5mm and width (b) of 25mm. For ENF specimens the lay-up was $[0_9//0_9]$ with the initial crack length (a_0) of 25mm, total length (L) of 170mm, thickness (2h) of 5mm, width (b) of 20mm and half of the span length (L) of 50mm. The lay-up of MMB specimens was the same as DCB specimens with the initial crack length (a_0) of 27mm, total length (L) of 150mm, thickness (2h) of 5mm and width (b) of 20mm.

End Notched Flexure (ENF) test was used to quantify the interlaminar mode II shear fracture toughness, GIIC, of laminated composites. The experiment consisted of a three point bending test on an end notched GFRP composite laminated beam. Compliance Calibration Method (CCM), Modified Beam Theory (MBT), Direct Beam Theory (DBT), Corrected Beam Theory with Effective crack length (CBTE) and Compliance Based Beam Method (CBBM) were used for analysis of the tests. End Notched Flexure (ENF) Mode II fracture toughness was first projected by [9] and [10]. Further works were carried out by [11-15]. ENF testing is standardized by the ASTM D-30 Committee to produce ASTM standardization. In ENF testing [16] there is a major difficulty in designing test specimens for pure Mode II. The difficulty lies in preventing any crack opening without introducing excessive friction between the two crack faces.

Mixed-Mode Bending (MMB) test is used for characterisation of the delamination under mixed mode loading. MMB test results were analysed using beam theory to calculate mode I and mode II fracture toughness and to obtain the energy release rates GI and GII under different mode mixity. MMB testing was developed through the works of [17-23]. In 2006, ASTM released a standard test method for MMB fracture toughness of unidirectional fibre reinforced polymer ASTM [24].

The objective of the current chapter is to introduce the procedure for producing the fracture envelope under various loading conditions for FRP laminates. For analysis of delamination, mechanical properties of the FRP are required. The mechanical properties such as Young's modulus and shear modulus can be found from tensile testing of 0°, 90° and ±45° shear testing and the volume fraction of the composite can be obtained from burnout tests. The UD prepreg glass fibre/epoxy matrix E722-02 UGE400-02 material supplied by TenCate Ltd. was used for preparation of all specimens in this chapter. The mechanical properties of this material obtained from various tests are summarised in Table 3.1. For the detail of the tests, see Appendix A.

Table 3.1 Mechanical properties of GFRP laminate.

Material property	
Longitudinal Young's modulus E_{11} (GPa)	38.9±0.2
Transverse Young's modulus E_{22} (GPa)	13.0±1.5
Shear Modulus G_{12} (GPa)	5.0±0.2
Poisson's ratio υ12	0.24±0.01
Tensile strength in fibre direction Xt (MPa)	619±6
Tensile strength normal to fibre direction Yt (MPa)	69±6
Compressive strength in fibre direction Xc (MPa)	230±15
Compressive strength normal to fibre direction Yc (MPa)	180±10
Shear strength S (MPa)	47±1
Fibre volume fraction	61±2

3.3 Mode I Delamination Testing: Double Cantilever Bending (DCB) Test Analysis and Results

ASTM [7] States that the simple beam theory (SBT) for the strain energy release rate of a flawlessly built-in double cantilever beam, where it is clamped at the delamination front, can be found from:

$$G_{IC} = \frac{3P\delta}{2ba} \tag{3.1}$$

Where; crack length (a), specimen width (b), the corresponding load (P), and cross head displacement (δ).

There is some inaccuracy in using Eq. (1) as the beam is supported by an elastic foundation and experiences large deformation of the bending arm. Taking this into account, the modified beam theory (MBT) is derived:

$$G_{IC} = \frac{3P\delta}{2b(a+|\Delta|)} \tag{3.2}$$

The Mode I interlaminar fracture based on Compliance Calibration Method (CCM) can be found from Eq. 3.

$$G_{IC} = \frac{nP\delta}{2ba} \tag{3.3}$$

Also based on ASTM [7] and from the plot of the delamination crack length normalized by the thickness of specimen (a/h) vs. cube root of compliance $C^{1/3}$, the slope A_1 can be determined. Then the interlaminar fracture toughness can be found from:

$$G_{IC} = \frac{3P^2C^{\frac{2}{3}}}{2A_1bh} \tag{3.4}$$

Where

$$A_1 = \frac{a/h}{C^{1/3}} \tag{3.5}$$

Using the Irwin-Kies equation

$$G_{IC} = \frac{P^2}{2b}\frac{dC}{da} \tag{3.5b}$$

G_{IC} can be directly found using a power law for compliance calibration [5]. In Eq. (3.6) constants n and k are both experimentally determined. G_{IC} is found by differentiating Eq. (3.6) and substituting in Irwin-Kies results in Eq. (3.7). The constants F and N are correction factors for arm shortening and end block stiffening.

$$C = ka^n \tag{3.6}$$

$$G_{IC} = \frac{nP\delta}{2ba}\frac{F}{N} \tag{3.7}$$

The DCB tests were performed on a Zwick tensile testing machine as shown in Figure 3.1 at constant displacement rate of 2mm/min. The testing was carried in dry laboratory conditions at a constant temperature of 21±1°C. The specimens were measured for their length, width and thickness, with three measured values taken to produce an average value for each.

During the test, load-displacement was recorded. Figure 3.2 shows a typical load-displacement trace of a stable delamination fracture test. The data recorded for the analysis are the crack length (a), the corresponding load (P), and cross head displacement (δ). Several sets of values of a, P and δ are defined for further analysis:

NL is the point at which the load-displacement trace first deviates from linearity.

VIS corresponds to the point of visual observation of the delamination onset, i.e. the first point at which the delamination is observed to propagate.

5% is the point of the load-displacement trace at which the initial compliance C_0 has increased by 5%.

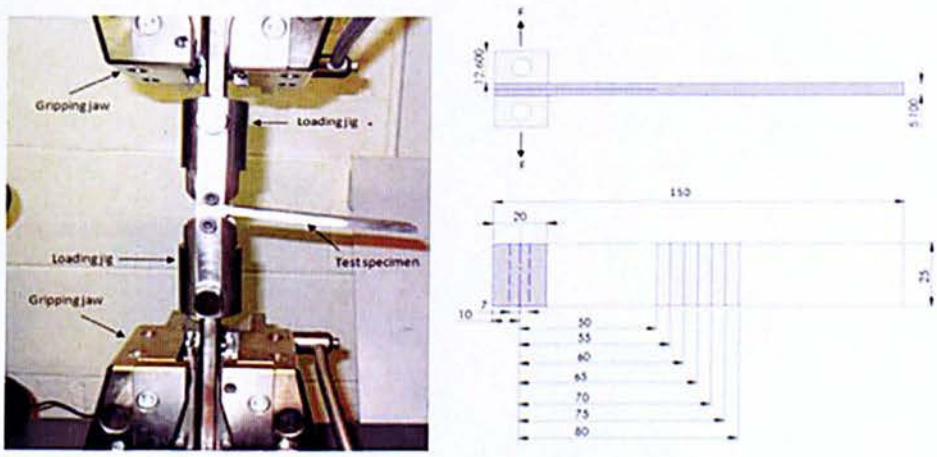

(a) (b)

Fig. 3.1. (a) Double Cantilever Beam (DCB) test set up. (b) Specimen dimensions (all dimensions in mm).

MAX is the maximum load point of the force/displacement curve, used only if it occurs before the 5% offset value.

When using these initiation points, the crack length used during the data analysis is assumed to be the original crack length at the start of the test, often measured by observation of the specimen when it opens.

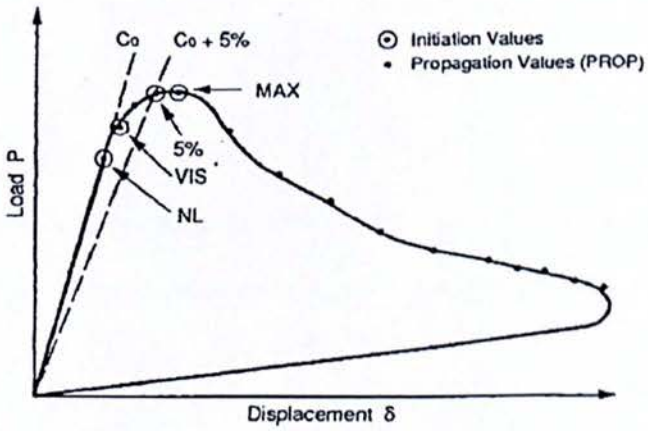

Fig. 3.2. Load-displacement curve of a delamination fracture test with initiation points NL, VIS, 5%, MAX and the propagation values (PROP) ISO 15024 [25].

The load-opening displacement tests results for 4 specimens are shown in Figure 3.3. Samples of the crack front in DCB test are shown in Figure 3.4. Table 3.2 summarises the

results of DCB tests from various methods. It can be seen G_{IC} value obtained by SBT is overestimating and MBT and CCM are very close and a correct representation of Mode I delamination fracture toughness.

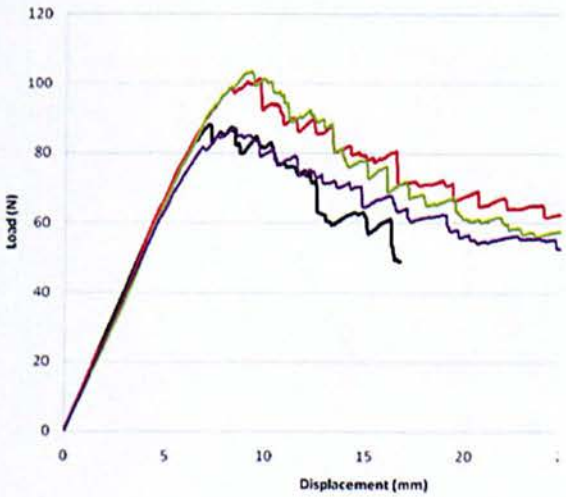

Fig. 3.3. Experimental results of load-opening displacement for DCB tests.

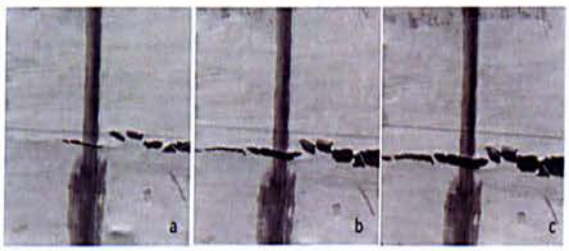

Fig. 3.4. Crack front in DCB test. (a) Crack begins to form (b) multiple bridging (c) growing of crack.

Table 3.2 Results of interlaminar fracture toughness in mode I testing DCB.

Method of Analysis	MBT	CCM	MCC	ECM	SBT
G_{IC} (J/m^2)	699 ± 100	778 ± 90	694 ± 100	804 ± 100	1018 ± 100

3.4 Mode II Delamination Testing: End Notched Flexure (3ENF) Analysis and Results

The experimental set-up of the 3-point End-Notched Flexure (3ENF) test and the specimen dimensions are shown in Figure 3.5. The analysis of 3ENF by Compliance Calibration Method (CCM) was developed by Russell [9] and Russell and Street [10]. The classical data reduction schemes to acquire the Mode II critical fracture energy (pure) G_{II} are:

$$C = C_0 + ma^3 \tag{3.8}$$

$$\frac{dC}{da} = 3ma^2 \tag{3.9}$$

$$G_{II} = \frac{P^2}{2b}\frac{dC}{da} = \frac{3ma^2P^2}{2b} \tag{3.10}$$

Based on the Direct Beam Theory (DBT), Murri and O'Brien [11] derived Eq. (3.11) that uses crack length within the calculation to obtain G_{IIC}. However measuring the crack length is not so easy in mode II as the position of crack tip is not well defined due to the formation of shear bands.

$$G_{IIC} = \frac{9P\delta a^2}{2b(2L^3+3a^3)} = \frac{9P^2a^2C}{2b(2L^3+3a^3)} \tag{3.11}$$

Williams [13] and Wang and Williams [14] derived a Modified Beam Theory (MBT) for ENF analysis. In MBT, Eq. (3.15), the crack correction length Δ_{II} is calculated from Eq. (3.14)

$$\Delta_I = h\sqrt{\frac{E_{11}}{11G_{13}}\left[3-2\left(\frac{\Gamma}{1+\Gamma}\right)^2\right]} \tag{3.12}$$

$$\Gamma = 1.18\frac{\sqrt{E_{11}E_{22}}}{G_{13}} \tag{3.13}$$

$$\Delta_{II} = 0.42\Delta_I \tag{3.14}$$

$$G_{IIC} = \frac{9(a+\Delta_{II})^2P^2}{16b^2h^3E_{11}} \tag{3.15}$$

Murri and O'Brien [11] used the Corrected Beam Theory with Effective crack length (CBTE) stating that when using certain methods such as MBT, DBT or CCM to obtain G_{IIC}, accurate crack length measurements during propagation are required, which not an easy task are. Because of this issue, significant errors can occur during the fracture characterization under pure mode II loading. CBTE is one of the few methods that do not require crack length to obtain G_{IIC}.

$$C = \frac{\delta}{P} \tag{3.16}$$

$$C_C = C - \frac{3L}{10G_{13}bh} \tag{3.17}$$

$$a_e = \sqrt[3]{\frac{8E_f bh^3 C_C}{3} - \frac{2L^3}{3}} \tag{3.18}$$

$$G_{IIC} = \frac{9P^2 a_e^{\,2}}{16b^2 E_f h^3} \tag{3.19}$$

Murri and O'Brien [11] also used the Compliance Based Beam Method (CBBM) to calculate G_{IIC}. In CBBM also, the crack length is not required to obtain G_{IIC}. Eq. (3.21) is used to calculate the flexural modulus, E_f, from three point bending test of composites.

$$C_{0C} = C_0 - \frac{3L}{10G_{13}bh} \tag{3.20}$$

$$E_f = \frac{3a_0^{\,3} + 2L^3}{8C_{0C}bh^3} \tag{3.21}$$

$$C_C = C - \frac{3L}{10G_{13}bh} \tag{3.22}$$

$$a_e = \left[\frac{C_C}{C_{0C}} a_0^{\,3} + \frac{2}{3}\left(\frac{C_C}{C_{0C}} - 1\right)L^3\right]^{\frac{1}{3}} \tag{3.23}$$

$$G_{IIC} = \frac{9P^2 a_e^{\,2}}{16b^2 E_f h^3} \tag{3.24}$$

Four 3ENF tests were performed on a Zwick tensile testing machine as shown in Figure 3.5 with the specimen dimensions. Results of load-displacement of ENF tests are shown in Figure 3.6. Table 3.3 summarises the test results in mode II loading. The results from CCM and DBT are very close and CBTE gave the highest estimate for Mode II delamination toughness.

Table 3.3 Results of interlaminar fracture toughness in mode II testing (ENF)

Method of Analysis	CCM	DBT	MBT	CBBM	CBTE
G_{IIC} (J/m^2)	831 ± 12	1103 ± 27	940 ± 22	1467 ± 26	1950 ± 15

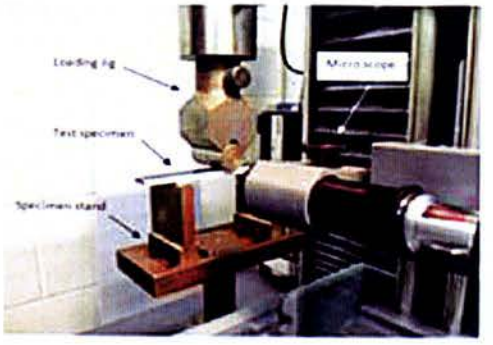

(a)

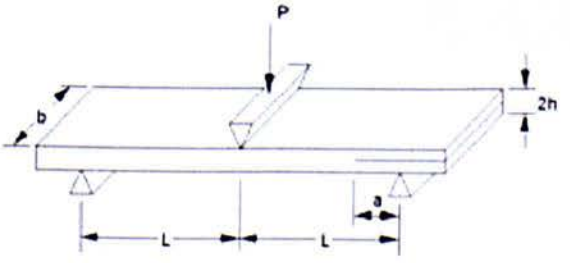

(b)

Fig. 3.5. (a) End-Notched Flexure (ENF) test set-up, (b) ENF specimen dimensions (all dimensions in mm).

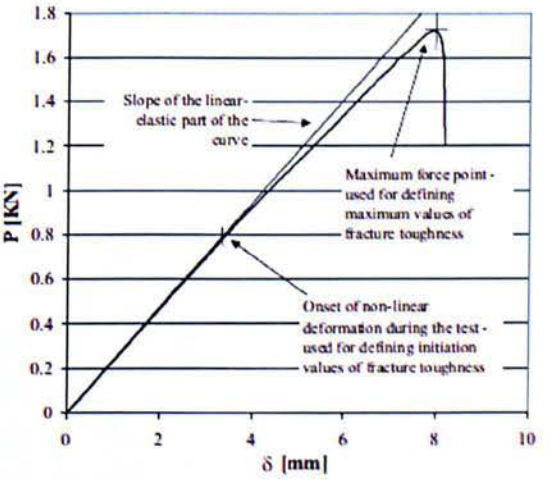

(a)

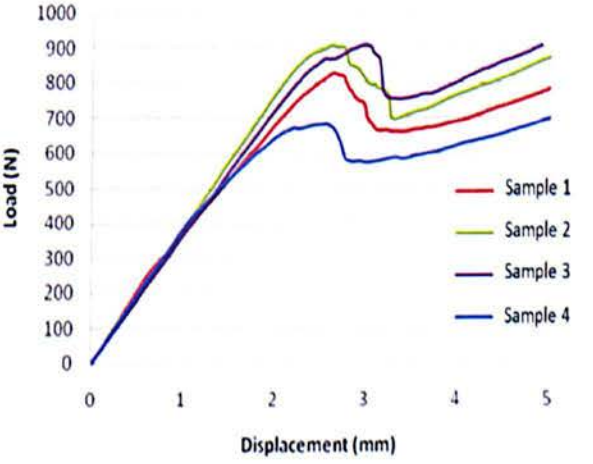

(b)

Fig. 3.6. (a) Load-displacement plot under mode II loading (b) Experimental results of load-displacement ENF tests.

3.5 Mixed Mode I/II Delamination Testing: MMB Analysis and Results

The MMB test is a combination of mode I (DCB) and mode II (ENF) tests. The Mixed Mode Bending (MMB) experimental set-up and the apparatus dimensions are shown in Figure 3.7.

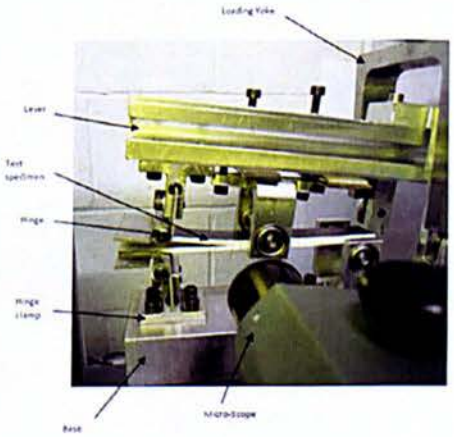

(a)

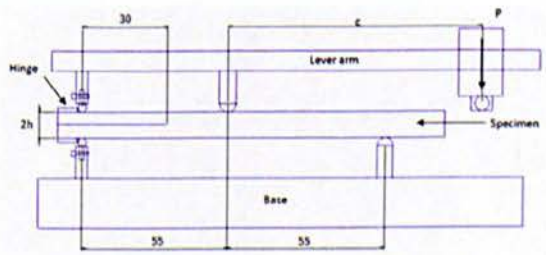

(b)

Fig. 3.7. (a) Mixed Mode Bending (MMB) experimental set-up, (b) Apparatus dimensions (all dimensions in mm). C = 42 mm and 97 mm.

Five different methods have been used to analyse MMB test results i.e. Simple Beam Theory (SBT), Corrected Beam Theory (CBT), Compliance Based Beam Method (CBBM), Simple Beam Theory with Elastic Foundation (SBTEF) and ASTM 6671/D 6671M-06.

The MMB test is a combination of two tests, the DCB and ENF, typically the two tests are used to characterize mode I and mode II.

$$P_I = \left(\frac{3c - L}{4L}\right)P \tag{3.25}$$

$$P_{II} = \left(\frac{c+L}{L}\right)P \tag{3.26}$$

$$G_I = \frac{12a^2P_I^2}{b^2h^3E_{11}} \tag{3.27}$$

$$G_{II} = \frac{9a^2P_{II}^2}{16b^2h^3E_{11}} \tag{3.28}$$

$$\frac{G_I}{G_{II}} = \frac{4}{3}\left(\frac{3c-L}{c+L}\right)^2, c \geq \frac{L}{3} \tag{3.29}$$

$$G_I = \frac{12(a+h|\Delta_I|)^2P_I^2}{b^2h^3E_1} \tag{3.30}$$

$$G_{II} = \frac{9(a+0.42h|\Delta_I|)^2P_{II}^2}{16b^2h^3E_{11}} \tag{3.31}$$

$$\frac{G_I}{G_{II}} = \frac{4}{3}\left(\frac{3c-L}{c+L}\right)^2\left(\frac{a+h\Delta_I}{a+0.42\Delta_I h}\right)^2 \tag{3.32}$$

The Simple Beam Theory with Elastic Foundation (SBTEF) is based on Kanninen [26] assumption that each arm is a beam supported by an elastic foundation:

$$G_I = \frac{12P_I^2}{b^2h^3E_{11}}\left[a^2 + \frac{2a}{\lambda} + \frac{1}{\lambda^2}\right] \tag{3.33}$$

Where:

$$k = \frac{2bE_{22}}{h} \tag{3.34}$$

$$\lambda = \left(\frac{3k}{bh^3E_{11}}\right)^{\frac{1}{4}} \tag{3.35}$$

Reeder and Crews Jr [19] modified the beam theory equations further more for strain energy release rate by taking into account the shear deformation energy associated with bending by adding the shear deformation components of strain release rate to Eq. (3.33). The contribution of shear effect will change Eqs. (3.30) and (3.31) to Eqs. (3.36) and (3.37):

$$G_I = \frac{3P^2(3c-L)^2}{4b^2h^3L^2E_{11}}\left[a^2 + \frac{2a}{\lambda} + \frac{1}{\lambda^2} + \frac{h^2E_{11}}{10G_{13}}\right] \tag{3.36}$$

$$G_{II} = \frac{9P^2(c+L)^2}{16b^2h^3L^2E_{11}}\left[a^2 + \frac{0.2h^2E_{11}}{G_{13}}\right] \tag{3.37}$$

ASTM D D6671/D 6671M-06 [24] explains the procedure for measuring the mixed mode delamination fracture toughness where the mode mixtity G_{II}/G_T depends on correction for delamination length and for rotation at the crack front. The equations presented in the ASTM are based on researches by Williams [13], Wang and Williams [14], Kinloch and Wang [27].

$$c = \frac{12\beta^2 + 3\alpha + 8\beta\sqrt{3\alpha}}{36\beta^2 - 3\alpha}L \tag{3.38}$$

$$\alpha = \frac{1 - \frac{G_{II}}{G}}{\frac{G_{II}}{G}} \tag{3.39}$$

$$\beta = \frac{a + \Delta_I h}{a + 0.42\Delta_I h} \tag{3.40}$$

$$C_{cal} = \frac{2L(c+L)^2}{E_{cal}b_{cal}t^3} \tag{3.41}$$

$$C_{sys} = \frac{1}{m_{cal}} - C_{cal} \tag{3.42}$$

$$E_{1f} = \frac{8(a_0 + \Delta_I h)^3(3c-L)^2 + \left[6(a_0 + 0.42\Delta_I h)^3 + 4L^3\right](c+L)^2}{16L^2bh^3\left(\frac{1}{m} - C_{sys}\right)} \tag{3.43}$$

$$G_I = \frac{12P^2(3c-L)^2}{16b^2h^3L^2E_{1f}}(a + \Delta_I h)^2 \tag{3.44}$$

$$G_{II} = \frac{9P^2(c+L)^2}{16b^2h^3L^2E_{1f}}(a + 0.42\Delta_I h)^2 \tag{3.45}$$

$$G_T = G_I + G_{II} \tag{3.46}$$

$$\frac{G_{II}}{G_T} = \frac{G_{II}}{G_I + G_{II}} \tag{3.47}$$

Compliance based beam method follows the Timoshenko Beam Theory (TBT). C_{sys} is calculated using the slope of calibration curve and compliance calibration specimen. There are a few issues within this method such as stress concentration and root rotation effects, where at the crack tip it influences the compliance that is not accounted for in the beam theory. Oliveira et al. [22] states that when using this method on wood the flexural modulus is significantly specimen dependant due to the wood heterogeneity, and this requires measurements of the modulus for each test specimen. Therefore a corrected flexural modulus is estimated using the initial compliance C_{0I} and the crack length $a_0$which also considers the root rotation effects, shown in Eq. (3.49), where Δ_I is given in Eqs. (3.12) and (3.13) using E_{fl} instead of E_{11}. A repetitive process should be used to obtain a converged value of E_{fl} using Eq. (3.12) and (3.13). During the crack growth, Fracture Process Zone (FPZ) develops at the crack tip. To account for the dissipated energy in this region, a corresponding crack in mode I, a_{eqI}, is estimated from the existing specimen compliance by using Eq. (3.54). a_{eqI} is the equivalent crack length in mode I. The FPZ influences the specimen compliance and the effect is accounted for via the equivalent crack length. The solution of cubic Eq. (3.52) can be obtained by standard math tools such as MATLAB software [22].

$$C_I = \frac{8a^3}{E_{11}bh^3} + \frac{12a}{5bhG_{13}} \tag{3.48}$$

$$E_{fl} = \left(C_{0I} - \frac{12(a_0 + h|\Delta_I|)}{5bhG_{13}}\right)^{-1} \frac{8(a_0 + h|\Delta_I|)^3}{bh^3} \tag{3.49}$$

$$G = \frac{P^2}{2b}\frac{dC}{da} \tag{3.50}$$

By using Eq. (3.48), leading to

$$G_I = \frac{6P_I^2}{b^2h}\left(\frac{2a_{eqI}^2}{h^2E_{fl}} + \frac{1}{5G_{13}}\right) \tag{3.51}$$

Where

$$\alpha a_{eqI}^3 + \beta a_{eqI} + \gamma = 0 \tag{3.52}$$

$$\alpha = \frac{8}{bh^3E_{fl}}; \quad \beta = \frac{12}{5bhG_{13}}; \quad \gamma = -C_I \tag{3.53}$$

$$a_{eqI} = \frac{1}{6\alpha}A - \frac{2\beta}{A} \tag{3.54}$$

Where A is given by

$$A = \left(\left(-108\gamma + 12\sqrt{3\left(\frac{4\beta^3 + 27\gamma^2\alpha}{\alpha}\right)}\right)\alpha^2\right)^{1/3} \tag{3.55}$$

A similar procedure can be used for mode II. Eq. (3.56) is used for compliance where $C_{II} = \delta_{II}/P_{II}$. The displacement δ_{II} is obtained from $\delta_{II} = \delta C + \delta_I/4$ [22], displacement δ_C is measured at the specimen mid span by the loading lever; displacement δ_I is measured at the edge of the specimen. The corrected flexural modulus is obtained using the crack length and initial compliance. a_{eqII} is the equivalent crack length in mode II.

$$C_{II} = \frac{3a^3 + 2L^3}{8E_{11}bh^3} + \frac{3L}{10bhG_{13}} \tag{3.56}$$

$$E_{fII} = \frac{3a_0^3 + 2L^3}{8bh^3}\left(C_{0II} - \frac{3L}{10G_{13}bh}\right)^{-1} \tag{3.57}$$

Equivalent crack accounting for the Fracture Process Zone (FPZ) effects is estimated from Eqs. (3.58) and (3.59).

$$a_{eqII} = \left[\frac{C_{IIcorr}}{C_{0IIcorr}}a_0^3 + \frac{2}{3}\left(\frac{C_{IIcorr}}{C_{0IIcorr}} - 1\right)L^3\right]^{1/3} \tag{3.58}$$

Where

$$C_{IIcorr} = C_{II} - \frac{3L}{10G_{13}bh} \text{ and } C_{0IIcorr} = C_{0II} - \frac{3L}{10G_{13}bh} \tag{3.59}$$

$$G_{II} = \frac{9P_{II}^2 a_{eqII}^2}{16E_{fII}b^2h^3} \tag{3.60}$$

Results of load-displacement of MMB tests are shown in Figure 3.8. Table 3.4 summarises the test results in mode I/II loading. The results of CBT and SBTEF are close and ASTM is the lowest estimate of Mixed-Mode delamination toughness.

Table 3.4 Results of MMB experiment C = 42 mm and C = 97 mm

Method of analysis	C=42 mm				C=97 mm			
	G_I (J/m^2)	G_{II} (J/m^2)	G_T (J/m^2)	G_{II}/G_T (%)	G_I (J/m^2)	G_{II} (J/m^2)	G_T (J/m^2)	G_{II}/G_T (%)
CBT	382 ± 9	484 ± 9	866 ± 15	56 ± 2	314 ± 21	85 ± 21	399 ± 13	22.3
ASTM	265 ± 11	336 ± 11	601 ± 11	56 ± 2	354 ± 11	96 ± 11	451 ± 11	22.3
SBT	321 ± 15	448 ± 15	769 ± 15	58 ± 2	246 ± 21	77 ± 13	322 ± 21	23.7
SBTEF	367 ± 14	453 ± 15	821 ± 15	56 ± 2	307 ± 21	84 ± 21	391 ± 21	22

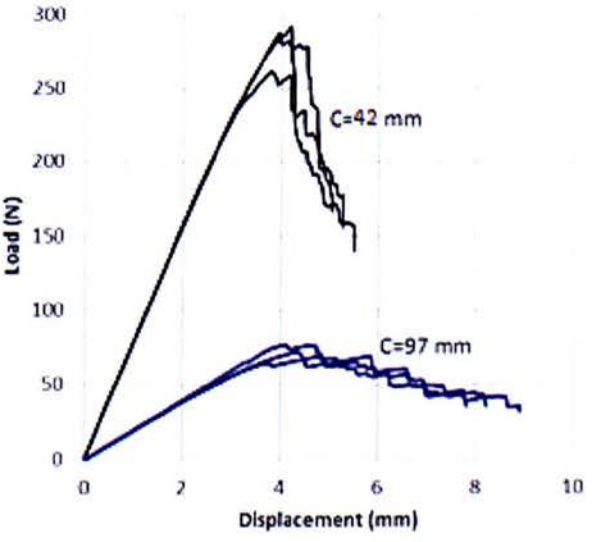

Fig. 3.8. Experimental results of load-displacement for MMB tests at c = 42 and 97mm.

3.6 Fracture Failure Envelope

The failure envelope for the GFRP is shown in Figure 3.9 where G_{IC} is the vertical axis (from DCB-CBT) and G_{IIC} is the horizontal axis (from ENF-CBBM) together with the results of MMB C97 and MMB C42. Inside the envelope, the material is safe from delamination under full range of mode mixity and outside of the envelope, it will delaminate.

Figure 3.10 shows variation of G_T vs. G_{II}/G_T. The DCB results are shown at G_{II}/G_T =0 and the ENF results are at G_{II}/G_T =1. Between these two extreme is mix mode I/II loading. Two set of MMB at G_{II}/G_T = 0.22 (C97) and G_{II}/G_T = 0.56 (C42) has been shown. As from pure mode I interlaminar delamination to pure mode II, the resistance to delamination increases.

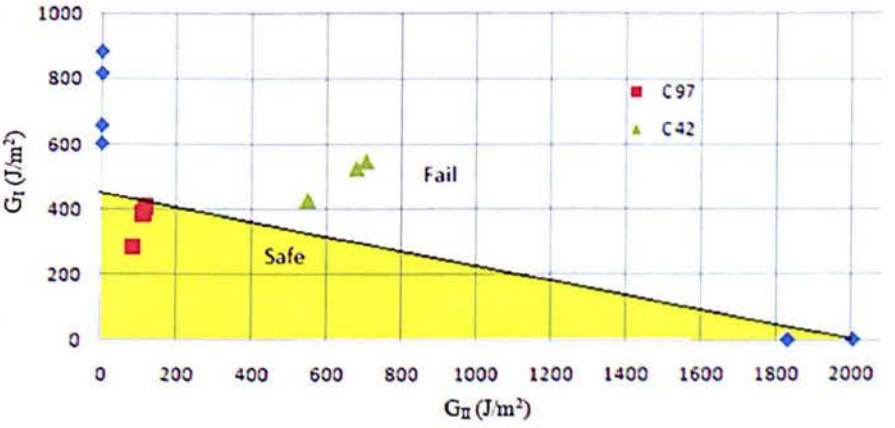

Fig. 3.9. Failure envelope for the GFRP composite.

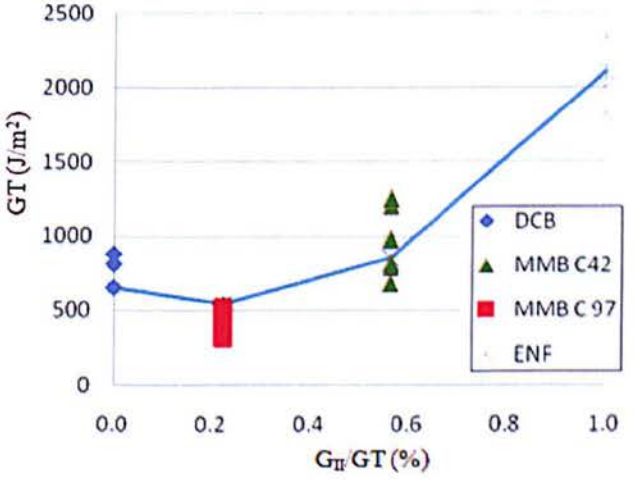

Fig. 3.10. Variation of total delamination fracture toughness, G_T, with respect to mode mixity ratio G_{II}/G_T

3.7 Conclusion

Laminated FRP composite materials are used in many parts of wind turbine blade. These materials are susceptible to delamination, separation of the plies in the low resistance thin resin-rich interface between adjacent layers particularly under compressive loading, impacts or free-edge stresses. The existence of high stress gradients near geometric discontinuities in composite structures such as holes, cut-outs, flanges, ply drop-offs, stiffener terminations, bonded and bolted joints promote delamination initiation. Other causes of delamination are

the existence of contaminated fibres during the manufacturing process, insufficient wetting of fibres, curing shrinkage of the resin, and out-of-plane impact.

As there is always possibility of birds and other objects crashing or impacting a wind turbine blade, the delamination characterisation of laminated materials is quite important. The wind turbine designers must be aware of the behaviour of delaminated structure and take into account the delamination properties during design stage of the blade as the presence and growth of delamination significantly reduces the overall buckling strength and bending stiffness of a structure.

In this chapter, three test methods for characterisation of delamination fracture toughness of FRP composite materials are discussed. These tests are Double Cantilever Beam (DCB) for pure mode I delamination, 3 points End-Notched Flexure (3ENF) test for pure mode II delamination and Mixed-Mode Bending test (MMB) for mixed mode I/II delamination. For each test method, various available methods for analysis of the test results were presented and the results obtained from experiments of each method were compared.

By using these three test methods, the delamination fracture envelope under various loading conditions, from pure mode I (DCB) to various mode mixity to pure mode II (ENF) has been obtained. The delamination envelope is an essential tool for the application of the FRP material in different products.

Nomenclature

A_1	the slop of the graph of a/h vs. $C^{1/3}$
a	crack length
a_0	initial crack length
a_e	corrected crack length
b	specimen width
C	experimental compliance
C_{cal}	compliance of calibration specimen
C_{sys}	system compliance
C_C	corrected compliance
C_0	initial compliance in ENF test
C_{0C}	initial corrected compliance
DCB	Double cantilever beam
E_{cal}	modulus of calibration bar
E_f	flexural stiffness
E_{11}	modulus of elasticity in the fibre direction
E_{22}	transverse modulus
ENF	End-notched flexure
F	correction fracture for shortening of arm in DCB test
G_T	total strain energy release rate
G_I	mode I strain energy release rate
G_{II}	mode II strain energy release rate
G_{II}/G_T	mode mixity ratio
G_{12}	shear modulus
h	half of the specimen thickness
k	stiffness of elastic foundation
L	span length in MMB test
m	slope to C vs. a^3 graph
MMB	Mixed mode bending
n	slope of plot of Log C vs. log a
P	load
P_I	mode I load
P_{II}	mode II load
Δ	crack length correction
Δ_I	crack length correction in DCB test
Δ_{II}	crack length correction in ENF test
δ	deflection
β	non-dimensional crack length correction for mode mixture
α	mode mixture transformation parameter for setting lever length
λ	elastic foundation parameter

3.8 References

[1] Williams, J.G. (1989). End corrections for orthotropic DCB specimens, Composites Sciences and Technology, 35, 367-376.

[2] Blackman, B.R.K., Hadavinia, H., Kinloch A.J., Paraschi M. and Williams J.G. (2003). 'The calculation of adhesive fracture energies in mode I: Revisiting the tapered double cantilever beam (TDCB) test', Engineering Fracture Mechanics, Vol. 70(2), pp233-248.

[3] Davies, P., Blackman, B.R.K., Brunner, A.J. (1998). Standard test methods for delamination resistance of composite materials: current status. Applied composite materials 5: 345-364

[4] Ozdil, F. and Carlsson, L.A. (1999). Beam analysis of angle ply laminate DCB specimens. Composites Science and Technology, 59, 305-315.

[5] Gordnian, K., Hadavinia, H., Mason, P.J., Madenci, E. (2008). Determination of fracture energy and cohesive strength in Mode I delamination of angle-ply laminated composites, Composite Structures, 82(4), 577-586.

[6] Adams, D.F., Carlsson, L.A., Pipes R.B. (2002). Experimental characterization of advances composite materials, CRC Press; 3rd edition, ISBN-10: 1587161001.

[7] ASTM D 5528-01, (2007). Standard test method for mode I interlaminar fracture toughness of unidirectional fibre reinforced polymer matrix composites, 261-270.

[8] Turmel. D.J.P, Szpicak. J.A., Singh. S and Partridge. I.K. (1995). Crack initiators and pre-cracking techniques for fracture testing of polymer matrix composites Proc. 3rd International Conference on Deformation and Fracture of Composites (DFC3), 27th 29th March, University of Surrey, Guilford, U.K.

[9] Russell, A.J. (1982). On the measurement of mode II interlaminar fracture energies, Defence Research Establishment Pacific, Victoria, Material report 82.

[10] Russell, A.J. and Street, K.N. (1982). Factor affecting the interlaminar fracture energy of graphic/epoxy laminates, Progress in Science and Engineering of composite, ICCM-IV, Tokyo, Japan, 279-296.

[11] Murri G.B. and O'brien T.K. (1985). Interlaminar GIIC evaluation of toughened resin matrix composites using the end-notched flexure test, the 26th AIAA/ASME/ASCE/AHS Structures, Structural Dynamics, and Materials Conference, Orlando, Florida, April

[12] Carlsson, L.A., Gillespie, J.W. and Trethewey, B. (1986). Mode II interlaminar fracture toughness in graphite/epoxy and graphite/PEEK composites, J. Reinf. Plast. Compos., 5, 170-87.

[13] Williams, J.G. (1989). The fracture mechanics of delamination test. Journal of Strain Analysis, 24, 207-214.

[14] Wang Y. and Williams J.G. (1992). Corrections for Mode II fracture toughness specimens of composite materials. Composites Sciences and Technology 43, 251-256.

[15] Ozdil, F., Carlsson, L.A. and Davies, P. (1998). Beam analysis of angle ply laminate end notched flexure specimens. Composites Science and Technology, 58, 1929-1938.

[16] Russell, A.J. and Street, K.N. (1985). Moisture and temperature effects can the mixed-mode delamination fraction of unidirectional graphic/epoxy, Delamination and Rebinding of Material, ASTM STP 876, Philadelphia, 349-356

[17] Russell, A.J. and Street, K.N. (1983). Moisture and temperature effects on the mixed-mode delamination fracture of unidirectional graphic/epoxy, DREP technical memo 83-22, Defence Research Establishment Pacific, Victoria, B.C., Canada.

[18] Russell, A.J. and Street, K.N. (1985). Moisture and temperature effects on the mixed-mode delamination fracture of unidirectional graphite/epoxy. Delamination and debonding of materials, ASTM STP 876, W.S. Johnson, Ed., Philadelphia, 349-370.

[19] Reeder, J.R. and Crews Jr., J.R. (1990). Mixed-mode bending method for delamination testing, AIAA Journal, 28(7), 1270-1276.

[20] Ozdil, F. and Carlsson L.A. (1999). Beam analysis of angle ply laminate mixed mode bending specimens. Composites Science and Technology 59, 937-945.

[21] Tenchev, R.T. and Falzon, B.G. (2007). A correction to the analytical solution of the mixed-mode bending (MMB) problem. Composite Science and Technology, 67, 662-668.

[22] Oliveira, J.M.Q. de Moura, M.F.S.F., Silva, M.A.L., Morais, J.J.L. (2007). Numerical analysis of the MMB test for mixed-mode I/II wood fracture. Composite Science and Technology 67, 1764-1771.

[23] de Morais A.B. and Pereira A.B. (2006). Mixed mode I+II interlaminar fracture of glass/epoxy multidirectional laminates-Part 1: analysis. Composite Science and Technology, 66, 1889-1895.

[24] ASTM Standard D6671/D 6671M-06 (2006). Test method for mixed mode I-mode II interlaminar fracture toughness of unidirectional fiber reinforced polymer matrix composites.

[25] ISO Standard 15024, Standard test method for Mode I interlaminar fracture toughness G_{IC} of unidirectional fibre reinforced polymer matrix composites

[26] Kanninen, M.F. (1973). An augmented double cantilever beam model for studying crack propagation and arrest. International Journal of Fracture, 9(1), 83-92.

[27] Kinloch, A.J. and Wang Y., Williams, J.G., Yayla, P. (1993). The mixed-mode delamination of fibre-composite materials. Composite Science and Technology, 47, 225-237.

4

Characterisation of Fatigue Behaviour of GFRP Composite Laminate

4.1 Introduction

The power train components of a wind turbine are subjected to a highly irregular loading condition from turbulent wind flow. As a result the number of fatigue cycles experienced by the blades is of orders of magnitude greater than other rotating machineries. The design lifetime of a modern wind turbine is 20-30 years and the wind turbine is almost always unattended. In comparison a manned motor vehicle frequently maintained and has a typical operational life of about 160,000 km, equivalent to 4 months of continuous operation.

In designing of composite wind turbine blades it is crucial to calculate the damage tolerance of the blade structures. In order to prevent damage formation and also correctly evaluate the stability of damaged blade under load, the appropriate mechanical properties under dynamic loads are required. In large horizontal axis wind turbines (HAWT), the blade acts as a long cantilever beam, of the order of 80-100 m experiencing cyclic loading throughout its service life. Selecting appropriate materials and design for the blade will guarantee the structure would not fail under its weight and the external operating load for the expected duration of 20-30 years is service.

Laminated fibre reinforced plastic is the best material for large wind turbine blades. Laminated glass fibre reinforced plastic (GFRP) is the preferred material for HAWT blades because of their high specific strength, low weight and low cost relative to the other FRPs. However these materials are susceptible to delamination by separation of the plies in the low resistance thin resin-rich interface between adjacent layers particularly under compressive loading caused under cyclic loading. The out-of-plane stresses, which naturally cause delamination, occur at many types of structural details in wind turbine blades, as indicated in Figure 4.1, are caused by ply drops, skin-stiffener intersections, sandwich panel, free edge, and trailing edge areas, near geometric discontinuities such as holes, cut-outs, flanges, stiffener terminations, bonded and bolted joints promote delamination initiation [1]. Other causes of delamination are the existence of contaminated fibres during the manufacturing process, insufficient wetting of fibres, curing shrinkage of the resin, and out-of-plane impact.

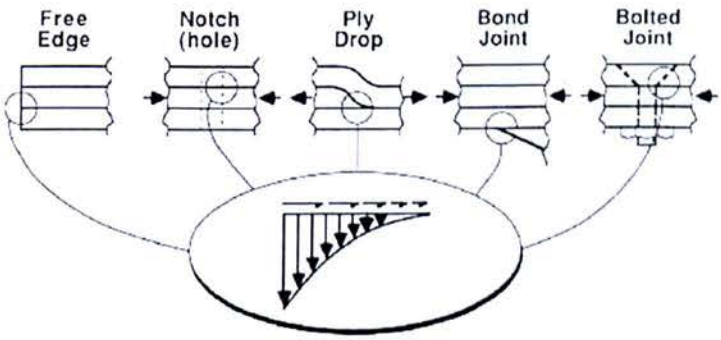

Fig . 4.1. Common structural elements which generate interlaminar stress concentrations [2].

In structures under fatigue loading R-ratio, the ratio of minimum stress to maximum stress, influences the fatigue behaviour of the materials and this effect has been investigated numerous times in the past by many researchers, e.g. [3-12]. The combined effects of mean stress and material anisotropy on the fatigue life of the composite materials are studied by constant life diagrams (CLD). CLDs are used to estimate the materials fatigue life. The basic fatigue terminology is shown in Figure 4.2.

This chapter looks at the characterisation of fatigue behaviour of GFRP composite material at two fibre orientations of 0° and 90°. The applied cyclic stress can be in the loading range of $0<R<1$ for tension-tension (T-T), $-\infty<R<0$ range for tension-compression (T-C), and $1<R<+\infty$ for compression-compression (C-C) fatigue loading. The cases investigated in this chapter are

tension-tension at R=0.1, 0.5, reverse tension-compression cycling at R=-1 (with σmin = 0) and compression-compression at R=2 and R=10 for 0° and 90° laminates.

A constant amplitude load waveforms showing definition of terms and illustration of R-values is shown in Figure 4.3. The data obtained from the fatigue testing of coupon specimens are used to produce S-N diagram at different R ratios and from there CLDs for 0° and 90° fibre orientation have been built.

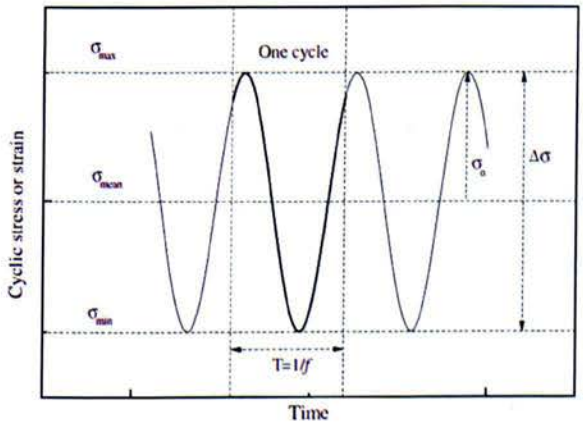

Fig. 4.2. Basic fatigue terminology.

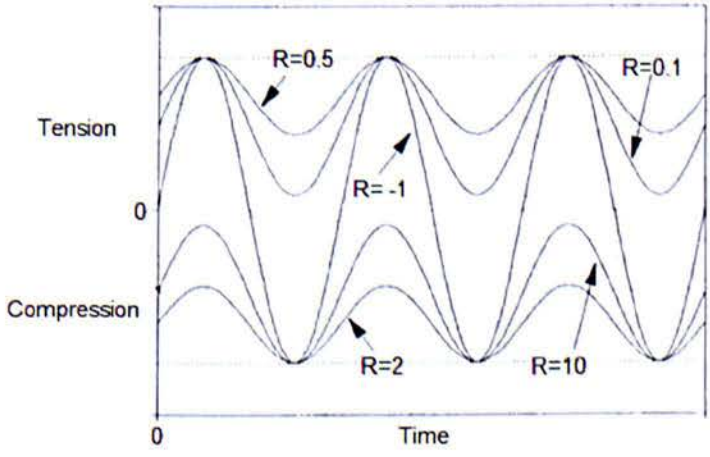

Fig. 4.3. Constant load amplitude waveforms showing different R-values.

4.2 Experimental Methodology

Two set of tests on fatigue performance of laminated GFRP materials are investigated. First the study is focused on the stress-life diagram of the coupon specimens and construction of constant life diagram in 0° and 90° laminates. Next the effects of fatigue loading on

delamination of laminated GFRP are studied. In this part fatigue delamination in mode I and mode II are characterised using DCB and ENF specimens.

4.2.1 Stress-Life Diagram (S-N Diagram)

The fatigue life of materials is often shown by an S-N diagram. The S-N curve describes the relationship between stress amplitude (or sometimes as percentage of material's UTS) versus the maximum number of cycles to failure usually for a uniaxial applied loading at a specified stress ratio R as shown in Figure 4.4. A log scale is normally used for N whereas a linear scale is often used for S, but sometimes a log scale is also used. At each R ratio up to six specimens are tested.

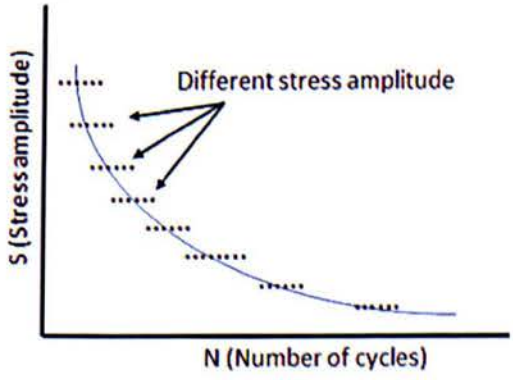

Fig. 4.4. A representative S-N diagram.

4.2.2 Constant Life Diagram (CLD)

For efficient evaluation of the fatigue lives of composites under different constant amplitude fatigue loading conditions another approach proposed by Rotem [13] and Rotem and Nelson [14] for predicting the S–N curves for general laminates at arbitrary stress ratios on the basis of a fatigue failure envelope similar to the (linear) Goodman diagram [15]. Constant Life Diagram (CLD) offers a tool to predict and estimate the fatigue life of a material under various combinations of uniaxial mean and alternative stresses for failure at a specified lifetime based on S-N curve where no experimental data exist. CLD is more useful than S-N diagram; however the construction of CLD requires many data points to cover the whole spectrum of fatigue loading by using many S-N data at different R values.

The main parameters that define a CLD are the mean cyclic stress, σ_m, the cyclic stress amplitude, σ_a, and the R-ratio defined as the ratio between the minimum and maximum

cyclic stress, $R = \sigma_{min}/\sigma_{max}$. Each line represents a single S–N curve at a given R-ratio and can be obtained using the following equation:

$$\sigma_a = \left(\frac{1-R}{1+R}\right)\sigma_m \tag{4.1}$$

A CLD is a half plane divided into three sections, any point where the stress ratio is between 0<R<1 is tension-tension loads, anywhere where -∞<R<0 is tension-compression and any point where the stress ratio is between 1<R<+∞ is compression-compression loads as shown in Figure 4.5.

The CLDs for composite materials are usually shifted towards the tension- or compression-domain, reflecting the degree of anisotropy of the examined material [16-20]. For laminates exhibiting significantly higher tensile strength than compressive strength, e.g. unidirectional carbon/epoxy laminates [15], the CLD is shifted towards the tension-dominated domain in the right side of CLD. For materials exhibiting higher compressive strength than tensile strength, e.g. short-fibre composites [20], the diagram is shifted towards the compression-dominated domain.

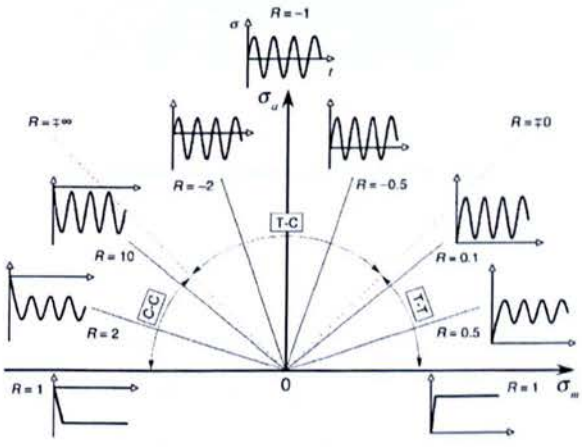

Fig. 4.5. Schematic representation of constant amplitude stress-time patterns at different levels of mean stress [10].

4.2.3 DCB and ENF mode II fatigue delamination growth

As explained in Chapter 2 delamination in wind turbine blades is a major design issue especially when the loading is cyclic. As a result in this chapter delamination crack growth in Mode I (DCB specimen) and Mode II (ENF specimen) are studied.

The initiation and propagation fracture toughness in these two modes are obtained and the results are compared with the static tests reported in Chapter 3.

4.3 S-N diagram experimental studies

4.3.1 Specimen coding, lay-up and material

In order to prevent ambiguity the specimens have been labelled using RX-AY-LZ-n key. The applied loading ratio, R, is X, the angle of laminate in direction of loading, A, is Y, the percentage of applied maximum loading relative to UTS or UCS is L, and n is the repeat number of sample. For example R0.5-A0-L50-4 is the fourth specimen tested at R=0.5 for a 0° laminate at maximum loading of 50% of UTS. The lay-up of coupon specimens for T-T, are $[0]_8$, $[90]_8$ and for T-C and C-C are $[0]_{14}$, $[90]_{14}$ using UD prepreg glass fibre/epoxy matrix E722-02 UGE400-02 materials supplied by TenCate Ltd. Note that for DCB and ENF fatigue specimen discussed later in this chapter the same material is used.

4.3.2 Specimen preparation

The dimensions of tension-tension (T-T) specimens are shown in Figure 4.6 for all R values conducted in this study.

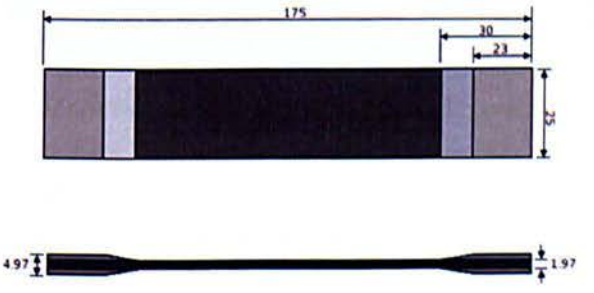

Fig. 4.6. Tension-tension specimen dimensions (mm).

In tension-compression (T-C) and compression-compression (C-C) tests the buckling of the coupons should be prevented and these are accounted for by calculating the proper size for the specimens. The proper dimensions for the specimen to avoid the buckling are specified and the specimen dimensions for all T-C and C-C are shown in Figure 4.7.

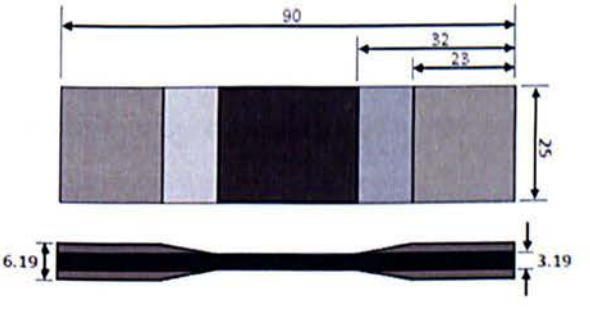

Fig. 4.7. Tension-compression and compression-compression specimen dimensions (mm).

GFRP coupon specimens in fibre direction are manufactured according to the following steps. Firstly marked and cut out 14 layers in fibre direction of 175×25 mm prepreg. The manufacturing process used to produce the coupon specimens are discussed in Appendix A. After the specimen cured and returned to room temperature applied 0.5mm of epoxy adhesive ESP110 for the end tabs (30mm×25mm), placed them on the ends of specimens using clamp. The specimen returned back to the oven for 60min at 120°C. The final product after curing with end tabs for tension-tension specimens are shown in Figure 4.8. The same manufacturing procedure is used for all other specimens in this study.

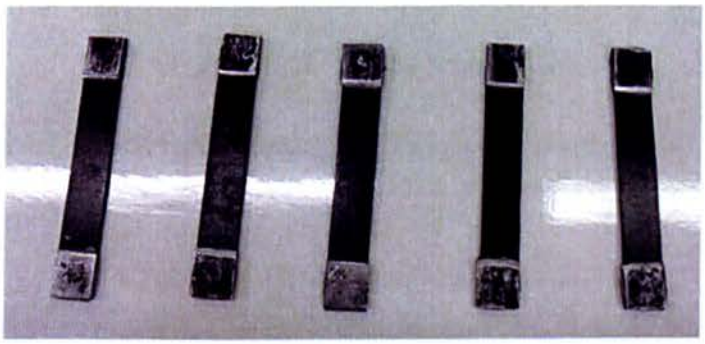

Fig. 4.8. Manufactured tension-tension fatigue test coupons.

4.3.3 Experimental results

The tensile and compression tests of the GFRP composite have been done and the mechanical properties are summarised in Table 3.1. The details of material characterisation can be found in Appendix A. The tests were carried out on a Zwick/Roell Z050 universal testing machine with a load cell of 50 kN and a MTS 200 kN machines.

All coupon fatigue tests were conducted on constant amplitude load control sinusoidal loading using a Zwick/Roell Amsler HC 25kN servo hydraulic fatigue testing machine (see Figure 4.9). Load ratios of R=0.1, 0.5 for T-T, R=-1 for T-C and R=2, 10 for C-C were examined. For each R-ratio, 16 test samples were prepared and depending to the applied R, tests were carried out at absolute maximum stress between 30-80% of UTS or UCS. The frequency of fatigue tests throughout the duration of the all tests was kept constant at of 5 Hz and force ramp time to maximum load was 10 second.

The experimental test condition for 90° and 0° fibre directions are summarised in Table 4.1.

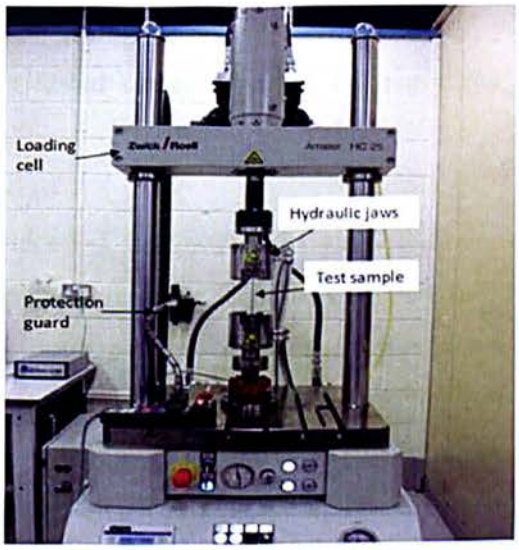

Fig. 4.9. Zwick/Roell Amsler HC 25 fatigue experiment layout.

Table 4.1 Experimental conditions.

90° specimens					0° specimens				
R Value	% of UTS	σ_{max} (MPa)	σ_{min} (MPa)	σ_{mean} (MPa)	R Value	% of UTS	σ_{max} (MPa)	σ_{min} (MPa)	σ_{mean} (MPa)
0.5	70	52.3	26.1	39.2	0.5	80	516.8	258.4	387.6
0.5	60	44.8	22.4	33.6	0.5	70	452.2	226.1	339.2
0.5	50	37.4	18.7	28.05	0.5	60	387.6	193.8	290.7
0.5	40	29.9	14.9	22.4	0.5	50	323	161.5	242.3
0.1	80	59.8	6	32.9	0.5	40	258.4	129.2	193.8
0.1	70	52.3	5.2	28.75	0.5	30	193.8	96.9	145.4
0.1	60	44.8	4.5	24.65	0.1	70	452.2	45.2	248.7
0.1	50	37.4	3.7	20.55	0.1	60	387.6	38.8	213.2
0.1	40	29.9	2.9	16.45	0.1	50	323	32.3	177.7
0.1	30	22.4	2.2	12.3	0.1	40	258.4	25.8	142.1
-1	70	52.3	-52.3	0	0.1	30	193.8	19.4	106.6
-1	60	44.8	-44.8	0	-1	80	184	-184	0
-1	50	37.4	-37.4	0	-1	75	172.5	-172.5	0
-1	40	29.9	-29.9	0	-1	70	161	-161	0
-1	30	22.4	-22.4	0	-1	63	144.9	-144.9	0
2	80	-72	-144	-108	-1	59	135.7	-135.7	0
2	75	-67.5	-135	-101.3					
2	74	-62.9	-125.8	-94.35					
2	70	-63	-126	-94.5					
2	60	-54	-108	-81					
10	70	-11.9	-119	-65.45					
10	60	-10.8	-108	-59.4					
10	50	-9	-90	-49.5					
10	40	-7.2	-72	-39.6					
10	30	-5.4	-54	-29.7					

4.3.4 Effect of R ratio on failure modes

Failure modes on coupon tested under dynamic loading differ from those tested under monotonic uniaxial tensile.

In 90° specimens tested under T-T load at R = 0.1 and 0.5 ratios, samples failed in direction normal to the applied load direction along the fibre direction and through the resin matrix as shown in Figure 4.10(a). Few samples broke near the end tabs and some in the middle of the coupons. For 90° coupon tests subjected to reverse loading of T-C at R = -1 the coupon specimens failed as shown in Figure 4.10(b). Tests of 90° coupon subjected to C-C at R = 2 and 10 were conducted. Representative failed specimens at 90° at R= 2 and σ_{min}= 75% of Xc are shown in Figure 4.11. In C-C tests delaminations and splaying plies are common failure mechanism.

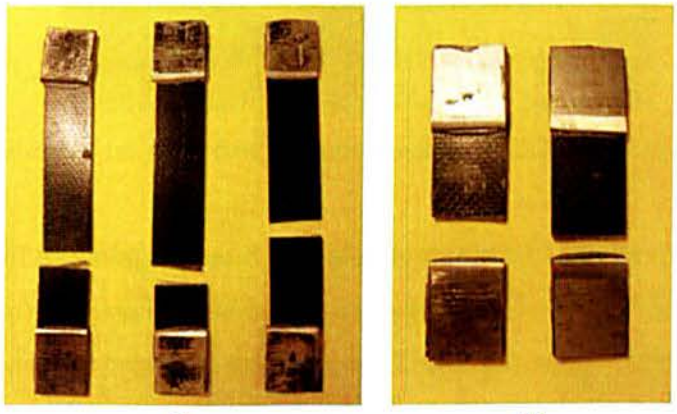

(a) (b)

Fig . 4.10. Failure of fatigued coupons specimens for 90° at 5 Hz (a) R=0.1 and (b) R=-1.

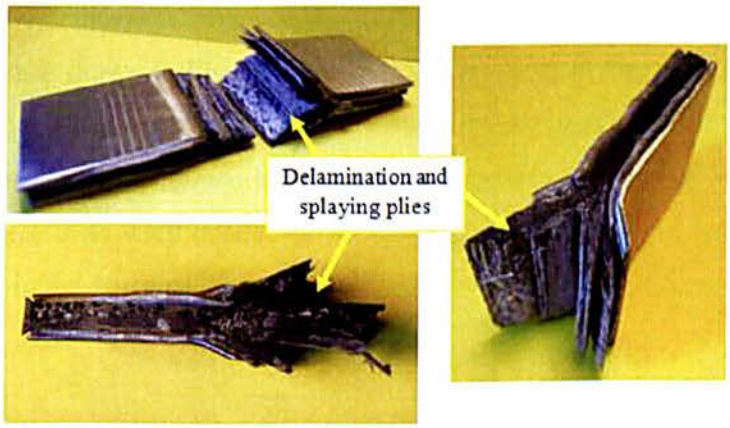

Fig. 4.11. Failure of fatigued coupon specimens at 90° at R= 2 and σ_{min}= 75% of Xc.

In 0° specimens under T-T load ratios of R = 0.1 and 0.5 samples failed by fibre breakage in irregular pattern as shown in Figure 4.12. For 0° coupon tests subjected to reverse loading T-C at R = -1 the coupon specimens failed in compression as shown in Figure 4.13. This is because compression strength in the fibre direction is Xc= 230 MPa while tensile strength is Xt=626 MPa.

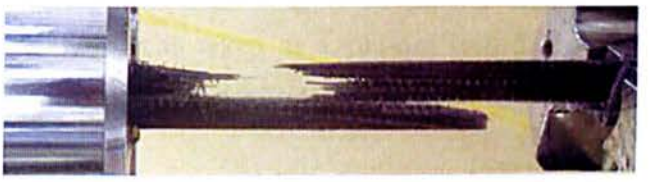

Fig. 4.12. Failure of fatigued coupon specimens at 0° at R= 0.1, σ_{max}= 60% of Xt.

Fig. 4.13. Failure of fatigued coupon specimens at 0° at R= -1 at σ_{min}= 80% of Xc.

4.3.5 The results of S-N diagram and stiffness degradation under cyclic loading

The maximum number of cyclic loading was set between 1.2×10^6 to 2.5×10^6 cycles and if the coupon specimen did not break the test stopped. Those specimens which did not break after maximum allowed number of cycles are marked as run-out specimens and they are showed by an arrow on S-N diagrams.

The results of the S-N diagram for specimens under T-T and T-C loading at R= 0.1, 0.5 and -1 for 0° direction are shown in Figure 4.14. The S-N diagram in Figure 14(a) shows that for 0° specimen at R = 0.1 at maximum load of 30% of Xt the specimen run out. Figure 14(b) shows S-N diagram for 0° specimen at R = 0.5 and at maximum load of 30% of Xt run-out test occurred. These tests were conducted at a frequency of 5 Hz. In Figure 14(c) the T-C results are shown in the range of 75-85% of UCS. The run-out after 10^6 cycles was at 75% of UCS.

The results of the S-N diagram for specimens under T-T loading at R= 0.1 and 0.5 for 90° are shown in Figure 4.15. The tests were run-out at maximum 1.2×10^6 cycles. The S-N diagram

in Figure 4.15(a) shows that for 90° specimen at R = 0.1 at maximum load of 30% of UTS the specimen run-out. However Figure 4.15(b) shows S-N diagram for 90° specimen at R = 0.5 and at maximum load of 40% of Yt the specimen run-out.

The results of the S-N diagram for specimens under T-C at R= -1 for 90° representing tension-compression reversed loading are shown in Figure 4.16. The tests were stopped at maximum 1.2×10^6 cycles. This is taken as a run-out test. The tests were conducted for maximum stress in the range of 40-70% of Yt.

The results of the S-N diagram for specimens under C-C loading at R= 10 for 90° are shown in Figure 4.17. The tests were stopped at maximum 1.2×10^6 cycles. This is happened at minimum stress of 60% of UCS. The tests were conducted from minimum stress equal to 40% of Yc.

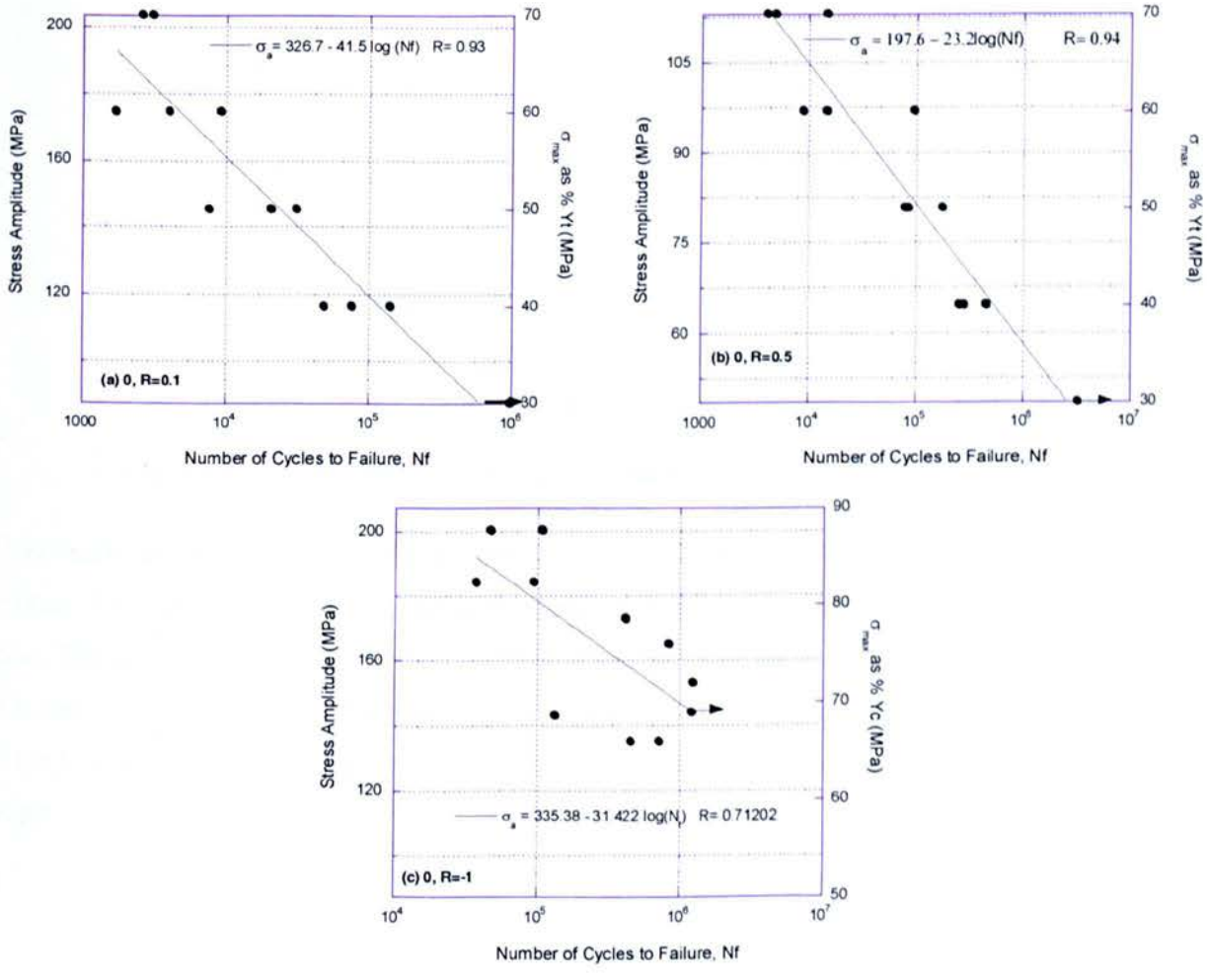

Fig. 4.14. S-N diagram for T-T loading (a) 0°, R=0.1 (b) 0°, R=0.5 and (c) T-C loading R=-1.

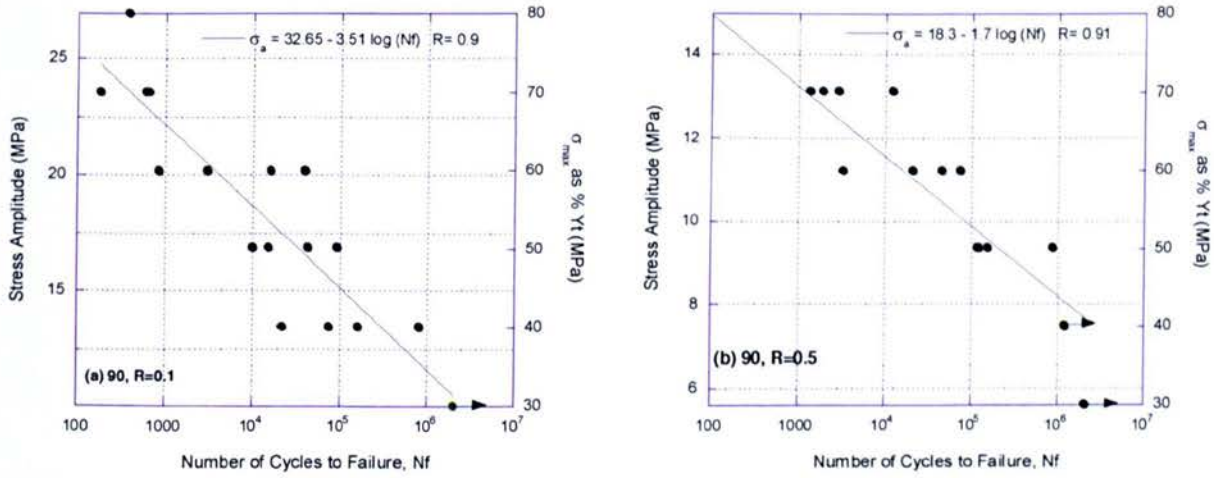

Fig. 4.15. S-N diagram for T-T loading (a) 90°, R=0.1 and (b) 90°, R=0.5.

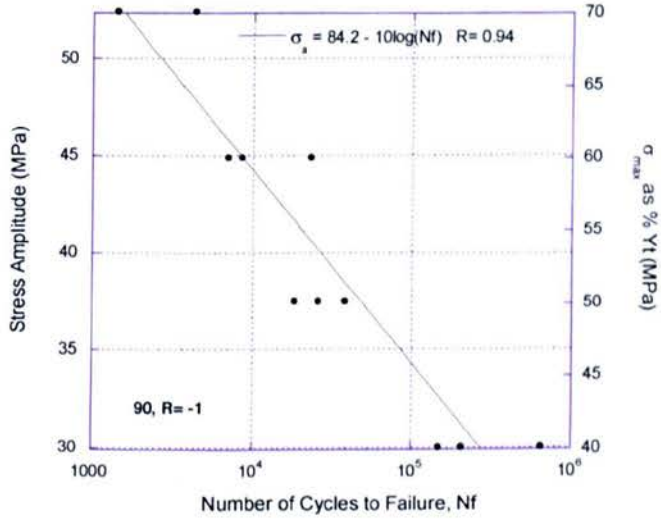

Fig. 4.16. S-N diagram for T-C reverse loading for 90° and R=-1 at 5 Hz.

The results of the S-N diagram for specimens under C-C loading at R= 2 for 90° are shown in Figure 4.17. The tests were stopped at maximum 1.2×10^6 cycles. This is taken as a run-out test. The tests were conducted from minimum stress equal to 60% of Yc. A higher scatter in the tests results was observed in compression-compression tests as can be seen in Figure 4.18. This is in accordance with other works reported in the literature for compression-compression tests.

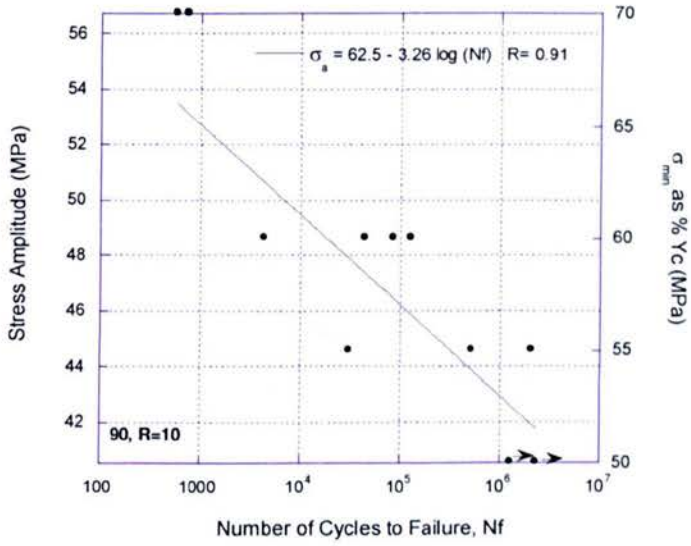

Fig. 4.17. S-N diagram for C-C reverse loading for 90° and R=10 at 5 Hz.

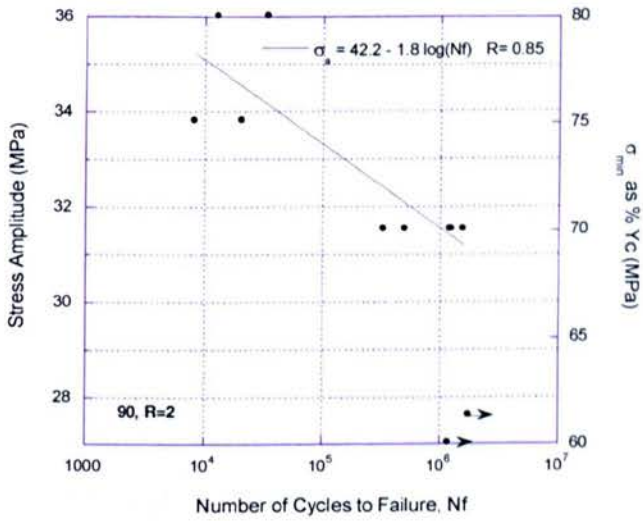

Fig. 4.18. S-N diagram for C-C reverse loading for 90° and R=2 at 5 Hz.

The degree of damage in a FRP composite material can be measured by the decrease of a relevant damage metric, usually the residual strength or residual stiffness. The stiffness of the coupon is the load/extension. The initial stiffness K(1) at first load cycle and stiffness K at subsequent intervals are recorded for each coupon. The results of stiffness degradation of 90° coupon specimens in fatigue loading at various R-ratios=0.1, 0.5, -1, 2 and 10 at 60% UTS for R>0 and 60% UCS for R<0 are extracted and plotted in Figure 4.19. The results show that the maximum stiffness damage during cyclic loading occurs at reverse loading of R=-1 and initial stiffness drooped to 30% at failure. However, the stiffness damage in C-C for R>1 is minimal and in these cases ''sudden-death phenomenon'' of the coupon is happened.

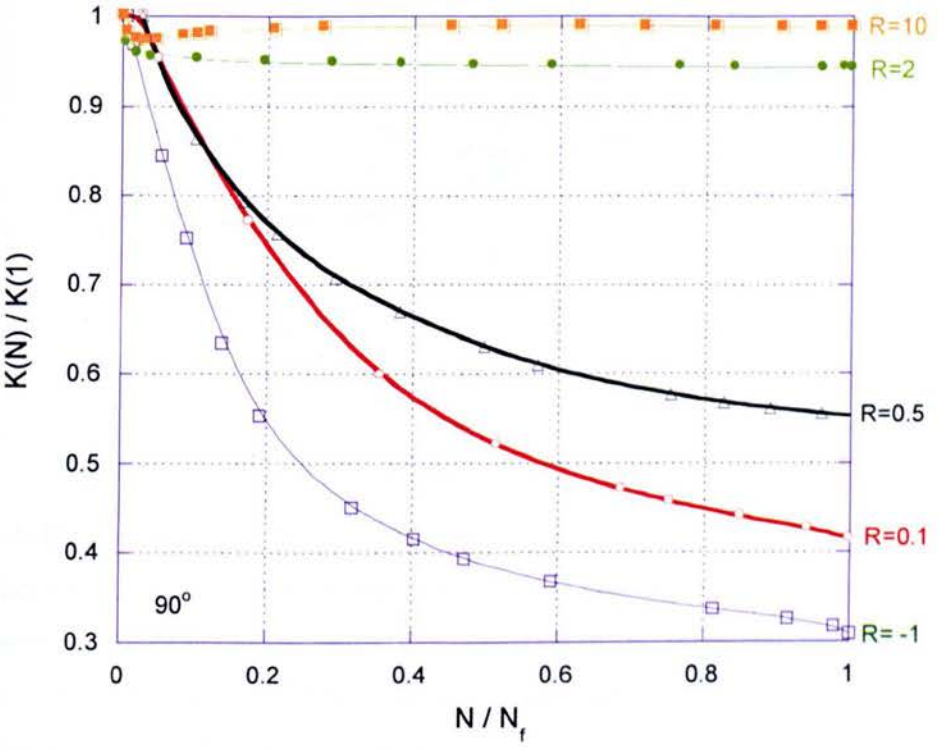

Fig. 4.19. Stiffness degradation of 90° coupon specimens in fatigue testing at various R-ratios at 60% UTS for R=0.1, 0.5 and 60% UCS for R=-1, 2 and 10.

4.4 Construction of constant life diagram (CLD)

The combined effect of mean stress and material anisotropy on the fatigue life behaviour of the examined composite material can be reflected on constant life diagrams. In addition CLDs offer a predictive tool for the estimation of the fatigue life of the composite under loading patterns for which no experimental has been done.

The CLD is the projection of the constant amplitude S-N fatigue data on a plane perpendicular to the life axis, at the N=1 in a 3D σ_a-σ_m-N space (see Figure 4.20) [22]. As discussed in section 4.3 each S-N curve is determined at a fixed R-value, and is therefore in a flat plane, at an angle to the horizontal plane. All 'S-N planes' intersect σ_a-σ_m plane with a straight line representing lines of constant R-value emanating from the origin since mean stress and stress amplitude are directly proportional to each other. As a result the ordinate of CLD and zero-mean stress line (R=-1) are at the same location.

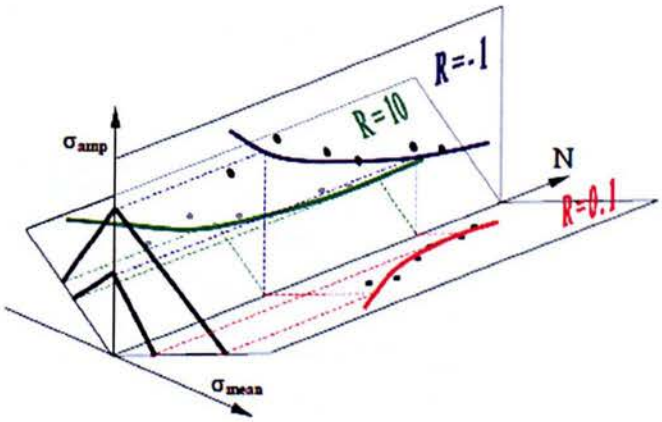

Fig. 4.20. Schematic of relation between S-N curves and CLD [22].

All the S-N fatigue data at R= 0.5, 0.1, -1, 10 and 2 for 90° and 0° specimens have been used to construct the CLD diagram as shown in Figure 4.21 and 4.22, respectively. These curves are of great importance for the study and applicability of these materials by designers. However, as these diagrams are built by using a small quantity of S–N curves, it will possible they underestimate or overestimate the real behaviour of the composite material. As a result, more tests should be carried out in order to obtain results with higher precision.

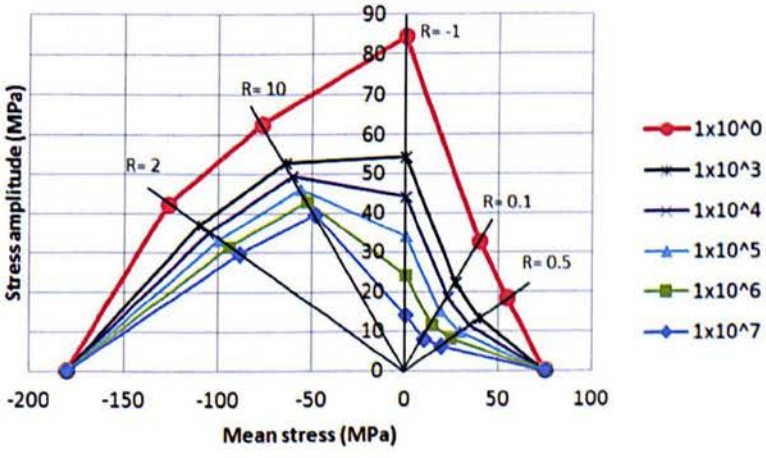

Fig . 4.21. CLD diagram for 90°, Yt = 74 MPa, Yc = 180 MPa.

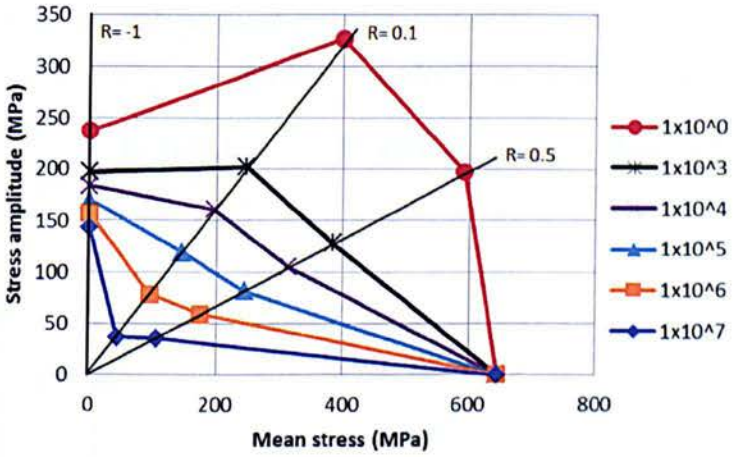

Fig . 4.22. CLD diagram for 0°, Xt = 626 MPa, Xc = 230 MPa.

4.5 Mode I fatigue delamination growth in GFRP laminates

4.5.1 Introduction

Delamination is a major weakness of laminated composite materials and understanding the resistance of the FRP materials to interlaminar fracture under cyclic loading is essential for establishing guidelines for allowable and damage tolerance design in the structures.

Fracture mechanics based models for prediction of fatigue lifetime and estimation of the remaining life of metallic components are well established. In FRP composite also delamination growth models are required for predicting fatigue lifetime and establishing suitable inspection intervals. It is well recognised that when delamination detected it should be repaired long before it reach to the critical length or the stress at the crack tip exceeds the residual strength of the component. Similar to metals in FRP composite materials fatigue delamination growth follows a sigmoidal curve when $\mathbf{log}\left(\frac{da}{dN}\right)$ plotted against $\mathbf{log}\left(\frac{G_{Imax}}{G_{IC}}\right)$ as shown schematically in Figure 4.23. This curve has three regions: Region I cover the threshold below the fatigue threshold (G_{th}) where the crack growth is normally less than 10^7 mm/cycle [23]. Region II is the stable growth. This region emerges after the fatigue threshold limit, and below the fracture toughness of the material. Region II follows the Paris' law equation:

$$\frac{da}{dN} = C\left(\frac{G_{Imax}(a)}{G_{IR}(a)}\right)^m \tag{4.2}$$

Finally in Region III the crack propagation becomes unstable and is characterized by its rapid and catastrophic growth. All these regions are needed for total life estimation of a component.

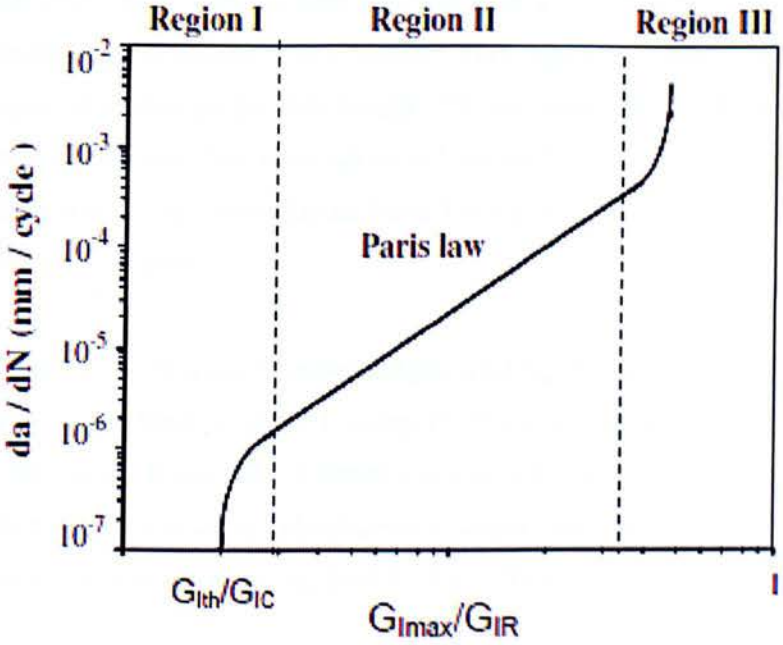

Fig. 4.23. Schematic curve of fatigue crack propagation.

There are standards and many publications regarding mode I delamination of FRP laminates under quasi-static loading. However, until now no standard has been developed for mode I delamination under fatigue loading for DCB specimen. In addition, the number of published works on mode I delamination of FRP composite under cyclic loading is very limited. In the following, a review of the published works on DCB delamination under fatigue loading are presented to establish the testing condition such as the frequency range and R-ratio for the DCB fatigue testing.

Shivakumar *et al.* [24] reported the total fatigue life model of woven-roving glass fibre/vinyl ester in mode I loading. The study included delamination growth in subcritical, linear and final fracture domains. The test conditions have been set to displacement control, with a frequency range between 1-4 Hz and R=0.1.

Hojo *et al.* [25] reported on delamination of CFRP prepreg under fatigue loading in mode I, using DCB test specimens. They used two materials $[0]_{16}$ CFRP prepreg of Toray T800H/3900-2 and $[0]_{24}$ CFRP prepreg of Toho UT500/111. Test were conducted at R-ratios of 0.1, 0.2 and 0.5 at a frequency of 10 Hz. Specimen dimensions were length 140mm, width

20mm, thickness 3mm and pre-crack 20-25mm. In further work Hojo *et al.* [26] looked at mode I fatigue delamination of Zanchor-reinforced CFRP laminates using DCB test specimen. CFRP cross-ply laminates were stitched with a Zanchor-reinforced high-strength intermediate-modulus dry carbon fibre fabric. Test specimen stacking sequence was $[0/90_2/0]_s$ and specimen dimensions were length 150 mm, width 10mm, thickness 1.8mm and pre-crack 35mm. The R-ratio has been set to 0.1 and 0.5, at a frequency of 10 Hz. They reported laminates with Zanchor-reinforced have 3.4-5.0 times higher fatigue threshold than without Zanchor reinforcement.

Arai *et al.* [27] studied delamination under fatigue loading of unidirectional CFRP pre-preg and plastics/carbon nano-fibre in mode I, using DCB specimens with dimensions of length 150mm, width 20mm, thickness 3.28-3.36mm and pre-crack length of 40mm. They reported an increase of 50% to the initiation delamination fracture toughness and 20% increase at the final fracture toughness when comparing the CFRP results to carbon nano-fibre one.

Coronado *et al.* [28] studied influences of temperature on delamination in CFRP under cyclic loading. The mode I experimental testing performed under monotonic and cyclic loading under operating temperatures of 90, 50, 20, 0, -30 and -60 °C. It is concluded that during the initiation of fatigue delamination G_{ICmax} increased as the temperature rose, but significantly decreased after the crack initiation. The crack growth rates at -30 and -60°C were significantly higher than previous results, showing the matrix has inherited brittle behaviour.

In the following sections the initiation and propagation fatigue life model of UD GFRP composite in mode I loading will be discussed. The study includes the on-set of delamination and propagation tests.

4.5.2 Specimen preparation

DCB specimens for T-T fatigue testing at R=0.1 are manufactured by the following steps. Firstly marked and cut out 30 layers 0° of 240×160 mm prepreg. Then removed the plastic lining from the prepreg and placed a GFRP ply on the face of a flat metal plate covered tightly in non-stick PTFE film. Then rolled out all the air bubbles, when doing so removed the plastic lining from the other side of prepreg and repeated this processes for all cut plies and placed a metal plate over the specimen. Next covered the plate using polyester cloth and

taped the edges tight with none flammable tape. Then placed the plate onto light weight breather fabric and taped the edges tight using none flammable tape. The next step was to place the plates on a plastic vacuum bag, placed an air extraction valve at the centre of the plate, used sealing tape to seal the bag across the edges to make it air tight, while vacuum was taking place. Finally placed the bag in the oven, connected the vacuum pump to the valve, checked if the bag has been sealed properly by listening for a whistling sound and left the bag in the oven for 60min at 80°C and then 4hours at 140°C. After the specimen cured and returned to room temperature applied 0.5mm of epoxy adhesive ESP110 to the end tabs (10mm×20mm) and placed them on the ends of specimens using clamp. The specimen returned back to the oven for curing for 60min at 120°C.

4.5.3 Mode I quasi-statics test

All fatigue tests were conducted under constant-amplitude displacement loading at a cyclic load frequency range of 5 Hz with the ratio of minimum to maximum displacement ($R = \delta_{min}/\delta_{max}$) of 0.1 on a Zwick/Roell Amsler HC 25kN servo hydraulic fatigue testing machine (see Figure 4.24).

Interlaminar fracture resistance (G_{IR}) in unidirectional composites increases with delamination crack length due to matrix cracking and fibre bridging. Therefore determination of $G_{IR}(a)$ for fatigue testing is needed. A quasi-static DCB test was conducted and initiation fracture toughness G_{IC} and variation of the energy release rate G_{IR} as a function of crack length was determined and a power law equation was fitted to the data as shown in Figure 4.25. The resulting resistance equation is:

$$G_{IR} = G_{IC} + 20.2(a - a_0)^{0.64} \tag{4.3}$$

The energy release rate was calculated from the modified beam theory (MBT) as described in Eq (3.2).

$$G_I = \frac{3P\delta}{2b(a+|\Delta|)} \tag{4.4}$$

The delamination length correction parameter $|\Delta| = 2.293\ mm$ was determined from the plot of the specimen compliance and delamination crack length data from quasi-static test.

Fig. 4.24. Mode I fatigue testing of DCB specimen.

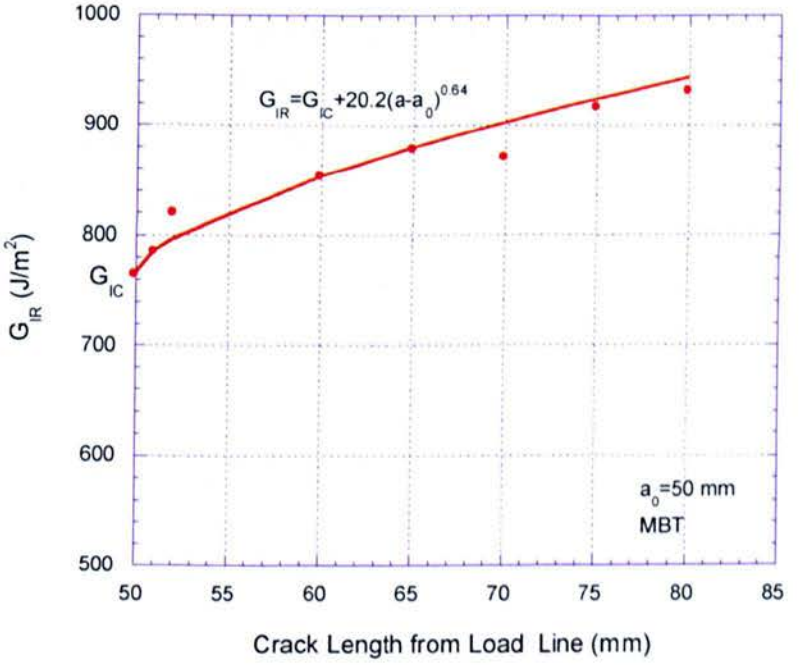

Fig. 4.25. Energy release rate versus delamination growth length for GFRP laminate in $[0_{15}//0_{15}]$ DCB test using MBT method.

4.5.4 Determination of mode I threshold toughness using onset life test

The ASTM D-6115 standard [29] recommends two criteria for determining the threshold onset life, namely 1 and 5% increase of compliance compared to the compliance at N=1 (see Figure 4.26). The number of cycles at 1% and 5% increase in compliance has been recorded to determine the initiation criteria.

The delamination threshold fracture toughness G_{Ith} can be determined by a curve fit to G_{Imax}/G_{IC} measured at 1 and 5% increase of compliance from the fatigue onset life test.

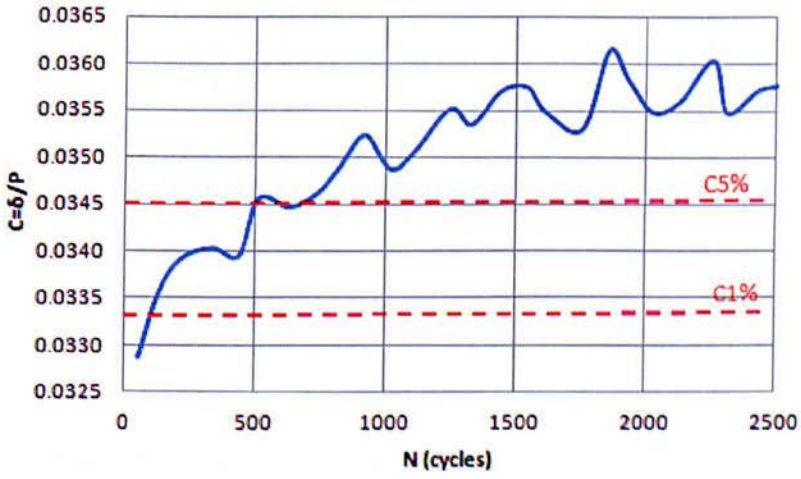

Fig. 4.26. Compliance versus number of cycles in DCB initiation test together with 1% and 5% increase in compliance.

Figure 4.27 shows the plot of G_{Imax}/G_{IC} versus log N for 1% and 5% criteria for the data collected from all tested DCB specimen where the first data point is obtained from the quasi-static test. O'Brien [30] suggested a linear relationship between G_{Imax} and log N data between $10^0<N<10^6$ and then he found the G_{Ith} value from fitted equation at $N=10^6$. For the present study following Shivakumar *et al.* [24] a power law curve was fitted to the data and the fitted equation is (see Figure 4.27):

$$\frac{G_{Imax}}{G_{IC}} = (logN + 1)^{-0.93} \tag{4.5}$$

The threshold energy release rate (G_{Ith}) calculated from the Eq. (4.5) at $N=10^6$ cycles is $G_{Ith} = 0.16G_{IC}$.

4.5.5 Fatigue crack propagation tests

The same set-up and three DCB specimens that were used for onset life tests also used in the propagation tests. All DCB fatigue tests were conducted in displacement control at a frequency of 5 Hz and a displacement ratio R=0.1. The displacement ratio is defined as $\delta_{min}/\delta_{max}$, where δ_{min} and δ_{max} are the minimum and maximum applied displacements, respectively. All test specimens were already precracked for fatigue delamination growth test and new delamination lengths were measured and recorded.

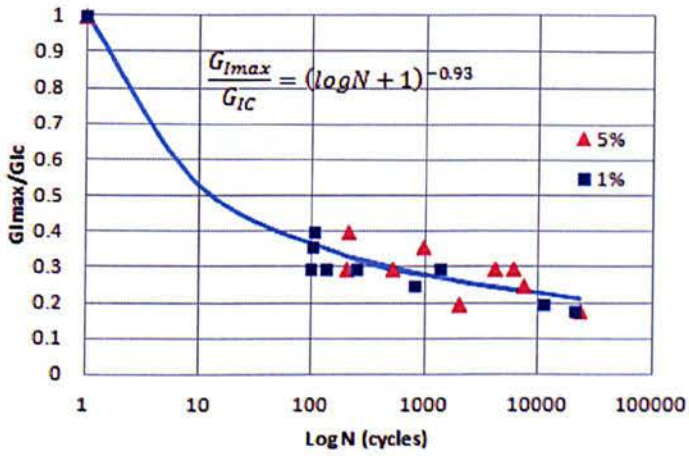

Fig. 4.27. Variation of onset fatigue life with G_{Imax}/G_{IC}.

Delamination growth rate data was generated by applying the δ_{Imax} corresponding to (G_{Imax}/G_{IC}) between 0.3 and 1. The fatigue test was run for a predetermined number of cycles. The test was stopped, the travelling microscope was examined to measure the final crack length at the end of the loading cycle and loads and delamination lengths were recorded. When no measurable delamination propagation was observed after some interval the load has been increased. At the end of each set of ΔN, the test was stopped and N, ΔN, a, Δa, P_{Imax} and δ_{Imax} were recorded. From these results, da/dN, G_{Imax}, and G_{IR} were calculated. The G_{Imax} was calculated using:

$$G_{Imax} = \frac{3P_{Imax}\delta_{Imax}}{2b(a+|\Delta|)} \tag{4.6}$$

where $|\Delta| = 2.293\ mm$ obtained from the quasi-static fracture test. Results of three delamination crack growth test are shown in Figure 4.28.

The test data and the equation are bounded by the limits G_{Imax}/G_{Ith} and G_{Imax}/G_{IR}=1. The G_{Ith} from the onset life test was determined at 0.16 G_{IC}. From the fitted curve to the propagation data the Paris' law coefficient for this GFRP for mode I loading are found to be m= 5.27 and C= 4.47×10^{-2}. Therefore the da/dN equation representing region II crack growth is:

$$\frac{da}{dN} = \mathbf{4.47 \times 10^{-2}} \left(\frac{G_{Imax}(a)}{G_{IR}(a)}\right)^{\mathbf{5.27}} \tag{4.7}$$

In Figure 4.29 compliance of two DCB specimens during propagation are compared with a monotonic one. It seems there are no differences in the compliance behaviour in monotonic and fatigue loading.

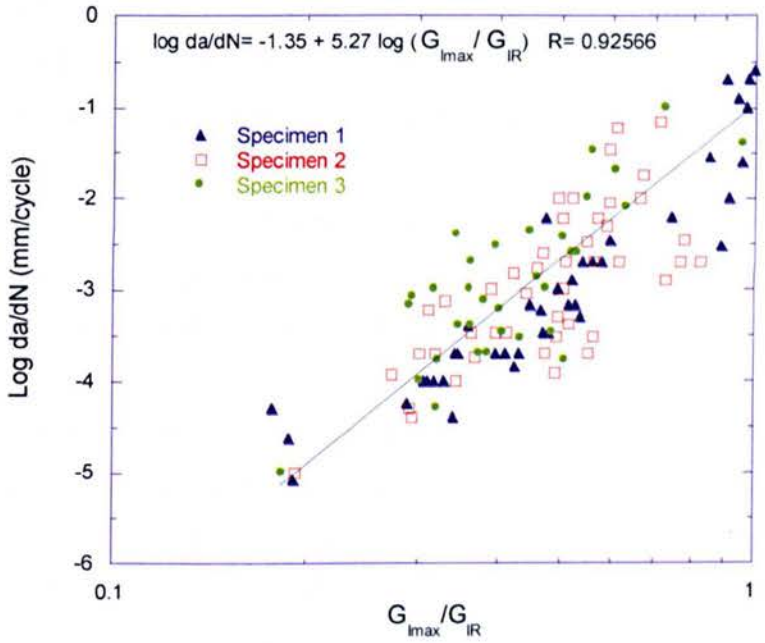

Fig. 4.28. Crack propagation in DCB specimens.

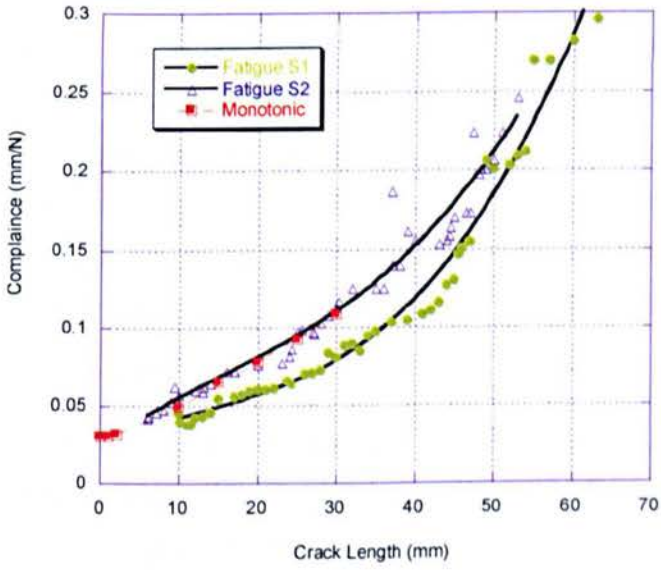

Fig. 4.29. Comparison of compliance in monotonic and fatigue loading in DCB specimens.

4.6 Mode II fatigue delamination growth in GFRP composite

The monotonic mode II delamination fracture toughness measurement using End-Notched Flexure (ENF) test is discussed in Chapter 3 where the test consisted of a three-point bending specimen with a pre-crack that leads to shear loading at the crack tip. Recently the ENF test is also used to analyse mode II interlaminar delamination toughness under cyclic loading.

As in the case for DCB specimen, there are standards and many publications regarding mode II delamination of FRP laminates under quasi-static loading. However, until now no standard has been developed for mode II delamination under fatigue loading for ENF specimen. In addition, there are a handful of publications on delamination of FRP composite under cyclic loading for ENF specimen. In the following, a review of most of the published works on ENF delamination under fatigue loading are reviewed to establish the testing condition such as specimen dimension, the frequency range and R-ratio for the ENF fatigue testing.

Hojo *et al.* [31] studied CFRP laminates under mode II fatigue loading. They tested CFRP unidirectional laminates $[0]_{24}$ and 50μm-epoxy-interleaved laminates $[0_{12}/\text{film}/0_{12}]$. End Notched Flexure (ENF) test method is used, using specimen dimensions: length 160mm, span 100mm, width 10mm, thickness 3mm and pre-crack 25mm. Tests performed at R ratio of 0.1 and 0.5 at a frequency of 10 Hz. They showed initiation interlaminar fracture toughness of 50μm-epoxy-interleaved laminates is 1.6 times higher than the base CFRP and 3.5 times higher in the propagation values.

Shindo *et al.* [32] reported GFRP laminates under mode II fatigue loading using a 4ENF specimens at a frequency of 2 Hz at an R = 0.1. The test is conducted at three different temperatures: room temperature, (77K) liquid nitrogen and (4K) liquid helium. The study was conducted both experimentally and numerically. The test specimen dimensions were length 90mm, width 20mm, thickness 3.65mm, pre-crack 30mm. They concluded that delamination growth rate is lower at low temperatures and when decreasing the temperature the threshold energy release rate becomes larger.

Landry *et al.* [33] explored CFRP material under mode II fatigue loading, at a frequency of 1 Hz at R= 0.2. The test has been conducted to investigate the effect of exposing the laminate to water, hydraulic fluid and deicing fluid. They studied was conducted experimentally and numerically. The test specimen dimensions used were length 94mm, width 20mm, thickness 2.25mm and 3mm and pre-crack 35.5mm. It is concluded that the results from compliance calibration method are good and can be obtained with minimum number of specimens. The delamination toughness adversely affected on those specimens which are exposed to fluids. In quasi-static monotonic testing delamination toughness reduced by 20-25% in water and deicing immersion, but only 4% reduction in hydraulic fluid.

Fernandez *et al.* [34] investigated CFRP laminates under mode II fatigue loading, The $[0]_{18}$ 3ENF specimens used had dimensions length 90mm, width 25mm, thickness 2.7mm, pre-crack length 45mm and tested at a frequency of 4 Hz and R= 0.1. They used Paris' law to establish the relationship between the fatigue crack growth rate and the variation of the applied energy release rate.

As a consequence of its success in the reviewed works, the ENF test was chosen to perform mode II fatigue crack propagation tests on GFRP material in this project (see Figure 4.30). The analysis is based on application of Paris' law as a function of energy release rate for mode II loading to characterize fatigue behaviour in this mode.

Fig. 4.30. Mode II Fatigue testing of ENF specimen.

As in the case of mode I crack propagation test a quasi-static ENF test performed to obtain the G_{IIC} at initiation and also the resistance curve of G_{IIR} during the crack propagation. Figure 4.31 shows the results of quasi-static test of ENF specimen. The onset of the nonlinear part and the point of maximum load used for definition of the initiation and maximum fracture toughness values, respectively.

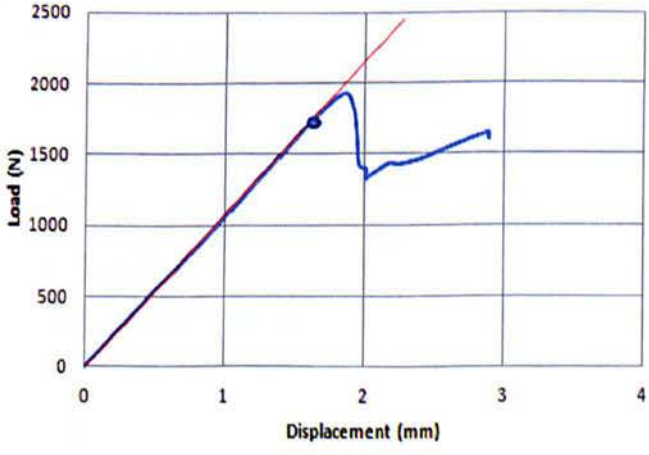

Fig. 4.31. Load-displacement diagram for mode II loading. G_{IIC}= 1150 J/m^2.

The initiation delamination toughness was determined from MBT method discussed in Chapter 3. The delamination resistance in ENF specimen at different crack length was also calculated and the results of G_{IIR} were plotted against the crack length as shown in Figure 4.32. The fitted curve to these data result is:

$$G_{IIR} = 0.16212\, a^{2.7739} \tag{4.8}$$

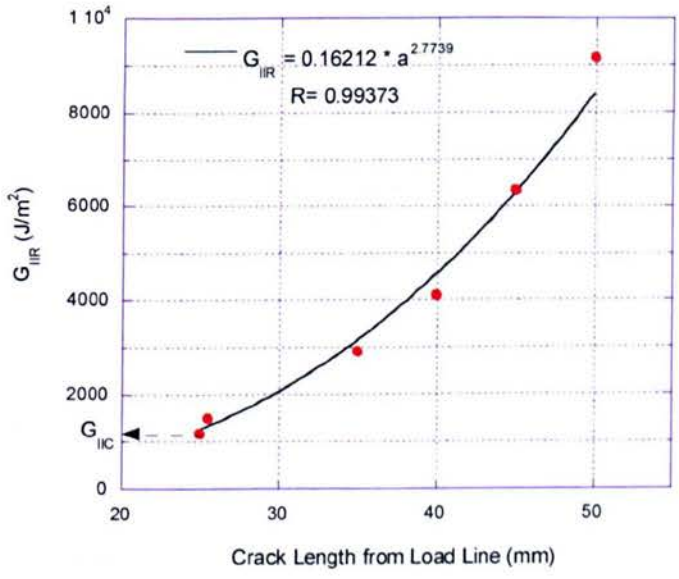

Fig. 4.32. Energy release rate versus delamination growth length for GFRP laminate in $[0_{15}//0_{15}]$ ENF test using MBT method.

Delamination growth rate data was generated by performing constant displacement fatigue tests. All ENF fatigue tests were conducted at a frequency of 5 Hz and a displacement ratio R=0.1. Each ENF fatigue test was run for a predetermined number of cycles. The test was stopped, the travelling microscope was examined to measure the final crack length at the end of the loading cycle and loads and delamination lengths were recorded. When no measurable delamination propagation was observed after some interval, the load was increased. At the end of each set of ΔN, the test was stopped and N, ΔN, a, Δa, P_{Imax} and δ_{Imax} were recorded. From these results, da/dN was calculated. The maximum strain energy release rate, G_{IImax}, was found from MBT method and G_{IIR} was calculated from Eq. (4.8). Finally the calculated data of log da/dN was plotted against log G_{IImax}/ G_{IIR} as shown in Figure 4.33. In this plot a curve was fitted to the propagation data and the Paris' law coefficient for this GFRP in mode II are found to be m= 4.0 and C= 13.49. Therefore the da/dN equation representing region II crack growth is:

$$\frac{da}{dN} = 13.49\left(\frac{G_{IImax}(a)}{G_{IIR}(a)}\right)^{4.0} \tag{4.9}$$

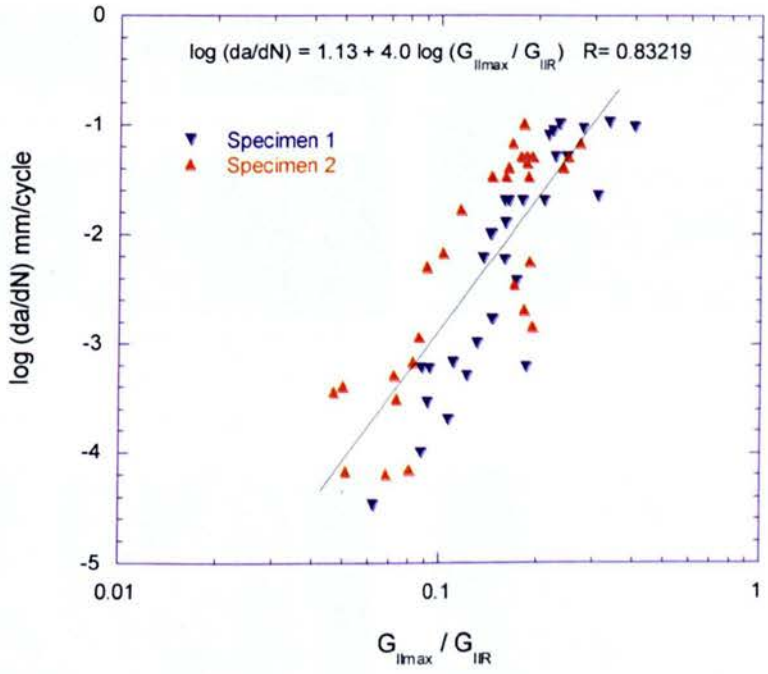

Fig. 4.33. Crack propagation in ENF specimens.

4.6.1 Fractography analysis of fracture surface in Mode II static and fatigue tests

A SEM fractography analysis was performed on samples of material extracted from the crack growth zone of specimens tested under mode II static and fatigue loading.

Figure 4.34 shows edge SEM micrographs of the fracture surface of the specimens in the growth zone for static and fatigue ENF testing. The images are shown at distance of 6, 12 and 18mm of delamination from the initial crack location. The fractography images under mode II monotonic loading show that the fibres debonded at interface and there are no visible matrix remains on the debonded fibres. However the images of fatigued ENF surfaces show that the fibres debonded cohesively through the matrix and remains of the matrix on the debonded fibres are visible and it seems some polymer matrix whitening at the cohesive zone. Also the size of matrix fragments on monotonic loading is many times bigger than those of fatigue fractured. In both monotonic and fatigued surfaces the typical fibre bridging as well as broken fibres can also be observed, Shindo *et al.* [32] experiences similar fracture surface and Landry *et al.* [33] also experience debris on the fracture surface of the fatigued

ENF specimens. Fibre/matrix interface decohesion plays a major role on delamination growth mechanism.

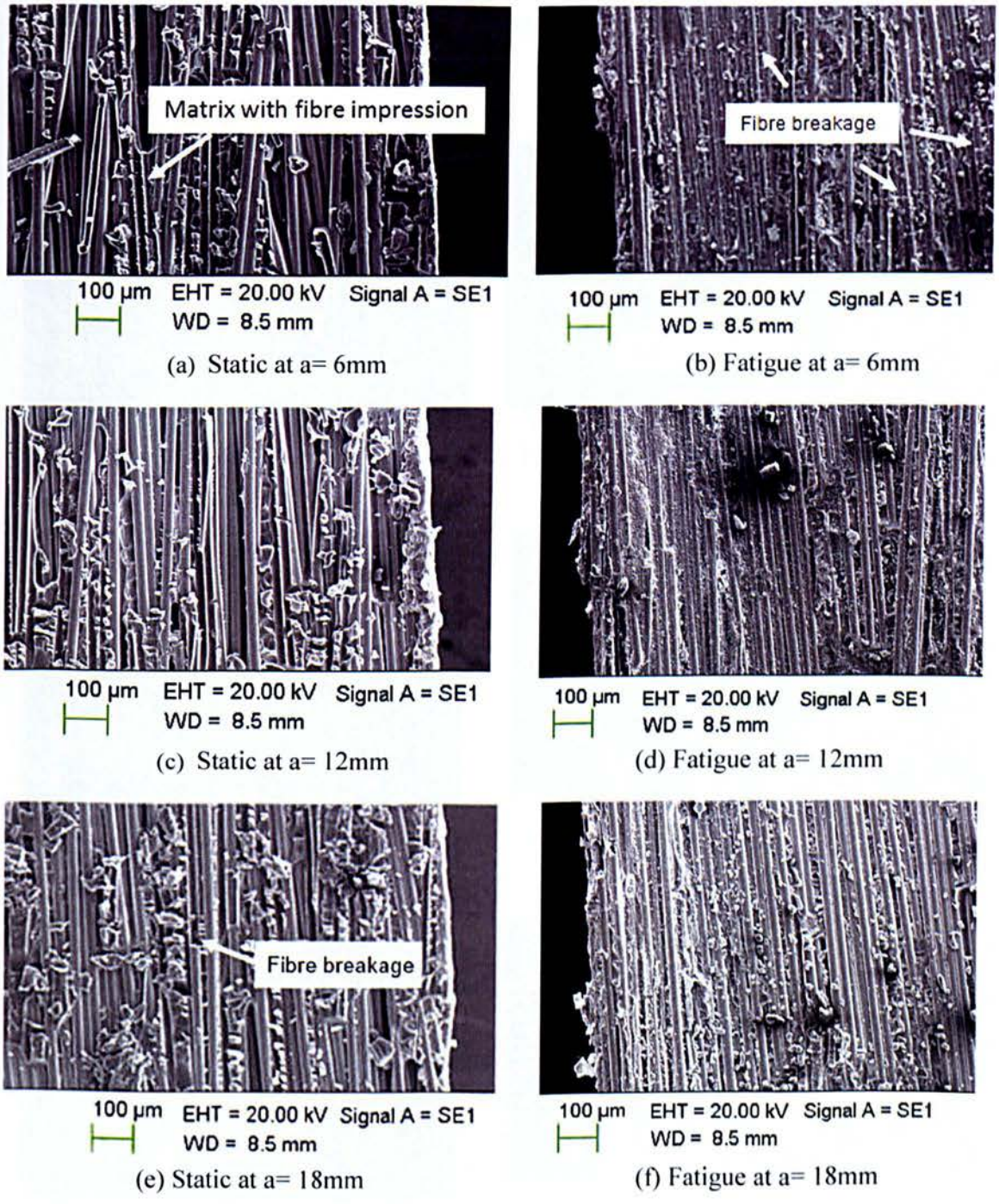

Fig. 4.34. Comparison of SEM image of fracture surface at the edge of ENF specimen after static and fatigue tests at different crack length (direction of delamination from bottom to top).

Figure 4.35 shows centre SEM micrographs of the fracture surface of the ENF specimens in the growth zone for static and fatigue images of for static and fatigue testing, the images are shown 6, 12 and 18mm of delamination. For the edge and centre for ENF fatigue resin debris is a dominant feature indicated in the SEM images, a characteristic feature of fatigue failure is when large amounts of resin debris is present.

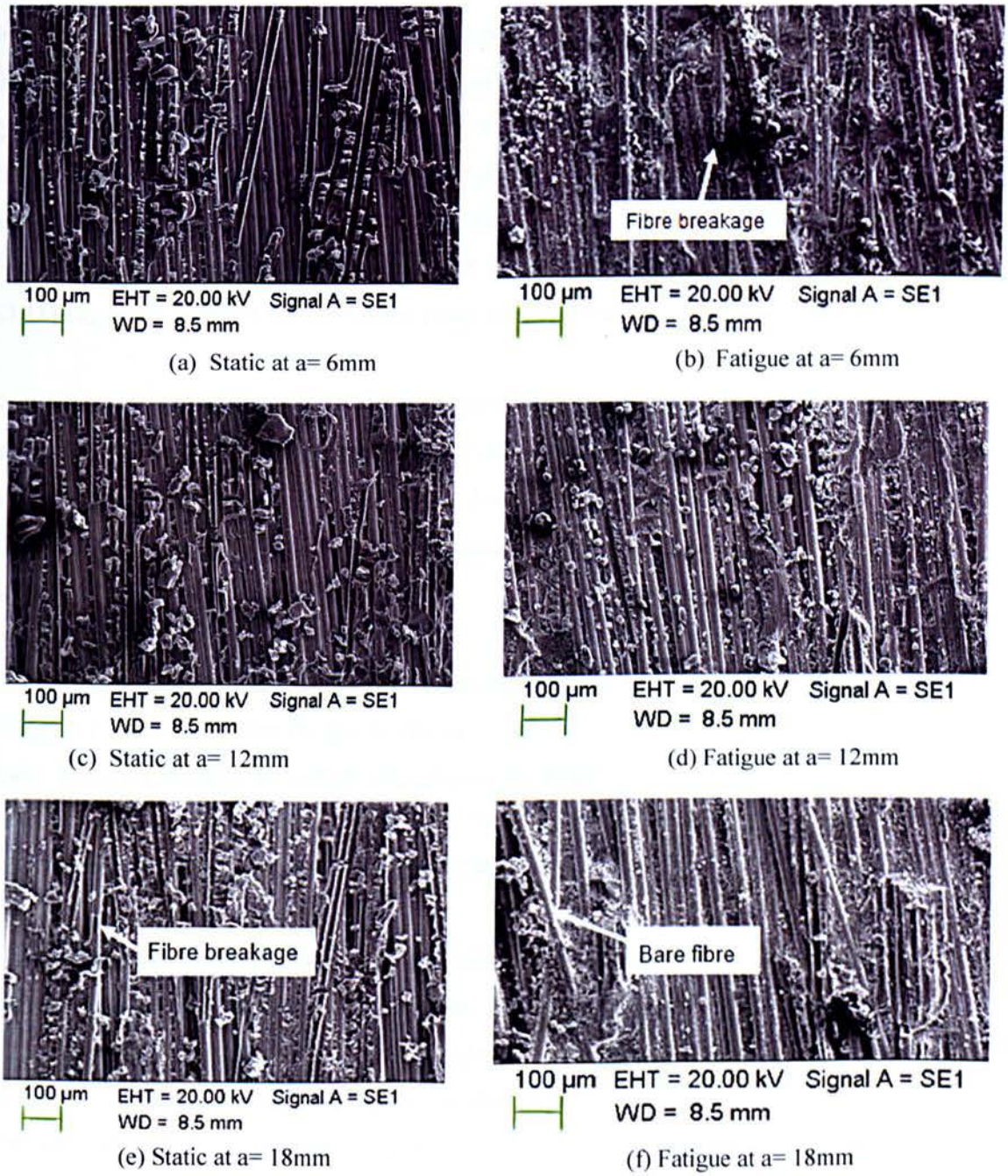

Fig. 4.35. Comparison of SEM image of fracture surface at the centre of ENF specimen after static and fatigue tests at different crack length (direction of delamination from bottom to top).

4.7 Conclusion

In the design of various parts of wind turbine blades such as the shear web, spar cap and the aerofoil the fatigue behaviour of FRP materials is required. The performance of these parts as well as the adhesively bonded joint under fatigue loading is crucial for structural integrity of a long lasting blade.

In this chapter different aspects of fatigue of GFRP were investigated. Firstly the fatigue lifetime of the GFRP was studied based on S-N diagram. Experiments on three different types of loading, i.e. tension-tension at R=0.1, 0.5, tension-compression at R=-1 and compression-compression at R=2 and R=10 have been performed. The S-N diagram for various R ratios shows a nearly linear behaviour with a fatigue limit of around 40%. From the S-N diagram data the CLD diagrams for 90° and 0° fibre directions were constructed. From CLD diagrams, a fatigue lifetime under other loading condition can still be estimated.

Secondly the onset life and propagation delamination crack growth of 0//0 interface of GRFP laminate in mode I loading using DCB specimens was investigated. The G_{Ith} from the onset life test was determined to be 0.16 G_{IC}. From the fitted curve to mode I experimental propagation data, the Paris' law coefficient for the laminated GFRP in mode I was determined at m= 5.27 and C= 4.47×10^{-2}.

The mode II fatigue crack growth in laminated 0//0 GFRP material was also investigated using ENF specimens. The fatigue behaviour in this mode is analysed based on application of Paris' law as a function of energy release rate for mode II loading. From the fitted curve to mode II experimental propagation data, the Paris' law coefficient for the laminated GFRP in mode II was determined at m=4.0 and C= 13.49.

The fractography images under mode II monotonic loading show that the fibres debonded at interface and no visible matrix remains on the debonded fibres. However the images of fatigued surfaces show that the fibres debonded cohesively through the matrix and remains of the matrix on the debonded fibres and whitening of polymer matrix are visible. Also the size of matrix fragments on monotonic loading is many times bigger than those of fatigue loading. In both monotonic and fatigued surfaces the typical fibre bridging as well as broken fibres

can also be observed. Fibre/matrix interface decohesion plays a major role on delamination growth mechanism.

Nomenclature

C-C	Compression-compression
E	Young's modulus (GPa)
F	Force (N)
G_{12}	Shear modulus (GPa)
N	Number of cycles
R	Stress ratio in load control and displacement ratio in displacement control
S	Shear strength (MPa)
T-C	Tension-compression
T-T	Tension-tension
UTS	Ultimate tensile strength
UCS	Ultimate compressive strength
V_f	Fibre volume fraction
Xc	UCS in fibre direction (MPa)
Xt	UTS in fibre direction (MPa)
Yc	UCS normal to fibre direction (MPa)
Yt	UTS normal to fibre direction (MPa)
ν	Poisson's ratio
σ_a	Stress amplitude (MPa)
σ_m	Mean stress (MPa)

4.8 References

[1] US Department of Defense, (1997). The Composite Materials Handbook, MIL-17 Mil-HDBK-17-1F, January.

[2] Mandell, J. F., Samborsky, D. D., and Cairns, D.S. (2002). Fatigue of Composite Materials and Substructures for Wind Turbine Blades, Contractor Report SAND2002-0771, Sandia National Laboratories, Albuquerque, NM.

[3] Sarfaraz. R. R, Vassilopoulos. A. P, Keller. T. (2012). Experimental investigation and modelling of mean load effect on fatigue behaviour of adhesively-bonded pultruded GFRP joints. *International Journal of Fatigue* **44** 245–252

[4] Vassilopoulos. A. P, Georgopoulos. E. F, Dionysopoulos. V. (2007). Artificial neural networks in spectrum fatigue life prediction of composite materials. *International Journal of Fatigue* **29** 20–29

[5] Vassilopoulos. A. P, Manshadi. B. D, Keller. T. (2010). Influence of the constant life diagram formulation on the fatigue life prediction of composite materials. *International Journal of Fatigue* **32** 659–669

[6] Vassilopoulos. A. P, Manshadi. B. D, Keller. T. (2010). Piecewise non-linear constant life diagram formulation for FRP composite materials. *International Journal of Fatigue* **32** 1731–1738

[7] Shah. D. U, Schubel. P. J, Clifford. M. J, Licence. P. (2013). Fatigue life evaluation of aligned plant fibre composites through S–N curves and constant-life diagrams. *Composites Science and Technology* **74** 139–149

[8] Freire Jr. R. C. S, Neto. A. D. D, de Aquino. E. M. F. (2005). Building of constant life diagrams of fatigue using artificial neural networks. *International Journal of Fatigue* **27** 746–751

[9] Freire Jr. R. C. S, Neto. A. D. D, de Aquino. E. M. F. (2007). Use of modular networks in the building of constant life diagrams. *International Journal of Fatigue* **29** 389–396

[10] Bortz. D. R, Merino. C, Martin-Gullon. I. (2012). Augmented fatigue performance and constant life diagrams of hierarchical carbon fiber/nanofiber epoxy composites. *Composites Science and Technology* **72** 446–452

[11] Kawai. M, Murata. T. (2010). A three-segment anisomorphic constant life diagram for the fatigue of symmetric angle-ply carbon/epoxy laminates at room temperature. *Composites: Part A.* **41** 1498–1510

[12] Kawai. M. (2004). A phenomenological model for off-axis fatigue behaviour of unidirectional polymer matrix composites under different stress ratios. *Composites: Part A* **35** 955–963

[13] Rotem A. (1991). The fatigue behavior of composite laminates under variable mean stresses. Compos Struct, 17:113–26.

[14] Rotem A. (1989). Nelson HG. Failure of a laminated composite under tension–compression fatigue loading. Compos Sci Technol, 36:45–62.

[15] Goodman J. Mechanics applied to engineering. Harlow (UK): Longman Green; 1899.

[16] Kawai M, Koizumi M. (2007). Non-linear constant fatigue life diagrams for carbon/epoxy laminates at room temperature. Compos Part A;38(11):2342–53.

[17] Ramani SV, Williams DP. (1977). Notched and unnotched fatigue behavior of angle-ply graphite/epoxy composites. In: Reifsnider KL, Lauraitis KN, editors. Fatigue of filamentary composite materials. ASTM STP 636; p. 27–46.

[18] Hahn HT. (1979). Fatigue behavior and life prediction of composite laminates. Composite materials: testing and design (Fifth Conference), ASTM STP 674 ed. Tsai SW; p. 383–417.

[19] Fernando G, Dickson RF, Adam T, Reiter H, Harris B. (1988). Fatigue behaviour of hybrid composites: part I carbon/Kevlar hybrids. J Mater Sci 23(10):3732–43.

[20] Towo AN, Ansell MP. (2008). Fatigue of sisal fibre reinforced composites: constant-life diagrams and hysteresis loop capture. Compos Sci Technol, 68(3–4):915–24.

[21] Andersons J, Paramonov Yu. (2011). Applicability of empirical models for evaluation of stress ratio effect on the durability of fiber-reinforced creep rupture susceptible composites. J Mater Sci 46(6):1705–13.

[22] Nijssen RPL. (2006). Fatigue life prediction and strength degradation of wind turbine rotor blade composites. ISBN-10: 90-9021221-3, Publisher: Knowledge Centre Wind turbine Materials and Constructions (KC-WMC).

[23] E 647 Standard test method for measurement of fatigue crack growth rates. ASTM; 2008.

[24] Shivakumar K, Chen. H, Abali. F, Le. D, Davis. C. (2006). A total fatigue life model for mode I delaminated composite laminates. International Journal of Fatigue 28, 33.

[25] Hojo. M, Matuda. S, Tanaka. M, Ochiai. S, Murakami. A. (2006). Mode I delamination fatigue properties of interlayer-toughened CF/epoxy laminates. Composites science and technology 66. 665-675

[26] Hojo. M, Nakashima. K, Kusaka. T, Tanaka. M, Adachi. T, Fukuoka. T, Ishibashi. M. (2010). Mode I fatigue delamination of Zanchor-reinforced CF/epoxy laminates. International journal of fatigue 32, 37-45.

[27] Arai. M, Noro. Y, Sugimoto. K, Endo. M. (2008). Mode I and mode II interlaminar fracture toughness of CFRP laminates toughened by carbon nanofiber interlayer. Composites Science and Technology 68, 516–525

[28] Coronado. P, Argüelles. A, Viña. A.J, Mollón. V, Viña. I. (2012). Influence of temperature on a carbon–fibre epoxy composite subjected to static and fatigue loading under mode-I delamination. International Journal of Solids and Structures 49, 2934–2940

[29] Standard test method for mode I fatigue delamination growth onset of unidirectional fiber-reinforced polymer matrix composites, ASTM standard D6115-97, ASTM annual book of ASTM standard, vol. 15.03. Philadelphia: American Society for Testing and Materials; 1999. p. 327–32.

[30] O'Brien TK. (1990). Towards a damage tolerance philosophy for composite materials and structures. ASTM Special Technical Publication, No. 1059; p.7.

[31] Hojo. M, Ando. T, Tanaka. M, Adachi. T, Ochiai. S, Endo. Y. (2006). Mode I and II interlaminer fracture toughness and fatigue delamination of CF/epoxy laminates with self-same epoxy interleaf. International journal of fatigue 28, 1154-1165.

[32] Shindo. Y, Takeda. T, Narita. F, Saito. N, Watanabe. S, Sanada. K. (2009). Delamination growth mechanisms in woven glass fiber reinforced polymer composite under Mode II fatigue loading at cryogenic temperatures. Composites science and technology 69, 1904-1911.

[33] Landry. B, LaPlante. G, LeBlanc. L. R. (2012). Environmental effect on mode II fatigue delamination growth in an aerospace grade carbon/epoxy composite. Composites: Part A 43, 475-485.

[34] Fernandez. M. V, de Moura. M.F.S.F, da Silva. L.F.M, Marques. A. T. (2013). Characterization of composite bonded joints under pure mode II fatigue loading. Composite structures 95. 222-226.

5

Calibration Pull and Modal Testing of a Full Scale Wind Turbine Blade

5.1. Introduction

Any new wind turbine blades undergo three types of full scale tests. The new blades are subjected to **static testing** before they are used in commercial turbines. Usually in static test a traction rig is attached to the blade by steel wires fixed at selected points and then the blade is deformed such that it is subjected to the prescribed extreme load. The appropriate extreme load is applied on all directions, i.e. leading edge, trailing edge, suction side and pressure side, to ensure that the blade withstands the extreme load in all directions. The whole static test is repeated after dynamic testing to ensure that the blade can handle extreme loads after it has been subjected to high cyclic loading.

In the **dynamic testing** the blade is subjected to cyclic loads corresponding to 20-30 years of normal wear and tear caused by fatigue load. For this purpose the blade exposed to at least five million cycles of loading in the edgewise and flapwise directions.

By application of new materials or other significant changes in the structural design of the blade, a **failure test** may be necessary in addition to the static and dynamic tests. In a crash

test, a static test is continued until the blade fractures. The blade is then cut open at the point of fracture, and the fracture surfaces are examined in detail to discover the root cause of failure. The design may be revised after the forensic analysis of the fracture surfaces.

The aim of the series of static and modal tests described in this chapter was to obtain detailed information for a full scale fatigue testing of the blade which will be discussed in Chapter 6. Also the sensitivity of blade to the damage growth under dynamics loading will be discussed in Chapter 6.

The length of the blade used in the full scale tests is 45.7m, which was supplied by The National Renewable Energy Centre (NaREC) as part of the project. The blade is mainly made from an epoxy glass fibre reinforced plastic (GFRP) composite laminates. This blade already had been exposed to loading and some damages were detected before starting the test covered in Chapters 5 and 6. In fact some visual damage on skin was noticed on the blade at around 33m from the blade's root.

The objective of the full scale blade test is to study the sensitivity of the blade to crack propagation under cyclic loading. Three stages of the study consists of fatigue testing on (i) Undamaged blade (ii) Damaged blade with an induced crack length of 0.2m at 9m distant from the root and (iii) Damaged blade with an induced crack length of 1m at 9m distant from the root. However, prior to fatigue testing the required information was obtained from calibration pull tests and modal test that will be discussed in this chapter.

During each test the blade was inspected and any damages were measured by means of visual inspection, strain gauges and acoustic emission sensors. Each test was stopped at every sign of damage and inspected visually. Cracks and propagation of the damages were identified. A simple tap test was also done to identify the propagation of delaminations.

5.2 Calibration pull test

Full scale wind turbine blade calibration pull test is performed prior to every three stages of the experiments, i.e. for (i) Undamaged blade (ii) Damaged blade with an induced crack length of 0.2m at 9m distant from the root and (iii) Damaged blade with an induced crack length of 1m at 9m distant from the root. Modal testing was carried out to find the natural frequencies of different modes experienced by the blade. A modal hammer testing in flapwise and edgewise was performed to obtain the first two modes of the blade in the uncracked blade

and first mode for crack inserted blade. Testing of the blade was undertaken using methods utilised during full scale wind turbine blade testing to IEC 61400-23 [1].

5.3 Test facilities

Full scale blade tests were performed in NaREC's 100m blade test facility. NaREC is the UK's national research centre and one of its objectives is to accelerate the development and deployment of offshore wind energy generation technologies. NaREC opened its testing facility for blades up to 50m in length in 2005. Later in 2012 a new 100m facility has been opened and developed to accommodate larger blades for offshore wind turbines. The blade test facility contains physical blade test hub and equipment and a main structure to house them. All the tests reported in Chapter 5 and 6 were performed on the new 100m facility. The overall 100m test facility is shown in Figure 5.1. A 45.7m blade is connected to the hub as shown in Figure 5.1

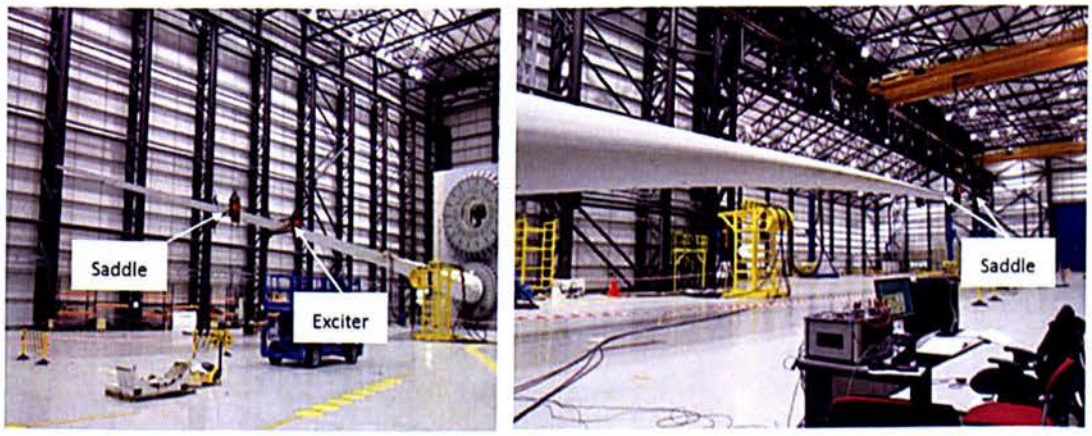

Fig. 5.1. Overall view of the blade test facility and view from the root (courtesy of NaREC).

The blade used during testing is cyclically loaded by exciter attached to the saddles. The saddles are placed at specified points along the blade to apply cyclic loading. The saddle is designed in such a way that it will be as close to the blade neutral axis as possible. Excitation device are attached on each side of the metal case of the saddle at Leading Edge (LE) and Trailing Edge (TE) to excite the blade for the fatigue testing and make the loads balanced.

During static testing, load is applied at specific location along the blade to obtain the intended target bending moment at the root of the blade. By proper positioning of the loading station, it is possible to achieve applied bending moment amplitude similar in curvature to the target bending moment amplitude. The target bending moment amplitude at the root of the blade is

the bending moment amplitude that produces the same amount of damage as the service life does.

In fatigue testing the dynamic bending moment is directly related to the mode shape of the blade. At the resonant natural frequencies of the blade and by adjusting the positions and magnitude of dynamic mass of the saddles, cyclic load similar to service life of the blade according to the target bending moment will be applied.

An optimisation analysis is required to determine the position, magnitude of dynamic mass and amplitude of the saddles. Courtesy to NaREC knowledge and experience in the uncracked blade dynamic tests a dynamic mass of 150kg on each side of the saddle at 30.05m and a dynamic mass of 75kg on each side of saddle at 35.05m are required to produce 50% of the target bending moment amplitude. The target bending moment is the magnitude of the bending moment that the blade will experience in the service life. These masses were also added to the blade in modal analysis testing to find the resonant frequencies of the blade accurately. The mass on the saddles has been increased when the crack extended to 1 m. The reason for adding mass to the saddle in this case was because at 70% of the blades target bending moment, the saddle resonance amplitude was reaching its limit and saddles operating beyond their capabilities. By adding weight to the saddles, the resonance amplitude reduces while the strain value required at strain gauge SG2 kept unchanged.

The saddle mechanism common to most methods of excitation are attached to the blade. The excitation device drives the saddle with a sinusoidal motion, and a closed loop control system controls the frequency and amplitude of this motion so that the strain amplitude on a selected strain gauge is maintained at the target level defined in the test specification.

5.4 Sensors positioning

5.4.1 Acoustic emission sensors

Acoustic emission (AE) sensors have been used to understand the initiation and propagation of any damage along the blade and the blade behaviour. The AE sensors are fixed on the blade internal and external surface to monitor the blade under the test. Table 5.1 indicates the sensors locations along the blade.

The positions of the AE sensors on the blade in various locations are shown in Figures 5.2 and 5.3. Ultrasonic gel was applied between the blade and the sensor to ensure good signals

are transmitted from the sensor. Inside the blade, this required sanding of the composite material to provide a smooth contact area. The sensors are clamped to the blade with magnets, which react off steel plates that are fixed to the blade using 2-part epoxy based adhesive. This will ensure that the sensors maintain a good connection with the blade during the testing process. Each AE sensor is connected to a pre-amplifier to increase the signal gain, before a 50m cable run to the Data Acquisition system (DAQ). The DAQ is located at the test hub, near the test control station.

Table 5.1 Acoustic emission sensor locations and objectives

Sensor Number	Monitoring Failure at	Location
AE1	33m skin crack	Pressure side, 33m +0.5m, near web
AE2	33m skin crack	Pressure side, 33m, near trailing edge
AE3	33m skin crack	Pressure side, 33m –0.5m near leading edge
AE4	9m web debond*	In between webs, 9.8m from root
AE5	9m web debond*	In between webs, 8.2m from root
AE6	9m web debond*	Trailing edge side of web, 8.4m from root
AE7	9m web debond*	Trailing edge side of web, 9.6m from root

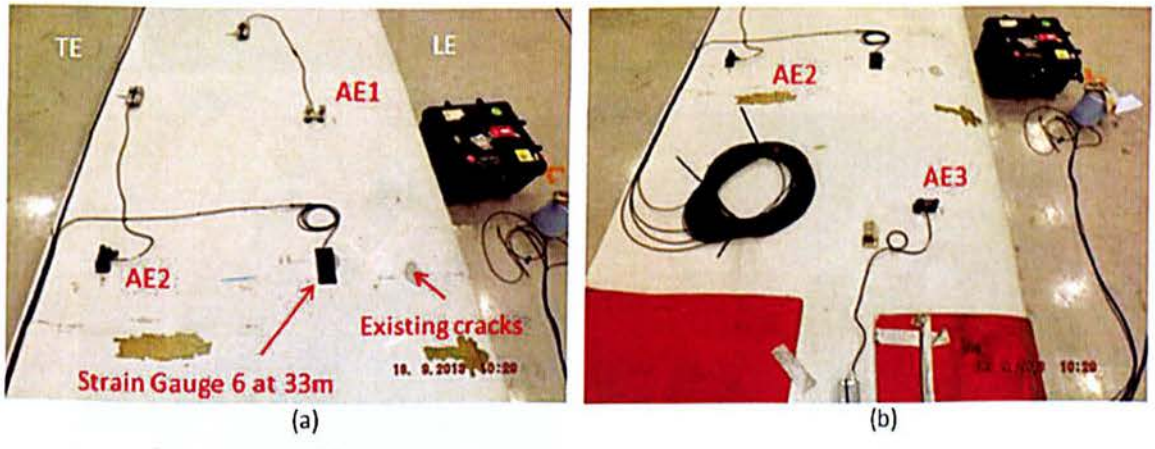

Fig. 5.2. (a) AE1 & AE2 and existing skin cracks (b) AE2 & AE3.

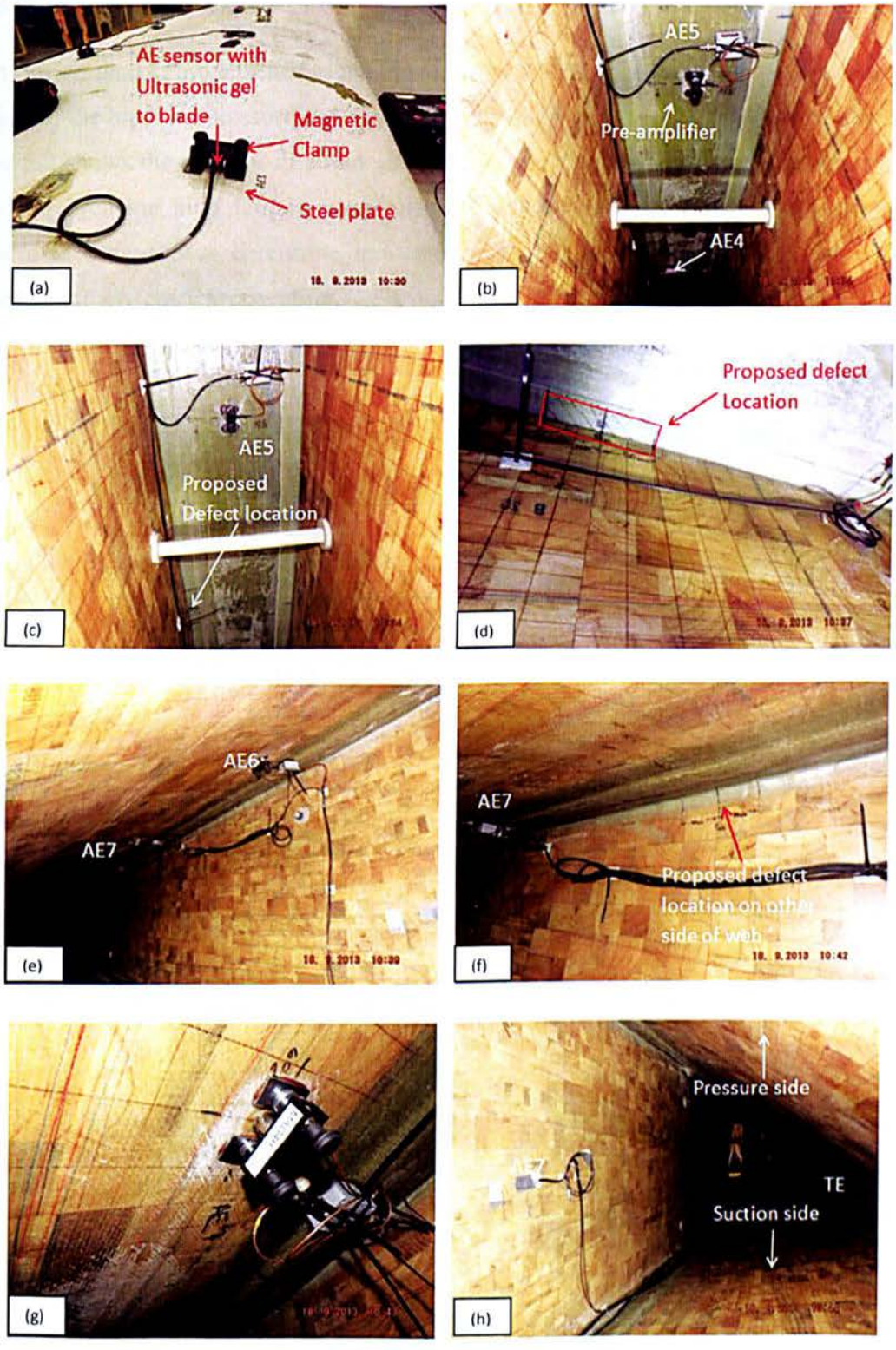

Fig. 5.3. (a) AE sensors installation, (b) AE5 & AE4, (c) AE5 & defect location (d) Defect location, (e) AE6 & AE7, (f) AE7 & proposed defect, (g) AE installation inside blade, (h) View towards blade root.

5.4.2 Strain gauges sensors

Thirty strain gauges are attached to the blade before testing. The strain gauges are attached to outside of the blade on pressure and suction sides as well as to the shear web inside the blade. Table 5.2 shows the distance of strain gauges from the blade root. The applied strain gauges were polyurethane high fatigue encapsulated 350Ω nominal-resistance strain gauge. The strain data are used to determine how the blade performs under loading and also for detections of any crack propagation.

Table 5.2 Strain gauge locations.

Gauge ID	Dist. from Root [m]	LW or WW	LE or TE	Edge Dist. [mm]	Long. or Trans.	Int. or Ext.
SG1	1.0	P	-	-	Long 0	Ext
SG2	8.0	P	-	-	Long 0	Ext
SG3	16.0	P	-	-	Long 0	Ext
SG4	24.0	P	-	-	Long 0	Ext
SG5	28.0	P	-	-	Long 0	Ext
SG6	33.0	P	-	-	Long 0	Ext
SG7	43.0	P	-	-	Long 0	Ext
SG8	1.0	S	-	-	Long 0	Ext
SG9	8.0	S	-	-	Long 0	Ext
SG10	16.0	S	-	-	Long 0	Ext
SG11	24.0	S	-	-	Long 0	Ext
SG12	28.0	S	-	-	Long 0	Ext
SG13	33.0	S	-	-	Long 0	Ext
SG14	43.0	S	-	-	Long 0	Ext
SG15	1.0	-	LE	0	Long 0	Ext
SG16	1.0	(p).	TE	0	Long 0	Ext
SG17	16.0	(p)	TE	50	Long 0	Ext
SG18	28.0	(p)	TE	50	Long 0	Ext
SG21	4.0	Shear Web TE, mid			+45	Int
SG22	4.0	Shear Web TE, mid			-45	
SG23	8.0	Shear Web TE, mid			+45	Int
SG24	8.0	Shear Web TE, mid			-45	
SG25	12.0	Shear Web TE, mid			+45	Int
SG26	12.0	Shear Web TE, mid			-45	
SG27	16.0	Shear Web TE, mid			+45	Int
SG28	16.0	Shear Web TE, mid			-45	
SG29	20.0	Shear Web TE, mid			+45	Int
SG30	20.0	Shear Web TE, mid			-45	

P= Pressure side, S= Suction side, LW=Leeward, WW=windward

5.4.3 Accelerometers sensors

In structural health monitoring (SHM) modal analysis is employed to determine any changes in the natural frequency of the structure due to any damage initiation and propagation that may occur. NaREC's standard testing procedure for modal testing PR10015 [2] is followed to capture the mode I and mode II in both flapwise and edgewise directions. During testing, accelerometers are mounted on brackets, which are in turn usually hot-glued to the blade for easy removal. However, since in the present work modal analysis will be repeated throughout the testing stages for determining the effect of the induced defects, these brackets are mounted to the blade using a two-part epoxy based adhesive (Araldite 2052). Table 5.3 summarises the accelerometer locations along the blade.

Table 5.3 Accelerometer location.

Accelerometer Number	Location
1	9m
2	18m
3	27m
4	36m
5	45.7m (tip)

Modal analysis testing is performed regularly throughout the testing phase to determine the effect of crack growth on the natural frequency. Therefore, it is important that the existing and induced defects are monitored closely during testing. Visual inspection, strain gauges and AE are used to monitor defects before each phase of modal testing to record crack growth rates.

5.5. Experimental procedure

5.5.1 Calibration pull test

The blade under test is 45.7m, and two saddles are attached along the blade. During the fatigue testing it is desirable to apply the correct target bending moment distribution over the blade length. This is accomplished by attaching the first saddle at 30.05m and the second saddle at 35.05m from the blade root as shown in Figure 5.4. An optimisation analysis is required to determine the position, dynamic mass and amplitude of the saddles. Courtesy to

NaREC knowledge and experience the location of the saddles has been selected. For flapwise test the saddles are closer to the tip of the blade. In the static calibration pull test the saddles are attached to the blade similar to the situation in the dynamic test.

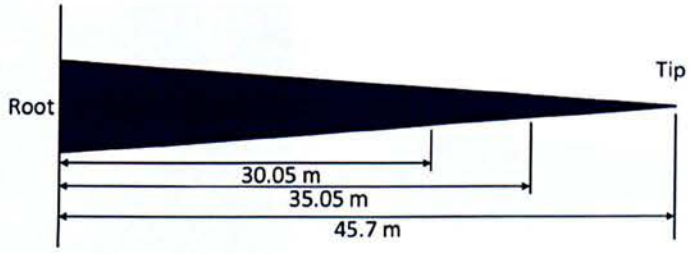

Fig. 5.4. Blade length and positions of the saddles on the blade.

A calibration pull test was used to obtain relationship between the load and the bending moment at root. This relationship will be used for extrapolation to find the required load to achieve the target bending moment.

Figure 5.5(a) shows the experimental test set up and Figure 5.5(b) shows the loading point on the blade. The static load is applied by attaching a cable to a hook attached to the saddle and the blade is deformed upward by pulling the cable incrementally and the strain readings were recorded along the blade at each load increment up to the maximum load. At the range of applied load the blade behaves linearly, a linear relationship was anticipated between the load and strain.

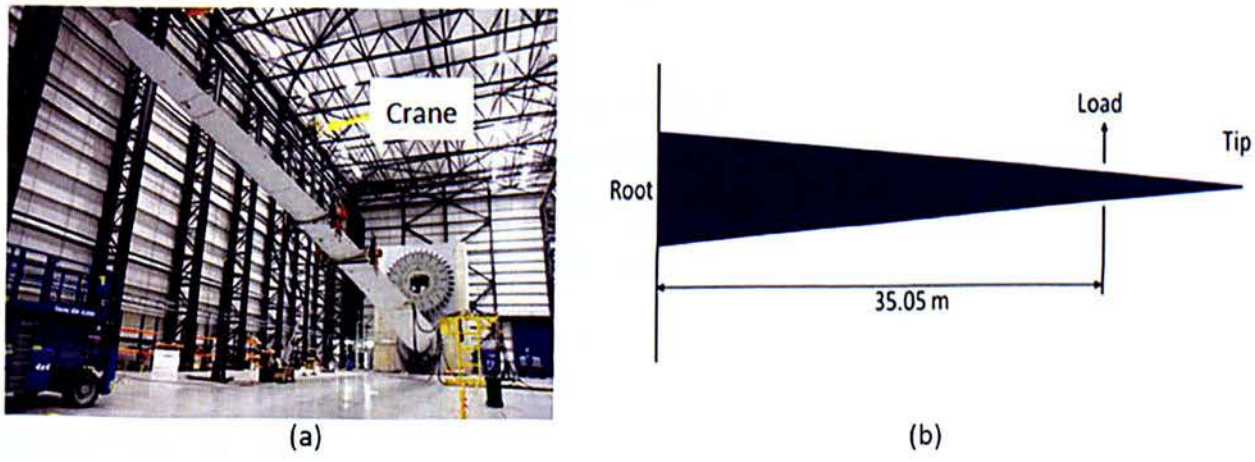

Fig. 5.5. (a) Calibration pull test and (b) Load point in upward direction.

The calibration pull test is repeated when the load is applied in downward direction at 35.05m from the root. Figure 5.6(a) shows application of the downward loading and Figure 5.7(b)

shows the loading point. The downward load is applied incrementally to reach to maximum load of 15 kN and strain readings were recorded along the blade at each load point. Therefore the relationship between the monotonic load and strain were obtained.

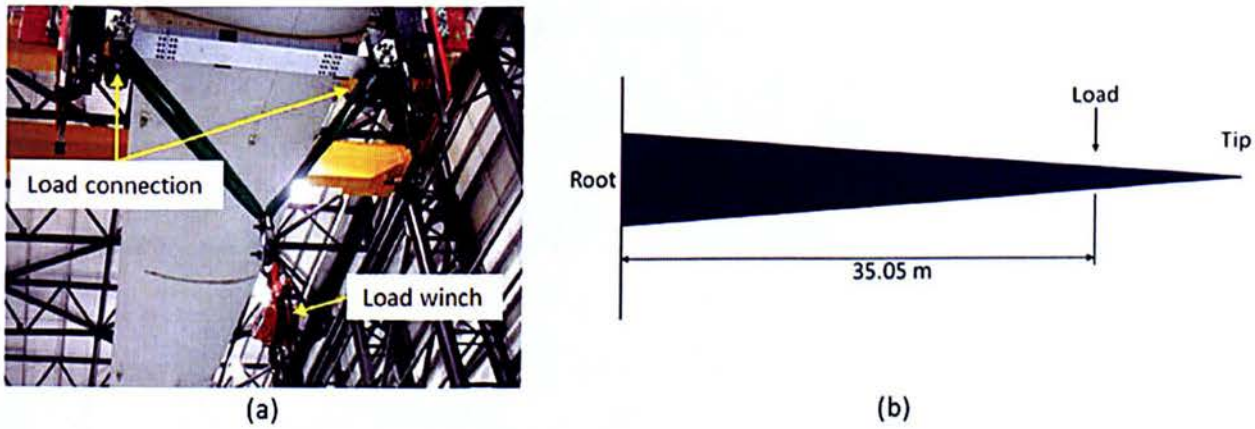

Fig. 5.6. (a) Calibration pull test in downward direction and (b) Loading point along the blade

5.5.2 Modal testing

Initially the blade is manually excited at three positions along the leading edge at 35m, 38.5m and 42m to find the proper position for excitation. The hammer impact is only applied on the middle of the cross section at 38.5m. The suitable location was chosen at 38.5m for both flapwise and edgewise directions.

Finally for flapwise modal testing, the blade is manually excited at 38.5m from the centre point of the blade cross section and hammer impact test has done at the same point in the centre of the blade. For edgewise modal testing, the blade has been excited manually at the same position but at the leading edge. Depending on the experiment the accelerometer direction has changed. In the edgewise modal test the accelerometers are all facing the transverse direction and in the flapwise modal test, the accelerometers are all facing the longitudinal direction along the blade.

5.6 Experimental results

5.6.1 Calibration pull test

Figure 5.7 shows the results of calibration pull test for all strain gauges on pressure and suction side along the blade when the load is applied at 35.05m.

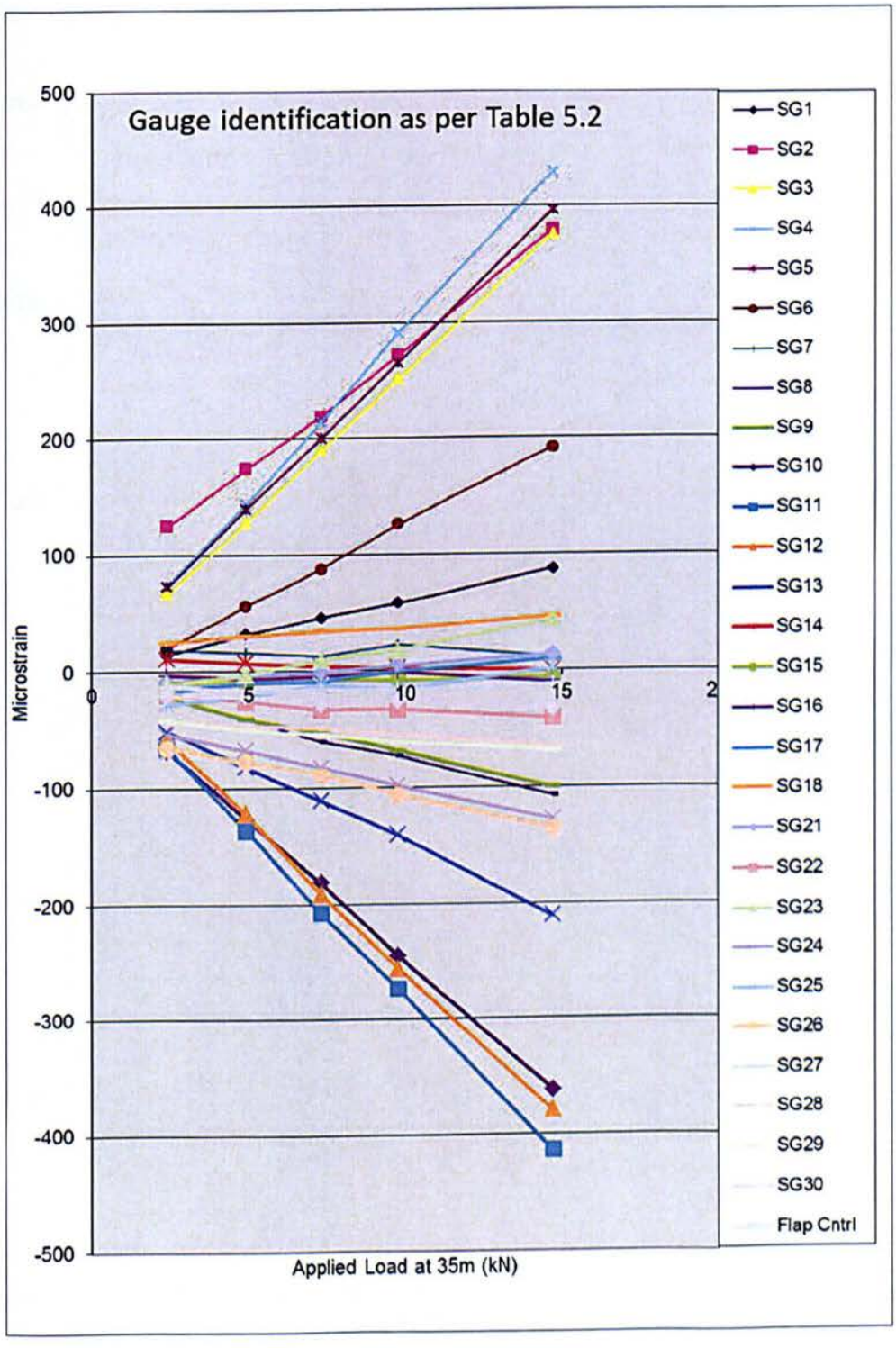

Fig. 5.7. Calibration pull test results.

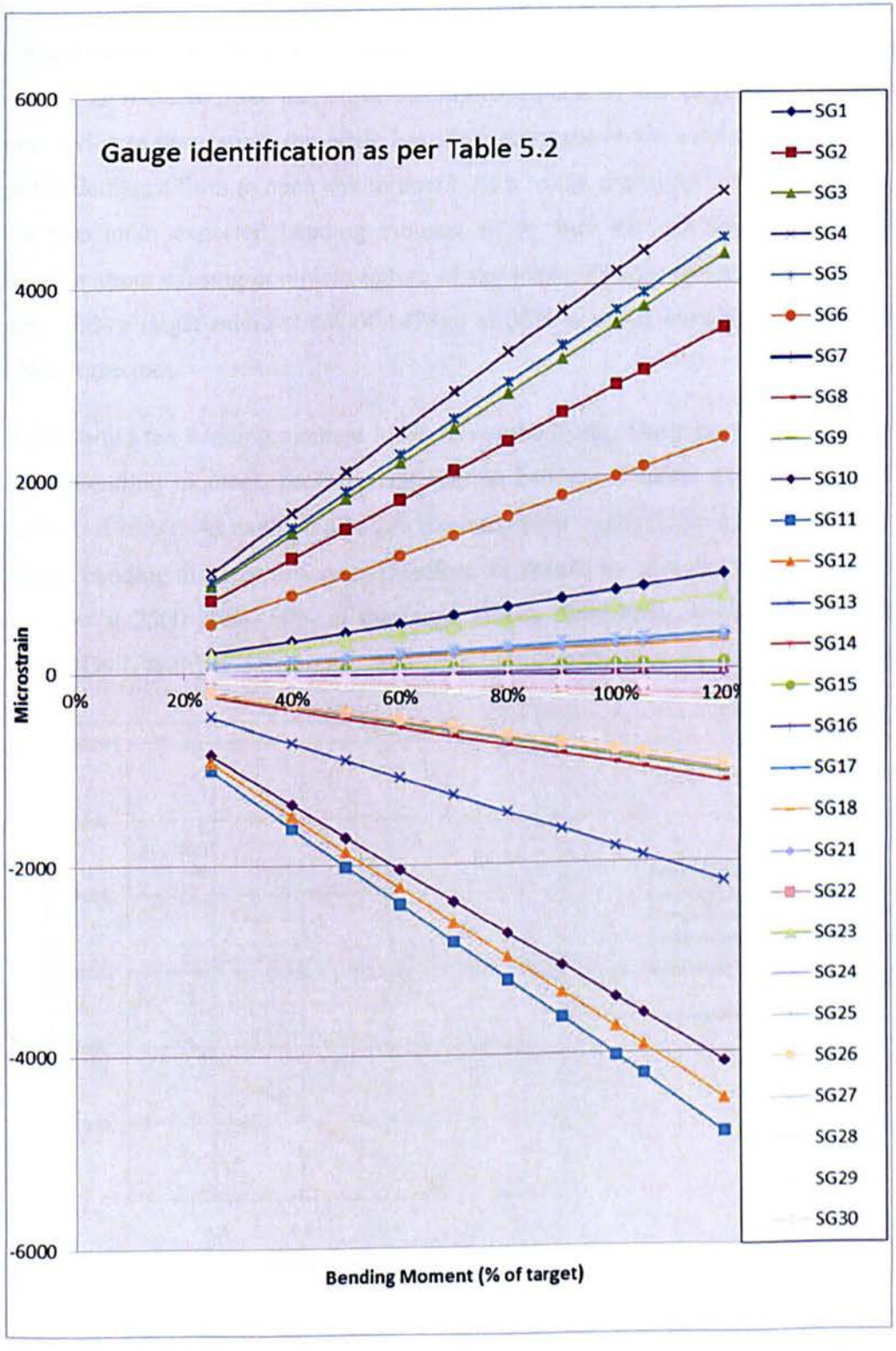

Fig. 5.8. Blade with saddle: Bending moment (% target).

From the results obtained from the calibration pull test; it is then possible to find the variation of the root bending moment with strain as shown in Figure 5.8. Therefore it is clear what micro-strain reading needs to be achieved in the fatigue test to reach to target bending moment. It is required that the observed strains equate to the target bending moment. However, prior to the testing, the blade has some damages on the aeroshell skin and it was exposed in damaged form to open environment. As a result, the target bending moment set to 50% of maximum expected bending moment to be sure that all fatigue tests could be completed without causing complete failure of the blade. Fatigue testing has followed SG2 readings, with a target micro-strain of 1478$\mu\varepsilon$ at 50% nominal bending moment (BM) of 5000kNm at the root.

Figure 5.9 shows the bending moment loads across the blade. There are three lines in Figure 5.9; target bending moment, pressure and suction bending moment extrapolated from the calibration test result. As explained before the maximum target bending moment set at 50% of expected bending moment in service therefore the results for pressure and suction bending moments are at 2500 kNm, 50% of the target BM at 5000 kNm. On the suction side the reading of SG9 is faulty and SG10 has been used for the analysis of the bending moment.

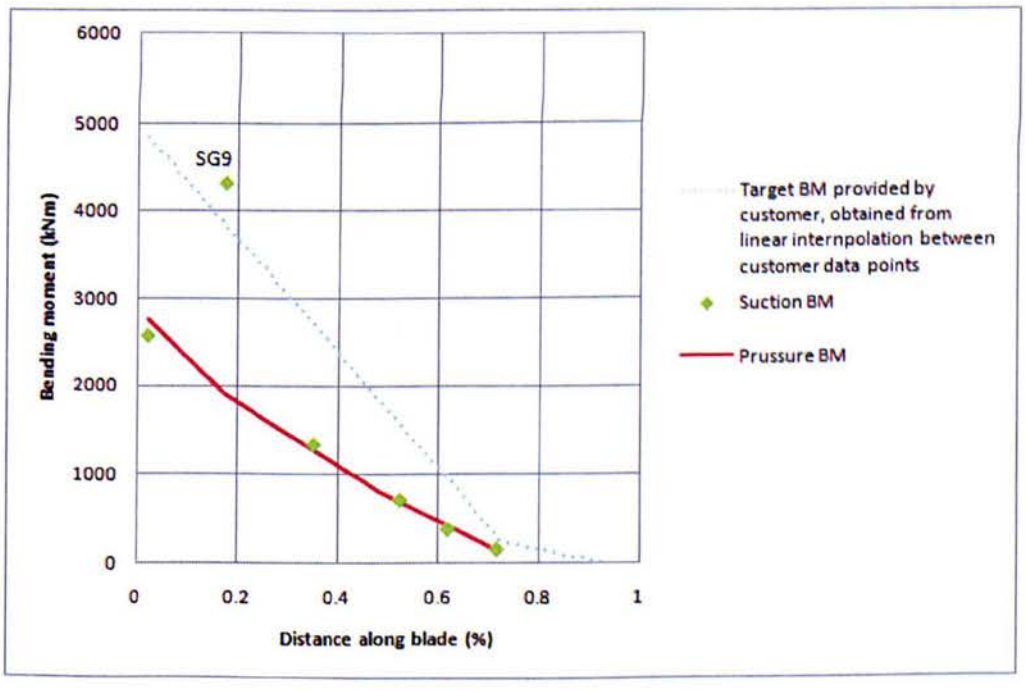

Fig. 5.9. Comparison of target and measured bending moment distribution for uncracked blade.

5.6.2 Calibration pull test results for the blade with induced crack of 0.2m

A crack of 0.2m length inserted between the shear web and spar cap by an electric saw where the adhesive between the spar cap and web joint is removed. A new calibration test was done to find the new bending moment distribution along the blade. The results of calibration pull test for the blade with 0.2m induced crack damage are shown in Figure 5.10. The results show variation of all strain gauges on pressure and suction sides of the blade versus the applied load at 35.05m.

Figure 5.11 compares the calibration pull test results of SG2 strain gauge for blade with crack insertion and with 0.2m induced crack damage. The strain gauge readings in the calibration pull test at SG2 with induced crack damage of 0.2m have decreased by about 50% at the initial load and decreased by about 16% at the final load. This is due to debonding of the spar cap from the shear web.

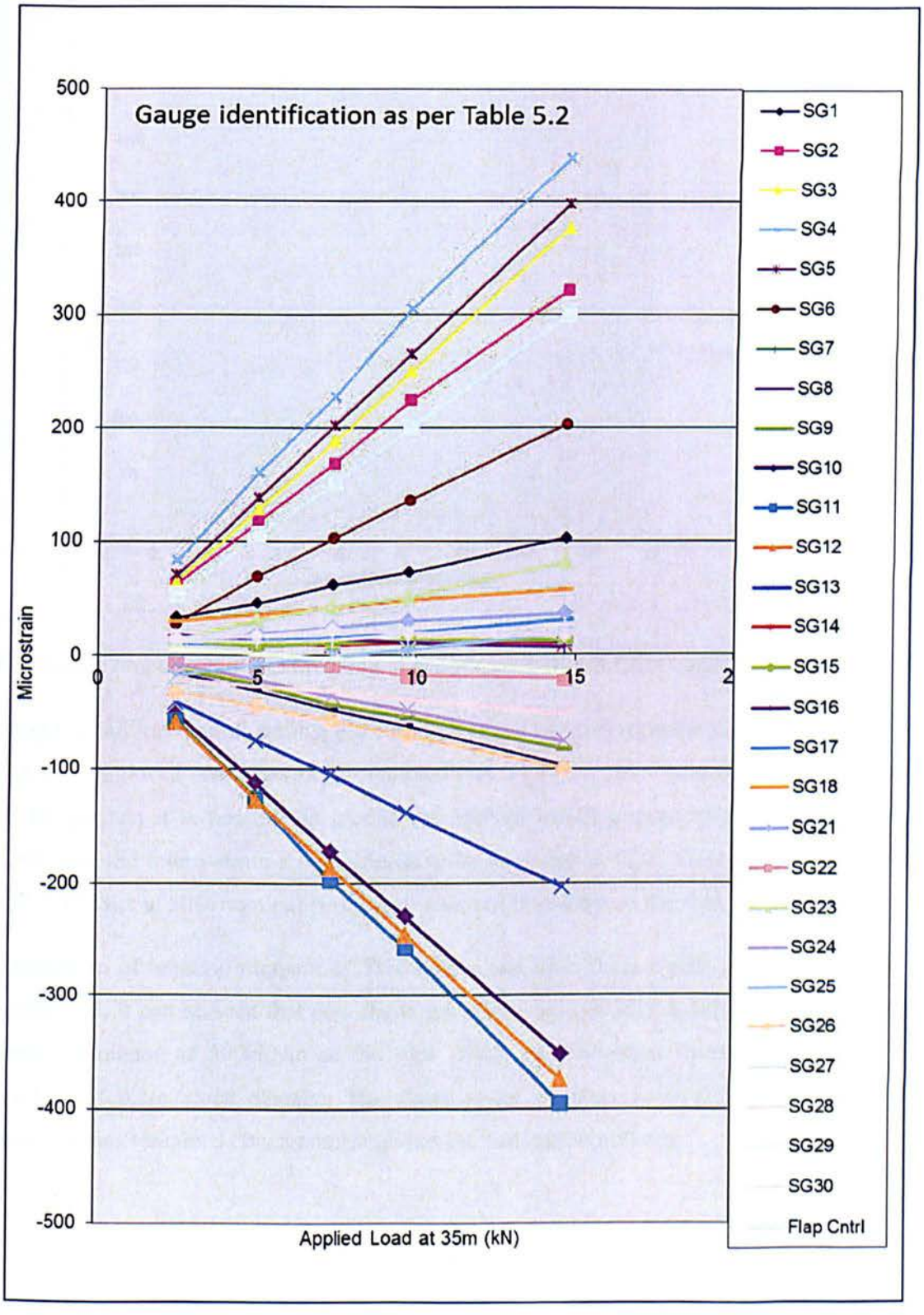

Fig. 5.10. Calibration pull test results for the blade with 0.2m induced crack.

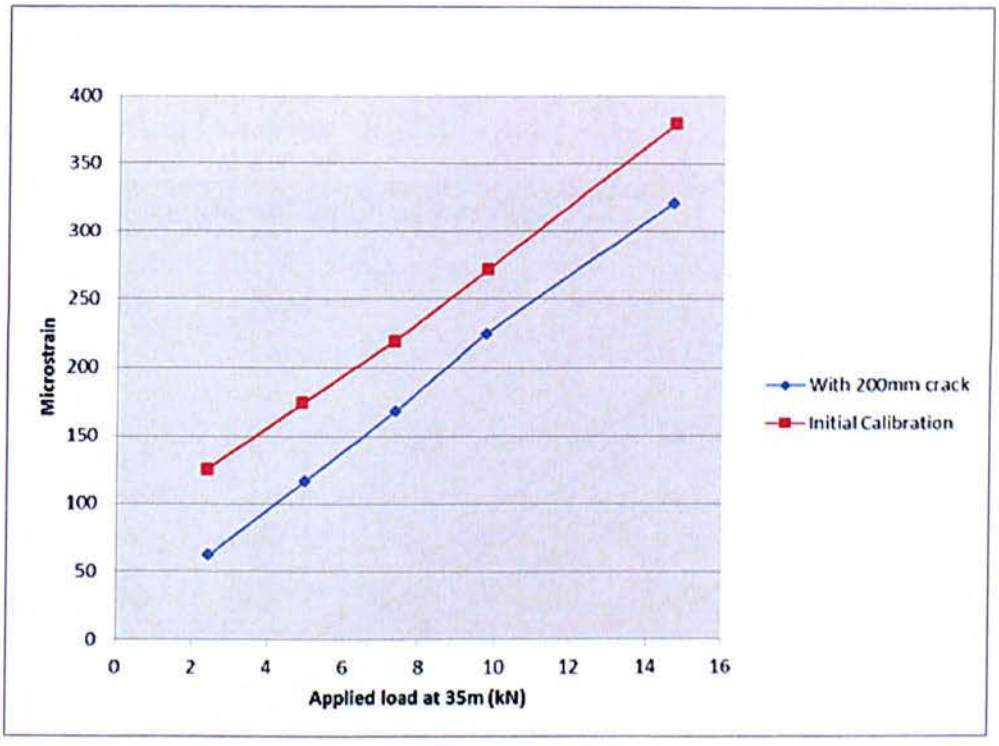

Fig. 5.11. Comparison of SG2 reading in calibration pull test before and after crack insertion.

Using the calibration pull results; the variation of the bending moment versus strain for blade with 0.2m induced crack has been predicted (see Figure 5.12). Therefore when performing the fatigue test it is possible to predict the applied bending moment at the blade root by monitoring the micro-strain reading needs to be achieved at SG2. The target micro-strain at SG2 is 1523$\mu\varepsilon$ at 50% nominal bending moment of 5000kNm at the root.

Comparison of bending moment of SG2 before and after 0.2m crack insertion is shown in Figure 5.13. It can be seen that now the target microstrain at SG2 is 1523$\mu\varepsilon$ at 50% nominal bending moment of 5000kNm at the root which has increased from 1478$\mu\varepsilon$ before the insertion of 0.2m crack damage. The strain gauge readings have shifted by 3% but the amplitude has remained constant through-out the calibration pull test.

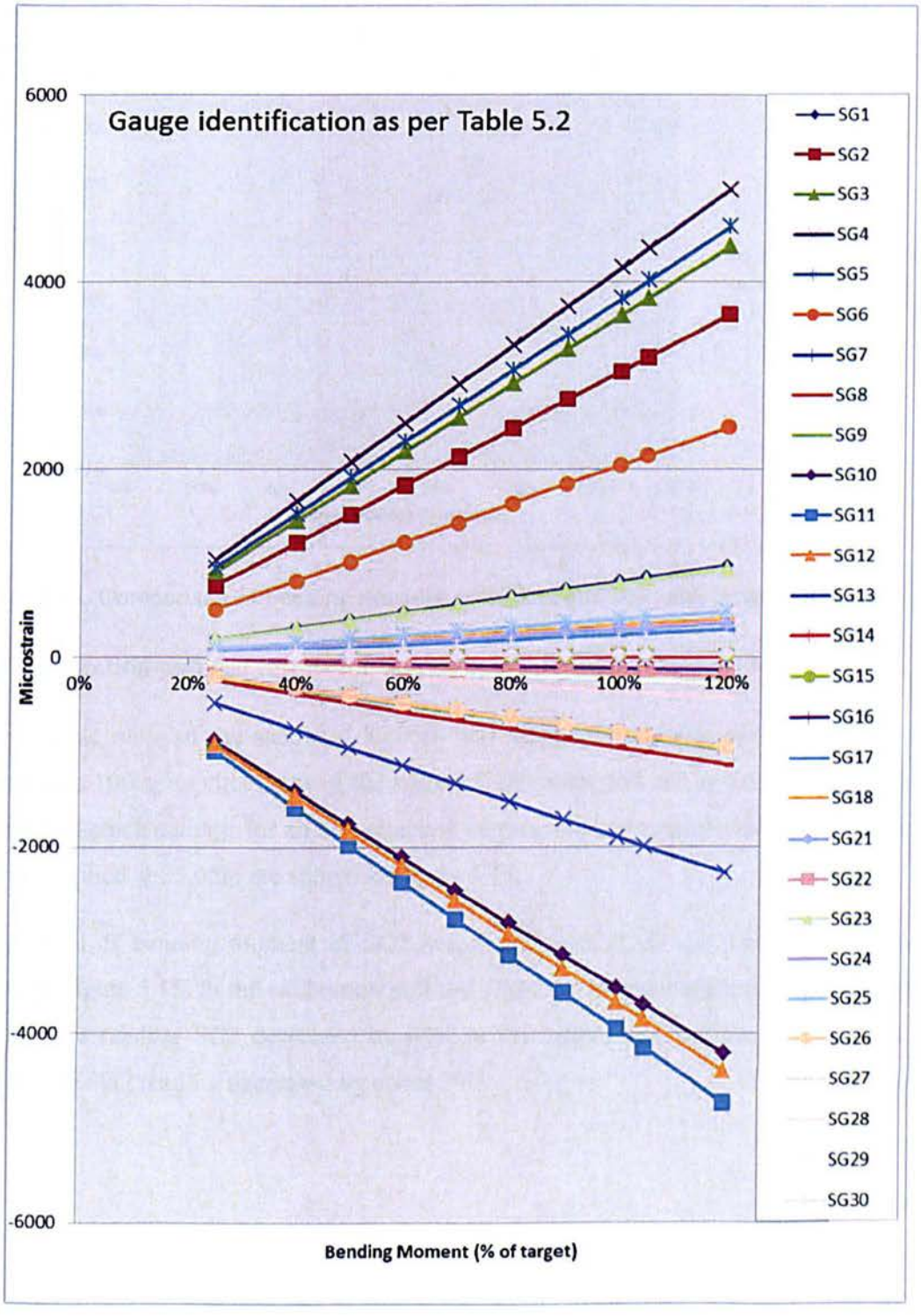

Fig. 5.12. Variation of strain at SG2 with bending moment in blade with 0.2m induced crack damage.

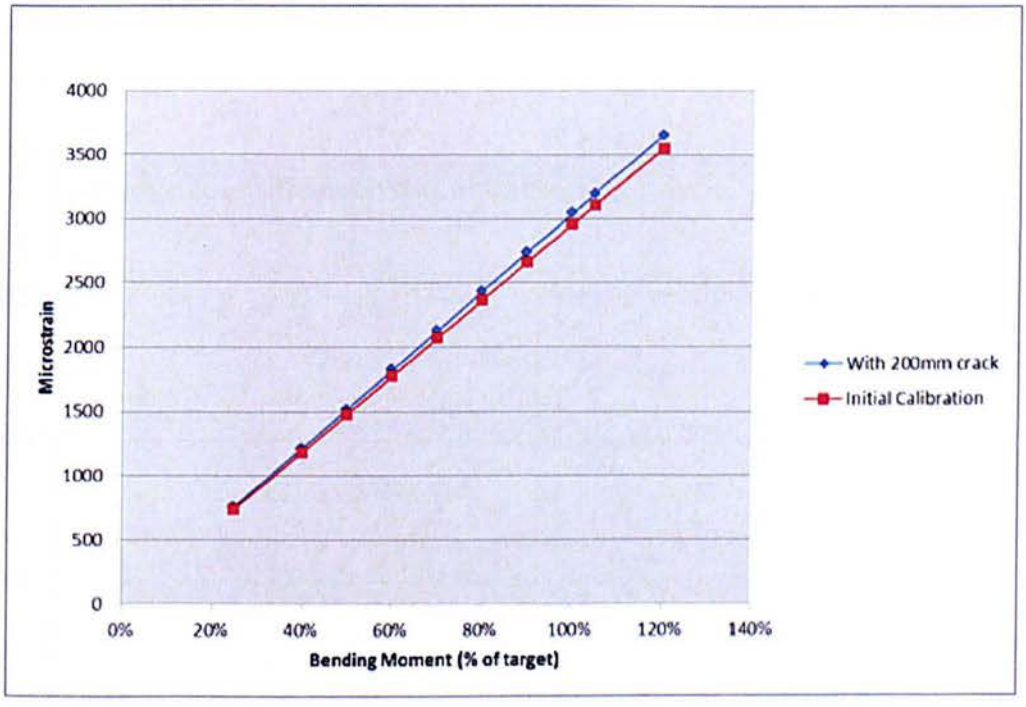

Fig. 5.13. Comparison of bending moment of SG2 before and after 0.2m crack insertion.

5.6.3 Calibration pull test results for the blade with induced crack of 1m

The dynamic mass of the saddle at 30.05m was increased to 200kg and at 35.05m it was increased to 100kg on either side of the saddle. Calibration pull test results for the blade with 1m induced crack damage for all SGs attached on pressure and suction sides of the blade with the load applied at 35.05m are shown in Figure 5.14.

Comparison of bending moment of SG2 before and after 0.2m and 1m crack insertion is shown in Figure 5.15. In the calibration pull test when the induced crack damage was 1m, the strain gauge reading SG2 decreased by 64% at the initial load while when the final load applied, the SG2 reading decreased by about 20%.

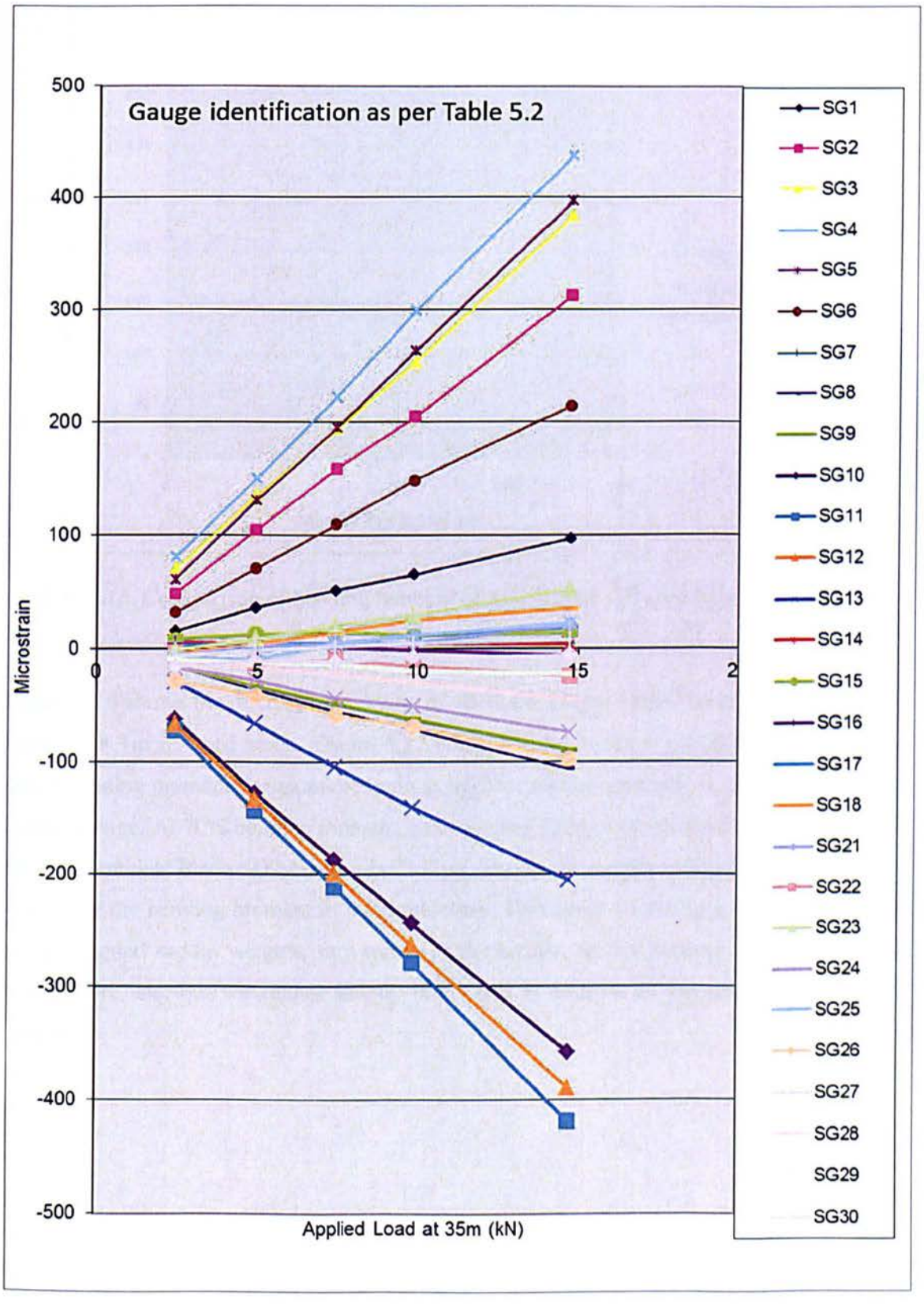

Fig. 5.14. Calibration pull results; blade with 1m induced crack damage.

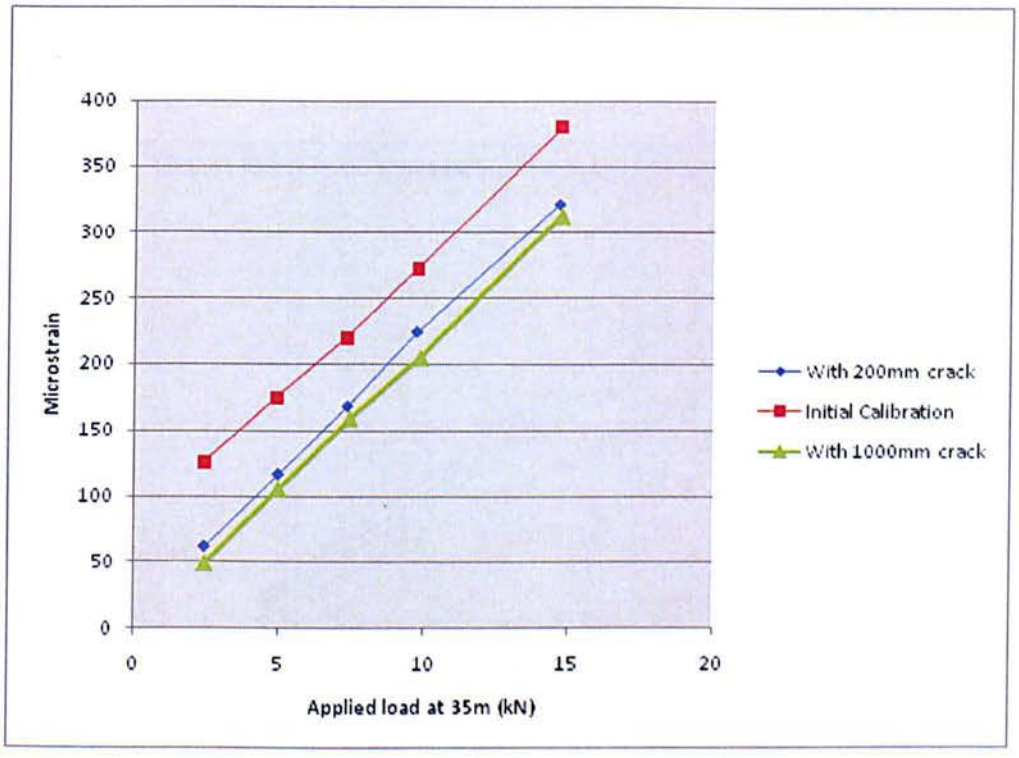

Fig. 5.15. Comparison of bending moment of SG2 before and after 0.2m and 1m crack insertion.

Figure 5.16 shows the microstrain reading of all strain gauges versus bending moment in the blade with 1m inserted crack. Figure 5.17 compares the bending moment as percentage of target bending moment versus microstrain at SG2 for uncracked blade, 0.2m and 1m induced crack damage. At 70% bending moment, SG2 reaches 2135$\mu\varepsilon$ for induced crack of 1m while for 0.2m cracked blade SG2 reading is 2132$\mu\varepsilon$. The strain gauge reading has a difference of 0.14% for the bending moment in the three cases. This could be due to a number of reasons such as added saddle weights, movement of the saddle, ±0.5% accuracy of strain gauges, temperature, etc. but we cannot strictly imply this is because of any change in the blade strength.

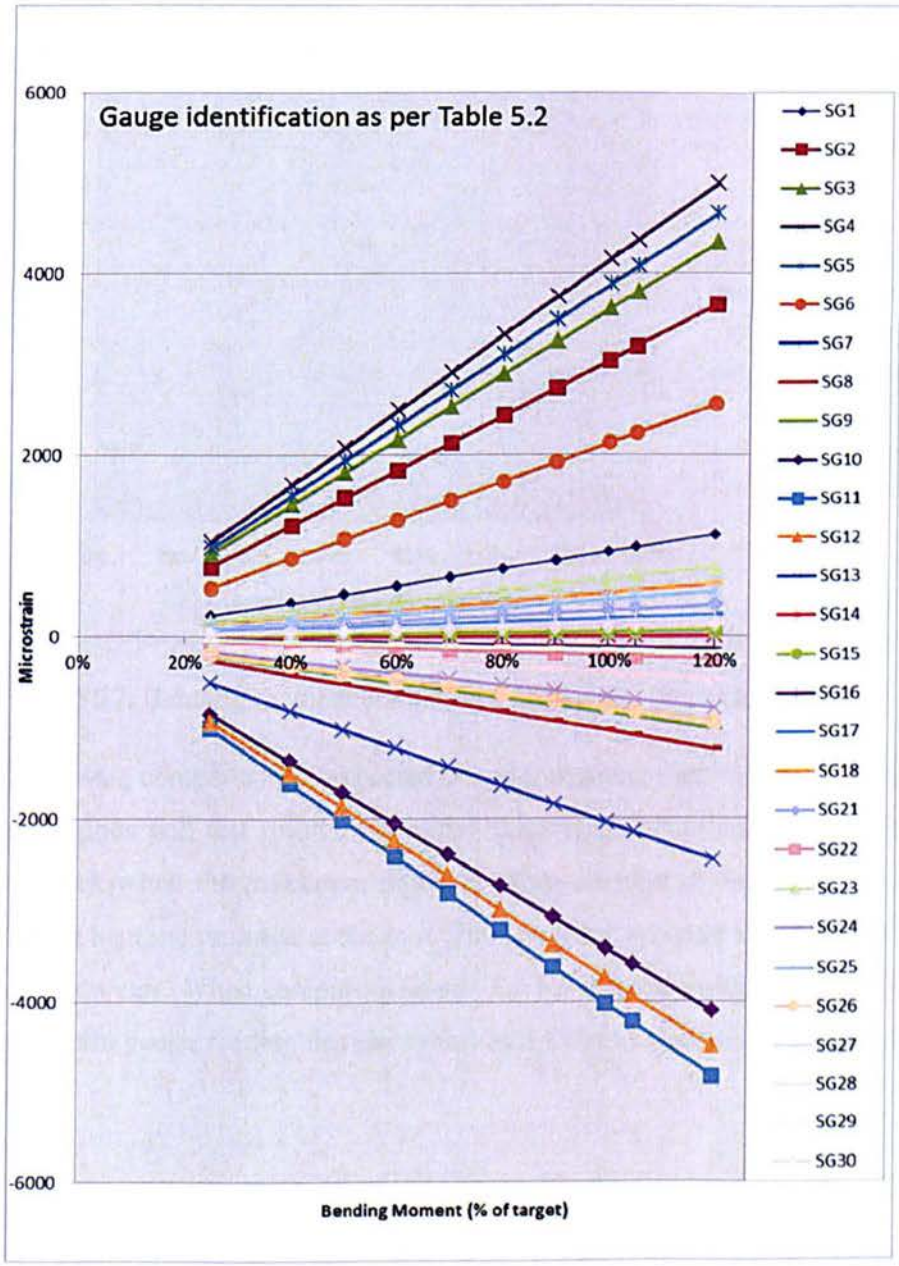

Fig. 5.16. Variation of strain at SG2 with bending moment in blade with 1m induced crack damage.

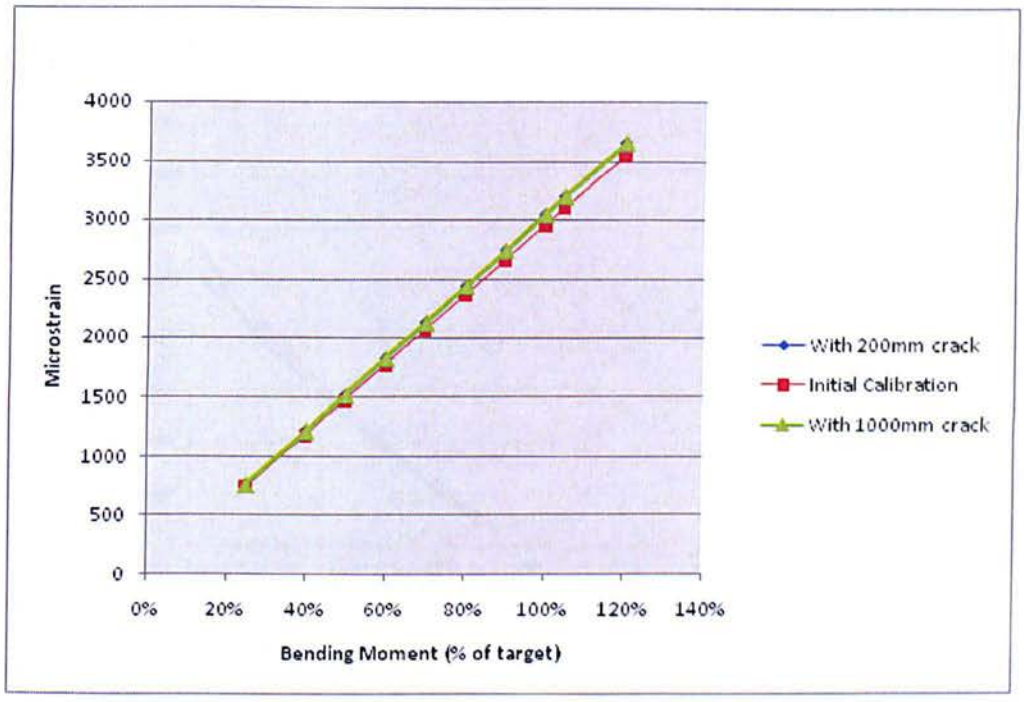

Fig. 5.17. Bending moment comparison of SG2 for three cases of blade.

Figure 5.18 shows a comparison of expected bending moment distribution along the blade in all three calibrations pull test results, i.e. initial undamaged blade and blade with 0.2m and 1m inserted crack when the maximum target bending moment at the root is set at 50% of maximum target bending moment at the root. The result for pressure side bending moment is lower than suction side. When comparing results for 1m induced crack damage at 10% of the blade length, strain gauge reading has decreased by 13.1% in comparison with 0.2m induced crack damage.

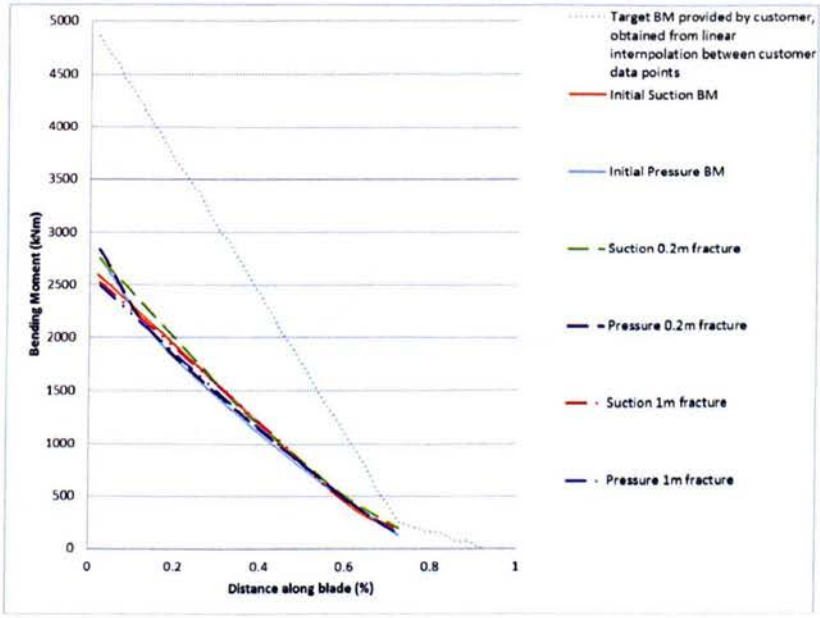

Fig. 5.18. Comparison of target and measured bending moment distribution with crack.

5.7. Modal Testing

5.7.1 Results of modal testing

The results of modal tests by manual excitation on the uncracked blade without saddles are shown in Figure 5.19(a) where the blue line is the results of flapwise direction, and green line is the results of edgewise direction.

Figure 5.19(b) shows a magnified area of Figure 5.19(a) between 0-2 Hz to quantify accurately the results for the natural frequencies. From the graph the first mode natural frequency occurred in flapwise direction at 0.713 Hz and the second mode occurred on the edgewise direction at 1.398 Hz, respectively. The third mode natural frequency occurred in the flapwise direction at nearly the same frequency of 1.4 Hz.

Figure 5.19(c) shows a magnified area of Figure 5.19(a) between 1.5-5 Hz where the higher mode shapes of the blade occur. The fourth natural frequency also occurred in flapwise direction at 2.1 Hz.

In addition to manual excitation hammer testing were carried out. Figure 5.20 shows the hammer impact raw data in flapwise and edgewise direction over a 60 second window, where the graph peaks at impact and ripples out over this period of time. The natural frequencies of the blade found from this method were the same as those reported in Figures 5.19.

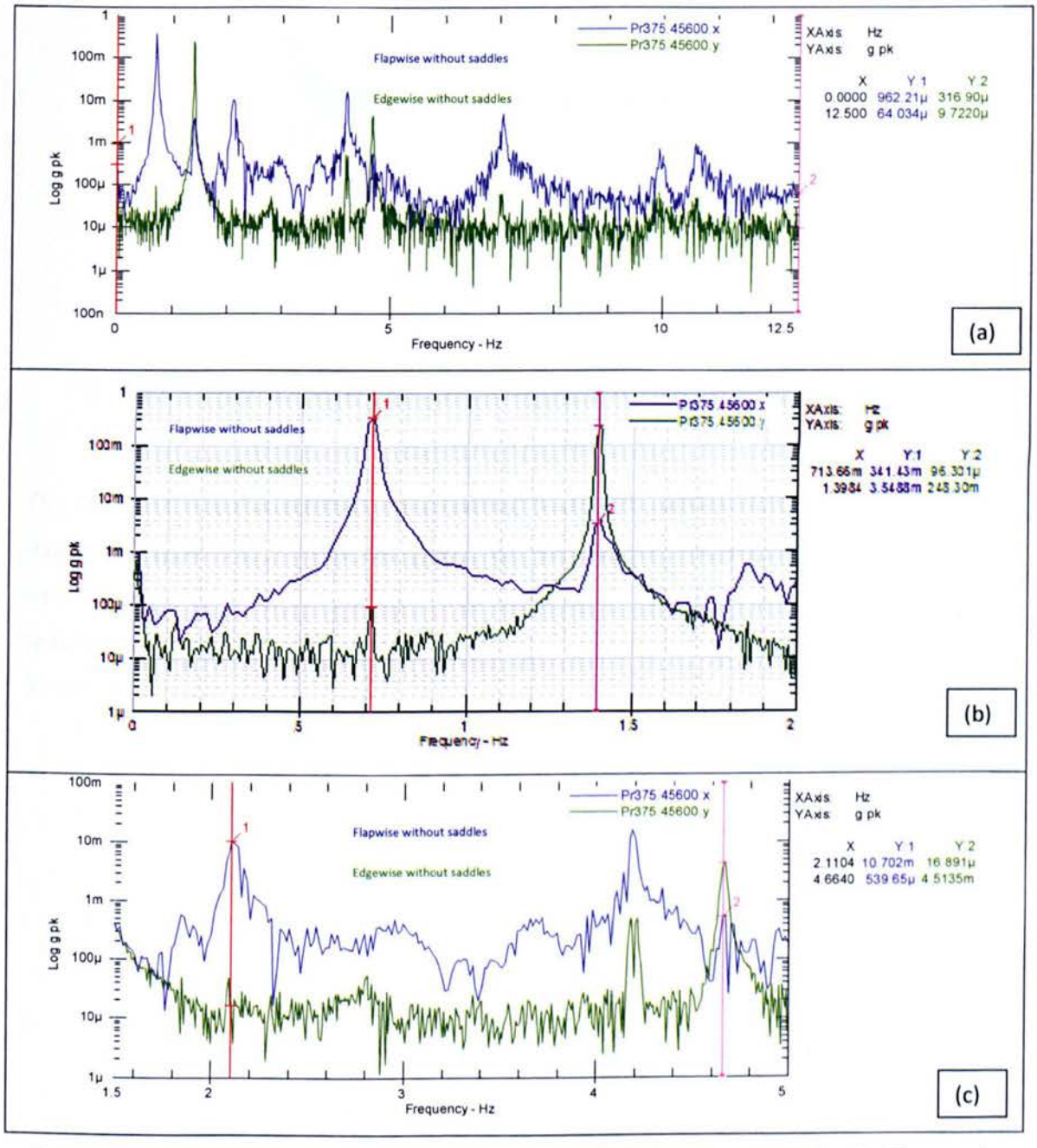

Fig. 5.19. (a) Overview of modal testing on uncracked blade without saddles (b) First mode natural frequency range on the flapwise (blue) and second mode in edgewise (green), (c) Higher modes in flapwise and edgewise directions.

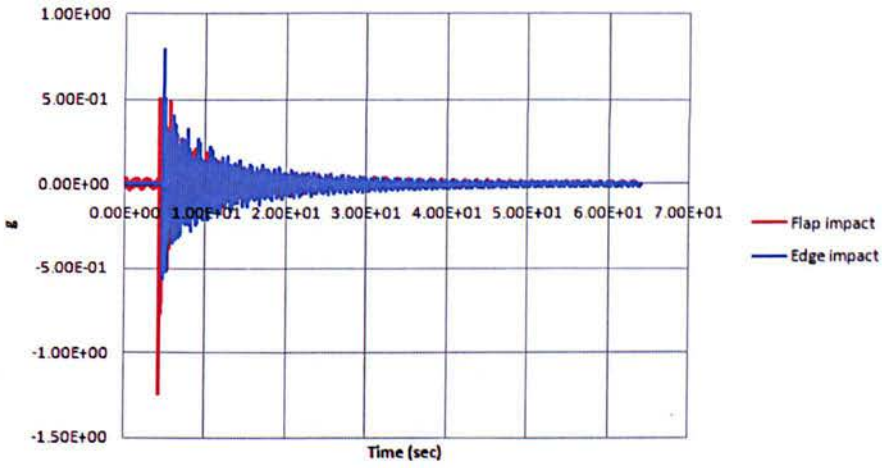

Fig. 5.20. Comparison of impact wave damping in flapwise and edgewise direction in uncracked blade.

The results of modal experiment on uncracked blade with saddles at 30.05m and 35.05m are shown in Figure 5.21. From the graph, the first natural frequency occurred in flapwise direction at 0.562 Hz when saddles were attached. It should be noted that attaching the saddles to the blade would reduce the natural frequencies both in flapwise and edgewise direction.

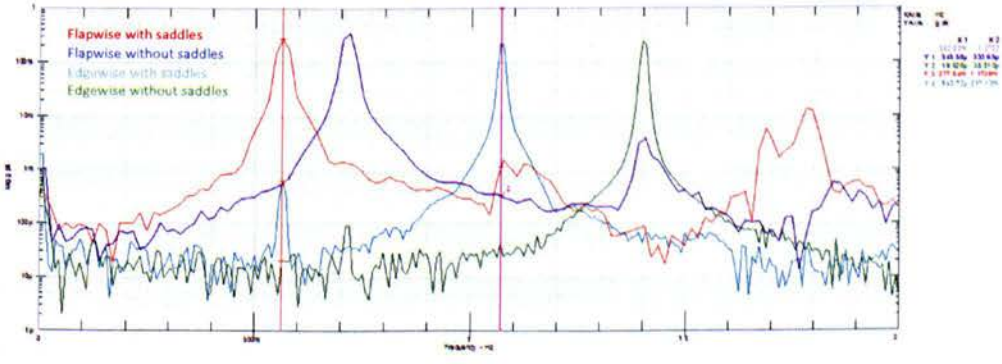

Fig. 5.21. Modal results with saddles on the uncracked blade.

Figure 5.22 compares the result of modal test for flapwise and edgewise directions of blade with 0.2m inserted crack damage and uncracked blade when the saddles were attached. The results show that there has been no shift in the first natural frequency and it remains at 0.562 Hz.

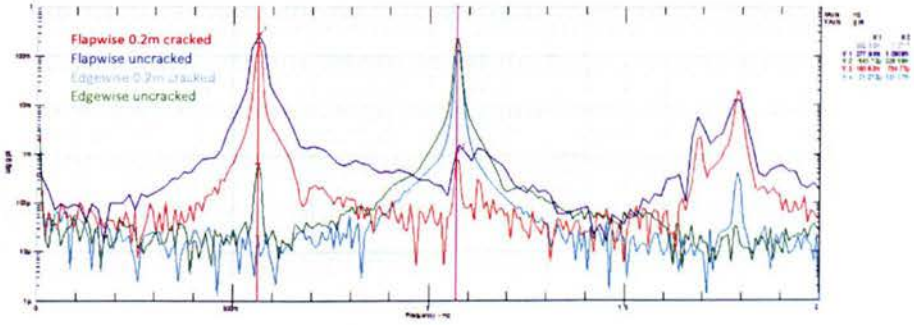

Fig. 5.22. Modal test results of 0.2m induced cracked blade and uncracked blade when the saddles were attached.

The results of modal testing for flapwise and edgewise directions of 0.2m cracked blade, 1m cracked blade and uncracked blade when the saddles were attached are shown in Figure 5.23. The results show that there is no shift in the natural frequencies and the first flapwise mode remains at 0.562 Hz.

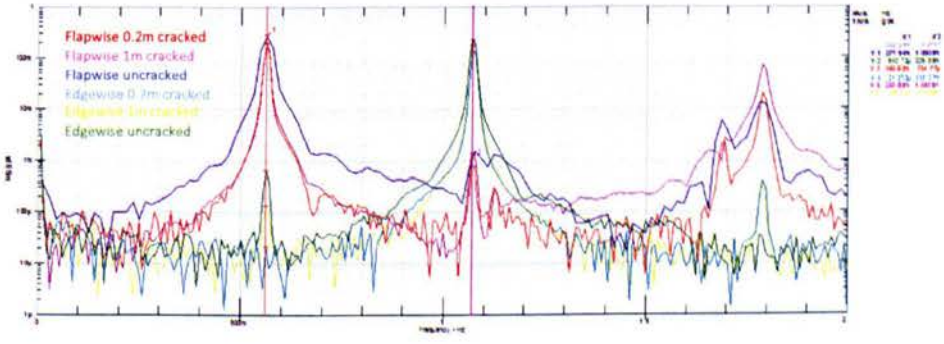

Fig. 5.23. Comparison of modal results of 0.2m and 1m cracked blade with uncracked blade.

Figure 5.24 compares the result of modal testing for flapwise and edgewise directions of 1m cracked blade with saddles having standard mass with those when adding 400kg weight to each saddle. It can be seen by adding the weight of the saddle there was a slight shift in the first mode natural frequency to 0.556 Hz.

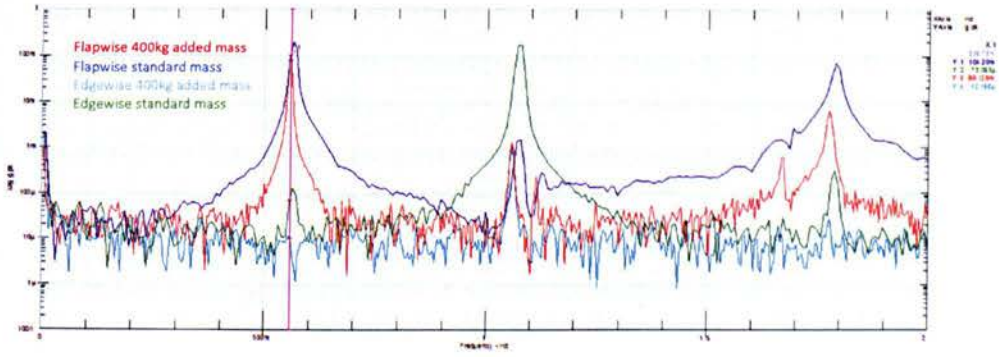

Fig. 5.24. Modal results with 1m induced crack damage with added weight on the saddles.

5.8. Conclusion

In this chapter the information required for fatigue testing of full scale blade has been quantified by appropriate experiment.

The magnitude of strain for monitoring the target bending moment at the root of the blade has been obtained by performing the calibration pull test. This test is performed at three different stages of the blade i.e. (i) undamaged blade, (ii) inserting 0.2m crack and (iii) extending the crack to 1m. For each of these cases the microstrain at strain gauge SG2 calibrated to appropriate applied bending moment at the root of the blade. These reading will be the controlling parameter for fatigue test which will be described in Chapter 6.

Modal testing is a crucial experiment to measure the blades natural frequencies over a range of frequency domain. The modal testing has been done in flapwise and edgewise, at all three stages of the blade while the dynamic masses were attached to the saddles.

The first mode natural frequency of undamaged blade and 0.2m induced crack damaged blade remained at 0.562Hz and remained unchanged for the 1m induced crack damaged. However, the first natural frequency had changed slightly by 0.006Hz for 1m induced crack damage when 400kg weight added to the saddles.

5.9. References

[1] BSI, BS EN61400-23 (2005) Wind turbine generator systems - Full scale structural testing of rotor blades International standard.
[2] NaREC's standard testing procedure for modal testing PR10015.
[3] BSI, BS EN 61400-1 Wind Turbines - Design requirements. 2005.

6

Full Scale Flapwise Blade Fatigue Testing and Blade Damage Tolerance

6.1 Introduction

The power train components of a wind turbine are subjected to a highly irregular loading condition from turbulent wind flow as well as gravity loading and inertial loading when the turbine accelerate or decelerate. As a result the number of fatigue cycles experienced by the blades is of orders of magnitude greater than other rotating machineries. In comparison a manned motor vehicle frequently maintained and has a typical operational life of about 160,000 km, equivalent to four months of continuous operation. Horizontal axis wind turbines components are subjected to fatigue, where most structural failures take place due to mechanisms driven by fatigue loading. Fatigue affects the structures where there is stress concentration or internal defects, therefore it is relevant to understand and test a full scale wind turbine blade under fatigue loading. The experiments laid out in this chapter consist of a full scale fatigue testing of an undamaged blade. The damage tolerance of the blade is examined by introducing a crack damage of 0.2m between the shear web and the spar cap and then propagating this crack to 1m. Full scale wind turbine blade fatigue testing for this experiment has been followed by IEC 61400-23 [1] standard.

6.2 Experimental fatigue procedure

The blade is excited from two points at 30.05m and 35.05m from the root using saddles as shown in Figure 6.1. The saddles excite the blade to reach a specific strain at a preselected strain gauge SG2 located at 8m from the root on pressure side in *longitudinal direction. The* fatigue was conducted at resonant frequency just below the first natural frequency of the blade.

Fig. 6.1. Position of Saddles loading points on the blade.

The blade spar consists of two shear webs connected with hollow piping running the length of the blade to reinforce strength. The blade is 45.7m in length. A view of the internal blade structure is shown in Figure 6.2

Fig. 6.2. Two shear webs seen inside the blade taken from the root.

6.2.1 Pre-existing damage

The same blade that is used in Chapter 5 is also used in this chapter for full scale fatigue testing. The blade initially inspected and some damage and hair line cracks has been found on the skin on the pressure side at a distance of approximately 33m from the blade root as shown in Figure 6.3(a). Figure 6.3(b) is an illustration of the second hair line crack located just below 32.8m on the TE. These minor pre-existing damages are only skin-deep and they did not affect the structural integrity of the blade. Three AE sensors have been fitted on the outside of the blade in this region to detect any crack growth during fatigue testing.

Also a crack is found approximately at 33m with a length of 460mm and 160mm from the LE as shown in Figure 6.4. Delamination was detected at 2m from the root on the TE as shown in Figure 6.5. Figure 6.6 shows an over view of the existing damage and cracks along the blade.

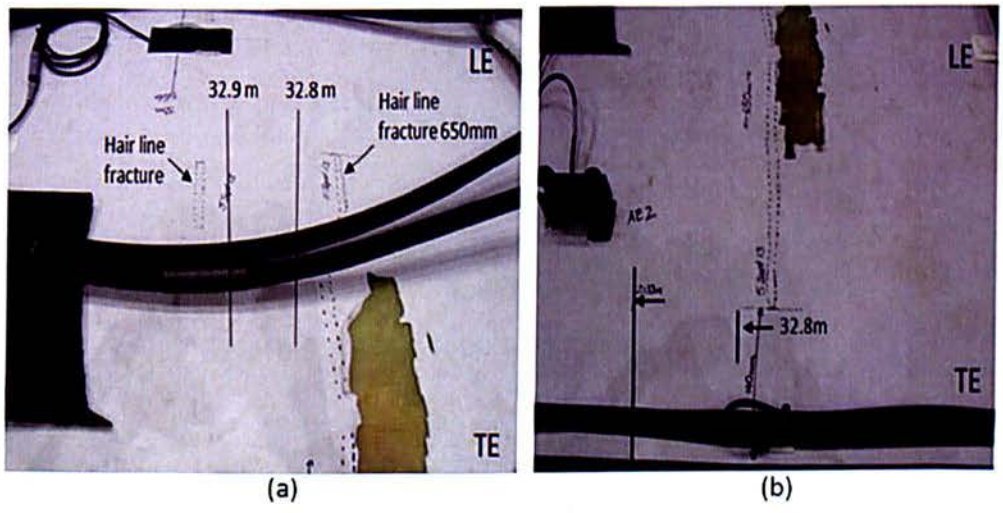

Fig. 6.3. (a) Existing damage and cracks on pressure side (b) TE existing damage.

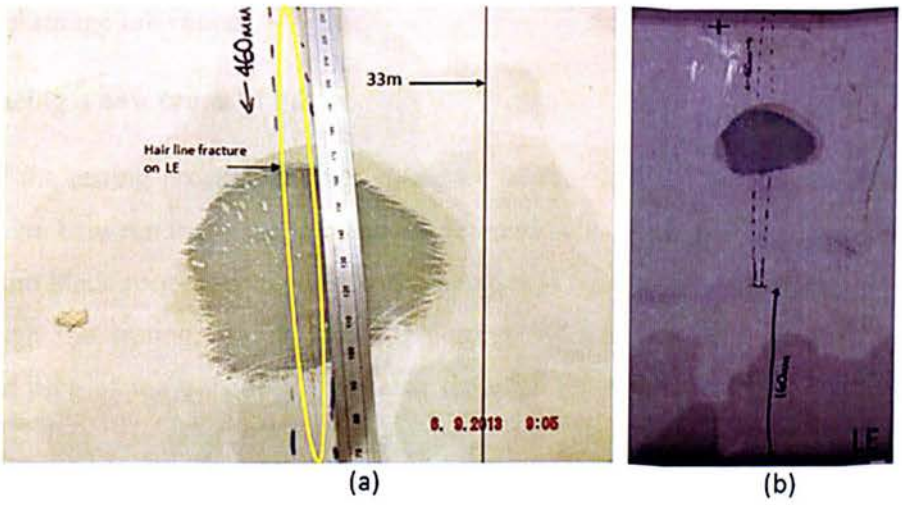

Fig. 6.4. (a) Existing cracks at about 33m from root (b) Position of crack from LE.

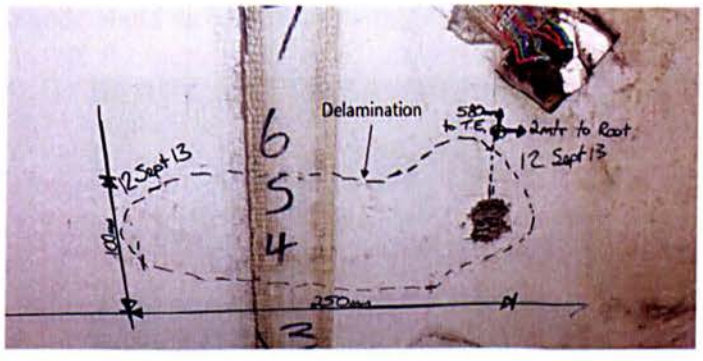

Fig. 6.5. Delamination on TE at 2m from root.

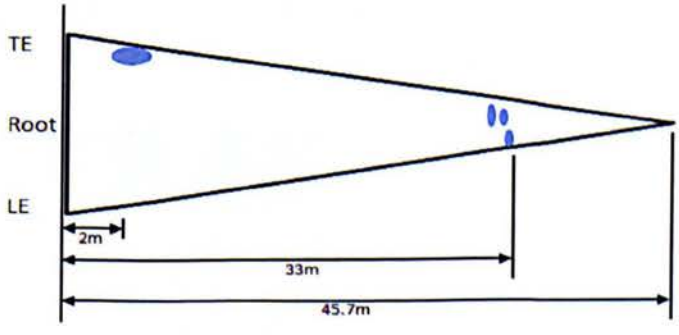

Fig. 6.6. Location of existing damage along the blade

The blade will be subjected to fatigue loading and growth of existing and/or formation of new cracks/damage will be monitored using the acoustic emission (AE) sensors and crack visualization.

6.3 Blade damage tolerance

6.3.1 Inducing a new crack of 0.2m

As part of the testing process, damage tolerance of the blade is examined by introducing a crack of 0.2m between the shear web and the spar cap. The shear web on the left-hand side as looking from blade root de-bonded from the blade skin (spar cap). The crack is induced part-way through the testing, which involves cutting off the adhesive bond material in the highlighted area of the outside web at a distance of 9m from the blade root, as shown in Figure 6.7.

Figure 6.8(a) shows the induced crack outside the shear web box and Figure 6.8(b) shows the crack inside shear web box. Four AE sensors are fitted on the shear web wall to monitor the crack growth and to understand its behaviour during cyclic loading.

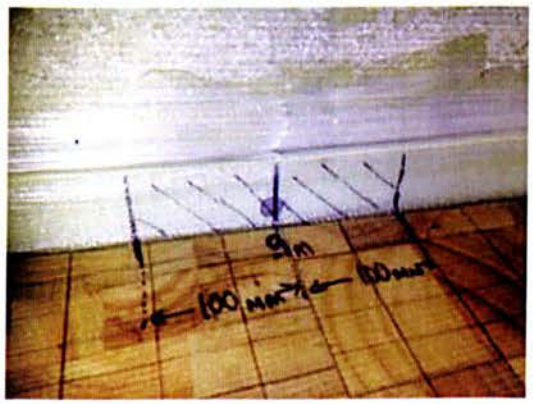

Fig. 6.7. Location of manually induced crack.

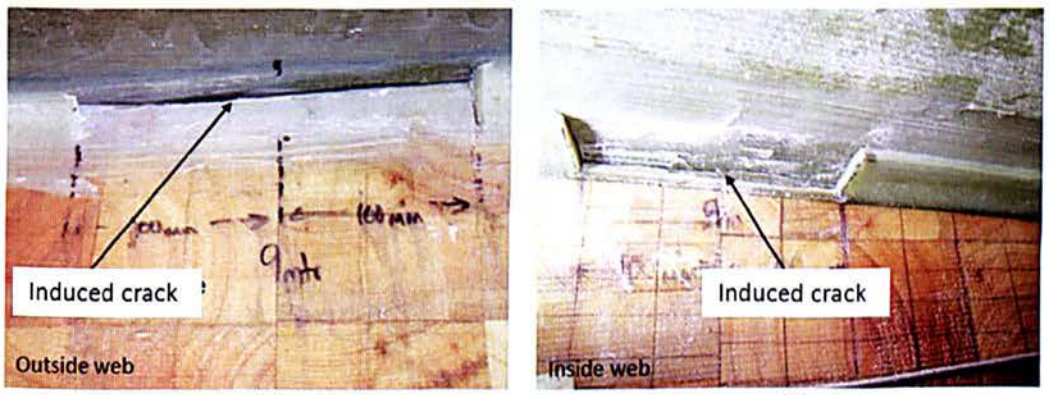

Fig. 6.8. Induced crack of 0.2mm (a) outside shear web box (b) inside shear web box.

6.3.2 Extending the induced crack to 1m

The blade structure sensitivity to crack propagation was studied by extending manually the 0.2m crack to 1m. The centre of de-bonded crack was kept at 9m from the blade root and it was extended symmetrically from both sides as shown in Figure 6.9. The view of the crack from inside the shear web box is shown in Figure 6.10. Also the induced crack extended into the web as shown in Fig. 6.11.

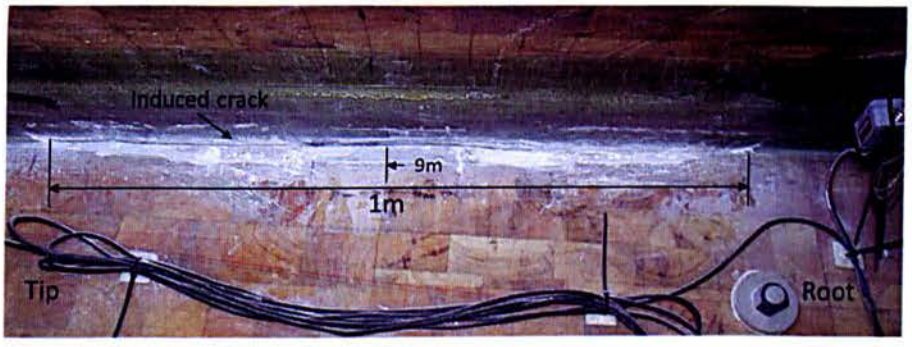

Fig. 6.9. View from outside shear web box, 1m induced crack.

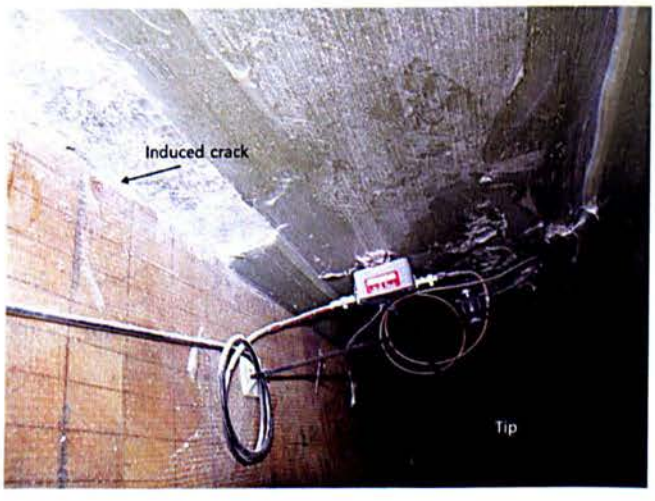

Fig. 6.10. View from inside shear web box of 1m crack.

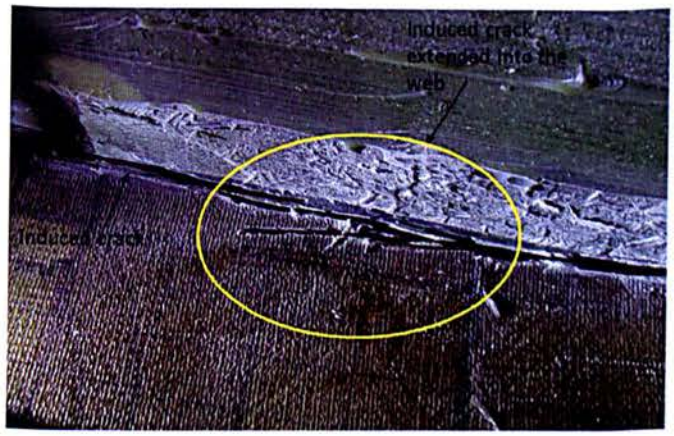

Fig. 6.11. Induced crack extended into web.

6.4 Fatigue testing

6.4.1 Fatigue test results before crack insertion

The test conditions and results before inserting the crack are shown in Table 6.1 where the target microstrain at SG2 is set at 1478με, reaching 50% bending moment of 5000kNm at the root which is predicted from the calibration pull test described in Chapter 5. After 5,241 cycles a visual inspection of the blade has been performed and three cracks have been detected. The first cracks appeared at 34m in the TE where a 450mm adhesive joint failure occurred as shown in Figure 6.12. The second crack of a length of 300mm occurred at adhesive joint in the TE at 31m from the root as shown in Figure 6.13. The third crack formed at adhesive joint in the LE at 28.36m as shown Figure 6.14.

The application of acoustic emission for non-destructive testing of materials, typically takes place between 100 kHz to 1 MHz. Contrary to ultrasonic testing. AE are commonly defined as transient elastic waves within a material, caused by the release of localized stress energy within the material during failure or loading, rather than actively transmitting waves. Hence, an event source is the phenomenon which releases elastic energy into the material, which then propagates as an elastic wave. AE tools collect these waves after they have travelled through the material. Rapid stress-releasing events generate a spectrum of stress waves starting at 0 Hz, and typically falling off at several MHz. In a material under active stress, such as our wind turbine blade, transducers mounted in an area can detect the formation of a crack at the moment it begins propagating. A group of transducers are used to record signals,

and then locate the precise area of their origin by measuring the time for the sound to reach different transducers.

In the current test the acoustic emission sensors recognised damage around the same regions as the visual inspection found. After 58,665 cycles the blade has been inspected visually and neither new crack was found nor any existing crack propagated. The first fatigue test stopped after 65,217 cycles. In the first fatigue test where no crack induced, the original cracks did not propagate more than what has been reported.

Table 6.1 Fatigue test results for the blade before crack insertion

% of BM nominal value	Cycles ±200	Cumulative cycles	Estimated microstrain at SG2 (με) ±0.5%	Frequency (Hz)	Crack distance from root (m)	Crack length (mm)	Location	Amplitude of resonance mass (mm)
25	2,217	2,217	740	0.43	-	-	-	77
50	3,024	5,241	1478	0.56	28.36 31 34	640 300 450	LE TE TE	154
50	12,096	17,337	1478	0.56	-	-	-	154
50	14,112	31,449	1478	0.56	-	-	-	154
50	14,112	45,561	1478	0.56	-	-	-	154
50	13,104	58,665	1478	0.56	-	-	-	154
50	6,552	65,217	1478	0.56	-	-	-	154

Fig. 6.12. Formation of a 450mm crack on TE at 34m from root.

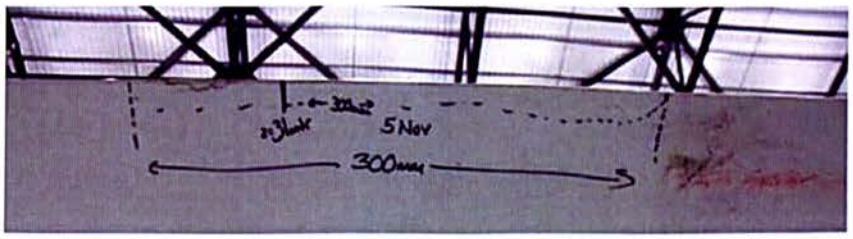

Fig. 6.13. Creation of a crack on TE at 31m from the root.

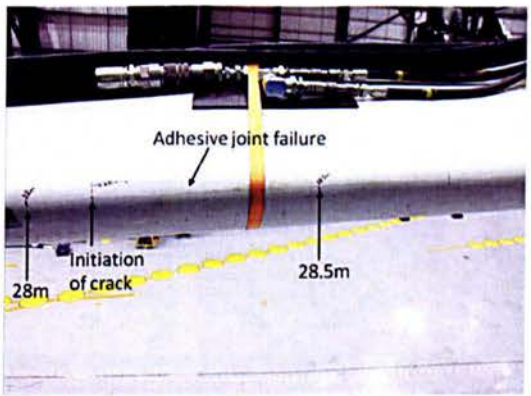

Fig. 6.14. Crack formation at 28.36m from the root.

The strain readings at the first cycle along the uncracked blade from 30 strain gauges are shown in Figure 6.15, where the highest microstrain readings are experienced between 35-65% of the blade length from the blade from root.

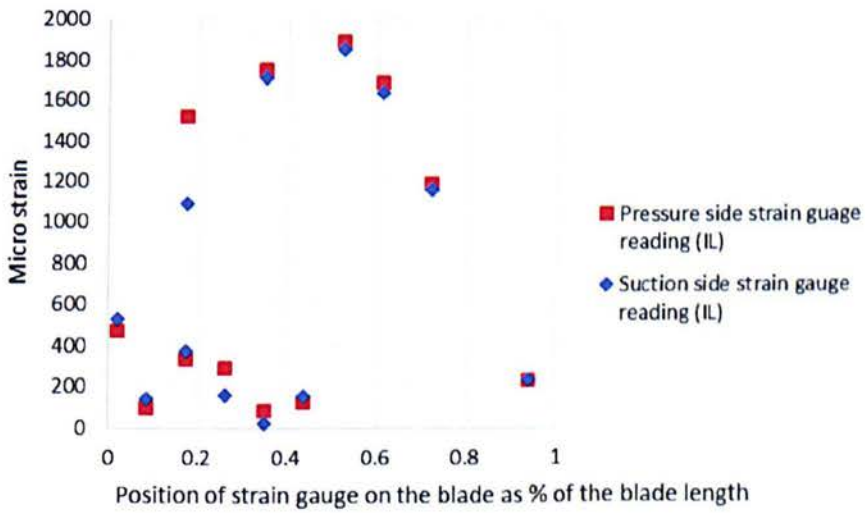

Fig. 6.15. Strain gauge reading at the first cycle along the uncracked blade.

Strain gauge results for the pressure and suction sides (on the skin) at the first cycle are shown in Figure 6.16, where the strain readings along the blade vary between 236 με to

1891με. The highest strain reading is at 52% of the overall length. The results are almost identical on the pressure side and suction side, apart at 17% blade location where pressure side shows a reading of 423με more than suction side. This indicating the strain gauge SG9 on the pressure side is faulty and it is reading should be ignored.

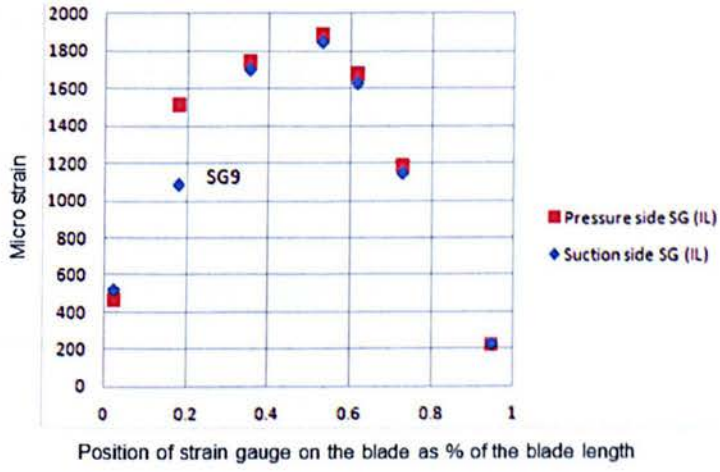

Fig. 6.16. Strain gauge reading on pressure and suction side at the first cycle.

Strain gauges SG21 to SG30 are attached to the shear web on TE side at ±45° and located from 4m to 20m. The readings from these gauges at the first cycle are shown in Figure 6.17, where the strain readings along the blade vary between 24.5με to 378με in the first half of the blade length from the root. The maximum strain reading when the blade is fatigued in flapwise is at SG23 and SG24, located at 17.5% of the blade length.

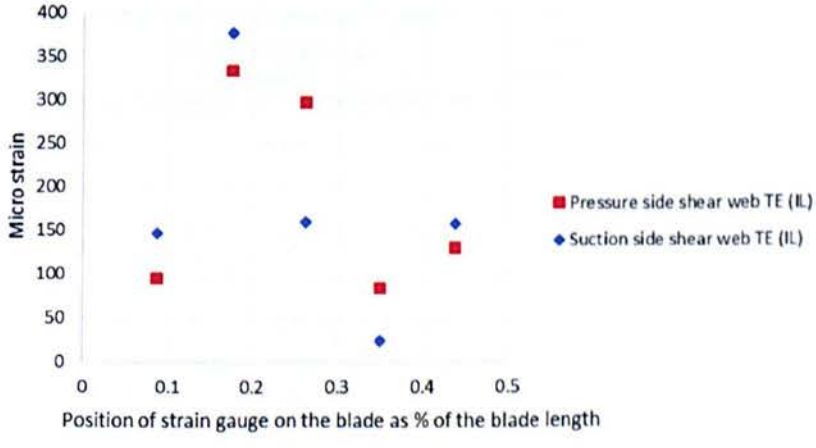

Fig. 6.17. SG readings on the shear web on TE side at the first cycle at initial loading.

6.4.2 Fatigue test results for blade with 0.2m induced crack

The test conditions and results for the blade with 0.2m induced crack are shown in Table 6.2. Initially 50% bending moment of 5000kNm at the root were applied which resulted in 1523με at SG2. The strain at this location has increased from 1478με before the insertion of crack showing 3% increase. A visual inspection has been done after 8,063 cycles to check if any existing cracks have been propagated or new ones developed. No changes to the existing cracks or to the induced crack at 9m were detected. Later on the visual inspection was repeated after 26,851 cycles. A pre-existing crack at ≈32.96m extended by 190mm in the middle of the blade as shown in Figure 6.18 with the overview image of the two cracks found. Figure 6.19 shows a close inspection of new cracks found at ≈32.83m which propagated for 110mm and 40mm on the middle cross section at this point. The next visual inspection is carried out after 39,934 cycles where the applied nominal bending moment value has been increased to 70% of the maximum target bending moment. At this stage the blade is shown in Figure 6.20. The visual inspection showed an existing crack at ≈32.96m propagated 15mm along the blade longitudinal direction at the TE midpoint as shown in Figure 6.21. Finally a visual inspection was made after 62,110 cycles and no further crack formation or propagation was observed and the induced crack stayed unchanged at its original length.

Table 6.2. Fatigue test results for the blade with an induced crack of 0.2m

% of BM nominal value	Cycles ±200	Cumulative cycles	Estimated microstrain at SG2 (με) ±0.5%	Frequency (Hz)	Crack distance from root (m)	Crack length (mm)	Location	Amplitude of resonance mass (mm)
50	2,923	2,923	1523	0.56	-	-	-	158
50	5,140	8063	1523	0.56	-	-	-	158
47	10,281	18,344	1478	0.56	-	-	-	154
50	8,507	26,851	1523	0.56	≈32.96 ≈32.83 ≈32.83	190 110 40	TE-Mid TE-Mid TE-Mid	158
50	806	27,657	1523	0.56	-	-	-	158
70	12,277	39,934	2132	0.56	≈32.96	15	TE-Mid	260
70	12,096	52,030	2132	0.56	-	-	-	260
70	10,080	62,110	2132	0.56	-	-	-	260

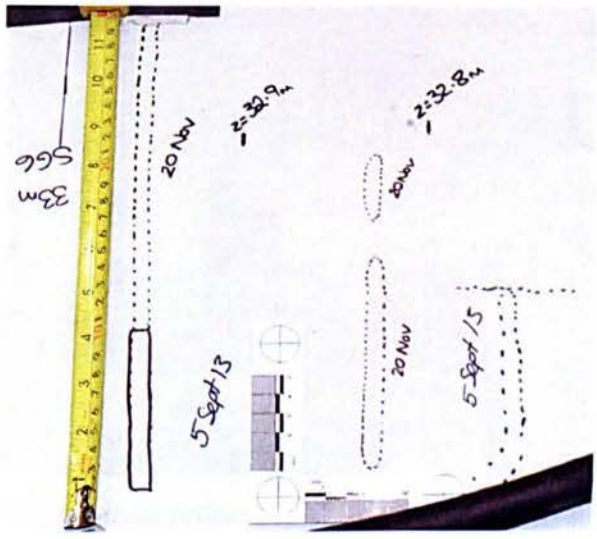

Fig. 6.18. Propagation of existing crack at 32.96m after 26,851 cyclic loading.

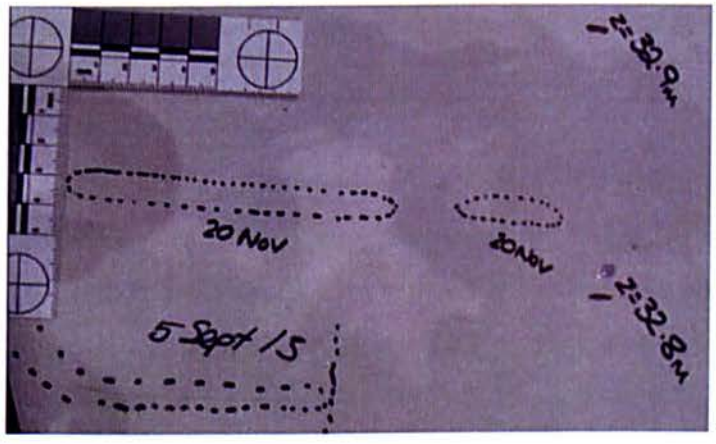

Fig. 6.19. Formation of hair line cracks at 32.8m after 26,851 cyclic loading.

Fig. 6.20. LE visual inspection after 39,934 cycles at applied bending moment of 70% of the maximum target bending moment.

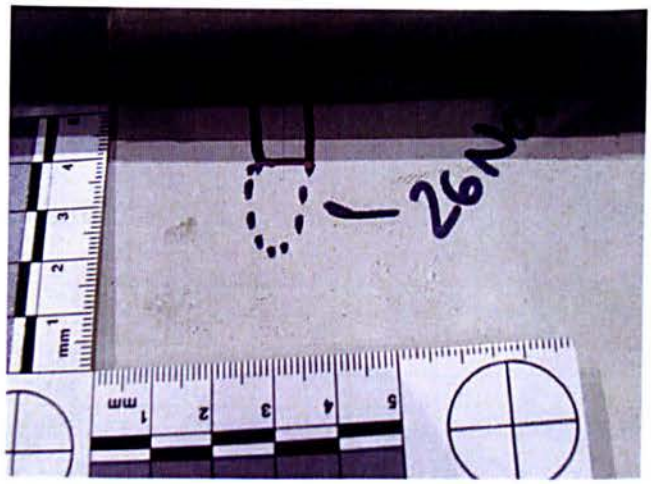

Fig. 6.21. 15mm crack propagation after 39,934 cycles at ≈32.96m.

6.4.3 Fatigue test results for blade after extending the crack to 1m

The test conditions and results for the blade after extending the inserted crack to 1m are shown in Table 6.3.

Initially 70% bending moment of 5000kNm at the root were applied which resulted in 2135με at SG2. The strain at this location remained nearly unchanged close to 2132με before the extension of crack from 0.2m to 1m,. Visual inspections of the blade have been done after 3,967 and 16,781 cycles and 18,764 cycles to check if any existing cracks have been propagated or new ones developed. No changes to the existing cracks or to the induced crack at 9m were detected.

The load has been increased to 90%, 100%, 105% and 110% of the blades nominal target BM value. For these cases to save time the blade first mode natural frequency is obtained using NaREC software rather than doing a modal test while the blade was under cyclic loading.

Weights have been added to the saddles to reduce the saddle stroke. The reason behind adding weight to the saddle is due to the increase of the load to 70% of the blade target bending moment. At this stage the saddle amplitude resonance mass was close to its maximum limit. Adding dynamic mass will reduce the resonance amplitude while the required SG value at SG2 kept unchanged. Using the optimisation programme at NaREC the mass on the saddle at 30.05m has increased to 150kg on each side of the saddle and at 35.05 increased to 75kg on each side.

Table 6.3. Test parameters of 1m induced fracture

% of BM nominal value	Cycles ±200	Cumulative cycles	Estimated micro strain at SG2 (με) ±0.5%	Frequency (Hz)	Crack distance from root (m)	Crack length (mm)	Location	Amplitude of resonance mass (mm)
70	3,967	3,967	2130	0.551	-	-	-	219
70	12,814	16,781	2135	0.551	-	-	-	219
70	1,983	18,764	2135	0.551	-	-	-	219
90	5,970	24,734	2737	0.535	-	-	-	234
90	4,603	29,337	2737	0.535	-	-	-	234
100	4,451	33,788	3040	0.524	-	-	-	230
105	94	33,882	3211	0.524	-	-	-	250
100	894	34,776	3040	0.497	8.5 9.2 9.5	35.83 - -	IW*, OW IW IW, OW	174
100	12,430	47,206	3040	0.497	9.5 9.1 8.5	DD** DD DD	IW, OW IW IW, OW	174
105	357	47,563	3201	0.497	-	DD	-	220 at 30.05m 165 at 35.05m
110	9,199	56,762	3380	4962	8.5 9.5	DD DD	IW, OW IW, OW	220 at 30.05m 165 at 35.05m

* IW= Inside the web, OW= Outside the web
** DD= Detailed discussion in the report

The added mass to the saddle at 30.05m has increased to 200kg on both sides of the saddle and at 35.05m has increased to 100kg on both sides of the saddle when the load increased to 70% of nominal target BM. For reaching to 90% of the nominal BM value, the dynamic mass of the saddle at 30.05m increased to 325kg on both sides of the saddle and at 35.05m increased to 150kg on both sides of the saddle. For reaching to 100% of the nominal BM value, mass of the saddle at 30.05m increased to 400kg and at 35.05m increased to 200kg on both sides of the saddle. Finally to reach 110% of the nominal BM value, mass of the saddle at 35.05m increased to 400kg on both sides of the saddle and at 30.05m remained unchanged.

A visual inspection of the blade after 34,776 cycles showed a number of cracks around the 1m extended induced crack at distance 9m from the root. Inside the web box at 8.5m from the root, two delaminated areas each at 10mm in width were detected. The delamination connected to the web has a delamination length of 83mm and the delamination furthest away from the web has a length of 35mm as shown in Figure 6.22(a). At 8.5m the induced crack through the adhesive joint has propagated from the corner of the induced crack and extended through the plies causing delamination on the web lip indicating that the crack plane has been

deviated from its original path; see Figure 6.22(b). At 9.5m delamination has occurred at the corner of the induced crack as shown in Figure 6.23. Figure 6.24 shows delamination at 9.1m where it was the location of the corner of 0.2m induced.

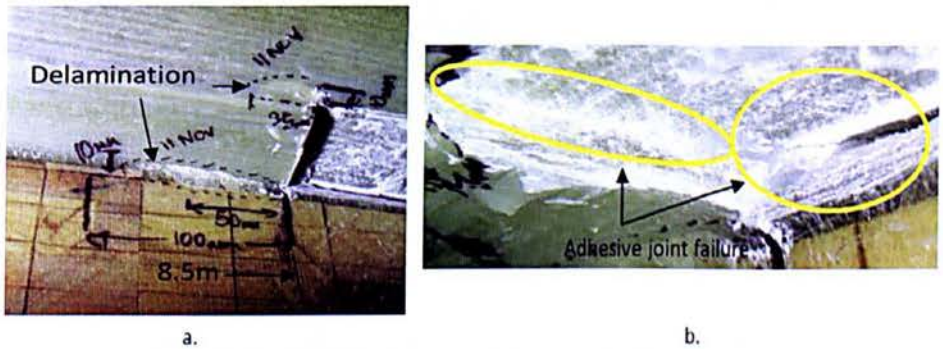

Fig. 6.22. At 8.5m from the root and inside the web box (a) Delamination (b) Adhesive joint failure.

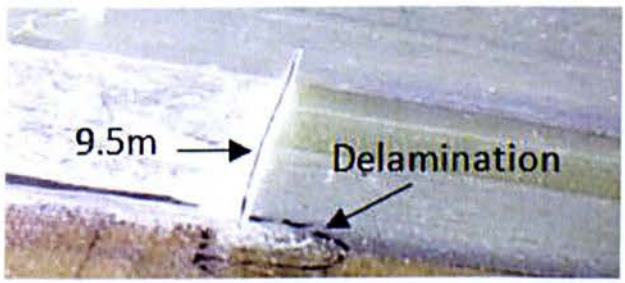

Fig. 6.23. Delamination inside the web box at 9.5m.

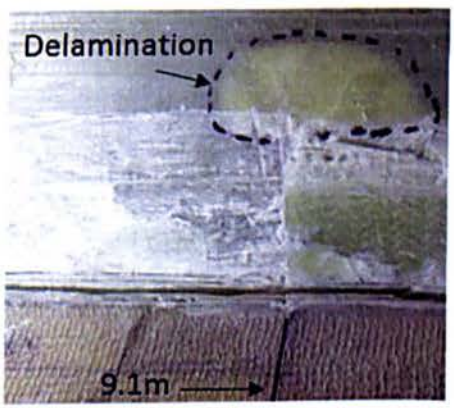

Fig. 6.24. Delamination inside the web box at 9.1m.

Outside the web box experiences adhesive joint failure at 8.5m as shown in Figure 6.25 indicating that crack has propagated all the way through the web. At 9.5m the blade experiences multiple local buckling under compression and sandwich debonding going into the web as shown in Figure 6.26.

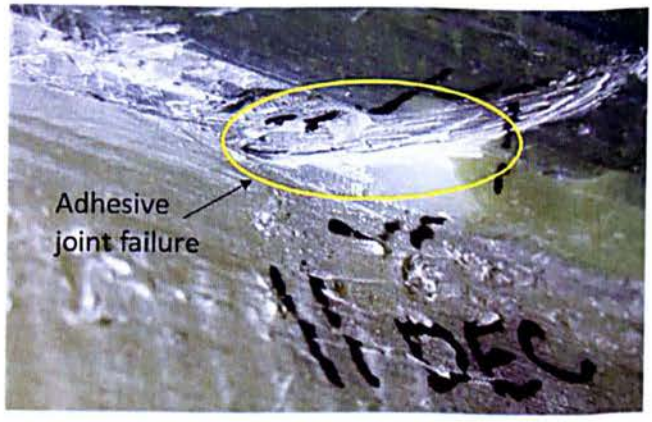

Fig. 6.25. Adhesive debonding outside the web box at 8.5m.

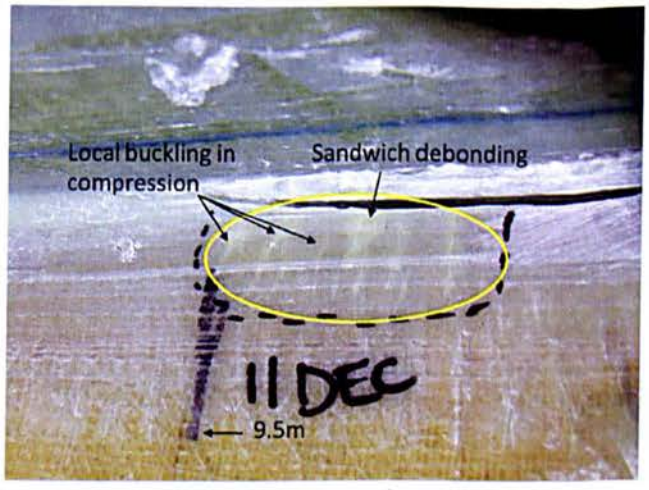

Fig. 6.26. Local buckling under compression and sandwich debonding outside the web box at 9.5m.

A visual inspection of the blade after 47,206 cycles showed a number of damage around 9m in the 1m extended induced crack. At 8.5m inside the web box, there are two areas of delamination each 10mm in width. The delamination connected to the web, where the delamination length extended by 25mm as shown in Figure 6.27. At 8.9m inside the web box delamination is visible at the corner of the original 0.2m induced crack; see Figure 6.28. Inside the web box at 9.5m delamination has extended from the corner of the induced crack to the lip of the web; see Figure 6.29.

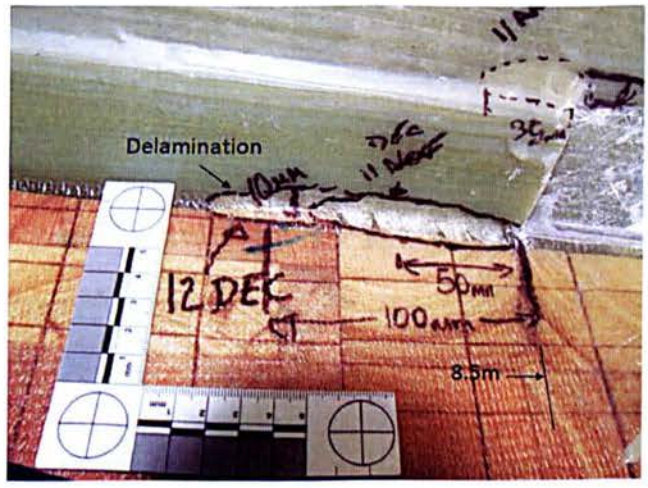

Fig. 6.27. Delamination inside the web at 8.5m extended by 25mm.

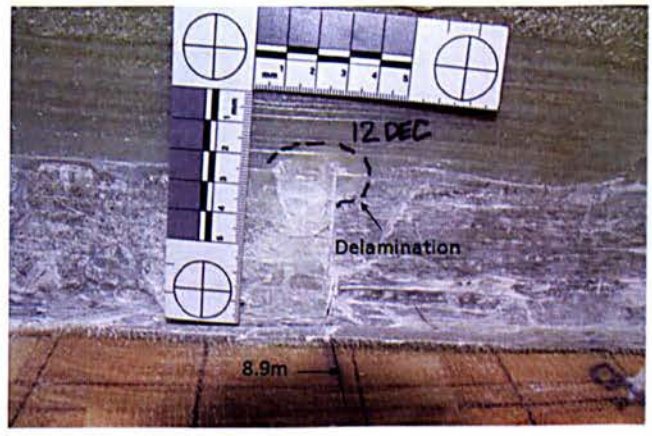

Fig. 6.28. Delamination inside the web box at 8.9m.

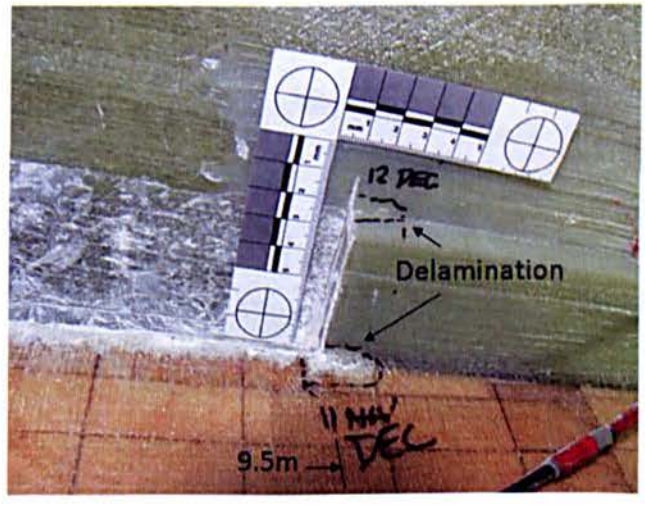

Fig. 6.29. Delamination inside the web at 9.5m.

Figure 6.30(a) shows outside the web box at 9.5m with an overview of the damaged areas. The blade experiences multiple local buckling under compression and sandwich debonding going into the web. Figure 6.30(b) is the magnified view of the damaged area at 9.5m and Figure 6.30(c) shows the magnified view of the damaged area at 9.3m. Figure 6.31 shows the propagation of the crack in adhesive joint at 8.5m by 100mm.

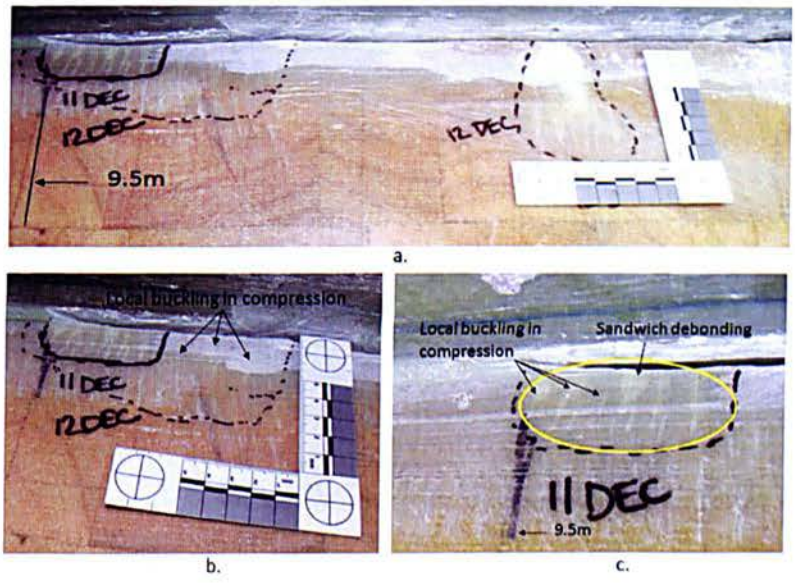

Fig. 6.30. Outside web at 9.5m (a) Overview of local buckling under compression and sandwich debonding (b) Magnified view of damage at 9.5m (c) Magnified view of damage at 9.3m.

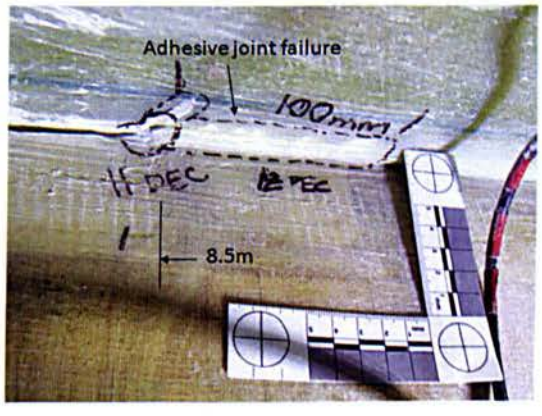

Fig. 6.31. Crack propagation through adhesive joint outside the web at 8.5m.

A visual inspection of the blade after 56,762 cycles showed that many of the cracks have extended along the web within the 1m induced crack area as illustrated in Figure 6.32. Figure 6.33 shows at 9.5m inside the web delamination has begun to occur within the web of the wind turbine blade.

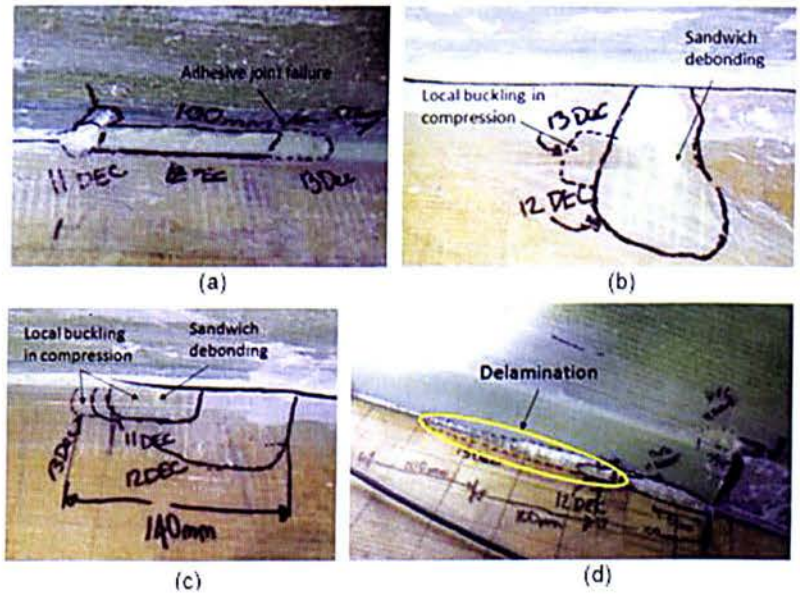

Fig. 6.32. Crack propagation within the web; (a) Adhesive joint failure outside the web, (b) and (c) Local buckling under compression outside the web, (d) Delamination inside the web.

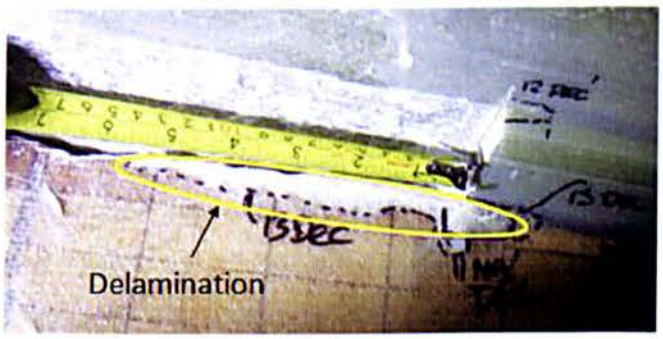

Fig. 6.33. Delamination inside the web.

Figure 6.34 shows the strain experienced by the blade at SG2 at different stages of the fatigue testing versus number of cycles. Figure 6.35 shows variation of strain at SG2 versus percentage of applied bending moment experienced by the blade at all stages of the fatigue testing. As evident in Figure 6.35, the strain versus % of applied moment relationship remains linear, implying that the induced damage has not deteriorated the structural integrity of the blade yet.

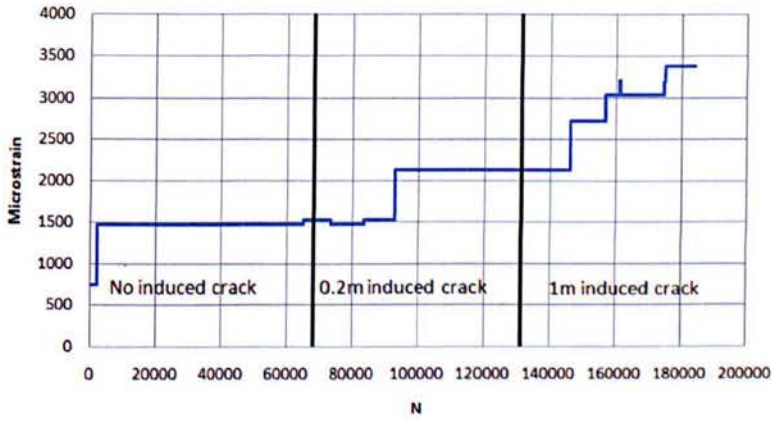

Fig. 6.34. SG2 reading versus number of cycles throughout fatigue testing.

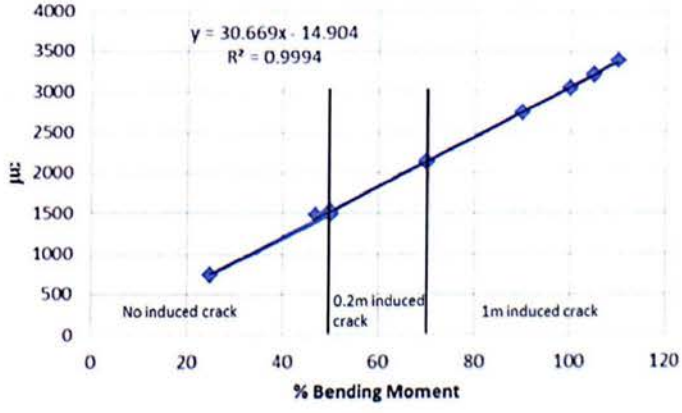

Fig. 6.35. Variation of strain at SG2 with BM throughout the complete stages of fatigue testing.

6.5 Conclusion

The blades are one of the most critical components of the wind turbines and the structural integrity of the whole wind turbines depend on the blade. Therefore, they have to be tested in order to ensure that their specifications are consistent with the actual performance of the blade. It must be verified that the blade can withstand both the ultimate loads and the fatigue loads to which the blade is expected to be subjected during its design service life. Testing of the wind turbine blades statically and dynamically helps in improving the designs and the manufacturing processes.

In Chapter 5 in the calibration pull test the strain-bending moment relationship of the blade has been identified according to the target bending moment which the blade expected to

experience in its service life. These data were used for monitoring the applied load in the fatigue tests as described in this chapter.

Acoustics emission (AE) as one of the most effective NDT technique was used to immediately indicate the location and onset of damage during loading. This allowed the investigation into the causes and growth of the various damage types. AE also helped the test operators to control the test more efficiently. The AE data can also warn of unwanted damage such as localised crushing at loading points.

Before start of calibration and fatigue testing the blade has two areas of defects at 4% and 71% of blade length. After cyclic loading the blade 184089 times the areas that experienced most damage and fracture is between 62-74% of the blade length from the root, but there was no damage found within the web.

When a 0.2m crack induced at 9m by debonding the web from spar cap, the crack did not propagate at 50% of the target bending moment. When the load increased to 70% of target bending moment, some damages have been detected on the pressure side of the blade. However the 0.2m crack did not propagate under these conditions and up to 62,110 cycles.

Finally the crack at 9m from the root has been extended to 1m. The crack began to propagate when the applied load exceeded 100% target bending moment. The blade experienced delamination around the crack tip of the induced crack at the C web, adhesive joint failure on the outside web, compression failure and sandwich debonding on the inside web, and delamination was visible on the web just below the induced crack. These findings indicate that there have been high stresses around 9m web due to the induced crack.

The understanding of how the damages start up (for example by delamination) is very essential for the strength of the blade and very difficult to decide in a full scale test even though the location of the damages is known.

6.6 References

[1] BSI, BS EN61400-23 (2005) Wind turbine generator systems - Full scale structural testing of rotor blades International standard.

7

Improvement of Joint Design in Wind Turbine Blade

7.1 Introduction

The wind turbine blade is a very challenging problem in terms of choice of materials, design and engineering as they are subjected to both static and dynamic lift, gravitational loads and drag during an approximately 20 year life cycle [1]. The rotor blade is designed with different thickness and cross-sections along its lengths and this is because the speed of a long blade shows variations in its magnitude from the tip of the blade to the rotor hub and leads to different aerodynamics requirements.

Adhesive joining is among the most important joining techniques used for bonding composite structures. Joint design technology has become a main factor in structural integrity to design composite sub-structures in wind turbine blades for strengthening.

Adhesive joining and failure has been extensively investigated in the literature. Many researchers [2-7] have shown that transverse stitching can significantly improve both mode I and mode II delamination toughness of laminated composites. Several studies have also

shown that transverse stitching the overlap of single lap joint may remarkably increase fatigue life [8].

Tong *et al.* [9,10] investigated adhesively bonded composite lap joints with transverse stitching experimentally and numerically. They showed that the ultimate tensile strength of stitched single lap joints is 40% greater than unstitched specimens and axial displacement of stitched specimens is 25% greater than unstitched specimens. The observed failure modes of the stitched specimens were fibre breakage and fibre pull out.

Yudhanto *et al.* [11] experimentally investigated tensile properties, damage initiation and development in stitched carbon/epoxy composites subjected to tensile loading. Modified-lock stitch pattern is adopted, and stitch density is varied. Effect of stitch density on the mechanical properties is assessed, and it is found that stitched 3×3 modestly improves the tensile strength by 10.4%, while stitched 6×6 reduces the strength by only 1.4%. In stitched 3×3 cases, the strength increase is mainly due to an effective impediment of edge-delamination (see Figure 7.1).

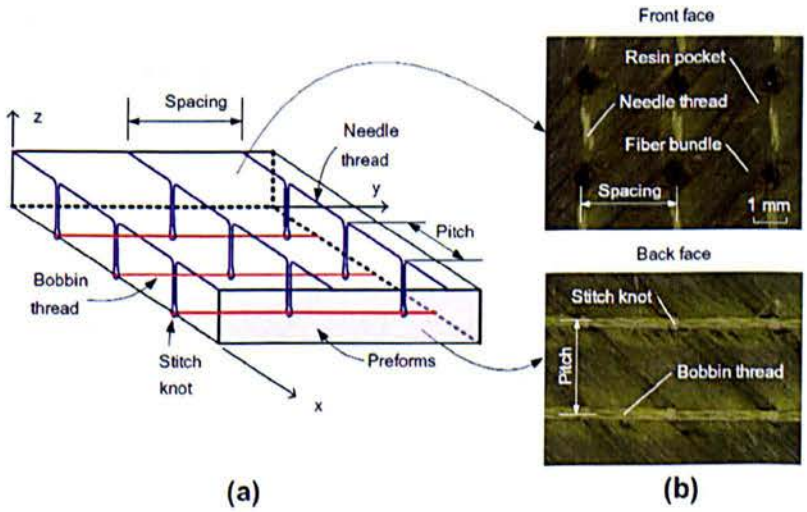

Fig. 7.1. (a) Modified-lock stitch pattern, (b) top and back faces of stitched composites [11].

Tan *et al.* [12] experimentally studied the damage failure and behaviour of stitched composites under compression after impact (CAI) loading. Experimental findings show that stitched composites have higher CAI failure load and displacement, which corresponds to higher energy absorption during CAI damage, mainly attributed to greater energy consumption by stitch fibre rupture.

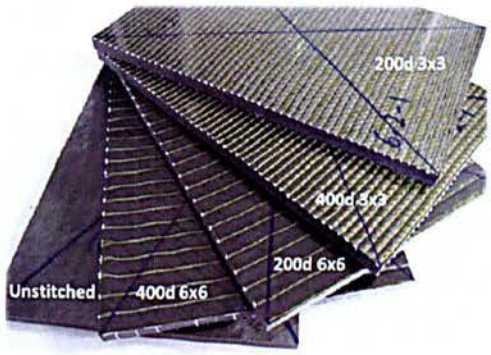

Fig. 7.2. (a) Unstitched and stitched composite specimens [12].

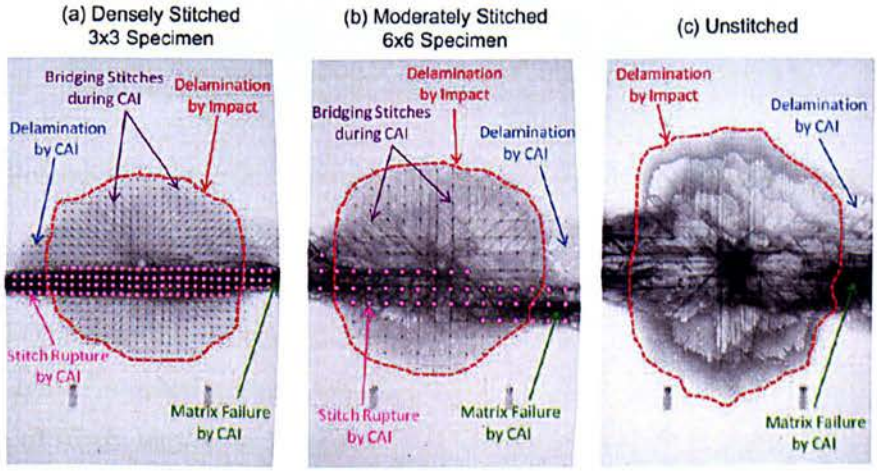

Fig. 7.3. X-ray radiographs of CAI specimens impacted at 40.6 J [12].

Tan *et al.* [13] also investigated experimentally the damage progression and failure characteristics of stitched composites under out-of plane loading. They showed damage progression can be identified in three stages: (i) damage initiation, (ii) damage propagation and (iii) final failure. Their results show that damage initiation occurs at a lower load in stitched composites due to the presence of resin-rich regions which act as crack initiation sites. During damage propagation, stitching becomes highly effective in suppressing delamination growth, resulting in stitched laminates having much smaller delamination area compared to unstitched laminates, and the rate of delamination growth being inversely related to stitch density. In final failure stage a sharp drop in the load–displacement curve occurs. However, the final failure load increases with increasing stitch volume fraction. The final failure mechanism in unstitched and moderately stitched composite is mainly delamination

failure; while densely stitched composite failed by indenter penetration comprising of in-plane fibre fracture and matrix crushing.

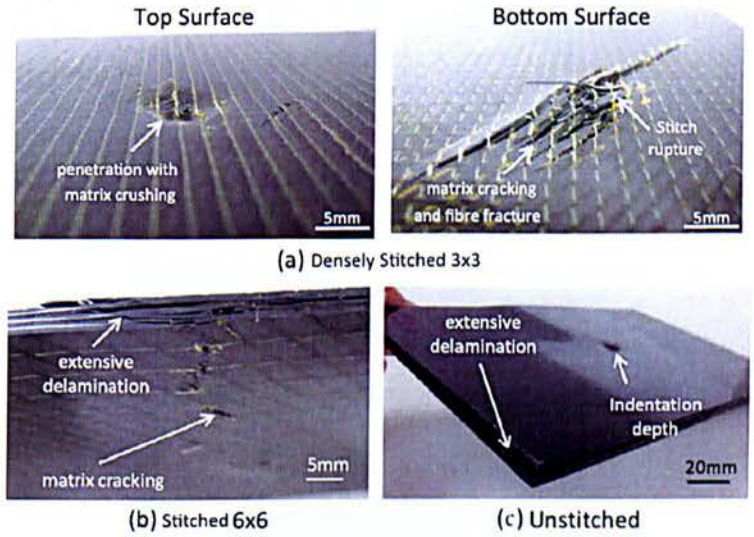

Fig. 7.4. Post-mortem examination of (a) densely stitched 6×6 laminates (b) stitched 3×3 laminates and (c) unstitched laminates [13].

Tan *et al.* [14] studied the effect of stitch density and stitch thread thickness on low-velocity impact damage of stitched composites. According to their results, the absorbed energy is independent of stitch density and thread thickness, the proportion of energy consumption for damage mechanisms like delamination, matrix cracks and stitch deboning are different for laminated composites stitched with different stitch parameters.

Wood *et al.* [15] conducted stitched DCB experiments using three types of stitch distribution (see Figure 7.5) with the same stitch density, and they showed the stitch distribution plays an important role in determining the steady state strain energy release rate. Also they revealed that for stitched specimens with identical stitch densities but different stitch distributions, there exist significant variations in critical strain energy release rates, G_{IC}.

Lopresto *et al.* [16] studied low-velocity impact tests on stitched CFRP laminates of various thicknesses. The overall force–displacement behaviour, first failure load, penetration, indentation and damage extent of these laminates were studied. Their results show that the presence of stitches did not affect substantially the material behaviour in terms of force-displacement curve, first failure load, and indentation. However, the stitched laminates exhibited penetration energy about 30% lower than their 2D equivalent.

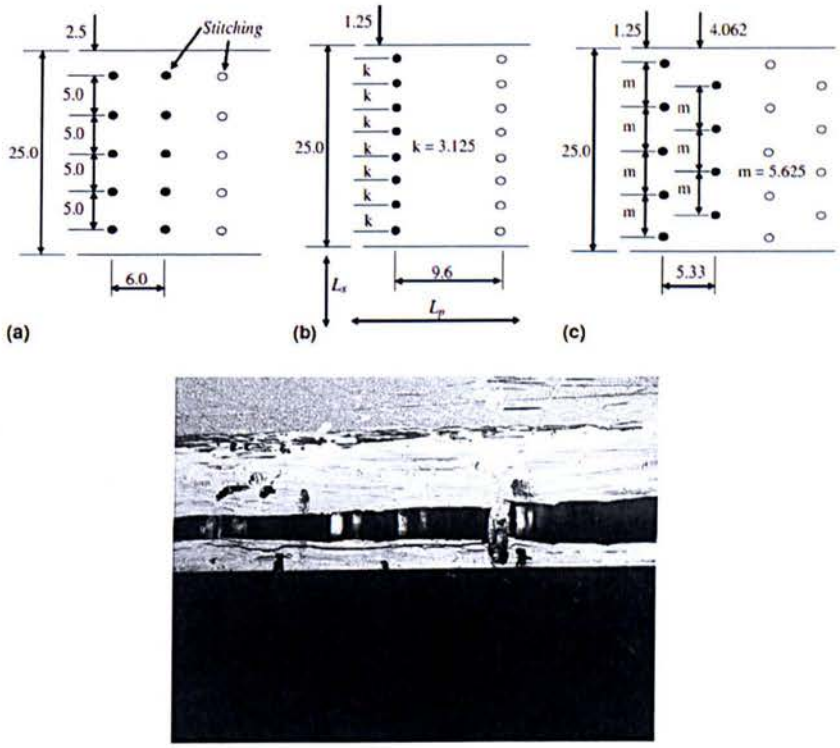

(d)

Fig. 7.5. (a) Plain short pitch, (b) Plain long pitch and (c) zigzag and (d) 5c and 5d. Photographs displaying crack wake for stitched TDCB specimens [15].

Potluri *et al.* [17] developed stitch-bonded sandwich structures (see Figure 7.6) using commercial close-cellular core and woven broadcloth. They showed firstly through the thickness stitching reduces the bottom skin debonding area quite significantly. Secondly, both the top and bottom skin failure loads increase with stitch density. Finally, the stiffness of the sandwich panels, up to the top skin failure increases with increase in stitch density.

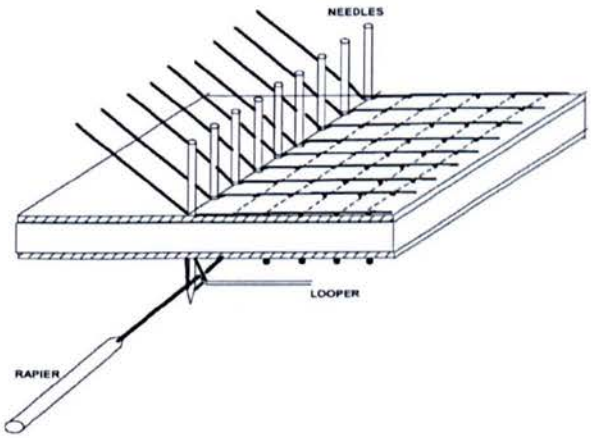

Fig. 7.6. Multiple-needle sewing machine Illustration for sandwich composite structures [17].

Chun *et al.* [18] showed that the transverse and in-plane shear moduli and Poisson's ratios for UD fabric composites are increased by decreasing stitch line space and increasing the thickness of the UD fabric composites. They also showed the longitudinal modulus is decreased with stitching because of fibre misalignment and formation of fibre depleted regions, later filled with resin and by spreading of fibres due to the stitches.

Hosur *et al.* [19] studied response of stitched/unstitched woven fabric carbon/epoxy composite laminates subjected to high velocity impact loading. Their results showed that the ballistic impact damage was well contained within the stitch grid in case of stitched laminates. However, ballistic limit was higher for the unstitched laminates.

Mouritz [20] published a comprehensive review into polymer composite laminates reinforced in the through-thickness direction with z-pins. Research into the manufacture, microstructure, delamination resistance, damage tolerance, joint strength and mechanical properties of z-pinned composites is described. Benefits of reinforcing composites with z-pins are assessed, including improvements to the delamination toughness, impact damage resistance, post-impact damage tolerance and through-thickness properties. Other experimental researches [21-25] have shown that z-pinning reduces the amount of delamination damage caused by impact events from low energy objects, ballistic projectiles and high-speed hailstones. However, few researches have been performed to determine the performance of z-pins and stitching to increase the mechanical properties of box-beam and T-joint [26-30], which are one of the most common joint designs.

A typical blade structure of large MW-scale wind turbines is shown in Fig. 7.7. Depending on the manufacturer, the spar structure of the blade varies considerably but it is typically in the form of a box-beam or one or more webs, which integrated to aero-shell structure using a joining method.

In this chapter stitching and bonding methods will be used to join spar cap to the aerofoil shell and to shear webs as shown in Figure 7.7. In order to achieve this, the laminated composite beams were stitched before curing process or it is adhesively bonded after curing. Four different joints of bonded T-joint; stitched T-joint; bonded box-beam and stitched box-beam were studied. These specimens were tested under quasi-static loading condition to compare the strength of joint of adhesive bonded and stitched joints. Experimental results

indicated that stitching significantly improve failure load and interlaminar fracture resistance of the joints and they have potential application for use in wind turbine blade construction and other composite structures.

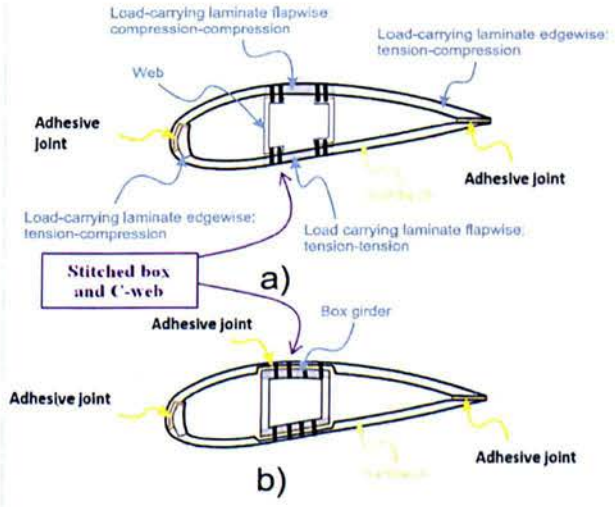

Fig. 7.7. Schematics of the cross-section of two common designs of wind turbine blades: (a) Using load-carrying laminates in the aero-shell and webs for preventing buckling and (b) Using a load-carrying box [31]. Note stitches added to the original referenced diagram.

7.2 Specimen preparation and testing

7.2.1 Mechanical characterisation

The mechanical characteristics of unidirectional glass/epoxy were obtained in Chapter 3. The tests were tensile [32]; shear [33] and fibre volume fraction [34]. A summary of the findings for tensile modulus, shear modulus, Poisson's ratio, tensile and compression strength in fibre and normal to fibre directions and fibre volume fraction are summarised in Table 3.1.

7.2.2 Specimen manufacturing

Four different joint designs of (i) Bonded T-joint using two types of epoxy adhesives; (ii) Stitched T-joint using synthetic fibres (glass, carbon or Kevlar); (iii) Bonded box-beam using two types of epoxy adhesives and (iv) Stitched box-beam with synthetic fibres (glass, carbon or Kevlar) were studied in this work. The material characteristics used for the work in Chapter 7 are the same materials used in previous chapter (see details in Appendix A). The needle used for stitching has a diameter of 2mm and sewing thread has a diameter of 1mm.

Box-beam joint using adhesive or stitches

One of the common blade designs is attaching the aero-shell to the box girder as shown in Figure 7.7. As a result the first type of joint investigated is bonding a box section to a beam using epoxy adhesives. The mould design for this joint consists of three parts as shown in Figure 7.8. Part A is the centre box in which 14 layers of GFRP is laminated around the box with total thickness of 5mm after curing. Parts B and C were designed to lock part A. In this joint the beam is accommodated with a 5mm gap between the blocks B and C to create a 5mm thick beam. Note that parts B and C are interlocked with each other to avoid any movement during curing process. A PTFE film was placed between the box and the beam before curing making unconnected box and beam. The depth of all box-beam joints are 25mm.

The next joint is stitched box-beam that the box stitched to beam before curing process using the same mould as shown in Figure 7.8. There are stitching slots in the A and B blocks that will allow a needle to pin through the layers, and then before curing process the hole will be covered up by a bung. Different stitch patterns as will be explained later were used.

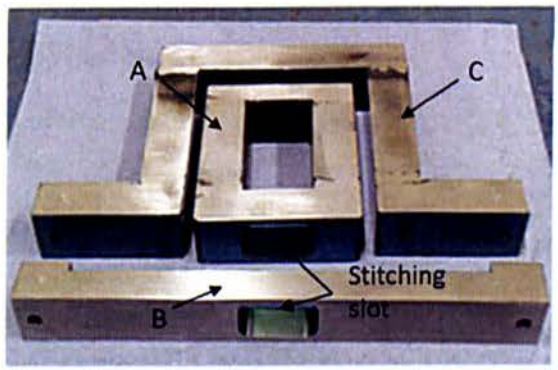

Fig. 7.8. The mould assembly of box-beam for adhesive bonded and stitches joint.

T-joint using adhesive or stitches

The next design is a T-joint typically found in many blade structures. The mould design for this joint is shown in Figures 7.9. The mould consists of three parts: the base (A), female and male web blocks (B and C). The parts interlock with each other to allow a gap of 5mm at the base and 5mm gap down the middle resulting in a 5mm thick web section.

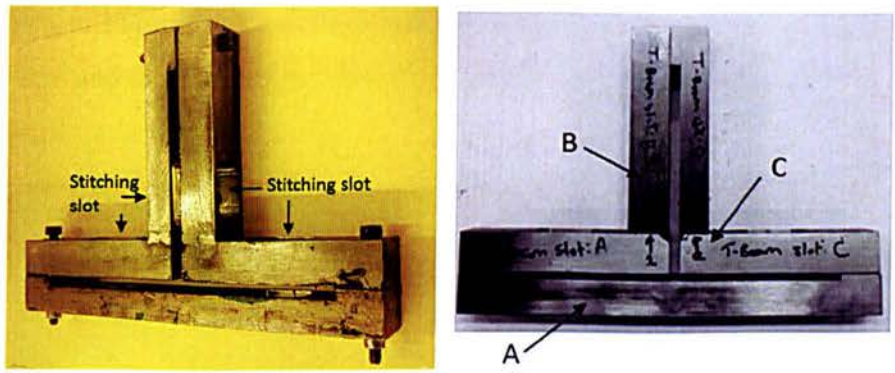

Fig. 7.9. The mould assembly of T-joint stitched to composite beam before curing process.

Using the above mould two types of bonded and stitched T-joints have been made. For the bonded T-joint a PTFE film was placed at 2.5mm in the middle of the flange in block A. Then after curing the two pieces were bonded together using epoxy adhesive with a bondline thickness of 0.5mm. For stitching specimens slots have been put in place to allow stitching of the flange between A-B and A-C sections. In the re-design of this joint stitches were used in the web between B-C. The depths of all T-joints are also 25mm.

7.3 Machining of the moulds and lamination

Before beginning the lamination process the moulds were checked and the basic finishing operations are performed. The lamination process would be performed on the moulds and thus the inner surfaces of all moulds are thoroughly cleaned by acetone to improve adhesion. The inner surfaces were then covered by heat resistant tape. The required 14 layers are marked and cut from the prepeg roll. The GFRP layers were then laid layer by layer on the mould and after every layer a roller was used to remove the air trapped between the plies. In the case of adhesive bonded T-joint, 7 layers were stacked on one side of the mould and the remaining seven layers on the other side. An additional 7 layers were stacked at the bottom part of block A to make a 2.5mm thick beam. After curing the beam is bonded to the T-section and the joint cured in the oven.

In the case of stitched specimens, upon the completion of lay-up of GFRP on all the parts of the mould, they were fitted together and the stitching was carried out on the T-joint and the box-beam specimens. A steel needle with fibres thread was run through the lay-up of GFRP material at through the slots in the moulds. Initially the stitching was carried out in 3 rows by 6 columns within the designated area in the beam. The stitching process and loading arrangement for T-

joint is shown in Figure 7.10 and for box-beam is shown in Figure 7.11. The diameter of each stitch is 10 mm and the distance between each stitch is 1.5 mm in both directions.

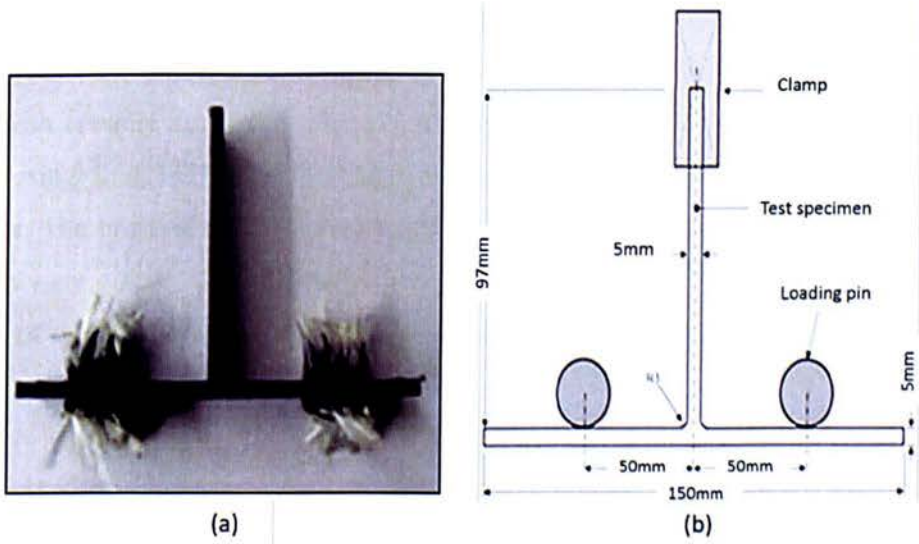

Fig. 7.10. (a) Stitching T-joint using yarns and (b) Loading arrangement in T-joint

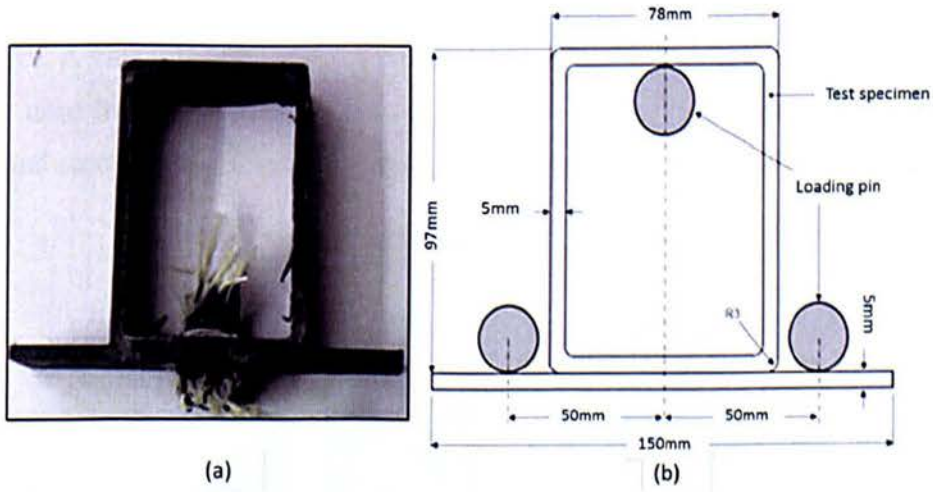

Fig. 7.11. (a) Stitching skin-stiffener using yarns, (b) Loading arrangement in box-beam

The specimens were put on a plate covered by non-stick PTFE layer and properly covered with breather cloth and placed in a vacuum bag. An air suction valve was inserted through the vacuum bag and a pipe connected the valve to a vacuum pump to evacuate the bag. To cure the specimens the temperature was initially raised to 80°C and held for 60 minutes and then increased to 140°C and held for 4 hours. This stepped heat-up meant the heat was raised gradually to 140°C instead of quickly, allowing the epoxy matrix to fully infuse the reinforcement before hardening. After curing, the specimen was left in the oven to cool down

to room temperature. Each specimen was labelled with the specimen lay-up and specimen number prior to testing. For bonded specimens, surface preparation was carried out by cleaning the bonding surfaces with acetone, and then sanded with 1000 grit silicon carbide paper. It was then immersed in dichromate sulphuric acid solution for 60min at 25°C and cleaned with acetone again and wiped in dry air at 40°C. The composite parts were bonded together using LOCTITE ESP110 adhesive and FRS6005 to make two types of T-joint specimens. The bead of adhesive was applied along the centre line of the bond area and the adherends were placed. A gentle pressure was applied to squeeze out the extra adhesive. The thickness of the adhesive was controlled as 0.5 mm. Metal spacers were used to maintain the required bond-line thickness.

7.4 Pull-out testing process

The three point quasi-static pull out test was performed on all specimens using 50kN Zwick universal testing machine. The test speed was set at 2 mm/min. As there were two different types of specimens (T-joint and box-beam), two different clamping were used as shown in Figure 7.12. A vice grip was attached to the machine which was common for all tests. Different jigs were used for the T-joint and box-beam, which would firstly prevent the specimens from slipping and secondly to centralise the load. Three tests were carried out for each joint.

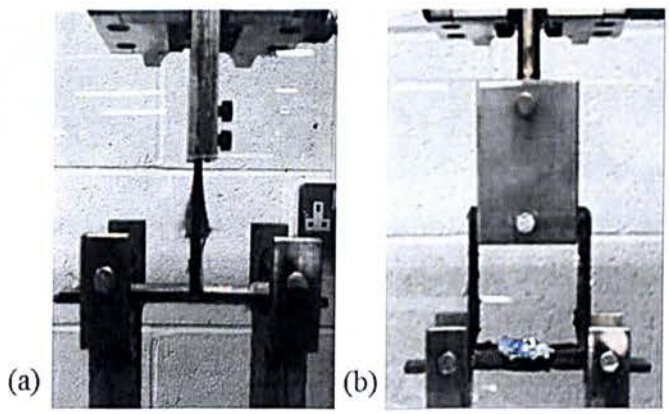

Fig. 7.12. Clamping techniques for (a) T-joint and (b) Box-beam.

7.5 Experimental results

7.5.1 Bonded and stitched T-joint

All the tests were continued until rupture of the joints as shown in Figure 7.13. The load-displacement results were obtained as shown in Figure 7.14. In the adhesively bonded T-joint

joint, the average maximum load was 457±18 N and the debonding initiated at a load of 20±6 N. The average maximum load of T-joint with FRS6005 adhesive was 391±20 N with a debonding initiated at a load of 25±12 N.

The behaviour of two types of adhesively bonded T-joints is compared in Figure 7.14. The average maximum load of these T-joint was 656±36 N with debonding initiated at a load of 16±4N.

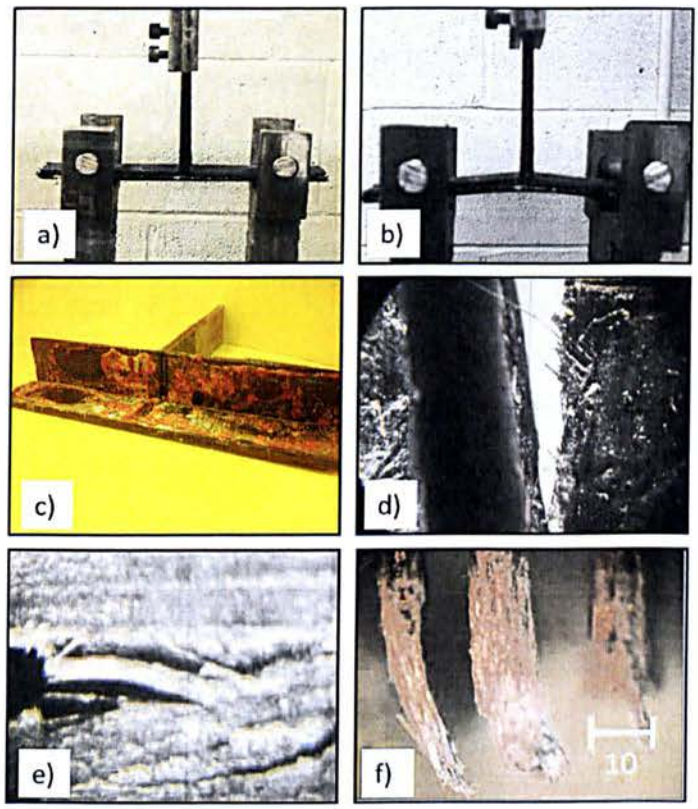

Fig. 7.13. Quasi-static pull out test (a) Adhesively bonded T-joint, (b) T-joint under load, (c) debonded adhesively bonded joint after test (light fibre tear failure), (d) Debonded area in spar T-joint specimen (e) Crack propagation at the interface and (f) Broken stitches.

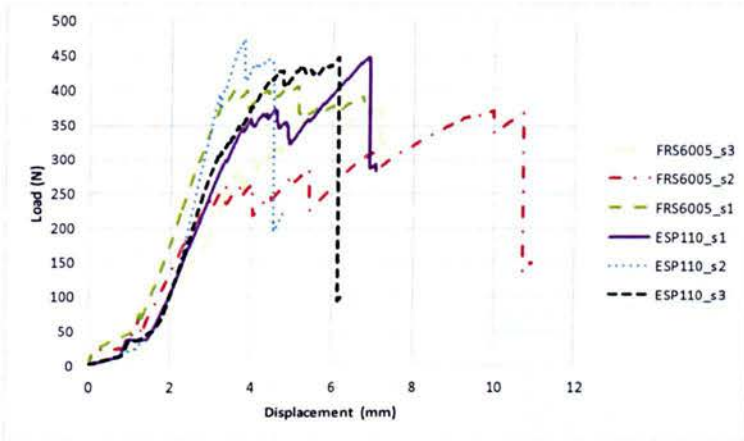

Fig. 7.14. Comparison of load-displacement for bonded T-joint using ESP110 and FRS6005 adhesives.

The second test was carried out on T-joint with three types of glass, carbon and Kevlar stitches. The average maximum load of 2267±253 N with a debonding initiated at a load of 614±23 N obtained for glass stitches. The average maximum load of 1460±150 N with a debonding initiated at a load of 641±34 N for carbon stitches and the average maximum load of 1523±17 N with a debonding initiated at a load of 610±40N for Kevlar stitches was observed (see Figure 7.15).

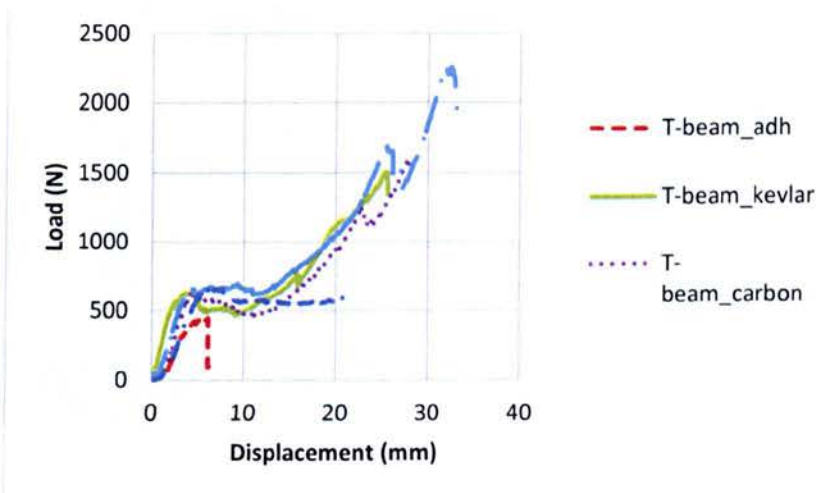

Fig. 7.15. Comparison of load-displacement results of adhesively bonded and glass, carbon and Kevlar stitched T-joints.

In all cases, the initial cracks appeared in the middle at the interface between the web and the flange. In case of adhesively bonded T-joint, the crack propagated extremely fast in the adhesive plane, which resulted in failure of adhesive bond. However, there had been interlaminar failure of the GFRP material in addition to the failure of the adhesive layer. More in depth observations

showed that there was transverse cracking in the web resulted in light-fibre-tear failure which occurs within the GFRP adherend, near the surface, characterized by a thin layer of the FRP resin matrix visible on the adhesive, with few or no fibre transferred from the adherend to the adhesive (see Figure 7.16).

Fig. 7.16. Cohesive failure through adhesive in bonded box-beam using FRS6005 epoxy adhesives.

7.5.2 Re-design of stitched T-joint

In T-joint at some stage of loading the delamination started from the bottom and along the centre of the web section. To rectify this problem the T-joint mould was modified and in the re-designed mould a 3 row by 6 columns stitching located at 30mm from the base is introduced through part B and part C. In T-joint with stitched web and flange, the average maximum load was 3760±160 N and the debonding initiated at a load of 500±38 N. Figure 7.17 compares the behaviour of re-designed T-joint with original stitched T-joint using glass fibre stitches.

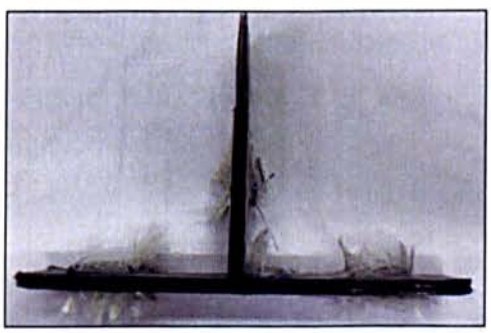

(a)

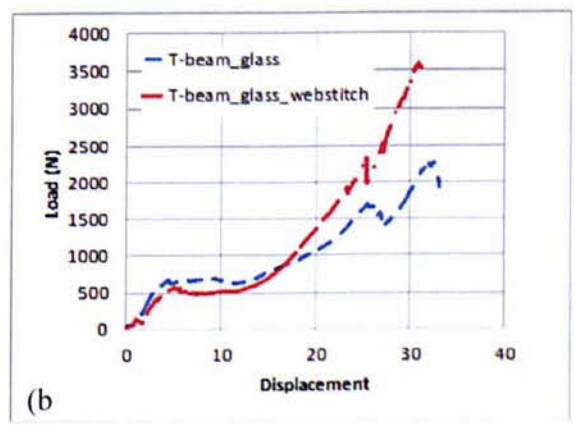

(b

Fig. 7.17. (a) Re-designing of stitched T-joint specimen; (b) Comparison between behaviour of re-designed T-joint with original stitched T-joint.

7.5.3 Bonded and stitched box-beam

The pull out test was carried out for bonded and stitched box-beams joints. The average maximum load of box-beam with ESP110 adhesives was 605±55 N with a debonding initiated at

a load of 50±15 N and the average maximum load of box-beam with FRS6005 adhesive was 533±50 N with debonding initiated at a load of 50±10 N.

The load-displacement for bonded box-beams is compared in Figure 7.18. For integrated box-beam the average maximum load was 1163±116 N with debonding initiated at a load of 105±85N.

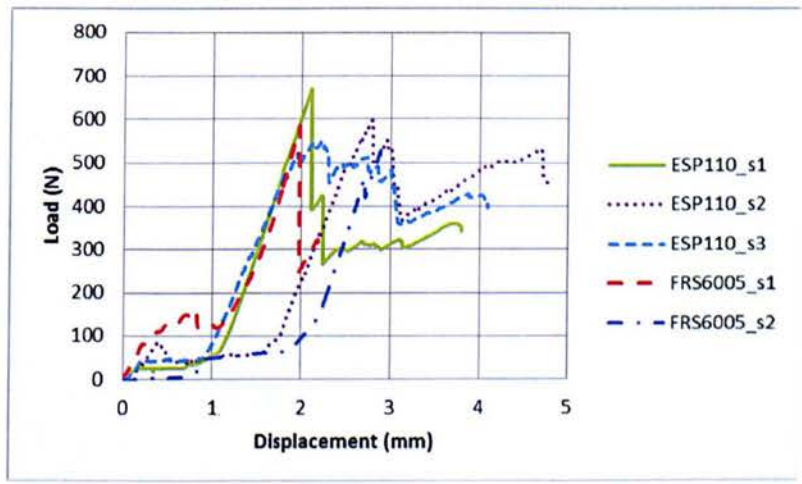

Fig. 7.18. Comparison of load-displacement for bonded box using ESP110 and FRS6005 adhesives

For stitched box-beam, the average maximum load of 2847±247 N and debonding initiated at a load of 740±40 N obtained for glass stitches. The average maximum load of 2933±63 N with debonding initiated at a load of 849±100 N for carbon stitches and the average maximum load of 3053±187N with debonding initiated at a load of 1006±20N for Kevlar stitches were recorded (see Figure 7.19). Figure 7.19 also shows that stitching improves the energy absorption capability.

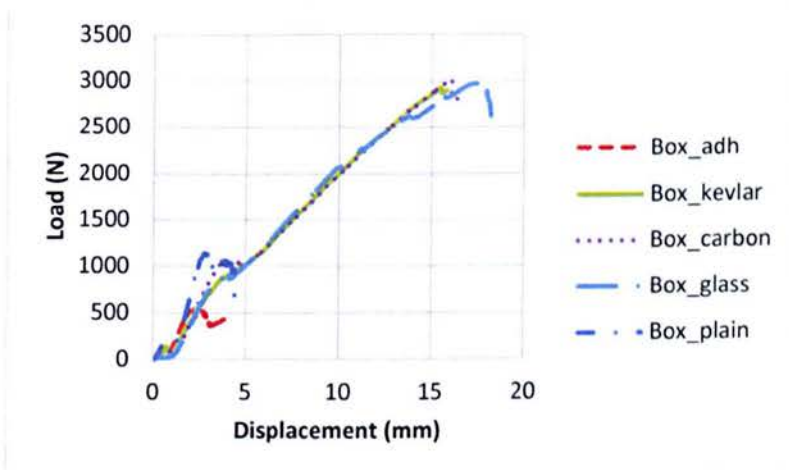

Fig. 7.19. Comparison of load-displacement results of ESP110 adhesively bonded and glass, carbon and Kevlar stitched box-beam joints.

In adhesively bonded box-beam specimens, the failure started with crack initiating from the bottom right hand corner and caused adhesive debond toward the centre. For some of the specimens the light-fibre-tear failure which occurs within the GFRP adherend, near the surface was observed.

In stitched box-beams the crack initially propagated from the edge towards the centre and then caused failure of stitched area in the beams. This then quickly caused global failure of the whole specimen (see Figure 7.20).

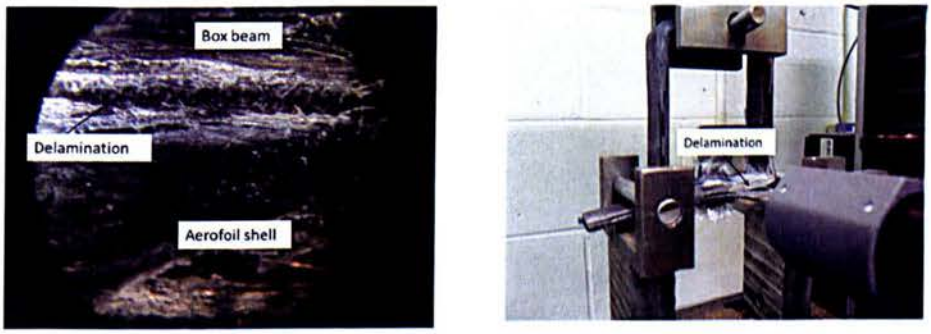

Fig. 7.20. Failure mechanisms of stitched box-beam

7. 6 Effect of stitching pattern on the T-joint strength

The effect of number of stitches and their arrangement on the T-joint strength were investigated. The glass fibres were used for stitching and arrays of 3×2, 3×3, 3×4 and 3×6 stitches were used (see Figure 7.21).

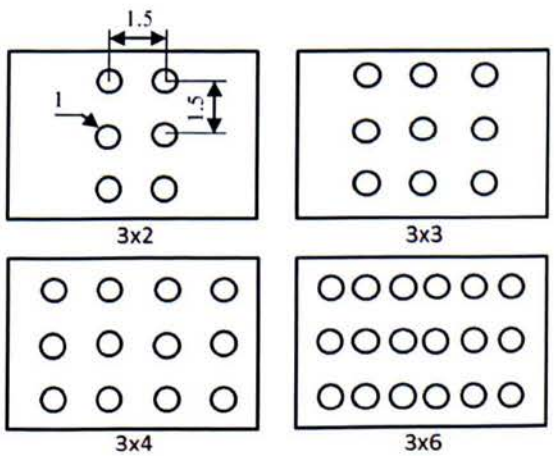

Fig. 7.21. Stitching combination for T-joint and box-beam. All dimensions in mm.

In T-joint with 3×2 stitches a maximum load of 1500 N with a debonding initiated at a load of 500 N, 3×3 stitching maximum load of 2100 N with a debonding initiated at a load of 550 N,

3×4 stitching maximum load of 2400 N with a debonding initiated at a load of 550N were recorded as can be seen in Figure 7.22. In Figure 7.23 the maximum load achieved before debonding were plotted against number of stitching column and 3×3 arrangement is the optimum one.

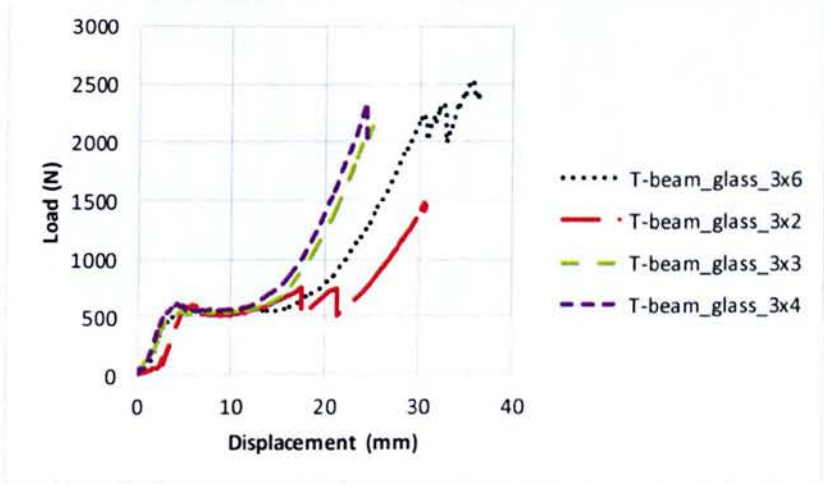

Fig. 7.22. Comparison of load-displacement for various glass fibre stitching combinations in T-joint.

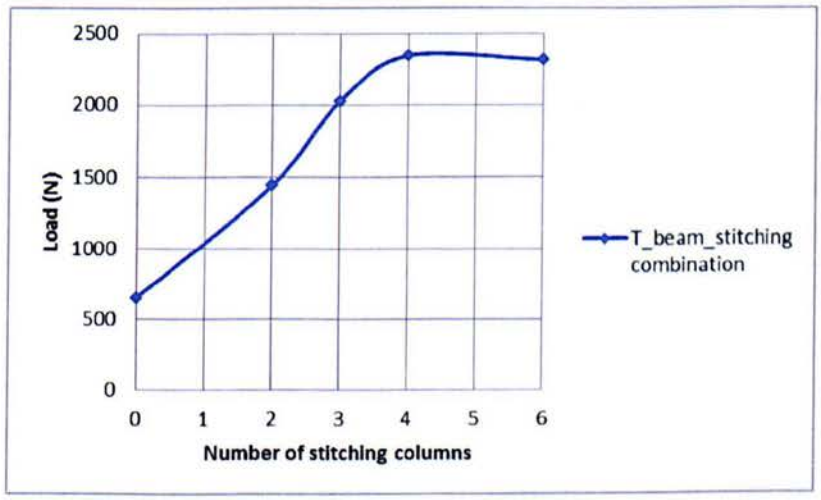

Fig. 7.23. Maximum load versus number of stitching columns in T-joint.

7.7 Effect of stitching combination on the box-beam joint strength

The crack in the stitched box-beam propagated up to the stitches where the crack arrested there (see Figure 7.24). In box-beam with 3×2 stitches a maximum load of 2000 N with a debonding initiated at a load of 800 N, 3×3 stitching maximum load of 2900 N with a debonding initiated at a load of 850 N, 3×4 stitching maximum load of 3100 N with a debonding initiated at a load of

850N were recorded as can be seen in Figure 7.25. In Figure 7.26 the maximum load achieved before debonding were plotted against number of stitching column and 3×3 arrangement is the optimum one and further increase of the number of stitches has no significant effect.

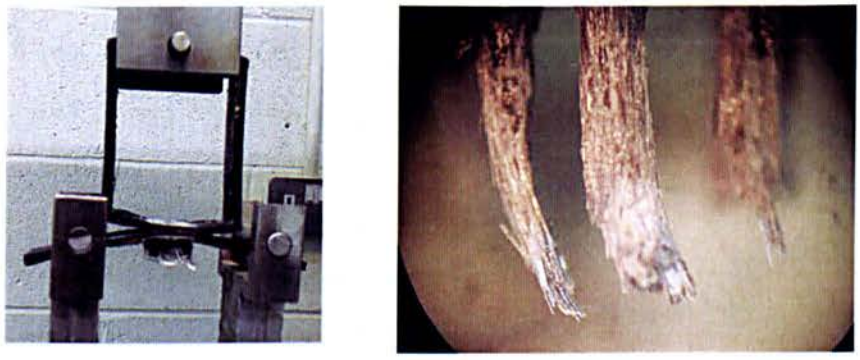

(a) (b)

Fig. 7.24. (a) Debonded stitched box-beam and (b) Failed glass stitched in box-beam.

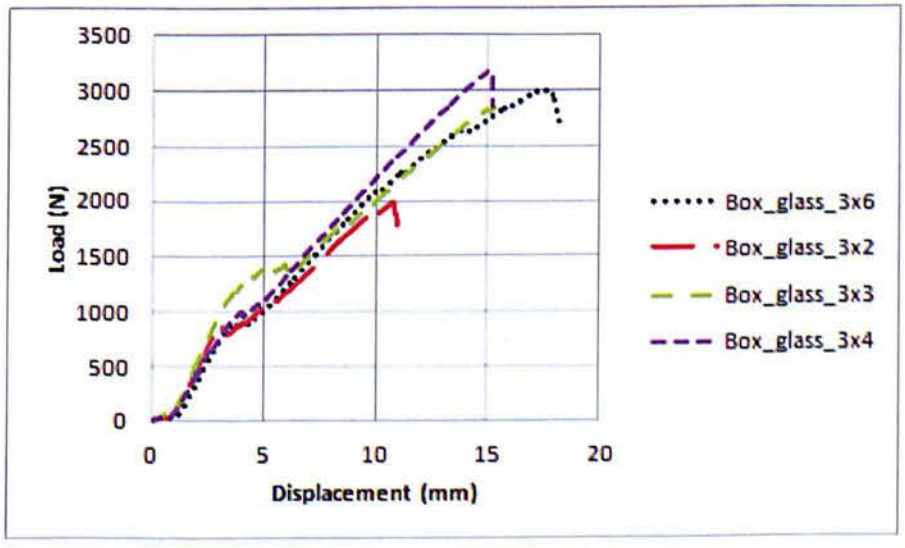

Fig. 7.25. Comparison of load-displacement for various glass fibre stitching combinations in box-beam joint.

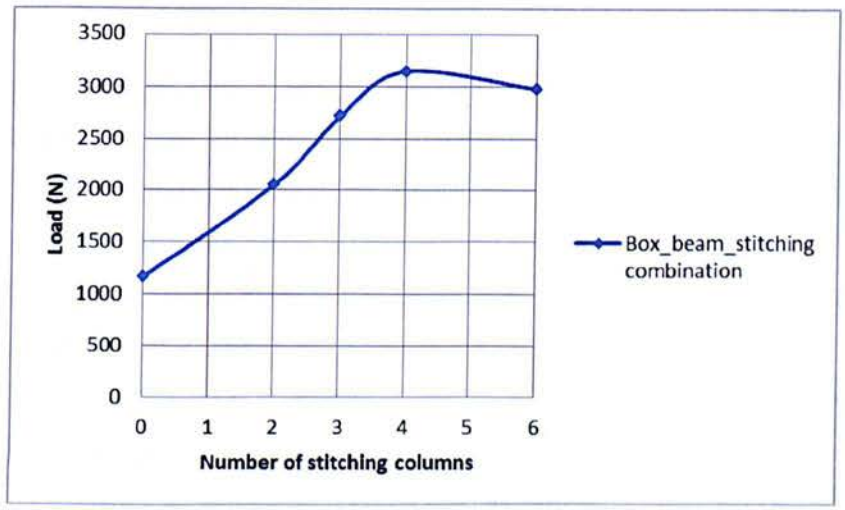

Fig. 7.26. Maximum load versus number of stitching columns in box-beam.

7.8 Conclusion

Two common designs in the wind turbine blade are attaching the aero-shell to the box girder or joining the shear webs to embedded spar cap in the aero-shell as a T-joint. As a result four different joint designs of (i) Bonded T-joint; (ii) Stitched T-joint; (iii) Bonded box-beam and (iv) Stitched box-beam were studied in this chapter. These specimens were tested under quasi-static loading condition to compare the strength and mode of failure in each joint.

Experimental results showed that the failure load and interlaminar fracture resistance increased significantly in stitched specimens very useful for application in wind turbine blade and other composite structures. It was also shown that stitching improves the energy absorption capability of the joints in wind turbine structures. T-joint re-designed by adding stitch along the web section. The test results showed the crack propagation delayed along the web and the flange. In addition to stitching the flange of T-joint, stitching the web of T-joint resulted in an increase of 23% in strength of the T-joint relative to a T-joint with only stitched flange.

Epoxy adhesive ESP110 and FRS6005 produced results less than expected when compared to integrated T-joint and box-beam.

The effect of number of stitch on strength of both T-joint and box-beam has also been studied and the results shows that the strength of both T-joint and box-beam increases by adding the number of stitch up to 3×3 and after that it remains plateau and further stitch has no measureable influence on the strength of the joints.

7.9 References

[1] Brøndsted, P., Lilholt, H., Lystrup, (2005) A. Composite Materials for Wind Power Turbine Blades. Annual Review of Materials Research;35:505-538.

[2] Sankar BV, Sharma SK. (1997) Mode II delamination toughness of stitched graphite/epoxy textile composites. Compos Sci Technol 57:729–37.

[3] Jain LK, Mai Y-W. (1994) On the effect of stitching on Mode I delamination toughness of laminated composites. Compos Sci Technol 1994;51:331–45.

[4] Jain LK, Dransfield KA, Mai Y-W. (1997) On the effects of stitching in CFRPs–II. Mode-II delamination toughness. Compos Sci Technol 58:829–37.

[5] Dransfield KA, Jain LK, Mai Y-W. (1997) On the effects of stitching in CFRPs–I. Mode Idelamination toughness. Compos Sci Technol 58:815–27.

[6] Gunnion AJ, Scott ML, Thomson RS, Hachenberg D. (2004) Thickness effects on the compressive stiffness and strength of stitched composite laminates. Compos Struct 66:479–86.

[7] Ghasemnejad H, Soroush VR, Mason PJ, Weager B, (2012) To improve impact damage response of single and multi-delaminated FRP composites using natural Flax yarn, in 'Materials and Design, 36:865–873.

[8] Beylergil B, Cunedioglu Y, Aktas A, (2011) Experimental and numerical analysis of single lap composite joints with inter-adherend fibre. Composites: Part B; 42:885–1896.

[9] Tong L, Steven GP. (1999) Analysis and design of structural bonded joints. Kluwer Academic Publishers.

[10] Tong L. (1998) Strength of adhesively bonded composite single lap joints with embedded cracks. AIAA J 36(3):448–56.

[11] Yudhanto A., Watanabe N., Iwahori Y., Hoshi H., (2013) Effect of stitch density on tensile properties and damage mechanisms of stitched carbon/epoxy composites, Composites Part B: Engineering, Volume 46, March, Pages 151-165

[12] Tan K.T., Watanabe N., Iwahori Y., Ishikawa T., (2012) Effect of stitch density and stitch thread thickness on compression after impact strength and response of stitched composites, Composites Science and Technology, Volume 72, Issue 5, Pages 587-598

[13] Tan K.T., Yoshimura A., Watanabe N., Iwahori Y., Ishikawa T., (2013) Effect of stitch density and stitch thread thickness on damage progression and failure characteristics of stitched composites under out-of-plane loading, Composites Science and Technology, Volume 74, Pages 194-204

[14] Tan K.T., Watanabe N., Iwahori Y. (2010) effect of stitch density and stitch thread thickness on low-velocity impact damage of stitched composites. Composites: Part A, 41:1857-1868.

[15] Wood M.D.K., Sun X., Tong L., Katzos A., Rispler A.R., Mai Y.W., (2007) The effect of stitch distribution on Mode I delamination toughness of stitched laminated composites – experimental results and FEA simulation, Composites Science and Technology, Volume 67, Issue 6, Pages 1058-1072

[16] Lopresto V., Melito V., Leone C., Caprino G., (2006) Effect of stitches on the impact behaviour of graphite/epoxy composites, Composites Science and Technology, Volume 66, Issue 2, Pages 206-214

[17] Potluri P., Kusak E., Reddy T.Y., (2003) Novel stitch-bonded sandwich composite structures, Composite Structures, Volume 59, Issue 2, Pages 251-259

[18] Chun H.J., Kim H.W., Byun J.H., (2006) Effects of through-the-thickness stitches on the elastic behavior of multi-axial warp knit fabric composites, Composite Structures, Volume 74, Issue 4, Pages 484-494

[19] Hosur, M.V., Vaidya, U.K., Ulven, C., Jeelani, S., (2004) Performance of stitched/unstitched woven carbon/epoxy composites under high velocity impact loading, Composite Structures 64 (3-4) , pp. 455-466

[20] Mouritz AP, Cox BN. (2010) A mechanistic interpretation of the comparative in-plane mechanical properties of 3D woven, stitched and pinned composites. Composites: Part A; 41:709–728.

[21] Childress JJ, Freitas G, (1992). Z-direction pinning of composite laminates for increased survivability. In: Proceedings of the AIAA aerospace design conference. Irvine, California, February. p. 92–109.

[22] Freitas G, Magee C, Dardzinski P, Fusco T. (1994) Fibre insertion process for improved damage tolerance in aircraft laminates. J Adv Mater 25:36–43.

[23] Freitas G, Fusco T, Campbell T, Harris J, Rosenberg S. (1996). Z-fibre technology and products for enhancing composite design. In: Proceedings of the 83rd meeting of the AGARD SMP conference on bolted/bonded joints in polymeric composites, paper 17, Florence Italy; 2–3 September.

[24] Partridge IK, Cartie DDR, Bonnington T. (2003) Manufacture and performance of z-pinned composites. In: Shonaike G, Advani S, editors. Advanced polymeric composites. FL: CRC Press.

[25] Partridge IK, Cartie′ DDR, Troulis M, Grassi M. and Zhang, X. (2004) Evaluating the mechanical effectiveness of z-pinning. In: Proceedings of the SAMPE technical conference. September.

[26] Rugg KL, Cox BN, Massabò R. (2002) Mixed mode delamination of polymer composite laminates reinforced through the thickness by z-fibre. Composites 33:177–90.

[27] Owsley GS. (2000) The effect of z-fibre™ reinforcement on fatigue properties of stiffened composite panels. In: Proceedings of the 15th technical conference on the American society of composites, Texas.

[28] Partridge IK, Cartie DDR, Bonnington T. (2003) Manufacture and performance of z-pinned composites. In: Shonaike G, Advani S, editors. Advanced polymeric composites. FL: CRC Press.

[29] Papadopoulos, F., Aiyappa, D., Shapriya, R., Sotirchos, E., Ghasemnejad, H. and Benhadj-Djilali, R. (2012) Advanced natural stitched composite materials in skin-stiffener of wind turbine blade structures. Key Engineering Materials, 45-48.

[30] Ghasemnejad H, Occhineri L, Swift-Hook DT, (2011) Post-buckling failure in multi-delaminated composite wind turbine blade materials, in 'Materials and Design, 32(10): 5106–5112.

[31] Sørensen B. F., (2009) Materials and structures for wind turbine rotor blades - an overview, proceeding of ICCM-17 17th International Conference on Composite Materials, Edinburgh, UK.

[32] BS EN ISO 2747, (1998) Glass Fibre Reinforced Plastics-Tensile Test, British Standard Institute, London.

[33] BS EN ISO 14129, (1998) Fibre Reinforced Plastics Composite-Determination of the In-plane Shear Stress/Shear Strain Response, Including the In-plane Shear Modulus and Strength by the ±45 Tension Test Method, British Standard Institute, London.

[34] ASTM D 3171-99, (2002) Standard test method for constituent content of composite materials. Annual book of ASTM standards, West Conshohocken, PA.

8

Conclusions and recommendations for further work

The results of the outcome of this study will be elaborated in this chapter in accordance to the objectives set out in Chapter 1. The research work is a continuing process and many lessons have been learnt from this project. At the end of this chapter from the lesson learnt suggestions will be made for further development on structural performance of wind turbine blades.

8.1 Conclusions

The power from wind turbines is proportional to the swept area of the blades. The trend of wind turbine powerplants is toward bigger swept area and as a result longer blades. At the present time the longest wind turbine blades, at 83.5m were manufactured by SSP Technology of Kirkeby, Denmark for Samsung Heavy Industries (SHI) on July 2013, for the installation on a 7 MW offshore turbine in Scotland. The blade is a cantilever beam connected to the hub and at such a length that the minimisation of the weight of the blades is a major design objective. Apart from laminated FRP materials it is hardly possible to find any other suitable material for such a situation. Laminated composite materials with high specific stiffness and specific strength are used in spar-cap, aerofoil-shell and webs of the blade. However laminated FRP materials are susceptible to delamination, i.e. separation of the plies in the low resistance thin resin-rich interface between adjacent layers particularly under

compressive loading, impacts or free-edge stresses. Also high stress gradients near geometric discontinuities in the structures such as holes, cut-outs, flanges, ply drop-offs, stiffener terminations, bonded and bolted joints promote delamination initiation. Delamination is also caused by the existence of contaminated fibres during the manufacturing process, insufficient wetting of fibres, out of plane impact and curing shrinkage of the resin. Under fatigue loading, the main causes of failure of composite wind turbine blades are delamination, debonding, matrix cracking, compression failure, buckling driven delamination, and split cracks on the surface. The wind turbine designers must be aware of the behaviour of delaminated structures and take into account the delamination properties during the design stage of the blade as the presence and growth of delamination significantly reduces the overall buckling strength and bending stiffness of a structure.

As a result understanding the delamination behaviour under monotonic and fatigue loading under different fracture modes and improving the resistance of FRP laminate to delamination is quite important and these areas becomes the focus of this research. By understanding these factors in FRP it is then logical to understand structural response of a full scale wind turbine blade under cyclic loading. Wind turbine blades are a key component of a wind turbine that is why they are tested thoroughly to ensure design specifications are consistent with the actual performance of the blade. The blade under test must demonstrate that it can withstand both the ultimate loads and the fatigue loads. The test must demonstrate loading conditions which the blade would be subjected to during its estimated service life.

In Chapter 3 three test methods for characterisation of delamination fracture toughness of FRP composite materials are discussed. These tests are Double Cantilever Beam (DCB) for pure mode I delamination, 3 points End-Notched Flexure (3ENF) test for pure mode II delamination and Mixed-Mode Bending test (MMB) for mixed mode I/II delamination. For each test method, various available methods for analysis of the test results were presented and the results obtained from experiments of each method were compared.

By using these three test methods, the delamination fracture envelope under various loading conditions, from pure mode I (DCB) to various mode mixity to pure mode II (ENF) has been established. By obtaining the delamination failure envelope for the UD GFRP material used in this project, it is possible to predict the safe/fail status of any laminate under various static

loading conditions. The delamination envelope is an essential tool for the application of the FRP material in different products.

In Chapter 4 different aspects of fatigue of GFRP were investigated. Firstly the fatigue life of the GFRP was studied based on S-N diagram. Experiments on three different types of loading, i.e. tension-tension at R=0.1, 0.5, tension-compression at R=-1 and compression-compression at R=2 and R=10 have been performed. The S-N diagram for various R ratios shows a nearly linear behaviour with a fatigue *limit of around* 40%. From the S-N diagram data the CLD diagrams for 90° and 0° fibre directions have been constructed. From the CLD diagrams a fatigue life under other loading condition that the test has not been conducted can be estimated.

Secondly the onset life and propagation delamination crack growth of 0//0 interface of GRFP laminate in mode I and mode II loading using DCB and ENF specimens were investigated. In mode I the G_{Ith} from the onset life tests was determined to be 0.16 G_{IC}. For this mode from the fitted curve to experimental propagation data the Paris' law coefficients for the laminated GFRP were determined. Also the fatigue crack propagation in mode II is analysed based on application of Paris' law as a function of energy release rate. From the fitted curve to experimental propagation data the Paris' law coefficients for mode II for the laminated GFRP were obtained.

The fractographic analysis of images under mode II monotonic loading show that the fibres debonded at interface and no visible matrix remains on the debonded fibres. However the images of fatigued surfaces show that the fibres debonded cohesively through the matrix and remains of the matrix on the debonded fibres are visible. Also the size of matrix fragments on monotonic loading is many times bigger than those of fatigued ones. In both monotonic and fatigued surfaces the typical fibre bridging as well as broken fibres can be observed. Fibre/matrix interface decohesion plays a major role on delamination growth mechanism.

The blades are one of the most critical components of the wind turbines and the structural integrity of the whole wind turbine depends on the blade. Therefore, they have to be tested in order to ensure that their specifications are consistent with the actual performance of the blade. It must be verified that the blade can withstand both the ultimate loads and the fatigue

loads to which the blade is expected to be subjected during its design service life. Testing of the wind turbine blades statically and dynamically helps in improving the designs and the manufacturing processes.

There are two main types of fatigue testing, single-axis testing and dual-axis testing. In single-axis testing loading is applied either in flapwise or edgewise direction. By contrast, in dual-axis testing loads are applied simultaneously to both flapwise and edgewise directions. In the current work single-axis testing has been used. The blade cyclic loading is applied by a resonance exciter system sitting on the blade. The fatigue is conducted at resonant frequency just below the first natural frequency of the blade. Therefore it is essential to measure the natural frequencies of the blade. All these issues have been dealt in Chapter 5.

For fatigue testing of a full scale blade, moment-strain and the modal analysis of the blade are required. The magnitude of strain for monitoring the target bending moment at the root of the blade has been obtained by performing the calibration pull test. Because part of the project was sensitivity of blade structure to damage, a 200mm crack has been inserted at a distance of 9m from the root of the blade between the shear web and spar cap. As a continuation of the sensitivity analysis the crack length has been extended to 1000mm. For each of these cases the measured strain at specific positions was calibrated to the appropriate applied bending moment at the root of the blade. These reading are the controlling parameter for the fatigue test which has been done at a later stage.

Acoustics emission (AE), as one of the effective NDT techniques, was used to indicate the location and onset of damage during loading. This has the potential for investigation into the causes and growth of the various damage types.

Modal testing is a crucial experiment to measure the blades natural frequencies over a range of frequency domains. At each stage before and after crack insertion the modal testing has been done in flapwise and edgewise directions. The first mode of undamaged blade natural frequency and 0.2m induced crack damage blade remained at 0.562Hz and remained unchanged for the 1m induced crack damage but the first natural frequency had changed slightly for 1m induced crack damage with added weight by 0.006Hz. The fatigue was conducted at resonant frequency just below the first natural frequency of the blade.

The results of the calibration tests and modal analysis were used for full scale testing of the wind turbine blade as discussed in Chapter 6. It is established that under fatigue loading the locations of most damage and cracks are between 60-75% of blade length from root where the web ends. But no damage was found within the web. Therefore in future designs this area should be reinforced properly.

On damage sensitivity investigation initially a 0.2m crack induced at 9m by deboning the web from spar cap and the crack did not propagate at 50% of the target bending moment under cyclic loading. When the load increased to 70% of target bending moment, some damage have been detected on the pressure side of the aero-shell of the blade. However the 0.2m crack did not propagate under these conditions up to 62,110 cycles.

For further investigation the crack at 9m from the root was extended to 1m. The crack began to propagate only when the applied load exceeded 100% of target bending moment. The blade experienced delamination around the induced crack tip at the C web, adhesive joint failure on the outside web, compression failure and sandwich debonding on the inside web, and delamination was visible on the web just below the induced crack. These findings indicate that there have been high stresses around 9m web due to the induced crack. The understanding of how the damage starts up (for example by delamination) is essential for the strength of the blade and very difficult to decide in a full scale test even though the location of the damage is known.

Different spar designs such as C-channel, I-beam, box-beam are used in wind turbines blades. The strength and stability of joining these shear web to spar cap is very important factor for lasting life of the blade. In Chapter 7 improving the joint strength of aero-shell to the box girder or the shear webs to the embedded spar cap in the aero-shell as a T-joint were investigated. As a result four different joint designs of (i) Bonded T-joint; (ii) Stitched T-joint; (iii) Bonded box-beam and (iv) Stitched box-beam were manufactured and tested under quasi-static loading condition to compare the strength and mode of failure in each joint.

Experimental results showed that the failure load and interlaminar fracture resistance increased significantly in stitched specimens, very useful for application in wind turbine blade and other composite structures. It was also shown that stitching improves the energy absorption capability of the joints. The T-joint design further improved by adding stitch along the web section. The

test results on the improved design showed the crack propagation delayed along the web and the flange. In addition to stitching the flange of the T-joint, stitching the web of the T-joint resulted in an increase of 23% in strength of the T-joint relative to a T-joint with only flange stitched.

The effect of the number of stitches on the strength of both the T-joint and the box-beam has also been studied and the results shows that the strength of both the T-joint and the box-beam increases by adding the number of stitch up to 3×3 and after that it remains plateaued and further stitches have no measureable influence on the strength of the joints.

8.2 Future work

The recommendations for future work are outlined below:

i) The interlayer plays an important role on increasing the interlaminar toughness of laminated composite plate. Research on finding a suitable interlayer is crucial for furthering the interlaminar toughness.

ii) The toughness of the matrix can be improved by adding novel nanoparticles to the matrix. This has potential in increasing the delamination toughness of FRP materials. Work on finding more efficient nanoparticles is of particular interest in wind turbine industry as the trend of growth of blade diameter will continue and the demand for a tougher and stiffer laminate will increase.

iii) An in-situ damage detection technique should be developed to remotely monitor the structural health of offshore wind turbines.

iv) Delamination fatigue tests in Mode I (DCB), Mode II (ENF) and mixed Mode I/II (MMB) under environmental conditions (e.g. humidity, temperature and salty water) needs further works. The work done on this project was in air without any control on the humidity.

v) Finite element simulation of the fatigue process for a full scale blade and verification of the results with the full scale tests.

vi) Although there are one piece blade designs in the market, the majority of the blade manufacturers still use adhesive for bonding various pieces of blade together (e.g. spar to the shell aerofoil). Therefore there is quite a lot of room for advancing joint design for wind turbine blades.

Appendix A: Mechanical Characterisation of GFRP Material

A1. Introduction

The GFRP material used for all specimens tested in Chapters 3, 4 and 7 of this project was UD prepreg glass fibre/epoxy matrix E722-02 UGE400-02 material supplied by TenCate Ltd.

Experimental tensile tests have been conducted to find E_{11}, ν_{12}, E_{22}, ν_{21}, G_{12}, Xt, Yt and S for 0°, 90° and ±45° laminates according to ASTM D3039/ D3039 [1] and ASTM D3518/ D3518M [2] standards.

A2. Manufacturing processes

The hand lay-up with vacuum bagging technique was used for manufacturing of laminates as described below. After the laminated plate was cured, the DCB, ENF, MMB, tensile and compression specimens were cut from the laminate.

Instruction: Cover an aluminium plate with PTFE film; make sure there are no scratches on PTFE, Figure A.1(a). Mark GFRP plies to the required size, place one ply onto the aluminium plate, before doing so, remove the plastic lining from one side as shown in Figure A.1(c). Using a roller, apply force onto the laminate strip and roll out all the air bubbles, Figure A.1(d). When doing so, remove the non-stick plastic lining from the other side and repeat this process for all plies. Cover the laminate layers with another aluminium plate and coat both plates using nylon and light weight breather fabric, secure edges tightly using none flammable tape. For the vacuum bag processes, place the two plates on a heavy-duty vacuum bag then place a valve at the centre of the plate and seal the edges by using rubber tape and extract the air using a vacuum pump. The curing cycle for the GFRP was 30min at 90°C and then increased to 130°C for 60min. After curing, the plate is cut roughly to the specified dimension using a band saw and then they made to precise dimension by milling machine. The dimensions for tensile specimens are shown in Figure A.2. For these specimens, mild steel end tabs with dimension of 1.5×23×50mm were manufactured for gripping the specimen onto the jaws of tensile testing machine. Epoxy adhesive EPS110 is used to bond the end tabs to each specimen, with a curing time of 45min at 150°C. Figures A.1 shows the various stages of manufacturing processes of tensile specimens.

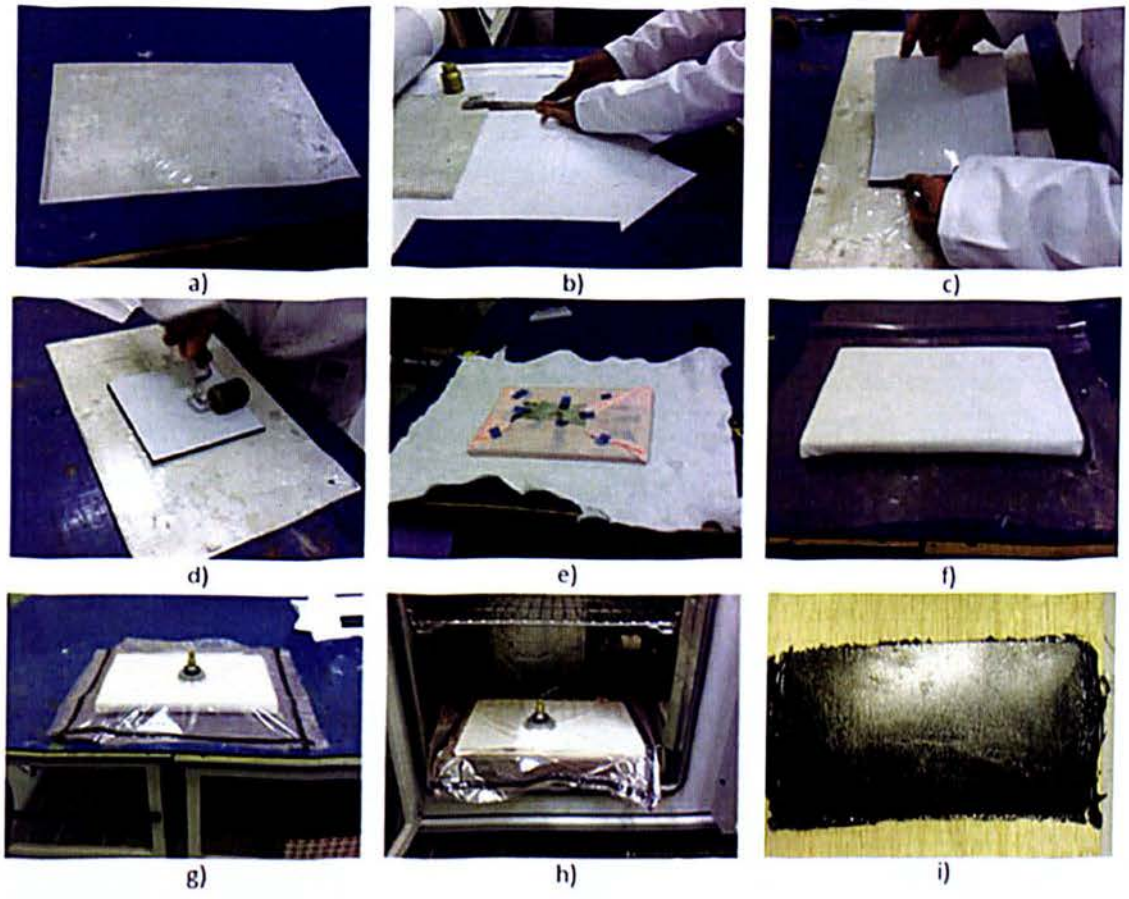

Fig. A.1. a) Aluminium plate, b) Marking GFRP plies, c) Placing plies on the plate, d) Rolling out the air bubbles, e) Wrapping the mould with light weight breather fabric, f,g) Vacuum bagging, h) Attaching the valve to vacuum pump in the oven, i) Laminate after curing.

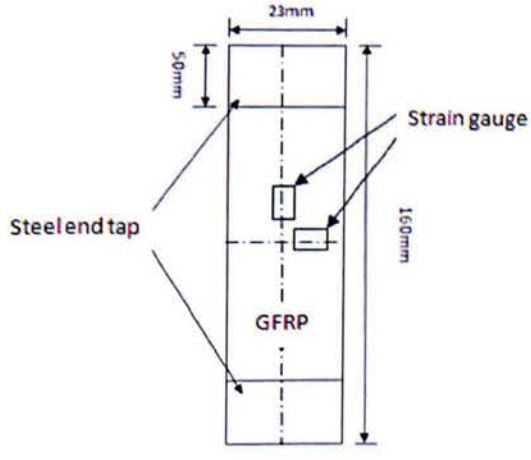

Fig. A.2. Location of strain gauges on tensile specimen and specimen dimension.

A3. The procedure for installation of strain gauges

The proper procedure for installation of strain gauges is as follows:

Mark-out the centre of each specimen at half the length and half the width of the specimen, then clean the surface of the test specimen to ensure no dirt will be trapped between the surface and strain gauge using an M-line rosin solvent. Place strain gauge on the specimen at the centre of the longitudinal direction using tape as shown in Figure A.3(a). Peel the strain gauge back cover and apply a 200 catalyst M-Bond adhesive for thirty seconds to accelerate the gluing process. Then apply M-Bond 200 (glue) at the desired location where the strain gauge required and apply an even pressure over the strain gauge for about two minutes until the adhesive set. Remove the tape from the strain gauge and clean it using M-line rosin solvent to remove any tape residue on the gauge surface. The same process is repeated for the transverse direction as shown in Figure A.3(b) and also for the rosette strain gauge for ±45° shown in Figure A.3(c).

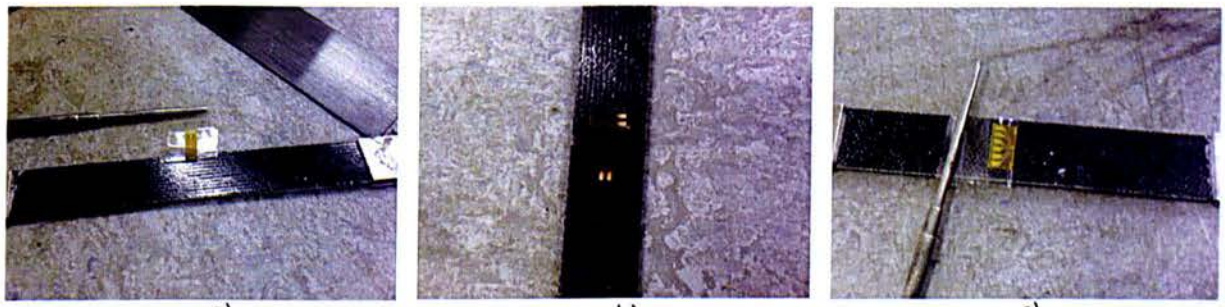

a) b) c)

Fig. A.3. a) Applying M-Bond adhesive, b) Strain gauges in longitudinal and transverse directions, c) Attaching a rosette strain gauge for ±45 specimens.

Figures A.4 and A.5 show the stress-strain response for 0° and 90° specimens. The Young's modulus, Poisson's ratios and tensile strength in fibre and normal to fibre directions E_{11}, ν_{12}, E_{22}, ν_{21}, Xt, Yt were found from these figures. Figure A.4 shows shear stress-shear strain response for ±45° specimens. Shear modulus G_{12} and shear strength S were found from this graph.

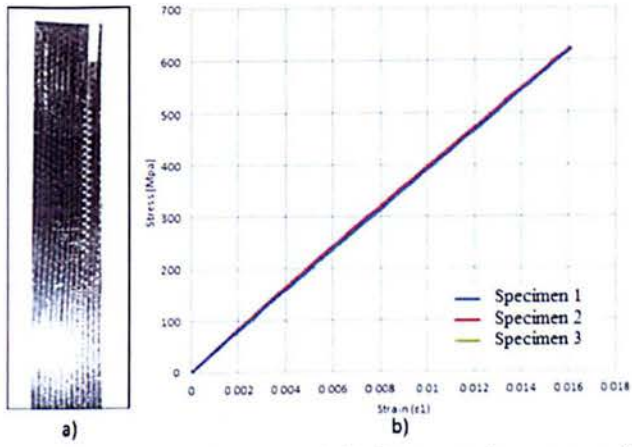

Fig. A.4. (a) Test specimen after failure and (b) Stress-strain response for 0° laminates.

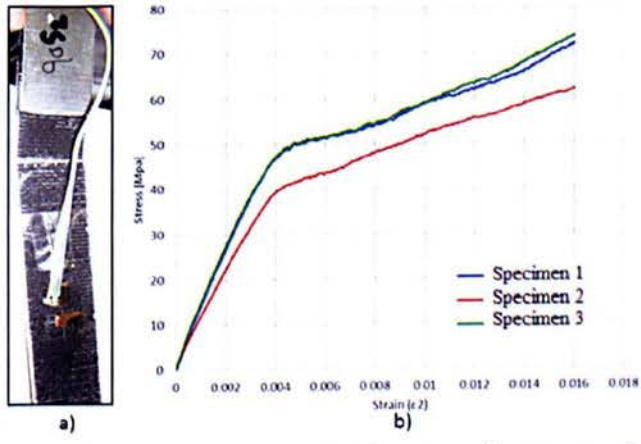

Fig. A.5. (a) Test specimen after failure and (b) Stress-strain response for 90° laminates.

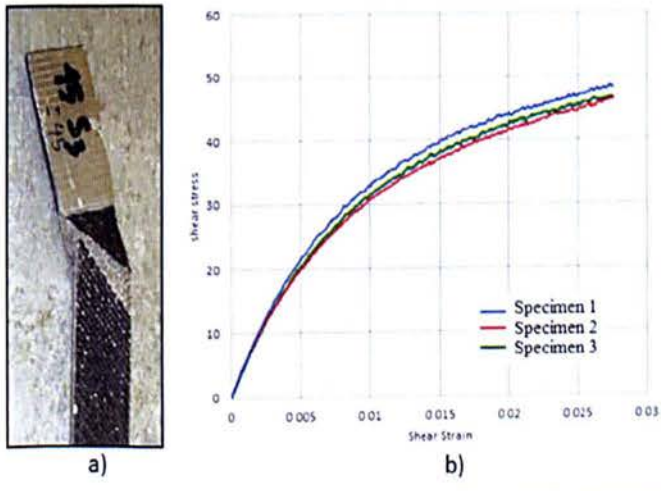

Fig. A.6. (a) Test specimen after failure and (b) Shear stress-shear strain response for ±45° laminates.

Table A.1 shows the summary of mechanical properties of GFRP, providing information for longitudinal Young's modules, E_{11}, transverse Young's modules, E_{22}, Poisson's ratios, ν_{12} and ν_{21}, shear modules, G_{12}, tensile strength in the fibre direction, Xt, tensile strength normal to fibre direction, Yt and shear strength, S.

Table A.1. GFRP material properties

Specimen	E_{11} (GPa)	E_{22} (GPa)	ν_{12}	ν_{21}	G_{12}	Tensile strength Xt (MPa)	Tensile strength Yt (MPa)	Shear strength S (MPa)
1	**38.8**	**14.0**	**0.24**	**0.09**	**5.2**	**611**	**71.5**	**48.5**
2	39.2	11.6	0.24	0.08	5.0	623	61.6	46.5
3	**38.8**	**13.9**	**0.23**	**0.1**	**4.8**	**622**	**73.5**	**46.6**
Average	**38.9±0.2**	**13.0 ±1.5**	**0.24±0.01**	**0.09±0.01**	**5.0±0.2**	**619±6**	**69±6**	**47±1**

A4. Burn out test

Burn out test is conducted according to ASTM D2584 [3] standard. Three cubic specimens were cut from a laminated plate manufactured and cured in the same way as for tensile and delamination specimens. Initially a crucible is heated to 600°C for 10 min and then cooled to room temperature in a desiccator and weigh to the nearest 1.0 mg. Next the specimen is placed in the crucible and weighted then put in a Bunsen flame and heated the crucible and specimen at 575°C for 3 hours until the specimen burned at a uniform and moderate rate until only fibres remain when the burning completed. Finally, the crucible cooled down to room temperature in a desiccator and the weight of the remaining content (fibres) measured (see all steps as shown in Figures A.7).

Burn out test calculations

Table A.2 shows the experimental results for mass of composite, mass of fibre, fibre weight fraction and fibre volume fraction for the three specimens. These were calculated from:

% of fibre weight fraction $w_f = \frac{M_f}{M_c} \times 100$

% of fibre volume fraction $v_f = \frac{V_f}{V_c} \times 100 = \frac{\frac{M_f}{\rho_f}}{V_c} \times 100 = \frac{M_f}{V_c \times \rho_f} \times 100$

where V_c is volume of composite, M_f mass of fibre (measured after burning), M_c mass of composite (measured before burning), and E-glass fibres density ρ_f =2600 kg/m^3.

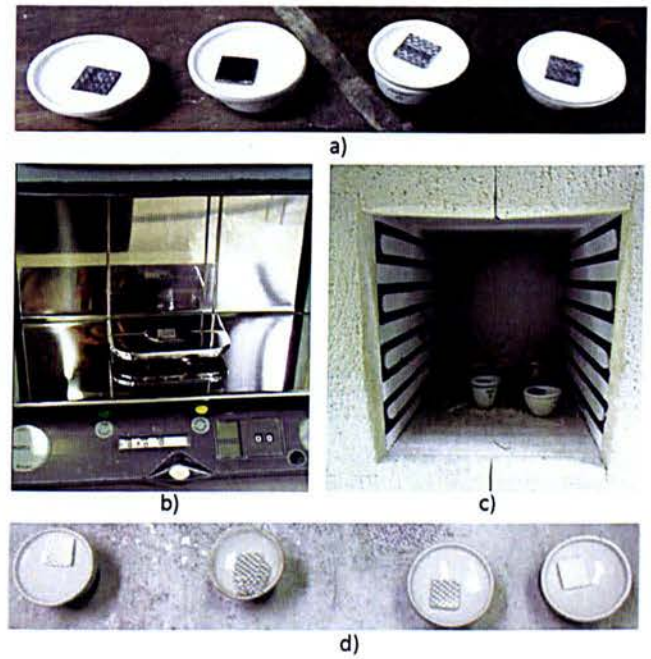

Fig. A.7. (a) Specimens before burning on the crucible, (b) Measuring specimen weight, (c) Specimens in the furnace, (d) Remain of glass fibres after burn out test.

Table A.2. Burn out test results

Sample	M_c (g)	V_c (mm^3)	M_f (g)	w_f (%)	v_f (%)
1	0.83	420	0.67	80.7	61.47
2	0.84	417	0.68	81.0	62.90
3	0.93	486	0.74	79.6	58.45
Average				**80.4±0.7**	**61±2**

A.5 References

[1] ASTM Specification D3039/D3039M. (2006). Standard test method for tensile properties of polymer matrix composites. Conshohocken, PA: ASTM International .

[2] ASTM Specification D3518/3518M. (2007). Standard test method for in-plane shear response of polymer matrix composite materials by tensile test of a +-45 laminate. Conshohocken, PA: ASTM International.

[3] ASTM Specification D2584. (2002). Standard test method for ignition loss of cured reinforced resins. Conshohocken, PA: ASTM International .